High-Performance Computing of Flow, Diffusion, and Hydrodynamic Dispersion in Random Sphere Packings

Dissertation zur Erlangung des Doktorgrades
der Naturwissenschaften (Dr. rer. nat.)
dem Fachbereich Chemie
der Philipps-Universität Marburg

vorgelegt von

Siarhei Khirevich

aus Gomel, Belarus

Marburg an der Lahn 2010

Vom Fachbereich Chemie
der Philipps-Universität Marburg
als Dissertation am 14. Januar 2011 angenommen

Erstgutachter:	Prof. Dr. Ulrich Tallarek
Zweitgutachter:	Prof. Dr. Andreas Seubert
Prüfungskommission:	Prof. Dr. Bruno Eckhardt
	Prof. Dr. Karl-Michael Weitzel

Tag der mündlichen Prüfung am 21. Januar 2011

Abstract

This thesis is dedicated to the study of mass transport processes (flow, diffusion, and hydrodynamic dispersion) in computer-generated random sphere packings. Periodic and confined packings of hard impermeable spheres were generated using Jodrey–Tory and Monte Carlo procedure-based algorithms, mass transport in the packing void space was simulated using the lattice Boltzmann and random walk particle tracking methods. Simulation codes written in C programming language using MPI library allowed an efficient use of the high-performance computing systems (supercomputers).

The first part of this thesis investigates the influence of the cross-sectional geometry of the confined random sphere packings on the hydrodynamic dispersion. Packings with different values of porosity (interstitial void space fraction) generated in containers of circular, quadratic, rectangular, trapezoidal, and irregular (reconstructed) geometries were studied, and resulting pre-asymptotic and close-to-asymptotic hydrodynamic dispersion coefficients were analyzed. It was demonstrated i) a significant impact of the cross-sectional geometry and porosity on the hydrodynamic dispersion coefficients, and ii) reduction of the symmetry of the cross section results in longer times to reach close-to-asymptotic values and larger absolute values of the hydrodynamic dispersion coefficients. In case of reconstructed geometry, good agreement with experimental data was found.

In the second part of this thesis i) length scales of heterogeneity persistent in unconfined and confined sphere packings were analyzed and correlated with a time behavior of the hydrodynamic dispersion coefficients; close-to-asymptotic values of the dispersion coefficients (expressed in terms of plate height) were successfully fitted to the generalized Giddings equation; ii) influence of the packing microstructural disorder on the effective diffusion and hydrodynamic dispersion coefficients was investigated and clear qualitative corellation with geometrical descriptors (which are based on Delaunay and Voronoi spatial tessellations) was demonstrated.

Zusammenfassung

Die vorliegende Arbeit beschäftigt sich mit Stofftransport durch Druckfluss, Diffusion und die aus beiden Prozessen resultierende hydrodynamische Dispersion in computergenerierten Packungen aus harten, undurchlässigen Kugeln, deren geometrische Anordnung in der Packung dem Zufallsprinzip unterliegt. Solche Zufallskugelpackungen wurden sowohl mit dem Jodrey–Tory-Algorithmus als auch mit einer Monte Carlo-basierten Methode generiert. Das dreidimensionale Geschwindigkeitsfeld von Druckfluss in den Zwischenräumen einer Zufallskugelpackung wurde mit der Gitter-Boltzmann-Methode berechnet; Diffusion und hydrodynamische Dispersion wurden mithilfe eines Zufallsweg-Partikelverfolgungs-Verfahrens simuliert. Die Programm-Codes wurden in der Programmiersprache C unter Benutzung der Messing Passage Interface-Bibliothek gezielt für die effiziente Anwendung auf Hochleistungs-Rechensystemen (Supercomputer) geschrieben.

Im ersten Teil der Arbeit wird untersucht, wie die Querschnitts-Geometrie des Behälters die hydrodynamische Dispersion in Zufallskugelpackungen beeinflusst. Dazu wurden Zufallskugelpackungen verschiedener Packungsdichten in Behältern mit kreisfömigen, quadratischen, rechteckigen, halbkreisförmigen, und trapezoidalen Querschnitten generiert, und die prä-asymptotischen und quasi-asymptotischen hydrodynamischen Dispersionskoeffizienten berechnet und analysiert. Außerdem wurden auch Zufallskugelpackungen in einem Behälter mit irregulärer Querschnittsgeometrie untersucht. Dafür wurde nicht nur der Querschnitt eines echten, mit kugelförmigen Adsorberpartikeln gefüllten Mikrochip-Kanals für die Trennung von Substanzen durch Hochleistungs-Flüssigkeitschromatographie rekonstruiert, sondern auch die Größenverteilung der Adsorberpartikel als Vorlage für die Größenverteilung der Kugeln in der Zufallspackung verwendet. Im zweiten Teil der Arbeit wurden die verschiedenen Längenskalen struktureller Inhomogeneitäten in Zufallskugelpackungen mit und ohne Behälter analysiert, welche das Fluss-Geschwindigkeitsprofil und damit die hydrodynamische Dispersion bestimmen. Außerdem wurde untersucht, wie sich die Packungsmikrostruktur von Zufallskugelpackungen auf die effektiven Diffusionskoeffizienten einerseits und die hydrodynamischen Dispersionskoeffizienten andererseits auswirkt.

Contents

Introduction

Transport processes in porous media occur in many diverse fields of science and engineering, including groundwater pollution, oil recovery, chromatographic separations, filtration, drug discovery and peptide engineering, evolution of rocks, diffusion in biological tissues, and many others. Accurate prediction and optimization of the transport processes requires understanding, both qualitative and quantitative, of the underlying physical phenomena. Solution of the *generic scalar transport equation* forms the basis for the quantitative description of the transport processes and provides an insight into their origin. Complexity of the geometry of pores and of their topological connectivity makes it infeasible to apply analytical methods for the solution of the generic scalar transport equation. As a result, it is necessary to employ numerical methods to solve the transport equation, or, in other words, to perform numerical simulations. Complex structure of the pore space requires utilization of the advanced numerical techniques as well as exceptional computational resources to perform pore-scale simulations of transport (such as flow, diffusion, and hydrodynamic dispersion) in porous media.

In this thesis we deal exclusively with the *random close sphere packings* which are one of the types of porous media. An exact description of the geometry and topology of sphere packings can be done relatively easy using coordinates and diameters of spheres. In this work, transport phenomena simulated in the pore space of sphere packings include i) advective motion caused by the flow of an incompressible fluid, ii) mass transport due to random motion (diffusion), and iii) transport due to combination of both advection and diffusion, resulting in the *hydrodynamic (eddy) dispersion*. Flow of an incompressible fluid, diffusion, and hydrodynamic dispersion can be described by the solution of the Navier–Stokes, diffusion, and advection–diffusion equations, respectively. These three equations, in turn, can be derived from the generic transport equation.

A widely used way to approximate the solution of the aforementioned transport equations is to employ classical Eulerian methods like finite difference, finite volume, or finite element. We used alternative numerical methods to approach the solutions of Navier–Stokes, diffusion, and advection–diffusion equations: the *lattice Boltzmann*[1] (LBM) and *random walk particle tracking*[2] (RWPT) methods, which do not solve the transport equations directly. The LBM operates with fictitious particles (forming a system called “lattice gas”) which propagate on a discrete lattice at discrete time steps. Under particular conditions such a system recovers the macroscopical behavior of a fluid. In RWPT, solute is represented by the ensemble of infinitely small particles (tracers), and time evolution of solute is simulated by the iterative displacement of each tracer in the volume of

[1] S. Succi. *The lattice Boltzmann equation for fluid dynamics and beyond*. Oxford University Press, 2001.

[2] J. A. Rudnick and G. D. Gaspari. *Elements of the random walk: an introduction for advanced students and researchers*. Cambridge University Press, 2004.

interest (which is the sphere packing void space here). Both methods have their advantages and limitations, however they allowed us to find precise solutions to the transport problems of interest. Further, LBM and RWPT are characterized by their local update rule, which makes them attractive for the usage on high-performance computing systems (supercomputers). These systems contain a large amount of processing units connected together with a network. Local update rule of both methods results in the minimization of the information transfer among the processing units during an execution of a parallel program, allowing to minimize communication time and to maximize time dedicated to the calculations. Effective use of the supercomputing facilities allowed us to perform large-scale simulations with largest production runs utilizing $100\,000$ CPU cores and 50 TB of random access memory, making it possible to obtain simulation results which would become available on desktop PCs only after at least $10-15$ years due to both CPU speed and memory limitations.[3]

Prediction of the transport properties of porous media is of particular interest in the field of chromatography. Chromatography (or separation science) is used to separate mixtures of substances into their components. The idea behind chromatography is that a mixture of compounds (sample, analyte) to be separated is transported with a carrier (fluid or gas) through a container filled with porous material, and, due to different retention times of the compounds resulting from the interaction with the stationary phase (i.e., with the porous material), compounds are carried with different effective velocities, and, therefore, get separated. Porous material in chromatographic columns is often formed by spherical particles. In an ideal case, a concentration delta pulse of a binary mixture injected at the column inlet would be separated into two delta pulses while the mixture migrates the column downstream. However, different processes (such as diffusion, non-uniformity of the flow field, sorption of the mixture species to the stationary phase) spread concentration profiles around their mean, introducing overlap of the profiles and decreasing quality of the separation or canceling the separation at all.

Advances in the development of microfluidic devices[4] enabled integration of a variety of laboratory functions, such as sample preparation, injection, detection, and chromatographic separation into a single device of credit-card size operating with very small sample volumes (as low as picoliters).[5] Nowadays such devices are powerful tools for applications in life sciences and medical diagnostics. While a typical separation column is a cylindrical tube of centimeter diameter[6,7] filled with porous material, separation channel in a microfluidic device (microchannel) has micrometer dimensions and typically non-circular cross sections. Non-circular geometries of the microchannel cross section are caused by the fabrication process (for example, photolithography) and materials used,[8] and have approximately semicircular,[9] elliptical,[10] rectangular,[11] or trapezoidal[12] cross sec-

[3] D. G. Feitelson. *Comput. Sci. Eng.*, **7**: 42–47, 2005.
[4] G. M. Whitesides. *Nature*, **442**: 368–373, 2006.
[5] H. Yin et al. *Anal. Chem.*, **77**: 527–533, 2005.
[6] G. Guiochon et al. *Fundamentals of preparative and nonlinear chromatography*. 2nd ed. Elsevier, 2006.
[7] J. W. Jorgenson. *Annu. Rev. Anal. Chem.*, **3**: 129–150, 2010.
[8] S. Koster and E. Verpoorte. *Lab Chip*, **7**: 1394–1412, 2007.
[9] K. W. Ro, J. Liu, and D. R. Knapp. *J. Chromatogr. A*, **1111**: 40–47, 2006.
[10] D. S. Reichmuth, T. J. Shepodd, and B. J. Kirby. *Anal. Chem.*, **77**: 2997–3000, 2005.
[11] J. Liu et al. *Anal. Chem.*, **81**: 2545–2554, 2009.
[12] C.-Y. Shih et al. *J. Chromatogr. A*, **1111**: 272–278, 2006.

tions with deviations from the ideal geometries. Influence of the microchannel geometry on the transport processes occurring within a channel was extensively studied for the open channels,[13] whereas little attention was given to the transport in packed non-cylindrical microchannels.[14] In the first part of this thesis (Chapters 2 to 4) we analyze advective–diffusive mass transport in the channels of various cross sections packed with spherical particles by the means of pore-scale simulations. Simulation workflow includes i) computer generation of a random packing of solid, impermeable spheres within a channel, ii) simulation of fluid flow in the channel void space with LBM, and iii) simulation of advective–diffusive mass transport in the channel void space with RWPT. Chapter 2 discusses mass transport in the channels with basic cross-sectional geometries (circular, quadratic, rectangular, and semicircular). Trapezoidal geometries with varied base angle and top-to-bottom base ratio are studied in Chapter 3. Finally, Chapter 4 deals with channels of the irregular geometry reconstructed from a high-resolution SEM image of the real microchannel cross section. Obtained results were published in the following publications:

- S. KHIREVICH, A. HÖLTZEL, D. HLUSHKOU, and U. TALLAREK. Impact of conduit geometry and bed porosity on flow and dispersion in noncylindrical sphere packings. *Analytical Chemistry*, **79**: 9340–9349, 2007. DOI: 10.1021/ac071428k
- S. KHIREVICH, A. HÖLTZEL, D. HLUSHKOU, A. SEIDEL-MORGENSTERN, and U. TALLAREK. Structure–transport analysis for particulate packings in trapezoidal microchip separation channels. *Lab on a Chip*, **8**: 1801–1808, 2008. DOI: 10.1039/b810688f
- S. KHIREVICH, A. HÖLTZEL, S. EHLERT, A. SEIDEL-MORGENSTERN, and U. TALLAREK. Large-scale simulation of flow and transport in reconstructed HPLC-microchip packings. *Analytical Chemistry*, **81**: 4937–4945, 2009. DOI: 10.1021/ac900631d

Part two of this thesis (Chapters 5 to 7) addresses fundamentals of the transport processes in the random monodisperse sphere packings. Chapter 5 investigates length scales of heterogeneity persisting in i) unconfined (periodic, bulk) sphere packings and ii) packings confined by the hard wall of a circular cross section. Length scales of heterogeneity in bulk and confined packings are analyzed and correlated with the time evolution of the hydrodynamic dispersion in both axial and transverse (relative to the flow) directions. Chapter 6 is concerned with the hydrodynamic dispersion in the bulk monodisperse sphere packings of different microstructural disorder. We generated packings with different degree of microstructural disorder (which was varied by the means of parameters of the generation algorithm) and performed analysis of the geometrical and transport properties of the packings. Finally, Chapter 7 discusses the influence of microstructural disorder on diffusion in the packing void space. Packings with different microstructural disorder were generated using two different generation algorithms each having its own set of parameters. The results presented in the second part of the thesis were published in the following publications:

- S. KHIREVICH, A. HÖLTZEL, A. SEIDEL-MORGENSTERN, and U. TALLAREK. Time and length scales of eddy dispersion in chromatographic beds. *Analytical Chemistry*, **81**: 7057–7066, 2009. DOI: 10.1021/ac901187d
- S. KHIREVICH, A. DANEYKO, A. HÖLTZEL, A. SEIDEL-MORGENSTERN, and U. TALLAREK. Statistical analysis of packed beds, the origin of short-range disorder, and its impact on eddy dispersion. *Journal of Chromatography A*, **1217**: 4713–4722, 2010. DOI: 10.1016/j.chroma.2010.05.019

[13] H. A. Stone, A. D. Stroock, and A. Ajdari. *Annu. Rev. Fluid Mech.*, **36**: 381–411, 2004.
[14] G. P. Rozing et al. *J. Sep. Sci.*, **27**: 1391–1401, 2004.

Chapter 1

Numerical methods

In this chapter we describe the algorithms and numerical methods used in this thesis to generate random sphere packings and simulate transport processes. Simulation approach consists of the following steps: i) generation of a random sphere packing, ii) discretization of the packing, iii) pore-scale simulation of a flow in the packing void space, and iv) simulation of (advection–)diffusion in the packing void space. Here we give a detailed description of the algorithms and numerical methods, their validation, and some aspects of program realization.

1.1 Random packing generation

The performance of chromatographic columns strongly depends on the column internal microstructure. A straightforward way to explore and study internal three-dimensional microstructure of packed columns is to use experimental imaging techniques such as X-ray tomography,[15–17] NMR,[18,19] or confocal laser microscopy.[20] However, until now the aforementioned methods do not allow imaging sufficiently large fragments of the channels packed with micrometer-sized particles with a spatial resolution sufficient for detailed analysis of mass transport. Another approach to represent the internal packing microstructure is numerical simulations of the real slurry packing process.[21] However, this approach still remains a challenging task due to the high complexity of the underlying physical processes and the large amount of particles contained in typical chromatographic columns.

Chromatographic columns are most frequently packed with particles of close-to-spherical shape by a slurry packing process.[6,22] Such a preparation process creates a structure similar to the random close sphere packing. Therefore, a different way to approach the microstructure of packed beds is computer generation of random sphere packings. By this approach simulation of the real packing process is avoided and packings are generated using a set of specific rules in order to match different target properties (such as porosity, coordination number, contact network, degree of heterogeneity, etc.) of real packed beds. Nowadays, simulation performance of the algorithms

[15] T. Aste, M. Saadatfar, and T. J. Senden. *Phys. Rev. E*, **71**: 061302, 2005.
[16] R. Mizutani et al. *Micron*, **41**: 90–95, 2010.
[17] M. Piller et al. *Transp. Porous Media*, **80**: 57–78, 2009.
[18] H. Freund et al. *Ind. Eng. Chem. Res.*, **44**: 6423–6434, 2005.
[19] B. Manz, L. F. Gladden, and P. B. Warren. *AIChE J.*, **45**: 1845–1854, 1999.
[20] D. Hlushkou, S. Bruns, and U. Tallarek. *J. Chromatogr. A*, **1217**: 3674–3682, 2010.
[21] J. P. C. Vissers et al. *J. Chromatogr. A*, **883**: 11–25, 2000.
[6] G. Guiochon et al. *Fundamentals of preparative and nonlinear chromatography*. 2nd ed. Elsevier, 2006.
[22] L. A. Colón, T. D. Maloney, and A. M. Fermier. *J. Chromatogr. A*, **887**: 43–53, 2000.

based on this approach allows generation of sphere packings with spatial dimensions sufficiently large for the simulation of transport processes and their correlation with the geometrical properties of packed beds. The algorithm performance can be evaluated using the time complexity[23] analysis. Time complexity T of a packing generation algorithm can be understood as a time, taken to generate a packing with given properties, which is a function of the number of spheres n contained in the packing. The algorithm time complexity is often expressed using *Big Oh notation*[23] which characterizes an upper bound of the growth rate of a given function. According to this notation, the only terms with the largest growth rate are kept while constants and terms with a smaller growth rate of a functional expression are ignored, i.e. $T(n) = 0.001n^3 + 2n^2 + 1$, $O(T(n)) = O(n^3)$. From the practical point of view, an algorithm with a computational complexity of $O(n^2)$ allowed us to generate dense sphere packings with $\sim 10^4 - 10^5$ spheres in a reasonable time period, while the $O(n)$-algorithm enabled generation of significantly larger packings, containing $\sim 10^7 - 10^8$ spheres. In this thesis no strict complexity analysis of referred algorithms is performed, and only rough estimates are given based on the algorithm description and benchmarks presented by their authors.

Currently there are numerous packing algorithms available in the literature.[24–32] For example, Zinchenko[29] proposed a packing algorithm with computational complexity of $O(n^2)$ for the generation of periodic monodisperse sphere packings. The idea of the algorithm is based on creating an initial dilute packing which forms a contact network, and then performing a densification of the packing by swelling the particles while maintaining the initial contact network as far as possible. The advantage of the algorithm is the perfect contact network between particles of the final packing.

An algorithm presented in the work of He et al.[30] randomly distributes particles in the container of reduced size and then displaces each overlapping particle simultaneously from all the neighbors overlapping it. A particle which neither overlaps nor contacts others is moved to its closest neighbor. While iterating, the algorithm expands the container by a factor depending on the current overlap rate. The algorithm is capable to create polydisperse sphere packings with periodic boundary conditions. To analyze the generated packings, He et al.[30] addressed such properties of the packings as coordination number, randomness, homogeneity, and isotropy. Despite the authors did not provide any algorithm benchmarks, one can assume a complexity of $O(n)$ because nearest neighbors search (i.e., location of particles overlapping a given one) can be realized using, for instance, the neighbor list algorithm.[33] However, a dense initial distribution of particle centers may reduce the effectiveness of such an approach.

Mueller et al.[32] presented an algorithm to produce monodisperse packings confined by a hard cylindrical wall. Starting from the wall, Mueller's algorithm sequentially places spheres in

[23] S. S. Skiena. *The algorithm design manual*. 2nd ed. Springer-Verlag, 2008.
[24] M. P. Allen and D. J. Tildesley. *Computer simulation of liquids*. Oxford University Press, 1989.
[25] B. D. Lubachevsky and F. H. Stillinger. *J. Stat. Phys.*, **60**: 561–583, 1990.
[26] B. D. Lubachevsky, F. H. Stillinger, and E. N. Pinson. *J. Stat. Phys.*, **64**: 501–524, 1991.
[27] A. Donev, S. Torquato, and F. H. Stillinger. *J. Comput. Phys.*, **202**: 737–764, 2005.
[28] G. T. Nolan and P. E. Kavanagh. *Powder Technol.*, **72**: 149–155, 1992.
[29] A. Z. Zinchenko. *J. Comput. Phys.*, **114**: 298–307, 1994.
[30] D. He, N. N. Ekere, and L. Cai. *Phys. Rev. E*, **60**: 7098–7104, 1999.
[31] C. S. O'Hern et al. *Phys. Rev. Lett.*, **88**: 075507, 2002.
[32] G. E. Mueller. *Powder Technol.*, **159**: 105–110, 2005.
[33] Z. Yao et al. *Comput. Phys. Commun.*, **161**: 27–35, 2004.

cylindrical container towards the cylinder center. The original realization of the algorithm has a computational complexity of $O(n^2)$. Generated packings were characterized by the analysis of the average porosity and its local oscillations induced by the confining wall.

In this work two algorithms are employed: modified Jodrey–Tory[34] algorithm and an algorithm based on Monte Carlo procedure,[24] which are described below.

We note that both real and artificial packings can be assumed, from the point of transport processes, as sets of obstacles (spheres) with corresponding spatial coordinates and diameters placed in a container of a given geometry. Hence, both artificial and real packings can be described by the identical *geometrical* parameters depending only on the number of spheres, their spatial arrangement, and geometry of the container. As of now (2010), the question of the influence of such parameters on the transport properties of sphere packings still remains unanswered. In this thesis an attempt is made to identify and correlate geometrical parameters, describing the packing, with transport processes occurring within the packing void space.

1.1.1 Modified Jodrey–Tory algorithm

Most of the sphere packings studied in this work are simulated using a Jodrey–Tory procedure[34] modified as described below. The *bulk* packings are generated with periodic boundary conditions along all spatial dimensions; packings referred to as *confined* are created inside of a container with hard walls along two dimensions and periodic boundary conditions along the third one. The packing void fraction was within the range of $0.366–0.50$ and the amount of spheres was varied from $7 \cdot 10^3$ to $8 \cdot 10^6$. Packings with such an amount of particles were found to be large enough for performing statistical analysis of the generated packings and hydrodynamic dispersion simulations within the packing void space.

The Jodrey–Tory (JT) algorithm can be classified as a "collective rearrangement" approach.[35] JT starts from a random distribution of n sphere centers in a simulation box of volume V_{box}. Obviously, sphere overlap is typical in the initial configuration if the sphere packing to be generated is dense. The value of n is calculated from the targeted (final) packing porosity $\varepsilon_{\mathrm{fin}}$, V_{box}, and the final sphere diameter d_{fin} as

$$\varepsilon = 1 - \frac{n d_{\mathrm{fin}}^3}{6 V_{\mathrm{box}}}. \tag{1.1}$$

Each iteration of the algorithm includes i) search of two particle centers C_1 and C_2 with the minimum pair-wise distance d_{min}, where d_{min} defines the maximal sphere diameter at which no overlap occurs in the current packing configuration and, consequently, the corresponding packing porosity

$$\varepsilon_{\mathrm{min}} = 1 - \frac{n d_{\mathrm{min}}^3}{6 V_{\mathrm{box}}}, \tag{1.2}$$

[34] W. S. Jodrey and E. M. Tory. *Phys. Rev. A*, **32**: 2347–2351, 1985.
[35] A. Bezrukov, M. Bargieł, and D. Stoyan. *Part. Part. Syst. Char.*, **19**: 111–118, 2002.

and ii) symmetrical spreading apart of these two particle centers along a line C_1C_2 up to a new distance, $d_{\max}$, according to the following equation:

$$d_{\max} = d_{\min}\left(1 + \alpha \log_{10}\left(\frac{d_{\text{fin}}}{d_{\min}}\right)\right), \tag{1.3}$$

where α is some constant. As $d_{\min}$ asymptotically approaches d_{fin}, $\varepsilon_{\min}$ approaches ε_{fin}. The algorithm exits when the condition

$$|\varepsilon_{\min} - \varepsilon_{\text{fin}}| < 1.001\,\varepsilon_{\text{fin}} \tag{1.4}$$

is satisfied. One should mention that a particular choice of functional dependence $d_{\max} = f(d_{\min})$ is optional assuming monotonically decreasing functions. However, the choice of function will affect the minimal packing porosity, convergence possibility, and convergence rate. To generate confined packings, the following boundary condition is used: if a sphere intersects a confining wall, such a move is rejected.

Packing microstructures are commonly referred to as "more homogeneous" or "more heterogeneous." For example, packings of disks (selected instead of spheres for better visualization) in the left gray block of Figure 1.1 are more homogeneous than their counterparts in the right block while all these packings have equal porosity. As will be shown later, the difference in microstructural disorder may and does lead to different transport properties of generated packings. Therefore it is meaningful to address not only porosity variation of the packings, but also their *degree of heterogeneity* (DoH). The JT algorithm offers a possibility to modify the DoH of packings to be generated by variation of the initial distribution of particle centers and the functional dependence $d_{\max} = f(d_{\min})$. The latter is varied by modification of the value of the constant α. The former is done by using two types of initial distributions, "R" and "S." Packings, where sphere centers are distributed uniformly random, are referred to as *R-packings*. To generate *S-packings*, the simulation box is initially divided into n equal cubic cells and each sphere center is then placed in a random position into a cell. Both types of initial distributions result in a uniform random distribution of sphere centers within the simulation box. The constant α in equation (1.3) defines the magnitude of each displacement of centers C_1 and C_2. With a small value of α the sphere centers tend to stay closer to their initial positions as far as possible during generation, and the final packing configuration reflects the randomness of the initial distribution of particle centers. A larger displacement value provides a more uniform distribution of sphere centers in the final configuration. In this work packings generated with JT algorithm are denoted as "TxA," where T is the type of initial distribution of particle centers (R or S) and A is the value of α. In case of $\alpha = 1$, the generated packings are referred to as just "T."

The influence of the initial distribution type and the value of parameter α on microstructural disorder is demonstrated in Figure 1.1, where three-dimensional packings of spheres are replaced with two-dimensional packings of disks for better clarity. The microstructure of the final packings for the selected regions is compared with the respective initial disk distributions in Figure 1.1. The generated packings indeed reflect what was intended by their respective packing protocols:

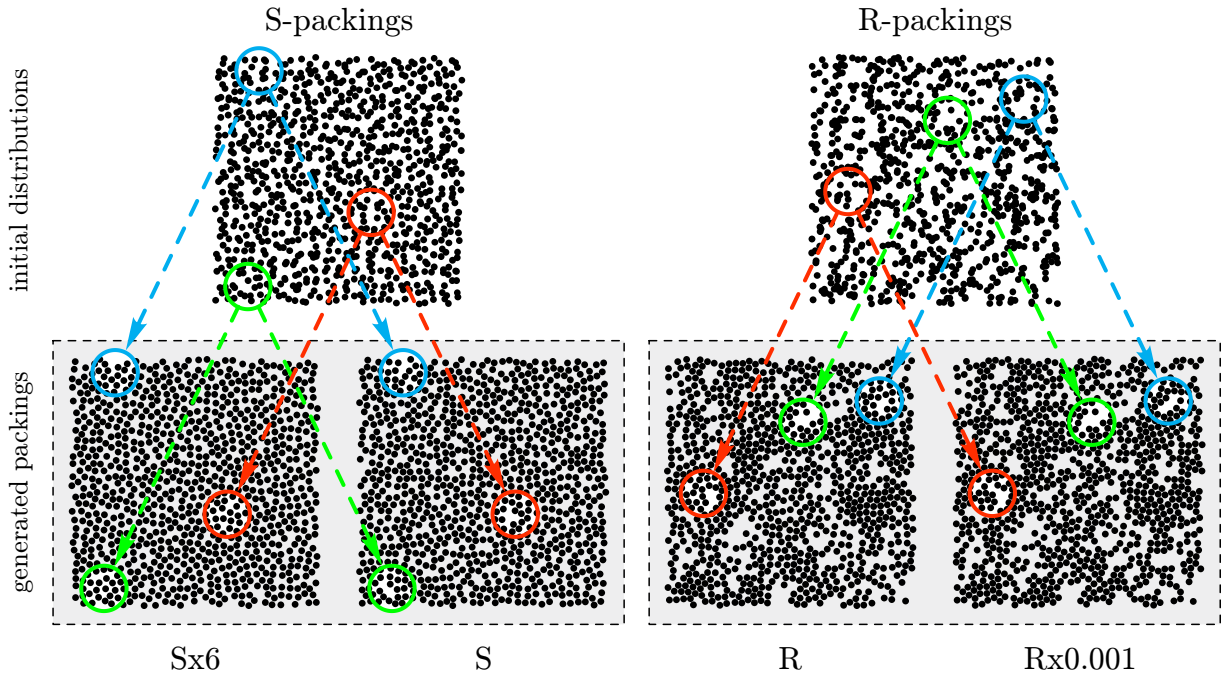

Figure 1.1: Bulk random packings of 900 monosized hard disks at $\varepsilon \approx 0.46$ generated with different parameters of the JT algorithm. Shown are the initial distributions of the disks for S- and R-configurations (top) and the generated two-dimensional packings ((Sx6, S), (R, Rx0.001); bottom). Circles around several regions help to compare the disk arrangement in the initial distributions with that of the final packings.

i) S-packings are more homogeneous than R-packings, due to the initial, uniform distribution of the disks, and ii) initial nonuniformities are best balanced in the Sx6 configuration and least balanced in the Rx0.001 configuration, where the former denotes S-packings with $\alpha = 6$ and the latter is R-packings with $\alpha = 0.001$.

The program realization of the JT algorithm is based on the work of Bargieł et al.[36] The initial step of the program i) creates a sorted list (SL) data structure,[23] where distances between particle centers (with corresponding particle indexes) are stored in ascending order; ii) partitions the space occupied by the simulation box into cubic cells (CC) where each cell contains the indexes and coordinates of all the particle centers enclosed by it. The main loop of the program contains the following four steps:

1. remove the head of SL containing distance and indexes of the closest particle centers $C_{1,2}$,
2. shift $C_{1,2}$ apart according to equation (1.3),
3. recalculate distances between $C_{1,2}$ and all their neighbors from 27 CCs (the CC containing C_1 (or C_2) plus its 26 neighbors),
4. update SL using information on the recalculated distances from step 3.

Computational time complexity of such a program realization is a sum of complexities of the corresponding steps: $O(1) + O(1) + O(m) + O(n) = O(m + n) = O(n)$, where m is the maximal amount of spheres which are currently located in 27 CCs and n is the number of particles in the

[36] M. Bargieł and J. Mościński. *Comput. Phys. Commun.*, **64**: 183–192, 1991.

packing. After the generation is complete, JT stores sphere diameters, multiplied by the current value of $d_{\min}$, and center coordinates.

Obviously, JT algorithm produces geometrically jammed, but mechanically unstable sphere packings, because interparticle forces are not taken into account. On the other hand, JT has the following advantages:

- packing porosity and degree of heterogeneity can be systematically varied via input parameters of the algorithm ε_{fin} and α,
- generated packings are isotropic contrary to the packings generated with sedimentation-based methods[37] (however, absence of a packing-scale anisotropy should not be mixed with particle-scale or local anisotropy[38] which is an inherent property any random sphere packing),
- JT avoids partial packing crystallization,[29]
- JT allows to simulate polydisperse packings in confined geometries of an arbitrary cross section,[39]
- the algorithm has computational time complexity of $O(n)$,[36] which enables generation of confined packings containing millions of spheres at relatively low porosities (0.40) on one CPU core.[40]

1.1.2 Monte Carlo procedure-based algorithm

The second packing method used in this thesis is based on the Monte Carlo procedure[24] (MC). MC starts packing generation from a uniform distribution of n spheres of diameter d_{p} in a dilute cubic array. This array is derived from the simple cubic packing via expansion by a factor f while keeping particle diameters constant. In our simulations we use $f = 2$ resulting in 8 times higher volume of initial packing domain compared to the packing where n spheres are arranged in a simple cubic packing. After initialization of sphere positions, MC moves every sphere in a random direction on a distance Δd. If a given sphere intersects another one, the move is rejected. The distance Δd depends on the current fraction of accepted moves a: Δd is decreased when $a < 0.5$ and vice versa. After the series of N ($= 5000$ in this work) iterations is performed for the whole ensemble of spheres, the minimal distance between particle centers $d_{\min}$ is calculated and the simulation box is scaled by the factor $d_{\text{p}}/[d_{\text{p}} + \Omega \cdot (d_{\min} - d_{\text{p}})]$ while keeping the sphere diameter constant. Here Ω is the compression rate, $0 < \Omega \leq 1$. By compressing, the packing porosity decreases and MC stops execution when the current porosity reaches the desired value ε_{fin}. Generated MC packings are denoted as "ΩxC" where C is the magnitude of the compression rate Ω used in the packing generation.

Monte Carlo procedure-based methods tend to create closely-packed (crystalline) regions within a packing in case of slow compressing rates *and* lower packing densities.[29] To demonstrate these phenomena, we use two-dimensional packings of disks, as in the case of JT packings. Packings generated at slower and faster compression rates ($\Omega = 0.025$ and 0.99, respectively) are shown

[37] E. M. Tory, N. A. Cochrane, and S. R. Waddell. *Nature*, **220**: 1023–1024, 1968.
[38] G. E. Schröder-Turk et al. *EPL*, **90**: 34001, 2010.
[39] S. Khirevich et al. *Anal. Chem.*, **81**: 4937–4945, 2009.
[40] S. Khirevich et al. *Anal. Chem.*, **81**: 7057–7066, 2009.

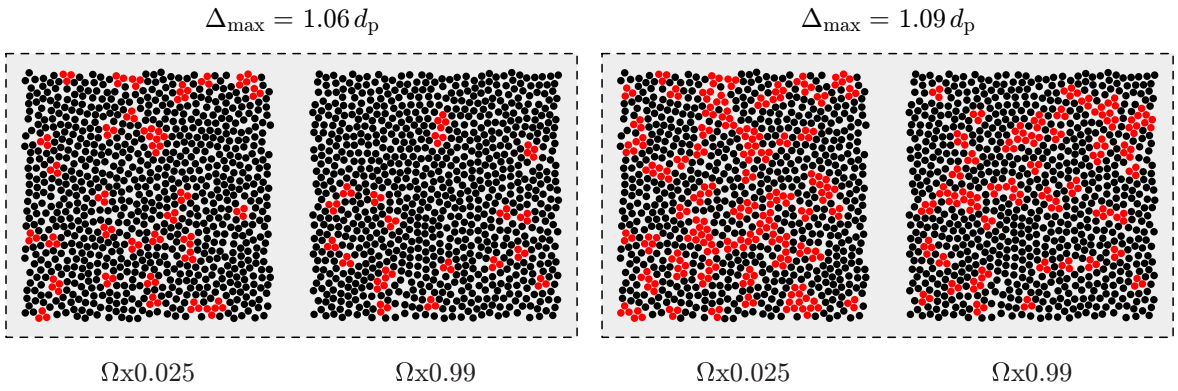

Figure 1.2: Bulk random packings of 900 monosized hard disks at $\varepsilon \approx 0.34$ generated with different parameters of MC algorithm. Disks marked in red form closely packed (crystalline) regions identified according to the value of $\Delta_{\max}$, which is indicated above the gray blocks. Lower values of the compression rate (Ωx0.025 packings) result in a larger amount of crystalline regions and higher heterogeneity of generated packings due to a maldistribution of available void space among packing.

in Figure 1.2. In order to identify densely packed disks, we employed *Delaunay triangulation*[41] performed on the centers of disks. Closely packed disks (marked in red) form close-to-regular triangles on the Delaunay mesh, and can be identified according to the criterion of maximal edge length $\Delta_{\max}$, i.e. disks forming triangles with a maximal edge length shorter than $\Delta_{\max}$ are assumed as closely packed. Note that a packing with a larger fraction of densely packed particles can be viewed as more disordered compared to the packing of the same porosity and a lower fraction of dense regions.

Program realization of MC is based on the cell list data structure, as a part of the JT algorithm, and therefore has a resulting in a computational complexity of $O(n)$. While JT requires information on the global minimal distance between sphere centers on each iteration, MC requires only local information on the intersection of a given sphere (after its displacement) with its neighbors. This enables an efficient parallel program realization of MC, for example, as in the work of Maier et al.[42]

1.2 Discretization

Computer simulation of macroscopic flow requires a discrete representation of the flow field and the corresponding geometry in which flow is simulated; this requirement is due to the continuous nature of a macroscopic flow field and limited amount of computer memory where information on this field is stored. Therefore, to simulate flow in the packings generated during the previous step, these packings must be *discretized*, i.e. a discrete spatial grid approximating the geometry of the sphere packing must be introduced.

The particular choice of the grid type is usually determined by the geometrical properties of the domain of interest and by the numerical method used for simulation of the flow field.[43] In this thesis,

[41] A. Okabe. *Spatial tessellations: concepts and applications of Voronoi diagrams*. 2nd ed. John Wiley & Sons, 2000.
[42] R. S. Maier et al. *Phys. Fluids*, **15**: 3795–3815, 2003.
[43] P. Wesseling. *Principles of computational fluid dynamics*. Springer-Verlag, 2001.

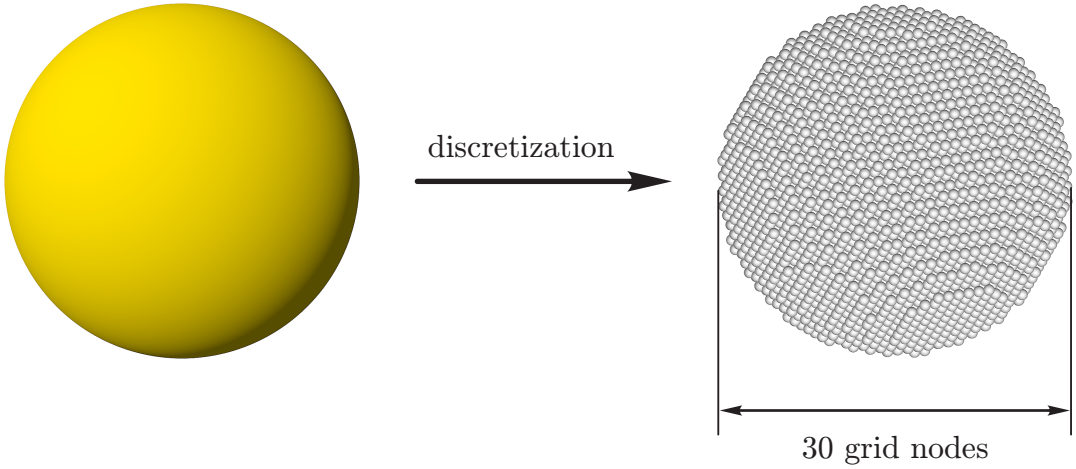

Figure 1.3: An example of a sphere and its counterpart discretized on a uniform cartesian grid (each small gray sphere on the right represents one grid node). Space around the sphere is discretized too, but, for better visualization, the figure shows only grid nodes belonging to the sphere. The discretization resolution of 30 grid nodes per sphere diameter presented here is used in this thesis for the most simulations of flow and hydrodynamic dispersion. Finite size effects are discussed in Subsections 1.3.5 and 1.4.6.

the simulation of fluid flow is done using the Lattice-Boltzmann method (see Subsection 1.3.3), and a uniform Cartesian grid is used for the discretization of the generated packings.

To perform discretization, a parallel program was implemented. The program creates a three-dimensional uniform cubic grid enclosing the generated packing. During execution, the program sets each voxel of the grid to "solid" or "fluid" according to the spatial position of the voxel, inside or outside the nearest sphere, respectively (Figure 1.3).

From the algorithmic point of view, there are two possibilities to examine the spatial position (inside/outside the nearest particle) of each lattice voxel: "particle-based" (PB) and "voxel-based" (VB). The PB approach includes the following steps: i) marking of all the voxels as "fluid," ii) for every sphere, identification of the lattice cube enclosing the sphere, and iii) iteration over all voxels within the cube and marking voxels as "solid" if their centers are in the sphere with which the lattice cube is associated. In the VB approach, iteration is done over all lattice voxels and for each lattice voxel the distances between its center and the centers of the nearest spheres are calculated (the list of nearest spheres is identified using the approach described in Subsection 1.1.1). While the PB approach is faster since only voxels in vicinity of a given sphere are examined, the VB provides a possibility to perform an approximation of *Voronoi S-tessellation*[41,44–47] of the packing void space (see Chapter 6). An important fact is that using the VB approach such a tessellation can be done in confined packings of any cross section packed with arbitrary-shaped particles.

[44] G. Voronoi. *J. Reine Angew. Math.*, **133**: 97–102, 1908.
[45] G. Voronoi. *J. Reine Angew. Math.*, **134**: 198–287, 1908.
[46] V. A. Luchnikov et al. *Phys. Rev. E*, **59**: 7205–7212, 1999.
[47] N. N. Medvedev et al. *J. Comput. Chem.*, **27**: 1676–1692, 2006.

1.3 Fluid flow simulation

1.3.1 Navier–Stokes equation

From the macroscopic point of view, a fluid can be assumed as a continuous medium. Under this assumption its behavior is described by the means of macroscopic quantities such as density ρ, pressure p, and velocity $\vec{v}$. Spatial and temporal evolution of the aforementioned quantities follows the conservation laws of mass and momentum, and these quantities are interrelated via the Navier–Stokes and continuity equations. These equations in the case of an incompressible fluid take the following form[48]:

$$\frac{\partial \vec{v}(\vec{r},t)}{\partial t} + (\vec{v}\cdot\nabla)\vec{v} = \mu\Delta\vec{v} - \frac{1}{\rho}\nabla p + \vec{F}, \tag{1.5}$$

$$\nabla\cdot\vec{v} = 0, \tag{1.6}$$

where μ denotes the kinematic viscosity and $\vec{F}$ is the body force. Numerical solution of equations (1.5) and (1.6) forms the basis of the majority of traditional computational fluid dynamics (CFD) approaches nowadays.

Apart from the macroscopic representation, a fluid can be described using microscopic and statistical approaches. The former is based on the representation of a fluid as a large number of molecules which are in random motion and collide with each other. However, the number of molecules in most real-life problems is too large to be handled by modern computers restricting the usability of the microscopic approach. On the other hand, when only macroscopic variables (like density, velocity, pressure) are of interest, a detailed description of each molecule is not necessary, and the statistical approach provides a suitable alternative to the microscopic one.

1.3.2 Boltzmann equation

Consider a thermodynamic system consisting of N identical particles in three-dimensional space. A point in $6N$-dimensional phase space (Γ-space) describes the velocity and position of all particles in the system. Next, introduce a six-dimensional space (γ-space) where every point contains velocity and coordinates of an individual particle. A point in Γ-space can be mapped onto N points in γ-space; the former and the latter represent the state of the system, and time evolution of the system is described by a trajectory in Γ-space or N trajectories in γ-space.

Let us introduce a γ-space distribution function $f(\vec{r},\vec{u},t)$ which is related to the number of molecules $dN(\vec{r},\vec{u},t)$ with coordinates $[\vec{r},\vec{r}+\mathrm{d}\vec{r}]$ and velocities $[\vec{u},\vec{u}+\mathrm{d}\vec{u}]$ as follows:

$$dN(\vec{r},\vec{u},t) = f(\vec{r},\vec{u},t)\mathrm{d}\vec{r}\mathrm{d}\vec{u}. \tag{1.7}$$

Due to motion and interparticle collisions particles change their coordinates and velocities. After time Δt particles will have the coordinate $\vec{r}+\vec{u}\Delta t$ and velocity $\vec{u}+\vec{a}\Delta t$ (where $\vec{a}$ is the acceleration

[48] L. D. Landau and E. M. Lifschitz. *Fluid mechanics*. 2nd ed. Butterworth–Heinemann, 2007.

due to external forces). Hence, using equation (1.7), we can write:

$$\left(f(\vec{r}+\vec{u}\Delta t,\vec{u}+\vec{a}\Delta t,t+\Delta t)-f(\vec{r},\vec{u},t)\right)\mathrm{d}\vec{r}\mathrm{d}\vec{u}=\left(\frac{\partial f}{\partial t}\right)_{\mathrm{c}}\mathrm{d}\vec{r}\mathrm{d}\vec{u}\Delta t, \tag{1.8}$$

where the term $(\partial f/\partial t)_{\mathrm{c}}$ is the time change of the distribution function due to the interparticle collisions. Let us expand the first term on the left hand side of equation (1.8) as a Taylor series to the first order about the point $(\vec{r},\vec{u},t)$:

$$\begin{aligned} f(\vec{r}+\vec{u}\Delta t,\vec{u}+\vec{a}\Delta t,t+\Delta t) &= f(\vec{r},\vec{u},t)+ \\ &+\Delta t\left(\vec{u}\cdot\frac{\partial f(\vec{r},\vec{u},t)}{\partial\vec{r}}+\vec{a}\cdot\frac{\partial f(\vec{r},\vec{u},t)}{\partial\vec{u}}+\frac{\partial f(\vec{r},\vec{u},t)}{\partial t}\right). \end{aligned} \tag{1.9}$$

Combining equations (1.8) and (1.9), we get

$$\left(\vec{u}\cdot\frac{\partial}{\partial\vec{r}}+\vec{a}\cdot\frac{\partial}{\partial\vec{u}}+\frac{\partial}{\partial t}\right)f(\vec{r},\vec{u},t)=\left(\frac{\partial f}{\partial t}\right)_{\mathrm{c}}. \tag{1.10}$$

Equation (1.10) is known as the *Boltzmann equation*, and it describes the time evolution of the one-particle distribution function in γ-space. However, equation (1.10) is of little practical use until the collision term $(\partial f/\partial t)_{\mathrm{c}}$ is explicitly specified. Let us make the following assumptions[49]:

- only binary particle collisions do occur;
- the velocity of a particle does not correlate with its position (*assumption of molecular chaos*);
- external forces have no influence on particle collisions;
- wall effects are ignored.

Under these assumptions, Boltzmann expressed the collision term of equation (1.10):

$$\left(\frac{\partial f}{\partial t}\right)_{\mathrm{c}}=\int|\vec{u}-\vec{u}_1|\sigma(\Omega)\left(f'f_1'-ff_1\right)\mathrm{d}\Omega\mathrm{d}^3\vec{u}_1. \tag{1.11}$$

Here Ω denotes the scattering angle of the binary collision $\vec{u}\vec{u}_1\rightarrow\vec{u}'\vec{u}_1'$ with the differential cross section σ, f and f' are the one-particle distribution functions before and after the collision, respectively. Such a representation of the collision term results in the complex integro-differential form of equation (1.10). The collision term can be significantly simplified assuming a system state *close to thermal equilibrium*. In such a state, a classical ideal gas has a uniform distribution of density ρ and average (macroscopic) velocity $\vec{v}$ of its particles, and the one-particle distribution function follows the Maxwell–Boltzmann distribution:

$$f^{\mathrm{eq}}(\vec{r},\vec{u})=\frac{\rho}{(2\pi k_{\mathrm{B}}T)^{3/2}}\exp\left[-\frac{(\vec{u}-\vec{v})^2}{2k_{\mathrm{B}}T}\right], \tag{1.12}$$

where ρ, $\vec{v}$, k_{B}, and T are the macroscopic density, macroscopic velocity, Boltzmann constant, and temperature, respectively. According to the *Boltzmann H-theorem*,[49] the entropy of an ideal gas never

[49] K. Huang. *Statistical mechanics*. 2nd ed. John Wiley & Sons, 1987.

decreases. So, we can expect an arbitrary one-particle distribution function to evolve according to the Boltzmann equation and relax to the Maxwell–Boltzmann distribution. This leads to the more simple definition of the collision term[50]:

$$\left(\frac{\partial f}{\partial t}\right)_{\mathrm{c}} = -\frac{f - f^{\mathrm{eq}}}{\tau}. \tag{1.13}$$

Here τ is the relaxation time and such a form of the collision term is known as the *BGK collision operator*. Using (1.13), the Boltzmann equation (1.10) can be rewritten as follows:

$$\left(\vec{u}\cdot\frac{\partial}{\partial\vec{r}} + \vec{a}\cdot\frac{\partial}{\partial\vec{u}} + \frac{\partial}{\partial t}\right) f(\vec{r},\vec{u},t) = -\frac{f - f^{\mathrm{eq}}}{\tau}. \tag{1.14}$$

It should be noted that the connection between Boltzmann BGK equation (1.14) and macroscopic equations (1.5) and (1.6) can be demonstrated using the Chapman–Enskog expansion of equation (1.14) in the low Knudsen number limit.[51] Macroscopic quantities such as density, velocity, and temperature can be determined from statistical moments of a given distribution function f:

$$\rho(\vec{r},t) = \int_{-\infty}^{\infty} f(\vec{r},\vec{u},t)\mathrm{d}\vec{u}, \tag{1.15a}$$

$$\vec{v}(\vec{r},t) = \frac{1}{\rho(\vec{r},t)}\int_{-\infty}^{\infty} \vec{u} f(\vec{r},\vec{u},t)\mathrm{d}\vec{u}, \tag{1.15b}$$

$$T(\vec{r},t) = \frac{1}{3k_B\rho(\vec{r},t)}\int_{-\infty}^{\infty} (\vec{u}-\vec{v})^2 f(\vec{r},\vec{u},t)\mathrm{d}\vec{u}. \tag{1.15c}$$

1.3.3 Lattice Boltzmann equation

The simulation of flow in this thesis is done using the *lattice Boltzmann method* (LBM).[1,52,53] Historically, the method was developed as an improvement of Lattice Gas Automata (LGA),[54–58] which in turn originates from Cellular Automata (CA) models.[59] At present time, LBM is probably the best method for simulation of microflows in porous media.[1]

The LBM is based on the solution of the lattice Boltzmann equation, which is a special discretized form of the Boltzmann equation.[60] The connection between both equations is briefly described below.

[50] P. L. Bhatnagar, E. P. Gross, and M. Krook. *Phys. Rev.*, **94**: 511–525, 1954.
[51] S. Chapman and T. G. Cowling. *The mathematical theory of non-uniform gases*. 3rd ed. Cambridge University Press, 1990.
[1] S. Succi. *The lattice Boltzmann equation for fluid dynamics and beyond*. Oxford University Press, 2001.
[52] S. Chen et al. *J. Stat. Phys.*, **68**: 379–400, 1992.
[53] S. Chen and G. D. Doolen. *Annu. Rev. Fluid Mech.*, **30**: 329–364, 1998.
[54] G. R. McNamara and G. Zanetti. *Phys. Rev. Lett.*, **61**: 2332–2335, 1988.
[55] J. Hardy, Y. Pomeau, and O. de Pazzis. *J. Math. Phys.*, **14**: 1746–1759, 1973.
[56] J. Hardy, O. de Pazzis, and Y. Pomeau. *Phys. Rev. A*, **13**: 1949–1961, 1976.
[57] U. Frisch, B. Hasslacher, and Y. Pomeau. *Phys. Rev. Lett.*, **56**: 1505–1508, 1986.
[58] U. Frisch et al. *Complex Syst.*, **1**: 649–707, 1987.
[59] S. Wolfram. *J. Stat. Phys.*, **45**: 471–526, 1986.
[60] X. He and L.-S. Luo. *Phys. Rev. E*, **56**: 6811–6817, 1997.

A simplified form (without the body force term) of the BGK Boltzmann equation (1.14) can be first order approximated as follows[60,61]:

$$f(\vec{x}+\vec{u}\Delta t,\vec{u},t+\Delta t)=f(\vec{x},\vec{u},t)-\frac{\Delta t}{\tau}\left(f(\vec{x},\vec{u},t)-f^{\mathrm{eq}}(\vec{x},\vec{u})\right), \tag{1.16}$$

where Δt is the time step. As the next step, let us approximate the equilibrium distribution function f^{eq} assuming values of the average velocity $\vec{v}$ are small compared to the speed of sound in the system (low Mach number limit). Then the equilibrium function can be approximated up to the second order:

$$f^{\mathrm{eq}}(\vec{r},\vec{u})=\frac{\rho}{(2\pi k_{\mathrm{B}}T)^{3/2}}\exp\left(-\frac{\vec{u}^2}{2k_{\mathrm{B}}T}\right)\left\{1+\frac{\vec{u}\cdot\vec{v}}{k_{\mathrm{B}}T}+\frac{(\vec{u}\cdot\vec{v})^2}{2(k_{\mathrm{B}}T)^2}-\frac{\vec{v}\cdot\vec{v}}{2k_{\mathrm{B}}T}\right\}. \tag{1.17}$$

In this form, the equilibrium function can be used to evaluate macroscopic quantities (1.15). After substitution of equation (1.17) into equations (1.15) and approximating the resulting integrals by Gaussian quadratures, we get

$$\int_{-\infty}^{\infty}\mathrm{P}(\vec{u})f(\vec{r},\vec{u},t)\mathrm{d}\vec{u}\approx\sum_{\alpha}\mathrm{P}(\vec{u}_\alpha)\mathrm{W}_\alpha f(\vec{r},\vec{u}_\alpha,t). \tag{1.18}$$

Here $\mathrm{P}(\ldots)$ is the polynomial of its argument, W_α are weight coefficients, and $\vec{u}_\alpha$ is the discrete velocity set. Using equation (1.18), macroscopic quantities and equilibrium function are defined similar to (1.15) and (1.17),[60] respectively:

$$\rho(\vec{r},t)=\sum_{\alpha}\mathrm{W}_\alpha f(\vec{r},\vec{u}_\alpha,t), \tag{1.19a}$$

$$\vec{v}(\vec{r},t)=\frac{1}{\rho(\vec{r},t)}\sum_{\alpha}\vec{u}_\alpha\mathrm{W}_\alpha f(\vec{r},\vec{u}_\alpha,t), \tag{1.19b}$$

$$T(\vec{r},t)=\frac{1}{3k_B\rho(\vec{r},t)}\sum_{\alpha}(\vec{u}_\alpha-\vec{v})^2\mathrm{W}_\alpha f(\vec{r},\vec{u}_\alpha,t), \tag{1.19c}$$

and

$$f_\alpha^{\mathrm{eq}}(\vec{r},\vec{u}_\alpha)=\mathrm{W}_\alpha\frac{\rho}{(2\pi k_{\mathrm{B}}T)^{3/2}}\exp\left(-\frac{\vec{u}_\alpha^2}{2k_{\mathrm{B}}T}\right)\left\{1+\frac{\vec{u}_\alpha\cdot\vec{v}}{k_{\mathrm{B}}T}+\frac{(\vec{u}_\alpha\cdot\vec{v})^2}{2(k_{\mathrm{B}}T)^2}-\frac{\vec{v}\cdot\vec{v}}{2k_{\mathrm{B}}T}\right\}. \tag{1.20}$$

Finally, the lattice Boltzmann equation takes the following form:

$$f_\alpha(\vec{x}+\vec{e}_\alpha\Delta t,t+\Delta t)=f_\alpha(\vec{x},t)-\frac{\Delta t}{\tau}\left(f_\alpha(\vec{x},t)-f_\alpha^{\mathrm{eq}}(\vec{x},t)\right), \tag{1.21}$$

where $f_\alpha(\vec{x},t)=\mathrm{W}_\alpha f(\vec{x},\vec{u}_\alpha,t)$, $\vec{e}_\alpha=\vec{u}_\alpha c=\vec{u}_\alpha\sqrt{3k_{\mathrm{B}}T}$ with $c=\Delta x/\Delta t$ ($=1$ in this thesis; Δx is the space step).

The exact choice of the discrete velocity set $\vec{u}_\alpha$ (or LBM lattice model) must satisfy the re-

[61] T. Abe. *J. Comput. Phys.*, **131**: 241–246, 1997.

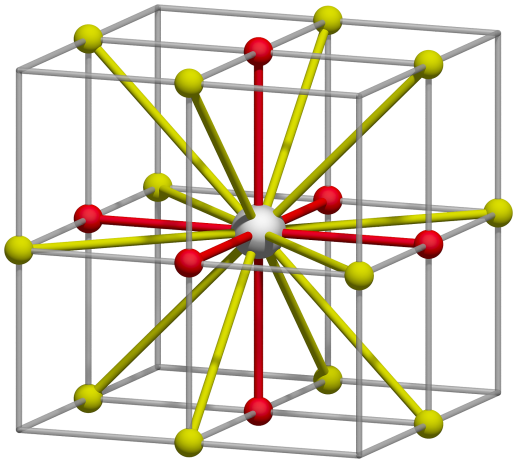

Figure 1.4: Lattice node (large gray sphere) with links to its 6 orthogonal (red spheres) and 12 diagonal (yellow spheres) neighbors in D3Q19 model.

strictions[62,63] of i) symmetry required by the Navier–Stokes equations, ii) exact calculation of macroscopic quantities (1.19), and iii) existence of a local equilibrium and its dependence only upon conserved quantities. LBM lattice models are intensively discussed in the literature,[64–70] and to date there have been proposed several two- and three-dimensional LBM models: D2Q7, D2Q9, D3Q13, D3Q15, D3Q19, D3Q27, and others. The lattice models are usually referred to as "D*x*Q*y*," where *x* is the lattice dimensionality and *y* is the amount of lattice links (discrete velocities u_α) of a given lattice node to its neighbors (located on a simple cubic lattice).[62] In this study, the D3Q19 lattice model was employed, which is a popular three-dimensional BGK LBM model nowadays. The set of discrete velocities u_α in the D3Q19 model is shown in Figure 1.4 and defined as

$$u_\alpha = \begin{cases} (0,0,0)c, & \alpha = 0; \\ (\pm 1,0,0)c, (0,\pm 1,0)c, (0,0,\pm 1)c, & \alpha = 1,2,\ldots,6; \\ (\pm 1,\pm 1,0)c, (\pm 1,0,\pm 1)c, (0,\pm 1,\pm 1)c, & \alpha = 7,8,\ldots,18. \end{cases} \tag{1.22}$$

Corresponding weight coefficients w_α (equation (1.18)) take the following form:

$$\mathrm{w}_\alpha = \mathrm{W}_\alpha \frac{1}{(2\pi k_\mathrm{B} T)^{3/2}} \exp\left(-\frac{\vec{u}_\alpha^2}{2k_\mathrm{B}T}\right) = \begin{cases} 1/3, & \alpha = 0; \\ 1/18, & \alpha = 1,2,\ldots,6; \\ 1/36, & \alpha = 7,8,\ldots,18. \end{cases} \tag{1.23}$$

[62] Y. H. Qian, D. d'Humières, and P. Lallemand. *EPL*, **17**: 479–484, 1992.
[63] X. B. Nie, X. Shan, and H. Chen. *EPL*, **81**: 34005, 2008.
[64] X. W. Shan and X. He. *Phys. Rev. Lett.*, **80**: 65–68, 1998.
[65] S. Ansumali, I. V. Karlin, and H. C. Öttinger. *EPL*, **63**: 798–804, 2003.
[66] W.-A. Yong and L.-S. Luo. *J. Stat. Phys.*, **121**: 91–103, 2005.
[67] X. Shan, X.-F. Yuan, and H. Chen. *J. Fluid Mech.*, **550**: 413–441, 2006.
[68] S. Ansumali et al. *Phys. Rev. Lett.*, **98**: 124502, 2007.
[69] S. S. Chikatamarla and I. V. Karlin. *Phys. Rev. E*, **79**: 046701, 2009.
[70] X. Shan. *Phys. Rev. E*, **81**: 036702, 2010.

Taking into account that $c = \sqrt{3k_{\mathrm{B}}T}$, equation (1.17) can be rewritten as

$$f_\alpha^{\mathrm{eq}}(\vec{r}, \vec{u}_\alpha) = \mathrm{w}_\alpha \rho \left\{ 1 + \frac{3\vec{u}_\alpha \cdot \vec{v}}{c^2} + \frac{9(\vec{u}_\alpha \cdot \vec{v})^2}{2c^4} - \frac{3\vec{v} \cdot \vec{v}}{2c^2} \right\}. \tag{1.24}$$

Equation (1.21) together with (1.24) provides a basis for the iterative calculation of an unknown distribution function $f_\alpha(\vec{x}, t)$. The kinematic viscosity in LBM is given by

$$\nu = \left(\tau - \frac{1}{2} \right) c_{\mathrm{s}}^2 \Delta t, \tag{1.25}$$

where $c_{\mathrm{s}} = c/\sqrt{3}$ is the speed of sound in the system. This choice of viscosity makes the discretization scheme (1.21) second order accurate both in space and time.[71]

1.3.4 Boundary conditions and pressure-driven flow

Apart from the calculating distribution function in the bulk region (i.e., away from the solid–liquid interface), simulation of pressure-driven flow in the system with obstacles requires specification of appropriate boundary conditions and a force driving the flow.

To implement the no-flux boundary conditions at the solid–liquid interface, we use the standard bounce-back boundary scheme (SBB): particles which meet the interface change their velocity to the opposite direction. SBB is widely used[18,42,72–76] due to the simplicity of its program realization and high computational efficiency. But at the same time SBB is often criticized.[77–82] The main arguments against SBB used in combination with BGK LBM are the following:

- In the general case, SBB is first order accurate in space,[83] and therefore degrades the second order accuracy of LBM,
- SBB locates the boundary *somewhere between* solid and adjacent fluid nodes;[81,83]
- SBB in combination with the BGK collision operator results in a viscosity dependent position of the boundary.[84]

In their study, Pan et al.[81] performed simulations of flow through random sphere packings using SBB with D3Q19 BGK LBM and demonstrated a significant error in the simulated permeability arising in the case of deviation of the lattice viscosity ν from $1/6$ (when relaxation parameter τ

[71] M. B. Reider and J. D. Sterling. *Comput. Fluids*, **24**: 459–467, 1995.
[72] A. Koponen et al. *Phys. Rev. Lett.*, **80**: 716–719, 1998.
[73] A. W. J. Heijs and C. P. Lowe. *Phys. Rev. E*, **51**: 4346–4352, 1995.
[74] C. Sun and L. L. Munn. *Comput. Math. Appl.*, **55**: 1594–1600, 2008.
[75] M. A. van der Hoef, R. Beetstra, and J. A. M. Kuipers. *J. Fluid Mech.*, **528**: 233–254, 2005.
[76] R. C. Acharya et al. *Water Resour. Res.*, **43**: W10435, 2007.
[77] D. R. Noble et al. *Phys. Fluids*, **7**: 203–209, 1995.
[78] A. M. Artoli, A. G. Hoekstra, and P. M. A. Sloot. *Int. J. Mod. Phys. C*, **14**: 835–845, 2003.
[79] J. Boyd et al. *Australas. Phys. Eng. Sci. Med.*, **27**: 207–212, 2004.
[80] S. Geller et al. *Comput. Fluids*, **35**: 888–897, 2006.
[81] C. Pan, L.-S. Luo, and C. T. Miller. *Comput. Fluids*, **35**: 898–909, 2006.
[82] A. Kuzmin. *Multiphase simulations with lattice Boltzmann scheme*. PhD thesis. Canada, University of Calgary, 2009.
[83] I. Ginzbourg and P. M. Adler. *J. Phys. II*, **4**: 191–214, 1994.
[84] X. He et al. *J. Stat. Phys.*, **87**: 115–136, 1997.

becomes less or greater than unity, see equation (1.25)). At the same time, SBB-based scheme with $\nu = 1/6$ performed well when the permeability was assumed as a measure of the method's accuracy. Using $\nu = 1/6$ (or $\tau = 1$), Maier and Bernard[85] found different convergence rates of numerical error (of D3Q19 BGK scheme implemented with different boundary conditions including SBB) for a number of geometrical configurations they studied: flow past a sphere, flow past a sphere near wall, and flow through ordered and disordered sphere packings. The authors observed a convergence rate of the SBB-based model between first and second order, depending on the value of interest (permeability, drag force, local velocities) and the configuration type. To conclude, the behavior of numerical error in the simulations of fluid flow using SBB technique as a boundary condition is not the same for different lattice models[86] and geometry types, and, therefore, SBB should be used with caution.

The sphere packings studied in this work have periodic boundary conditions along the principal flow direction that, in turn, enables the use of a body force instead of pressure boundaries.[87] Using the approach employed in the studies of He et al.[84] and Ginzbourg and Adler,[83] the body force $\vec{F}$ was added to the system by modification of equation (1.21) in the following way:

$$f_\alpha(\vec{x} + \vec{e}_\alpha \Delta t, t + \Delta t) = f_\alpha(\vec{x}, t) - \frac{\Delta t}{\tau} \left(f_\alpha(\vec{x}, t) - f_\alpha^{\mathrm{eq}}(\vec{x}, t) \right) + g_\alpha \vec{e}_\alpha \cdot \vec{F}, \tag{1.26}$$

where the coefficients g_α are defined as[84,88]

$$g_\alpha = \begin{cases} 0, & \alpha = 0; \\ 1/6, & \alpha = 1, 2, \ldots, 6; \\ 1/12, & \alpha = 7, 8, \ldots, 18. \end{cases} \tag{1.27}$$

1.3.5 Model validation

Here we present a validation of the flow simulation approach described in Subsections 1.3.2–1.3.4 and Section 1.5. Namely, we examine our implementation of the lattice Boltzmann method by i) comparison of the simulated results with an analytical solution available for a simple system like flow between two infinite parallel plates, ii) a study of the influence of grid resolution on the permeability of sphere packings, and iii) comparison of the simulated permeability with analytical predictions, empirical correlations, and literature data.

Flow in open channel

A first set of simulations was performed in a simple system, namely, Stokes flow in a channel formed by two infinite parallel plates, which is often referred to as "Poiseuille flow." This system has an analytical solution for the flow profile (having parabolic shape, with zero values at the channel walls and a maximum in the channel center) and corresponding mean flow velocity,

[85] R. S. Maier and R. S. Bernard. *J. Comput. Phys.*, **229**: 233–255, 2010.
[86] D. Kandhai et al. *J. Comput. Phys.*, **150**: 482–501, 1999.
[87] P. M. Adler, M. Zuzovsky, and H. Brenner. *Int. J. Multiphase Flow*, **11**: 387–417, 1985.
[88] J. M. Buick and C. A. Greated. *Phys. Rev. E*, **61**: 5307–5320, 2000.

thereby allowing a straightforward comparison of simulated values with analytical ones. For this system, LBM demonstrated an excellent agreement between simulated and analytical solutions, namely, the correct reproduction of the parabolic flow profile (data not shown) and the relative error of the mean flow velocity of 0.5% at a spatial resolution of 25 grid nodes per channel height.

In the next step, we simulated flow through closely packed arrays of spheres. We generated three types of sphere packings, each having the following varied properties: porosity, degree of heterogeneity (DoH), and confinement type. The values of packing properties were chosen to reflect the corresponding border values of the packings used in the simulations within this thesis.

Flow through ordered and disordered sphere packings

Packings of the first type are periodic cells formed by the body-centered cubic (BCC) structure. We studied three BCC packings with porosities of ~ 0.32 (touching spheres), 0.366, and 0.46 (both are expanded BCC). Packings of the second type are periodic ("bulk") random-close packings with porosities of 0.366 and 0.46 and dimension of $10 \times 10 \times 75\ d_\mathrm{p}^3$, where d_p is a sphere diameter. Packings of the third type are generated in containers of rectangular and circular cross sections in order to analyze packings with a smooth container wall and a wall with corners. Compared to the bulk packings, the porosity of the confined packings typically has larger values due to the restrictions of sphere positions induced by the confining wall. Hence, we simulated confined packings with porosities of 0.42 and 0.48. Lateral dimensions of these packings were chosen as $10\ d_\mathrm{p}$ for circular (diameter) and $8.86\ d_\mathrm{p}$ for square (edge length) cross-sections. Such lateral dimensions result in a significant influence of the confining wall on the spatial distribution of the packing void space fraction (see Chapter 2). Packings of the second and third type were generated at two values of DoH, Rx0.001 and Sx2, which results in homogenous and heterogenous microstructure of the packings (see Subsection 1.1.1 and Chapter 6).

Darcy's law and permeability

The average flow velocity of an incompressible Newtonian fluid flowing through porous material can be described using Darcy's law[89,90]:

$$u_\mathrm{av} = \frac{\varepsilon \kappa^* \Delta p}{\nu}, \tag{1.28}$$

which relates the average fluid velocity u_av with the pressure gradient Δp applied to the system, fluid viscosity ν, and porosity of the material ε. The proportionality constant κ^* is known as permeability and characterizes the ability of the material to transport a fluid. Hereafter we will operate with the dimensionless permeability, i.e. $\kappa = \kappa^* / d_\mathrm{p}^2$, where d_p is the sphere diameter.

Influence of grid resolution on permeability

In the next validation step, we studied the influence of grid resolution on the permeability of the generated packings. Grid resolution was varied from relatively coarse $n = 10$ (where n is the number of grid nodes per sphere diameter) up to relatively fine $n = 90$. One should note

[89] J. Bear. *Dynamics of fluids in porous media*. Dover Publications, 1988.
[90] F. A. L. Dullien. *Porous media: fluid transport and pore structure*. 2nd ed. Academic Press, 1992.

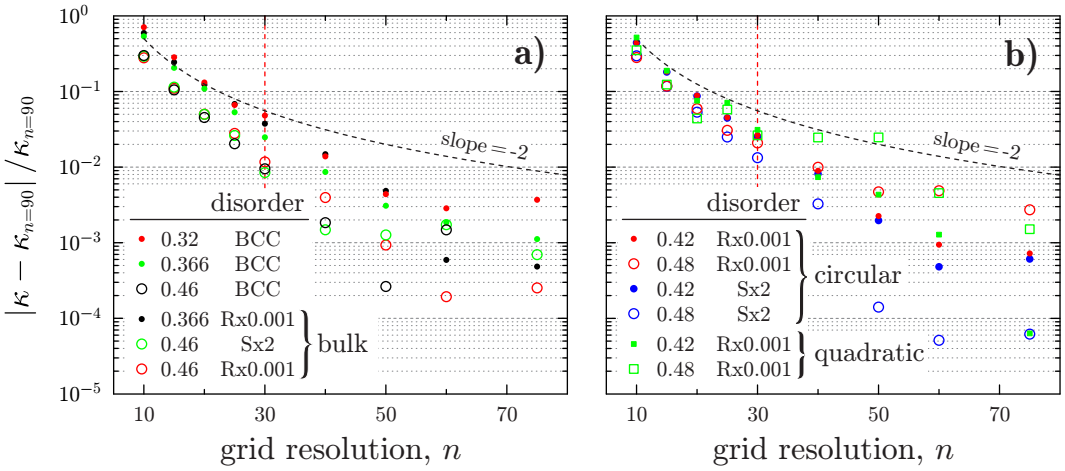

Figure 1.5: Dependence of the relative permeability error on the grid resolution: a) BCC and bulk packings, b) confined packings. Red dashed line indicates the grid resolution of 30 nodes per sphere diameter d_p, used in most simulations in this thesis.

that memory requirements grow as $O(n^3)$ and computational time as $O(n^5)$. Figure 1.5 shows the relative error in permeability, calculated in reference to the finest employed resolution of $n = 90$ lattice nodes per sphere diameter d_p. Packings of all three sets (BCC, bulk, and confined) demonstrate similar behavior in the convergence rate of the permeability error, independently of the order type (ordered, weakly and strongly disordered) and boundaries type (periodic or confined) as seen in Figure 1.5. The average porosity of the packings plays an important role, and the most dilute packings demonstrate significantly lower permeability error compared to the dense packings at a given grid resolution.

Simulations reveal a slope of the convergence lower than -2 while the employed method is of second order accuracy. This can be attributed to the large permeability error at lower grid resolutions,[85] which is caused by a higher "real" porosity of the packings, because, as mentioned, SBB locates the boundary between solid and adjacent fluid nodes (see Subsection 1.3.4). Similar convergence rate and magnitude of the permeability error was observed in the studies of Pan et al.[81] and Chun and Ladd,[91] although they used more advanced versions of LBM (multiple-relaxation-time MRT instead of single-relaxation-time BGK).

Permeability of BCC packing at high grid resolution

After the study of the grid convergence of permeability, permeability values calculated at high grid resolutions were compared with analytical predictions and empirical correlations. Simulated permeability of the densest BCC packing ($\varepsilon \approx 0.32$, $\kappa_{n=90} = 4.92 \cdot 10^{-4}$; see Table 1.1) is lower in comparison with analytical results of Zick and Homsy[92] ($\kappa = 5.01 \cdot 10^{-4} \pm 9.2 \cdot 10^{-7}$) and Sangani and Acrivos[93] ($\kappa = 5.01 \cdot 10^{-4}$) by 2%. A similar underestimation of the permeability of BCC packings was also observed in the simulations of Maier and Bernard[85] and Llewellin,[94] and can be

[91] B. Chun and A. J. C. Ladd. *Phys. Rev. E*, **75**: 066705, 2007.
[92] A. A. Zick and G. M. Homsy. *J. Fluid Mech.*, **115**: 13–26, 1982.
[93] A. S. Sangani and A. Acrivos. *Int. J. Multiphase Flow*, **8**: 343–360, 1982.
[94] E. W. Llewellin. *Comput. Geosci.*, **36**: 123–132, 2010.

attributed to the viscosity dependent permeability values obtained with the BGK/SBB model. One should note that such a behavior of the permeability is specific for the ordered structures[95] like BCC, FCC (face-centered cubic), and SC (simple cubic), and was not confirmed for the random sphere packings.[85]

Permeability of bulk random packings at high grid resolution

A detailed analysis of the permeability of the bulk random packings was performed using the set of packings generated with Jodrey–Tory (JT) and Monte Carlo (MC) algorithms (see Subsections 1.1.1 and 1.1.2). The set contained packings of six types and six porosity values (see Table 1.1); for each value of porosity and packing type we generated 10 random packing realizations. Packings of different types resulting from a variation of the parameters of JT and MC algorithms have different microstructure. A detailed analysis of the packing microstructure is given in Chapters 6 and 7, and further in this section only the permeability of the generated packings is discussed. Flow simulations were done in the packings discretized with a spatial resolution of $n = 60$ grid nodes per sphere diameter.

A widely used[73,75,95–101] way to estimate the permeability of dense ($\varepsilon < 0.50$) packings of spherical particles is to employ the Carman–Kozeny correlation,[89,90] originating from the model representation of the three-dimensional porous media as a bundle of capillary tubes:

$$\kappa = \frac{1}{k_{\mathrm{CK}}} \frac{\varepsilon^3}{(1-\varepsilon)^2}, \tag{1.29}$$

where k_{CK} is known as Carman–Kozeny constant. In case of sphere packings, the constant k_{CK} depends on *one-dimensional* tortuosity of the capillary model, and the value of $k_{\mathrm{CK}} = 180$ is widely used and assumed to be in a good agreement with experimental data on sphere packings.[89,90] Figure 1.6 shows permeability values of the bulk sphere packings simulated at high spatial resolution ($n = 60$) normalized by the permeability value calculated using equation (1.29) with $k_{\mathrm{CK}} = 180$. Each point in Figure 1.6 is calculated as an average value of 10 random realizations of each packing with fixed porosity and parameters of the generation algorithm.

As shown in Figure 1.6, both porosity and packing microstructure variation result in different values of the permeability. The important fact is that the trend in the porosity–permeability values of each packing type presented in Figure 1.6 is also reflected by i) independent estimates of the effective diffusion values characterizing tortuosity of the flow paths in a packing, and ii) geometrical analysis of the packing void space (see Chapter 7). Figure 1.6 demonstrates from one side, good agreement of the simulation results and equation (1.29) with $k_{\mathrm{CK}} = 180$, and from other side, the inability of equation (1.29) to provide an exact quantitative result. One should mention that

[95] R. S. Maier et al. *J. Colloid Interface Sci.*, **217**: 341–347, 1999.
[96] C. Pan, M. Hilpert, and C. T. Miller. *Phys. Rev. E*, **64**: 066702, 2001.
[97] D. Vidal et al. *Comput. Chem. Eng.*, **33**: 256–266, 2009.
[98] A. P. Philipse and C. Pathmamanoharan. *J. Colloid Interface Sci.*, **159**: 96–107, 1993.
[99] D. Coelho, J.-F. Thovert, and P. M. Adler. *Phys. Rev. E*, **55**: 1959–1978, 1997.
[100] R. P. Dias et al. *J. Hydrol.*, **349**: 470–474, 2008.
[101] P. B. Warren and F. Stepanek. *Phys. Rev. Lett.*, **100**: 084501, 2008.

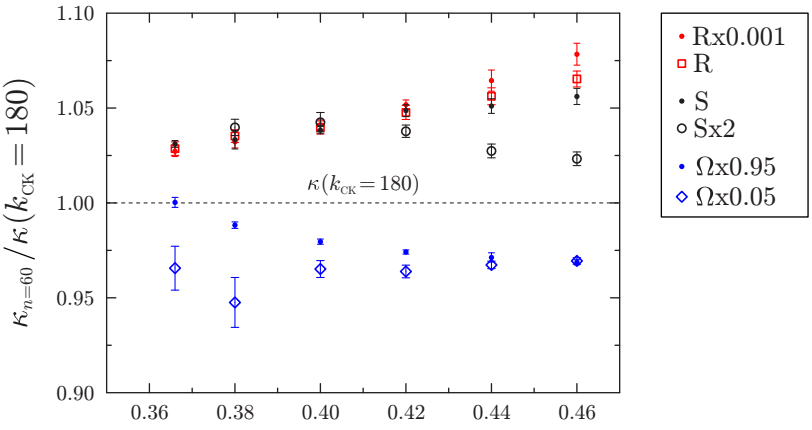

Figure 1.6: Dimensionless permeability $\kappa_{n=60}$ normalized by the Carman–Kozeny permeability $\kappa(k_{\mathrm{CK}} = 180)$ vs. porosity. Carman–Kozeny permeability is calculated according to equation (1.29) using $k_{\mathrm{CK}} = 180$. Error bars indicate 95% confidence intervals calculated using permeability of 10 random realizations of each packing with a fixed porosity and degree of heterogeneity.

a variety of porosity–permeability correlations are available in the literature,[75,89,90] but, to our knowledge, none of them takes into account an influence of the microstructural disorder, and, therefore, cannot be used to predict the data presented in Figure 1.6.

Permeability of confined random packings at high grid resolution

As the last validation step, permeability of the confined packings simulated at the resolution of $n = 90$ was analyzed (see Table 1.1). An introduction of a hard confining wall resulted in the decreasing permeability values, or, alternatively, in increasing values of the k_{CK} constant calculated using equation (1.29). Lower permeability of the confined packings was observed experimentally[102–105] and confirmed theoretically[106,107] for packings with a short lateral characteristic dimension ($L_{\mathrm{ch}} \approx 10–20\, d_{\mathrm{p}}$, where L_{ch}, for example, is the diameter of a packing of circular cross section), like those studied here. A simple explanation is that a confining wall results in the porosity and, respectively, flow velocity maldistribution in the vicinity of the wall (see Figures 2.2 and 2.4). Hence, confined packings can be assumed as a parallel combination of unequal resistances, and the resulting permeability of such a system will be smaller than that of a system with equal resistances, i.e., an unconfined packing. We note that this simple explanation cannot be applied to the pore-level maldistribution of void space: for example, uniform pores of a BCC crystal packing at an average porosity of $\varepsilon = 0.46$ result in significantly lower permeability than pores of random packings of equal porosity (see, for example, permeability values of BCC and random packings at $\varepsilon = 0.46$ in Table 1.1).

[102] R. Di Felice and L. G. Gibilaro. *Chem. Eng. Sci.*, **59**: 3037–3040, 2004.
[103] S. Jung et al. *J. Chromatogr. A*, **1216**: 264–273, 2009.
[104] B. Eisfeld and K. Schnitzlein. *Chem. Eng. Sci.*, **56**: 4321–4329, 2001.
[105] P. Mishra, D. Singh, and I. M. Mishra. *Chem. Eng. Sci.*, **30**: 397–405, 1975.
[106] Y. Cohen and A. B. Metzner. *AIChE J.*, **27**: 705–715, 1981.
[107] M. Winterberg and E. Tsotsas. *AIChE J.*, **46**: 1084–1088, 2000.

Table 1.1: Characteristic data and permeability of the simulated sphere packings.

packing set	ε	confinement type	n	microstructural disorder	κ	k_{CK}
BCC	0.3198	periodic	90	crystal	$4.92 \cdot 10^{-4}$	143.7
	0.366				$6.57 \cdot 10^{-4}$	185.6
	0.46				$1.21 \cdot 10^{-3}$	275.4
bulk	0.366	periodic	60	Rx0.001	$6.96 \cdot 10^{-4}$	175.2
				R	$6.97 \cdot 10^{-4}$	175.0
				S	$6.99 \cdot 10^{-4}$	174.6
				Ωx0.05	$6.54 \cdot 10^{-4}$	186.4
				Ωx0.95	$6.78 \cdot 10^{-4}$	179.9
bulk	0.38	periodic	60	Rx0.001	$8.19 \cdot 10^{-4}$	174.4
				R	$8.21 \cdot 10^{-4}$	173.9
				S	$8.19 \cdot 10^{-4}$	174.2
				Sx2	$8.25 \cdot 10^{-4}$	173.1
				Ωx0.05	$7.51 \cdot 10^{-4}$	190.0
				Ωx0.95	$7.84 \cdot 10^{-4}$	182.1
bulk	0.40	periodic	60	Rx0.001	$1.03 \cdot 10^{-3}$	172.9
				R	$1.03 \cdot 10^{-3}$	173.1
				S	$1.03 \cdot 10^{-3}$	173.3
				Sx2	$1.03 \cdot 10^{-3}$	172.7
				Ωx0.05	$9.53 \cdot 10^{-4}$	186.5
				Ωx0.95	$9.67 \cdot 10^{-4}$	183.8
bulk	0.42	periodic	60	Rx0.001	$1.29 \cdot 10^{-3}$	171.1
				R	$1.28 \cdot 10^{-3}$	171.8
				S	$1.28 \cdot 10^{-3}$	171.7
				Sx2	$1.27 \cdot 10^{-3}$	173.4
				Ωx0.05	$1.18 \cdot 10^{-3}$	186.7
				Ωx0.95	$1.19 \cdot 10^{-3}$	184.8
bulk	0.44	periodic	60	Rx0.001	$1.61 \cdot 10^{-3}$	169.1
				R	$1.59 \cdot 10^{-3}$	170.4
				S	$1.59 \cdot 10^{-3}$	171.3
				Sx2	$1.55 \cdot 10^{-3}$	175.2
				Ωx0.05	$1.46 \cdot 10^{-3}$	186.1
				Ωx0.95	$1.47 \cdot 10^{-3}$	185.3
bulk	0.46	periodic	60	Rx0.001	$2.00 \cdot 10^{-3}$	166.9
				R	$1.98 \cdot 10^{-3}$	169.0
				S	$1.96 \cdot 10^{-3}$	170.4
				Sx2	$1.90 \cdot 10^{-3}$	175.9
				Ωx0.05	$1.80 \cdot 10^{-3}$	185.7
				Ωx0.95	$1.80 \cdot 10^{-3}$	185.8
confined	0.42	circular	90	Rx0.001	$1.11 \cdot 10^{-3}$	199.2
				Sx2	$1.10 \cdot 10^{-3}$	199.7
confined	0.48	circular	90	Rx0.001	$2.19 \cdot 10^{-3}$	186.9
				Sx2	$1.98 \cdot 10^{-3}$	206.6
confined	0.42	square	90	Rx0.001	$1.11 \cdot 10^{-3}$	199.1
	0.48			Rx0.001	$2.21 \cdot 10^{-3}$	184.8

The employed model demonstrates close-to-monotonous convergence in the permeability towards grid-independent values obtained at high spatial resolution, which, in turn, agree well with the predictions available in the literature. Grid resolution of $n = 30$ (in Chapters 2–5) results in a *maximum* permeability error of 3.8%, which is a reasonable trade-off between accuracy and requirements in computational time and computer memory. One should note that permeability is an average value and its grid convergence doesn't provide an exact information on the convergence of the pore-scale details of the flow field. The value of most interest in this thesis, the hydrodynamic dispersion coefficient, is assumed to be more sensitive to the microstructural heterogeneities and corresponding pore-scale flow details than the permeability. The results of the study of grid resolution influence on the hydrodynamic dispersion coefficient are presented in Subsection 1.4.6.

1.4 Mass transport simulation

1.4.1 Advection–diffusion equation

A classical tool for the quantitative description of the mass transport due to advection and molecular diffusion is the solution of the advection–diffusion equation[89] (ADE):

$$\frac{\partial C}{\partial t} = \nabla \cdot (\mathbf{D} \nabla C) - \nabla \cdot (\vec{v} C). \tag{1.30}$$

This equation states that, with the absence of sources, evolution of solute concentration $C(\vec{x}, t)$ within a control volume is defined by diffusive flux (the first term on the right) and advective flux (the last term) entering this volume. The diffusion tensor is denoted by $\mathbf{D}$, and $\vec{v}$ is the fluid velocity. Equation (1.30) is a combination of parabolic and hyperbolic differential equations.[108] This causes difficulties while solving equation (1.30) numerically because a discrete equation of (1.30) changes its nature from parabolic to hyperbolic as advection starts to dominate diffusion.[109]

Discrete schemes based on the solution of equation (1.30) suffer from mass loss, oscillations of the solution,[110–112] and numerical dispersion.[112–114] The latter manifests itself as artificial distortions of concentration profiles in case of advection dominated regimes. High degrees of anisotropy often observed for hydrodynamic dispersion coefficients (comparing longitudinal and transverse ones, see, for example, Chapter 5) aggravate this problem.

Interesting is the fact that often the numerical solution of ADE is mentioned as not capable to reproduce non-Gaussian behavior of the dispersion.[115–118] However, it was shown that when spatial

[108] A. N. Tikhonov and A. A. Samarskii. *Equations of mathematical physics*. Dover Publications, 1990.
[109] O. C. Zienkiewicz, P. Nithiarasu, and R. L. Taylor. *The finite element method for fluid dynamics*. 6th ed. Elsevier Butterworth–Heinemann, 2005.
[110] M.-K. Liu and J. H. Seinfeld. *Atmos. Environ.*, **9**: 555–574, 1975.
[111] B. P. Leonard. *Comput. Methods Appl. Mech. Eng.*, **88**: 17–74, 1991.
[112] B. H. Devkota and J. Imberger. *Water Resour. Res.*, **45**: W12406, 2009.
[113] W. Kinzelbach. *Numerische Methoden zur Modellierung des Transports von Schadstoffen im Grundwasser*. 2nd ed. Oldenbourg Verlag, 1992.
[114] B. Lin and R. A. Falconer. *J. Hydraul. Eng.*, **123**: 303–314, 1997.
[115] A. Cortis and B. Berkowitz. *Soil Sci. Soc. Am. J.*, **68**: 1539–1548, 2004.
[116] S. Anwar, A. Cortis, and M. C. Sukop. *Prog. Comput. Fluid Dyn.*, **8**: 213–221, 2008.
[117] Y. Zhu and P. J. Fox. *J. Comput. Phys.*, **182**: 622–645, 2002.
[118] S. P. Kuttanikkad. *Pore-scale direct numerical simulation of flow and transport in porous media*. PhD thesis. Germany, Ruprecht Karl University of Heidelberg, 2009.

heterogeneities of porous media are resolved on the pore level, the numerical solution of ADE demonstrates correct behavior.[119] This fact points to the importance of the pore-level transport processes and their crucial influence on the macroscopic transport processes in porous media.

In this thesis, the Random Walk Particle Tracking (RWPT) method was employed; contrary to the Eulerian methods based on the solution of equation (1.30), RWPT is a Lagrangian approach and does not solve the ADE directly. A description of RWPT is given below.

1.4.2 Random walk particle tracking method

The basic idea of RWPT[2,120,121] is to simulate solute transport as the motion of a large number of representative particles, which, in this work, are referred to as *inert tracers*. Tracers have the following properties:

- infinitely small dimensions and no mass,
- no interaction with each other,
- no adsorption/desorption from the surface of porous media,
- they do not affect the motion of the fluid.

The time evolution of a tracer is defined by superposition of two processes: drift due to flow of carrier fluid and Brownian motion due to molecular diffusion. Mathematically, the tracer behavior can be described by a stochastic differential equation[122]:

$$\mathrm{d}\vec{r}(t) = \vec{v}(\vec{r}(t))\mathrm{d}t + \mathbf{B}\mathrm{d}\vec{W}(t). \tag{1.31}$$

Here $\vec{r}(t)$ and $\vec{v}(\vec{r}(t))$ are the tracer spatial coordinate and fluid flow velocity at the current location of the tracer, $\mathbf{B}$ is the second-order tensor with non-zero diagonal elements equal to $\sqrt{2D}$, where D denotes molecular diffusion coefficient; $\mathrm{d}\vec{W}$ is an increment of vector Wiener process (often called Brownian motion). The connection between equation (1.31), Fokker–Planck equation, and ADE is described elsewhere.[121]

In the general case, equation (1.31) cannot be solved analytically but only numerically. The simplest and often used[18,123,124] numerical solution of equation (1.31) is to employ the one-step Euler approximation in the following form[125]:

$$\vec{r}(t + \Delta t) = \vec{r}(t) + \vec{v}(\vec{r}(t))\Delta t + \sqrt{2D\Delta t}\vec{N}, \tag{1.32}$$

where Δt is the time step and $\vec{N}$ is a vector having random components normally distributed with zero mean and unity variance. A sequence of pseudo-random normally distributed random values,

[119] P. Salamon, D. Fernàndez-Garcia, and J. J. Gómez-Hernández. *Water Resour. Res.*, **43**: W08404, 2007.
[2] J. A. Rudnick and G. D. Gaspari. *Elements of the random walk: an introduction for advanced students and researchers*. Cambridge University Press, 2004.
[120] F. Delay, P. Ackerer, and C. Danquigny. *Vadose Zone J.*, **4**: 360–379, 2005.
[121] P. Salamon, D. Fernàndez-Garcia, and J. J. Gómez-Hernández. *J. Contam. Hydrol.*, **87**: 277–305, 2006.
[122] C. W. Gardiner. *Handbook of stochastic methods: for physics, chemistry and the natural sciences*. 2nd ed. Springer-Verlag, 1996.
[123] R. S. Maier et al. *Phys. Fluids*, **12**: 2065–2079, 2000.
[124] D. Spivakovskaya, A. W. Heemink, and E. Deleersnijder. *Ocean Dyn.*, **57**: 189–203, 2007.
[125] P. E. Kloeden and E. Platen. *Numerical solution of stochastic differential equations*. Springer-Verlag, 1995.

which is generated by the digital computers, can be used to approximate the increment of Wiener process $\mathrm{d}\vec{W}$,[125] and, consequently, to generate components of $\vec{N}$.

Depending on whether tracer trajectories or only statistical moments of tracers ensemble are of importance, strong or weak convergence criteria must be applied to equation (1.32), respectively.[125] The value of interest in this study is the hydrodynamic dispersion coefficient, which is calculated from the statistical moments of the tracer ensemble, and, therefore, a weak convergence criterion is used; the order of weak convergence in time step Δt of the approximation (1.32) is 1.0.

As advantages of RWPT, one can mention the simplicity of the method program realization and its further parallelization, absence of numerical dispersion, and conservation of mass (due to constant amount of tracers in the system). At the same time, due to statistical noise, whose amplitude decreases with the square root of the tracer amount, a large amount of tracers is needed to accurately reproduce the concentration profiles,[126,127] and high computational times in the case of mass transport simulations in homogenous systems[127,128] can be attributed to the limitations of RWPT.

1.4.3 Hydrodynamic dispersion coefficient and Péclet number

The value of most interest in this thesis is the *hydrodynamic dispersion coefficient*. As mentioned before, mass transport of a solute is simulated as motion of a large number of tracer particles. The value of the hydrodynamic dispersion coefficient is calculated as follows[129]:

$$D_z(t) = \frac{1}{2N}\frac{\mathrm{d}}{\mathrm{d}t}\sum_{i=1}^{N}\left(\Delta z_i(t) - \langle \Delta z_i(t)\rangle\right)^2, \tag{1.33}$$

where $\Delta z_i(t)$ is the z-displacement of i-th tracer after time t, $\langle \ldots \rangle$ denotes averaging over the whole tracer ensemble, and N is the number of tracer particles. Equation (1.33) states that the hydrodynamic dispersion coefficient along z-direction is proportional to the rate of the spreading of tracers around their mean position along the z-direction. In this thesis, the hydrodynamic dispersion coefficient is calculated along two principal directions, parallel and orthogonal to the direction of fluid flow. The coefficient calculated along the former direction is denoted as *longitudinal* (D_{L}) or *axial* (D_{ax}), while the latter as *transverse* (D_{T}).

It is more convenient to operate not with the absolute value of D_z, but with its value normalized by the molecular diffusion coefficient of the tracers, D_{m}. After such a normalization, the quantity D_z/D_{m} shows how large the rate of tracers spreading is relative to the rate of spreading due to the molecular diffusion only. In random sphere packings studied here, D_z/D_{m} takes values from zero to several thousands, depending on the packing geometry, spatial direction along which the coefficient is determined, and the flow velocity.

[126] H. V. Nguyen et al. *J. Hydrol.*, **215**: 188–201, 1999.
[127] P. H. Israelsson, Y. D. Kim, and E. E. Adams. *Environ. Modell. Software*, **21**: 1631–1649, 2006.
[128] A. E. Hassan and M. M. Mohamed. *J. Hydrol.*, **275**: 242–260, 2003.
[129] H. Brenner. *Philos. Trans. R. Soc. A*, **297**: 81–133, 1980.

Obviously, the hydrodynamic dispersion coefficient depends on the average flow velocity through a packing: higher flow velocity results in larger values of the coefficient. It is common to characterize the velocity of flow through the porous material in terms of the dimensionless Péclet number (or reduced velocity):

$$Pe = \frac{u_{\mathrm{av}} l_{\mathrm{c}}}{D_{\mathrm{m}}}, \tag{1.34}$$

which is the ratio of advection to diffusion transport rates occurring in a system with a given characteristic length l_{c}. In equation (1.34), u_{av} is the average flow velocity through the porous material and D_{m} is the molecular diffusion coefficient. In the systems studied in this thesis, mass transport can be formally characterized as "diffusion-dominated" if Pe takes values about unity and "advection-dominated" if Pe is on the order of hundreds or thousands (see Figure 5.6).

In-depth study of the hydrodynamic dispersion in sphere packings requires the simulation of mass transport over a wide range of Péclet numbers in each packing. Low Reynolds number flow ($Re \ll 1$, $Re = d_{\mathrm{p}} u_{\mathrm{av}}/\nu$, where ν is the kinematic viscosity), also known as creeping or Stokes flow, is a typical flow regime in chromatographic beds and is of interest in this study. According to Darcy's law (equation (1.28)), a change of the pressure gradient driving the fluid causes a corresponding *linear* change of the average flow velocity as far as $Re \ll 1$ is satisfied,[130] and local flow components follow the same linear scaling.[131,132] This allows us to calculate one flow field for a given packing and to perform further mass transport simulations in this packing using the simulated flow field linearly scaled according to the required Péclet numbers.

1.4.4 Boundary conditions

In this thesis the motion of tracers is simulated in the interparticle void space only (i.e., no motion occurs in the solid phase) using the no-flux boundary condition (BC) at the solid boundaries of the spheres and confining wall of a packing, while at the external boundaries of the packing periodic boundary conditions are used (along the axial direction/direction of the applied pressure gradient in the confined packings and along the three directions in the unconfined ones). The no-flux BC at a solid–liquid interface can be implemented using different approaches[133,134]:

- *Specular reflection*.[118,134,135] This BC implies mirror-like reflection of a tracer from the solid–liquid interface if a collision with the interface occurs.
- *Rejection*.[132,136–138] If a tracer crosses the solid–liquid interface, such a move is rejected, and the tracer stays at its previous position during the current iteration.

[130] D. Hlushkou and U. Tallarek. *J. Chromatogr. A*, **1126**: 70–85, 2006.
[131] J. C. Giddings. *Dynamics of chromatography: principles and theory*. Marcel Dekker, 1965.
[132] M. R. Schure et al. *Anal. Chem.*, **74**: 6006–6016, 2002.
[133] P. Szymczak and A. J. C. Ladd. *Phys. Rev. E*, **68**: 036704, 2003.
[134] R. K. Nandigam and D. M. Kroll. *Biophys. J.*, **92**: 3368–3378, 2007.
[135] J. Hrabe, S. Hrabětová, and K. Segeth. *Biophys. J.*, **87**: 1606–1617, 2004.
[136] I. C. Kim and S. Torquato. *J. Chem. Phys.*, **96**: 1498–1503, 1992.
[137] P. N. Sen et al. *Phys. Rev. B*, **49**: 215–225, 1994.
[138] A. S. Kim and H. Chen. *J. Membr. Sci.*, **279**: 129–139, 2006.

- *Multiple rejection*.[139,140] If at the current iteration a tracer hits the solid wall, such a move is cancelled and the diffusion component of the tracer displacement is recalculated until the tracer's final position (at the current iteration) will be in the fluid phase.
- *Interruption*.[18,123,141,142] Here a time step (Δt) of the tracer crossing the interface at the current iteration is split into two parts, before (Δt_1) and after ($\Delta t_2 = \Delta t - \Delta t_1$) the interface crossing, respectively. Then the tracer is moved to the point of the contact with the interface, and an additional displacement with the time step Δt_2 is performed.
- *Time step division*.[124,143,144] If a tracer crosses a boundary, such a move is cancelled, the default time step is divided into smaller steps, and the tracer performs several moves with the reduced time steps; this procedure is repeated until the total time step at the current iteration will be equal to the default one.

In our simulations we employ the multiple rejection BC. It has been demonstrated that rejection, multiple rejection, and interruption, contrary to the more precise and computationally expensive specular reflection approach, lead to an artificial distortion of concentration profiles near the solid–liquid interface.[133,134] In order to check how sensitive the hydrodynamic dispersion coefficient (Subsection 1.4.3) is to the error introduced by the multiple rejection BC, we performed simulations of mass transport using Δt, $\Delta t_{0.1}$, and $\Delta t_{0.02}$ time steps, where $\Delta t_{0.02} = 0.2\Delta t_{0.1} = 0.02\Delta t$, and Δt denotes the default time step used in this work. The reduction of the time step results in reduced relative influence of BC on the tracers motion. The default time step Δt is selected so that the maximal advective–diffusive displacement of a tracer does not exceed half of the lattice space step. Simulations were performed for both diffusion- and advection-dominated transport regimes in the most dense packing employed in this study. In such a packing the influence of an error introduced by the employed BC on the hydrodynamic dispersion coefficient is expected to be maximal compared to the more loose packings. The packing has a porosity of 0.366, a spatial dimension of $10 \times 10 \times 75\ d_\mathrm{p}^3$, and was discretized with a spatial resolution of $n = 30$ and $n = 90$ nodes per particle diameter (d_p).

The results presented in Figure 1.7 demonstrate weak influence of the time step refinement on the value of the hydrodynamic dispersion coefficient (this was also mentioned by Maier et al.[123]): the difference in close-to-asymptotic rates of the dispersion coefficient (calculated within the range $2–2.5\ \tau_\mathrm{D}$) between Δt and $\Delta t_{0.02}$ is -0.8% at low and $+3\%$ at high flow rates ($Pe = 5$ and $Pe = 500$, respectively). As was shown by Szymczak and Ladd,[133] the multiple rejection BC decreases tracer concentration near reflecting walls (cf. Figures 1 and 2 in Reference [133]). Therefore, we can assume that the reduction of the time step allows more tracers to approach the vicinity of the reflecting wall, which is the "*stair-step*" surface of the packing spheres and confining wall. In case of the low flow rate (Figure 1.7a), this results in a larger amount of tracer collisions with the wall,

[139] T. Rage. *Studies of tracer dispersion and fluid flow in porous media*. PhD thesis. Norway, University of Oslo, 1996.
[140] S. Trinh, P. Arce, and B. R. Locke. *Transp. Porous Media*, **38**: 241–259, 2000.
[141] J. Salles et al. *Phys. Fluids A*, **5**: 2348–2376, 1993.
[142] F. J. Jiménez-Hornero, J. V. Giráldez, and A. Laguna. *Vadose Zone J.*, **4**: 310–316, 2005.
[143] W. M. Charles. *Transport modelling in coastal waters using stochastic differential equations*. PhD thesis. The Netherlands, Delft University of Technology, 2007.
[144] J. W. Stijnen. *Numerical methods for stochastic environmental models*. PhD thesis. The Netherlands, Delft University of Technology, 2002.

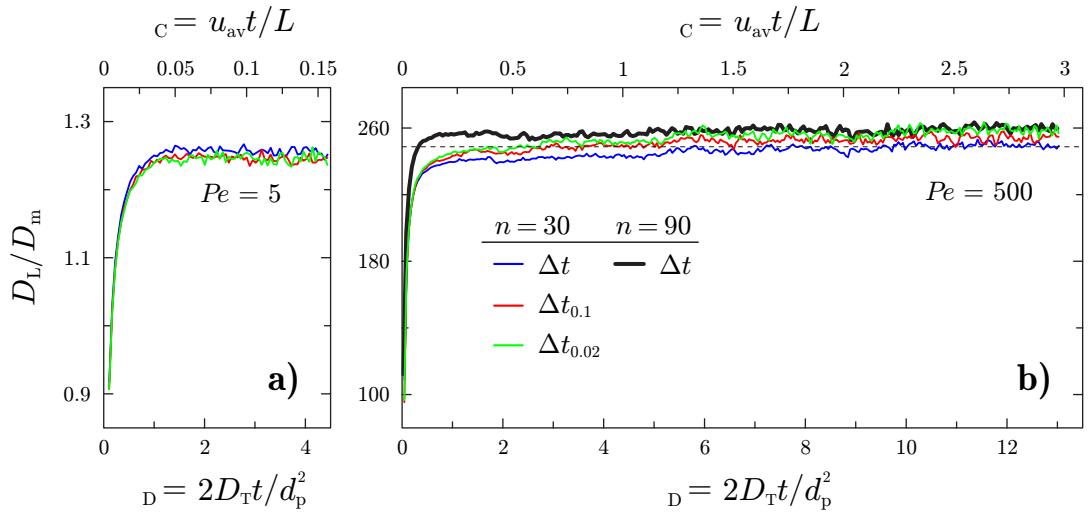

Figure 1.7: Normalized longitudinal hydrodynamic dispersion coefficient as a function of the dispersive (τ_D) and convective (τ_C) times in a periodic random sphere packing; $\tau_D = 2D_T t/d_p^2$ and $\tau_C = u_{av}t/L$, where D_T, d_p, u_{av}, and $L = 75\,d_p$ denote transverse dispersion coefficient, diameter of a spherical particle, the average (interstitial) flow velocity, and the packing length, respectively. Simulations were performed at $Pe = 5$ and $Pe = 500$ using different time steps of RWPT method and a lattice resolution of $n = 30$ grid nodes per sphere diameter. Bold black line in part b) denotes a simulation of the hydrodynamic dispersion at high grid resolution ($n = 90$). Horizontal dashed line in part b) helps to identify slow growth of the dispersion coefficient observed in simulations with $n = 30$.

the slow down of the tracer diffusion movement around spheres and, finally, in a reduction of the dispersion coefficient. At high flow rate (Figure 1.7b), the increase in the tracer concentration near the solid surfaces allows a larger fraction of the tracers to be slowed down due to exploring the stagnant fluid "boundary layers" surrounding spheres within a packing[145] and to get these "slow" tracers behind the tracers being away from the spheres and moving with the flow.

For all involved time steps, Figure 1.7b demonstrates a weak growth of the hydrodynamic dispersion coefficient after its close-to-asymptotic value is reached (i.e., after $\sim 2\,\tau_D$, see Chapter 5). This can be related to the used value of the grid resolution ($n = 30$): with an increase of the spatial resolution up to $n = 90$ (bold black line in Figure 1.7b), the growth rate of the dispersion coefficient after one τ_D decreases. Additional information on the influence of the grid resolution on the time evolution of the dispersion coefficient is given in Subsection 1.4.6.

1.4.5 Random displacement and initial conditions

As mentioned before, the diffusion displacement of a tracer is generated using random numbers calculated from the Gaussian distribution with zero mean and unity variance. To obtain weak convergence, the distribution has not necessarily Gaussian, the only requirements are the correspondence of its statistical moments to the ones of the Gaussian distribution and independency of the generated values. Often uniform distributions of finite-range are used[18,123,137,141,142,146] due to

[145] D. L. Koch and J. F. Brady. *J. Fluid Mech.*, **154**: 399–427, 1985.

[146] M. R. Schure. In: *Advances in Chromatography*. P. R. Brown and E. Grushka, eds. Vol. 39, 139–200. Marcel Dekker Publishing, 1998.

simplicity of handling and speed of the generated random numbers. Contrary to the finite-range distributions, normally distributed numbers take values in the infinite range due to tailing of the Gaussian distribution. To avoid very large values of the tracer diffusion displacement x_d, originating from tails of the Gaussian distribution, x_d is generated using *truncated* Gaussian distribution: if the diffusion displacement x_d of a tracer exceeds x_t, it is omitted and a new displacement is generated instead. In our simulations the minimal value of x_t is chosen equal to $4\sqrt{D_\mathrm{m}\Delta t}$ which is sufficiently large to make the error introduced by truncation negligible.[133]

In each simulation of mass transport, the initial distributions of tracers are done in the whole interparticle void space. This enables collection of the information on the heterogeneity and corresponding transport properties of a given packing more rapidly than in case of plane-wise distribution of tracers at the packing inlet (which is the case for the breakthrough experiments).

1.4.6 Numerical behavior and validation of the model

Hydrodynamic dispersion in open channels

We begin validation of the implemented RWPT method by the simulation of hydrodynamic dispersion in two simple geometries, open channels of circular and square cross section. Hydraulic flow of a viscous fluid in open channels, for example, formed by two parallel plates or a tube, results in the parabolic-like flow profiles (see Figure 4.2) with zero transverse and non-zero longitudinal components. A delta pulse of a solute injected at the channel inlet flows downstream along the channel and is dispersed due to molecular diffusion and non-uniformity of the flow field. Hydrodynamic dispersion in open channel geometries, also known as Taylor–Aris dispersion,[147–149] can be quantified as[150]

$$\frac{D_\mathrm{L}}{D_\mathrm{m}} = 1 + \frac{Pe^2}{210} f, \tag{1.35}$$

where D_L is the hydrodynamic dispersion coefficient calculated along the flow direction, D_m denotes the molecular diffusion coefficient, and Pe is the Péclet number (Subsection 1.4.3). Equation (1.35) with $f = 1$ describes dispersion in the system presented by two parallel plates. In the general case, f is a function depending on the geometry of a channel and $f \geq 1$ for most channel cross sections.[150] Channels with circular and square cross sections are characterized by $f_\mathrm{cir} = 210/192 \approx 1.09$[147] and $f_\mathrm{sq} \approx 1.75$,[150] respectively. It should be noted that an exact value of f_sq is still under discussion.[151,152]

Simulation of hydrodynamic dispersion was performed in the open channels of circular and square cross section with lateral lattice dimensions of 50 lattice nodes per circle diameter d_cir and square side a_sq, respectively. The Péclet number was specified as $Pe_\mathrm{cir} = u_\mathrm{av} d_\mathrm{cir}/D_\mathrm{m}$ and $Pe_\mathrm{sq} =$

[147] G. Taylor. *Philos. Trans. R. Soc. A*, **219**: 186–203, 1953.
[148] G. Taylor. *Philos. Trans. R. Soc. A*, **225**: 473–477, 1954.
[149] R. Aris. *Philos. Trans. R. Soc. A*, **252**: 538–550, 1959.
[150] D. Dutta, A. Ramachandran, and D. T. Leighton. *Microfluid. Nanofluid.*, **2**: 275–290, 2006.
[151] H. Ahn and S. Brandani. *AIChE J.*, **51**: 1980–1990, 2005.
[152] D. Liang et al. *Lab Chip*, **7**: 1062–1073, 2007.

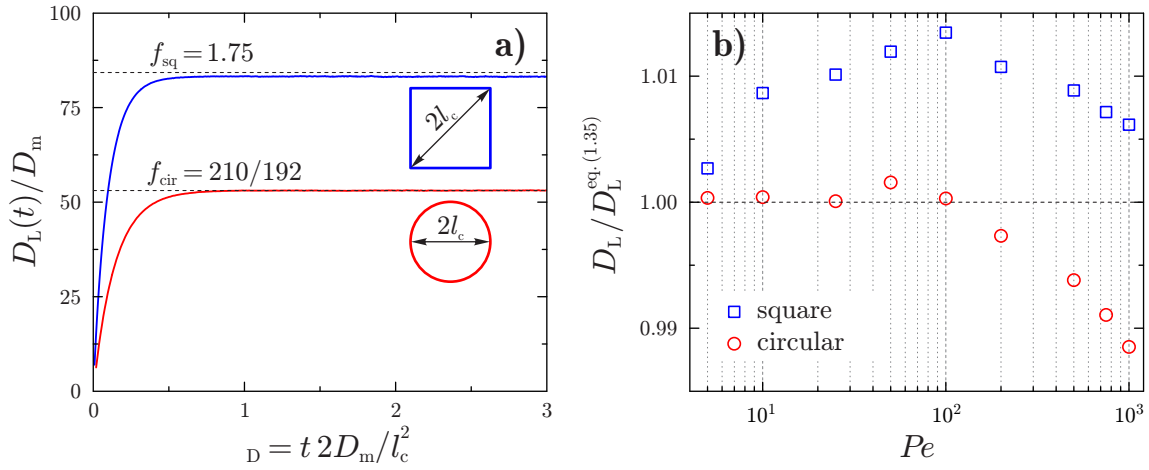

Figure 1.8: a) Time evolution of the hydrodynamic dispersion coefficient in open channel with circular and square cross sections at $Pe = 100$. b) Close-to-asymptotic values of the dispersion coefficient normalized by its value calculated using equation (1.35) with $f_{cir} = 210/192$ and $f_{sq} = 1.75$.

$u_{av}a_{sq}/D_m$ for circular and square geometries, respectively. Figure 1.8a shows the hydrodynamic dispersion coefficient $D_L(t)/D_m$ as a function of the diffusive time $\tau_D = t\,2D_m/l_c^2$ (here t is the simulation time and l_c is the characteristic length, selected as shown in Figure 1.8a). Time evolution of the dispersion curve in Figure 1.8a can be formally split into two parts: "pre-asymptotic" or "transient," where the dispersion coefficient grows with time, and "close-to-asymptotic," where it stays approximately constant. Growth of the dispersion coefficient in the transient part of the curve is related to the i) difference in convective and diffusive displacements, which depend on time as t and $\sqrt{t}$, respectively, and ii) nonuniformity of the flow field. At very short times ($t \ll \tau_D$) the solute is spread mainly due to diffusion and the value of the normalized hydrodynamic dispersion coefficient is close to unity. At longer times, nonuniform solute displacement due to a flow maldistribution leads to the growth of the dispersion coefficient. Molecular diffusion causes solute species to migrate between flow streamlines and the dispersion coefficient takes its close-to-asymptotic value after solute species have "explored" the longest distance between velocity extremes of the flow field.

An exact solution for the transient part of the dispersion curve is still unknown,[153,154] and we compared only close-to-asymptotic values of the dispersion coefficient simulated at different Péclet numbers with data available in the literature (i.e., using $f_{cir} = 210/192$ and $f_{sq} = 1.75$). As shown in Figure 1.8b, the comparison reveals an excellent agreement of the simulated dispersion coefficients with the literature data for the two simple systems studied here.

Hydrodynamic dispersion in ordered sphere packings

We do not analyze the accuracy of the RWPT model in the case of crystal structures because analytical solutions for the dispersion coefficient are not available for any of them (FCC, HCP, BCC, or SC) and only a limited amount of data on hydrodynamic dispersion coefficients is available

[153] A. Adrover et al. *Anal. Chem.*, **81**: 8009–8014, 2009.
[154] M. Giona et al. *Phys. Fluids*, **21**: 123601, 2009.

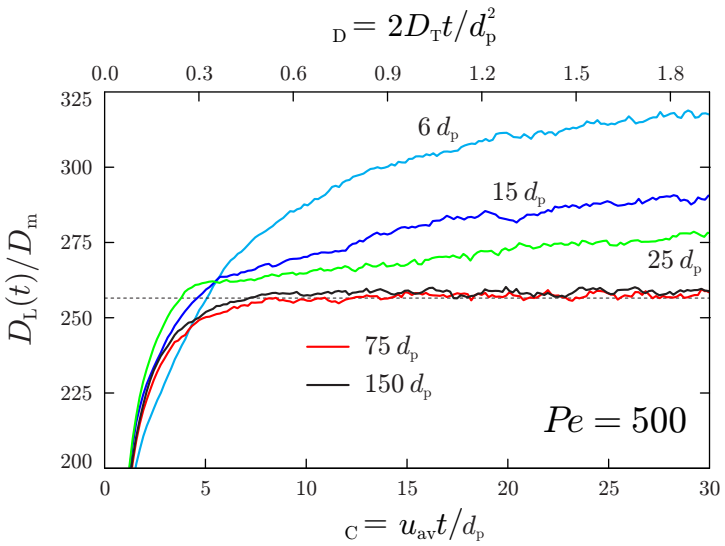

Figure 1.9: Evolution of the hydrodynamic coefficient as a function of the convective τ_C and dispersive τ_D times. $\tau_C = u_{av}t/d_p$, where u_{av} is the average flow velocity and d_p is the particle diameter. $\tau_D = 2D_T t/d_p^2$, where D_T denotes the transverse dispersion coefficient. Simulations are performed at $Pe = 500$ in sphere packings with length of 6, 15, 25, 75, and 150 d_p and transverse dimension of 10 d_p × 10 d_p, porosity of $\varepsilon = 0.366$, and discretized with spatial resolution of $n = 90$ grid nodes per sphere diameter.

in the literature.[123,132,155] Systematic numerical study of hydrodynamic dispersion in crystals requires a large amount of computational resources because the dispersion coefficient demonstrates anisotropic behavior in crystal structures,[141,156] contrary to the permeability in the case of Stokes flow ($Re \ll 1$) and effective diffusion, which are independent on the selected direction in a crystal.[99,157]

Influence of packing length on hydrodynamic dispersion coefficient

While for the simulations in crystal structures the simulation domain may contain one unit cell of a given crystal, the choice of the domain size for the random packings is not trivial. Figure 1.9 shows the evolution of the hydrodynamic dispersion coefficient in the bulk packings with the porosity of $\varepsilon = 0.366$ and the spatial dimension of $L\ d_p \times 10\ d_p \times 10\ d_p$, where d_p is the sphere diameter and L denotes the dimensionless packing length along the direction of flow. Simulations were performed for the following values of L: 6, 15, 25, 75, and 150. As Figure 1.9 shows, the dispersion coefficient converges to the lower values as the packing length increases from 6 to 75; a further increase of the packing length (up to $L = 150$) does not affect the time evolution and close-to-asymptotic value of the dispersion coefficient. Such a behavior is related to the situation when some of the tracers reentering periodic domain of the packing (after $\tau_C/L \approx 0.5$–1, where $\tau_C = u_{av}t/d_p$ and u_{av} are the convective time and mean flow velocity, respectively) explore regions of the packing void space with similar flow velocities. In other words, to determine the close-to-asymptotic hydrodynamic dispersion coefficient of a given packing which is free from the enhanced influence of some flow

[155] D. J. Gunn and C. Pryce. *Trans. Inst. Chem. Eng.*, **47**: T341, 1969.
[156] H. P. A. Souto and C. Moyne. *Phys. Fluids*, **9**: 2253–2263, 1997.
[157] H. P. A. Souto and C. Moyne. *Phys. Fluids*, **9**: 2243–2252, 1997.

paths, the length of the simulation domain must be long enough to observe close-to-asymptotic behavior of the dispersion coefficient before a fraction of the tracers will reenter the simulation domain. The influence of the packing length on the hydrodynamic dispersion coefficient was reported before,[42,123,158] and the minimal domain length to avoid recorrelation was suggested to be $\tau_C/L > 0.25–0.5$. It is important to note that we observed close-to-asymptotic behavior for the packings of all involved lengths ($6–150$, data not shown), i.e. the absence of growth of the dispersion coefficient does not imply that the observed value of the coefficient is free from a "recorrelation effect." If the domain length is short (according to the criterion above) and periodic conditions are not used along the domain length, the dispersion coefficient will be detected in its pre-asymptotic regime.

Despite the fact that the influence of the domain length was mentioned many times in literature, there is a number of recent studies[118,159–161] which have used short simulation domains to determine hydrodynamic dispersion coefficients, and some of them are done in two-dimensional systems, for which correlations persisting in the flow field have a longer range than those in three dimensional flows.[162,163]

Influence of grid resolution on hydrodynamic dispersion coefficient

Figures 1.10a,b,c show simulation results on the grid convergence of the hydrodynamic dispersion coefficient towards its value calculated at high grid resolution ($n = 90$). Comparing with the grid convergence of permeability values (Figure 1.5), data for hydrodynamic dispersion demonstrate significant scatter, especially for quadratic packings. This can be attributed to the high sensitivity of the hydrodynamic dispersion coefficient on the packing microstructure which, in turn, is varied with the discretization at different grid resolutions. In addition, corners of the quadratic packings are regions of advanced fluid flow (see Figure 2.4) and sources of a significant increase of the dispersion coefficient compared to the geometries without corners. The error resulting from the discrete representation of the corner regions causes an additional scatter of the hydrodynamic dispersion coefficient, as shown in Figures 1.10b,c.

Figure 1.10c has missing data points at low grid resolution ($n = 10–25$) for some of the studied packings. This issue is related to the situation demonstrated in Figure 1.10d, where we present the time evolution of the hydrodynamic dispersion coefficient in a bulk packing (Rx0.001, $\varepsilon = 0.46$) simulated at $Pe = 500$ and the grid resolutions of $n = 10$, 30, and 90. As a time unit, we selected dispersive time τ_D (see caption of Figure 1.10 for details) which allows us to unify the transient time of the hydrodynamic dispersion coefficient to its close-to-asymptotic value: as it will be demonstrated later (see Chapters 5 and 6), the hydrodynamic dispersion coefficient in bulk packings arrives at its close-to-asymptotic value after $\tau_D \approx 1–2$ for all studied Péclet numbers. As can be seen in Figure 1.10d, the dispersion coefficients simulated at a moderate flow rate

[158] C. P. Lowe and D. Frenkel. *Phys. Rev. Lett.*, **77**: 4552–4555, 1996.
[159] A. M. Tartakovsky. *Phys. Rev. E*, **82**: 026302, 2010.
[160] D. Buyuktas and W. W. Wallender. *Heat Mass Transfer*, **40**: 261–270, 2004.
[161] J. Billen et al. *J. Chromatogr. A*, **1073**: 53–61, 2005.
[162] B. J. Alder and T. E. Wainwright. *Phys. Rev. A*, **1**: 18–21, 1970.
[163] D. L. Koch, R. J. Hill, and A. S. Sangani. *Phys. Fluids*, **10**: 3035–3037, 1998.

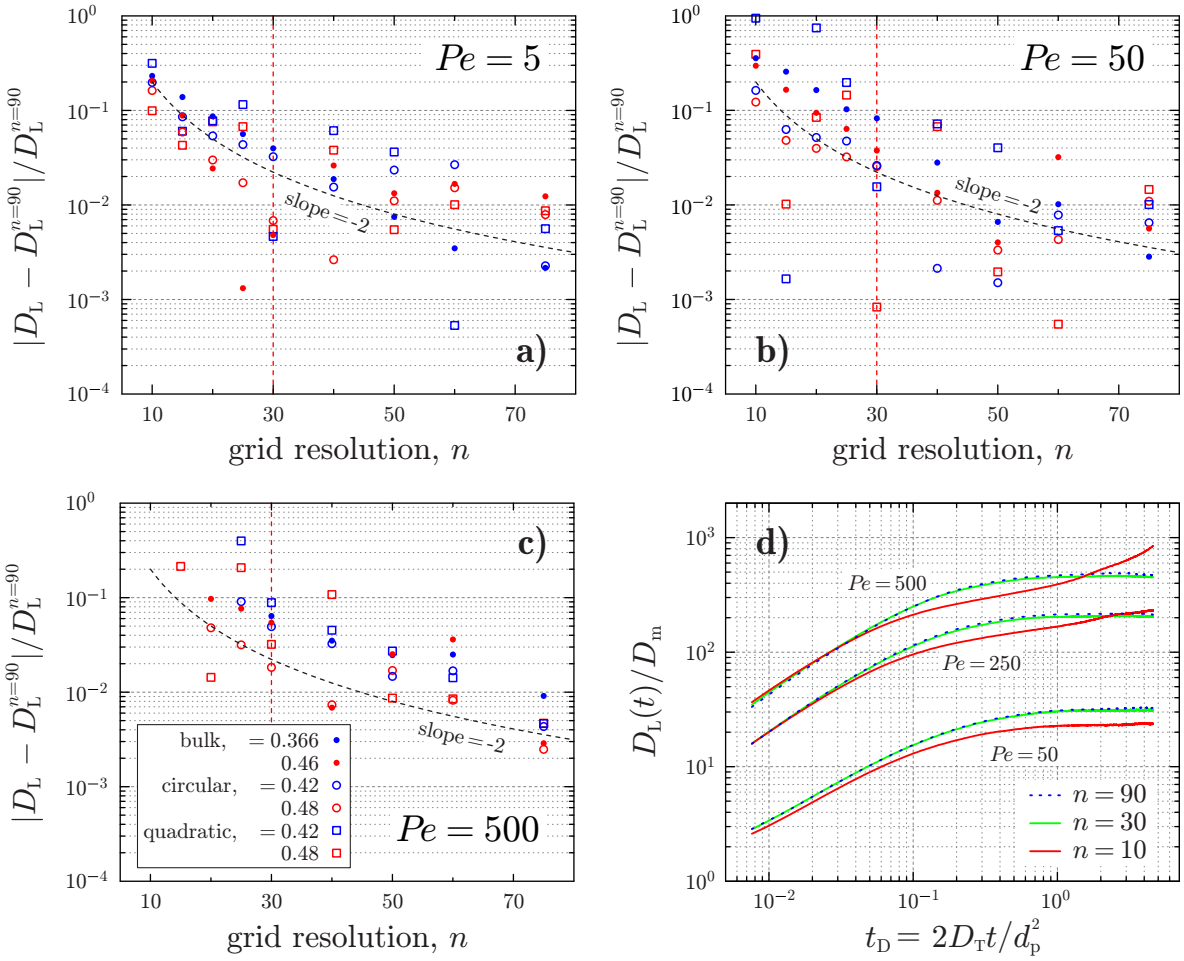

Figure 1.10: Dependence of the relative error in close-to-asymptotic values of the hydrodynamic dispersion coefficient on the grid resolution at $Pe = 5$ (a), 50 (b), and 500 (c) in Rx0.001 packings with type and porosity indicated in the figure legend. Part d) shows development of the hydrodynamic dispersion coefficient in a bulk packing (Rx0.001, $\varepsilon = 0.46$) at low ($n = 10$), moderate ($n = 30$), and high ($n = 90$) grid resolutions as a function of the transverse dispersive time, $\tau_D = 2D_T t/d_p^2$ (cf. Figure 5.3a). At $n = 10$–25 and $Pe = 500$ close-to-asymptotic behavior of the dispersion coefficient was not observed for some of the studied packings, and data for these simulations are not presented in part c).

($Pe = 50$) reach their close-to-asymptotic value after $\tau_D \approx 1$ for all used grid resolutions. This also holds for higher Péclet numbers ($Pe = 250$, 500) and $n = 30$, 90. However, packing discretized with a spatial resolution of $n = 10$ demonstrates qualitatively different behavior: at high Péclet numbers the dispersion coefficients diverge after $\tau_D \approx 1$, and the corresponding divergence rate strongly depends on the Péclet number (cf. red curves at $Pe = 250$ and $Pe = 500$ in Figure 1.10d). Such a behavior of D_L/D_m was observed but not commented upon in the study of Maier et al.[123] (see Figure 13 in their work).

The aforementioned divergence of the dispersion coefficients was reported in the work of Lowe and Frenkel,[158] (which was later criticized by Koch et al.[163] and Maier et al.[123]) who simulated advection–diffusion mass transport in a bulk sphere packing with a dimension of $10 \times 10 \times 28\, d_p$, porosity of $\varepsilon = 0.55$, and discretized with grid resolutions of $n = 5$ and $n = 9$. They used LBM and

the moment propagation method[164,165] to simulate flow and dispersion, respectively. (The authors analyzed time evolution of the dispersion coefficient by means of the velocity autocorrelation function $C(t)$ which is related to the dispersion coefficient as $D_{\mathrm{L}}(t)/D_{\mathrm{m}} = \int_0^t C(t')dt'$.) Observing a time behavior as indicated by the red lines in Figure 1.10d, these authors[158] posed a fundamental question on the existence of hydrodynamic dispersion coefficients. Maier et al.[123] argued that the divergence of the dispersion coefficients in the work of Lowe and Frenkel[158] could arise from numerical dispersion caused by the moment propagation method. However, as can be seen in Figure 1.10d, divergence can occur solely due to a poorly resolved simulation domain. We also note that a slight divergence of $D_{\mathrm{L}}/D_{\mathrm{m}}$ is observed in our simulations at $n = 30$ and $n = 90$ after long simulation time (Figure 1.7b). To our knowledge, such a behavior of the simulation approach has never been reported before.

Hydrodynamic dispersion in random sphere packings

Further, we compare the close-to-asymptotic values of the dispersion coefficient with experimental and simulation results from literature. In many studies of hydrodynamic dispersion a comparison of the dispersion coefficients with other literature data is done using double logarithmic scale graphics,[18,76,118,166–170] which, on one hand, is related to a wide range of employed Péclet numbers and corresponding dispersion coefficients, but, on the other hand, such a representation visually reduces a large scatter of the literature data and allows further description of a wide range of dispersion coefficients obtained at a fixed Péclet number to be characterized as "good agreement with the literature." In our study, we selected only two Péclet numbers, moderate ($Pe = 100$) and high ($Pe = 500$), in a way to i) closely match corresponding dimensionless flow rates of the studies chosen for comparison, and ii) use plots with linear scale for comparison.

We generated six types of bulk sphere packings, four with JT (R- and S-packings; Subsection 1.1.1) and two with MC (Ω-packings; Subsection 1.1.2) algorithms, resulting in six types of a packing microstructure or degree of heterogeneity (DoH). Packings of each type have a spacial dimension of approximately $10\ d_{\mathrm{p}} \times 10\ d_{\mathrm{p}} \times 70\ d_{\mathrm{p}}$ and porosities between random-close ($\varepsilon \approx 0.366$) and random-loose ($\varepsilon \approx 0.46$) packing limits,[171] and were discretized at relatively high resolution of $n = 60$ grid nodes per sphere diameter. We use different packing types because, as it is shown in Chapter 6, a packing microstructure can have significant influence on the hydrodynamic dispersion coefficient. To our knowledge, the influence of the packing microstructure on the hydrodynamic dispersion has never been reported before, and, therefore, explicit information on the DoH is missing in the literature data related to hydrodynamic dispersion. But in some cases, when the packing

[164] D. Frenkel and M. H. Ernst. *Phys. Rev. Lett.*, **63**: 2165–2168, 1989.
[165] R. M. H. Merks, A. G. Hoekstra, and P. M. A. Sloot. *J. Comput. Phys.*, **183**: 563–576, 2002.
[166] J. M. P. Q. Delgado. *Heat Mass Transfer*, **42**: 279–310, 2006.
[167] M. Quintard and S. Whitaker. *Chem. Eng. Sci.*, **48**: 2537–2564, 1993.
[168] M. Stöhr. *Analysis of flow and transport in refractive index matched porous media*. PhD thesis. Germany, Ruprecht Karl University of Heidelberg, 2003.
[169] A. Jafari et al. *Chem. Eng. J.*, **144**: 476–482, 2008.
[170] B. Bijeljic and M. J. Blunt. *Water Resour. Res.*, **42**: W01202, 2006.
[171] C. Song, P. Wang, and H. A. Makse. *Nature*, **453**: 629–632, 2008.

generation algorithm (or preparation protocol) is described in detail, the packing microstructure can be reproduced using the generation algorithm with its corresponding parameters taken from the study of interest.

Comparison of hydrodynamic dispersion coefficients with literature data

Figure 1.11 shows close-to-asymptotic values of the dispersion coefficient for all six types of the generated packings. As can be seen, dispersion coefficients in the packing of each type demonstrate different dependence on porosity. For example, dispersion coefficients of Ωx0.95 packings are almost independent of porosity (what was also mentioned in other studies where MC algorithm was employed[158,172]) while dispersion in Rx0.001 packings is strongly affected by the value of porosity. We note that the porosity behavior of the dispersion coefficients shown in Figure 1.11 is also captured by the geometrical measures based on the Voronoi tessellation of the packings. The reader is referred to Chapters 6 and 7, where we perform a detailed analysis of the microstructure of the bulk packings used here.

Simulated dispersion coefficients of the bulk packings were compared with (Figure 1.11, crosses) i) data from NMR[173–175] measurements of Seymour and Callaghan,[176] ii) dispersion coefficients from the simulations of Augier et al.[177] which are based on the numerical solution of Navier–Stokes and advection–diffusion equations, iii) dispersion coefficients simulated by Maier et al.[123,172] in computer-generated sphere packings, and iv) NMR data of Scheven et al.[178] The authors of the aforementioned studies have used Péclet numbers different from $Pe = 100$ or $Pe = 500$. Therefore, we have taken values of the dispersion coefficient $D_{\mathrm{L}}/D_{\mathrm{m}}$ at Péclet numbers Pe used by these authors and scaled $D_{\mathrm{L}}/D_{\mathrm{m}}$ to the closest value of the current study, $Pe = 100$ or $Pe = 500$, according to the $D_{\mathrm{L}}(Pe)/D_{\mathrm{m}}$ correlations proposed by the authors or using widely accepted power law scaling ($D_{\mathrm{L}}(Pe)/D_{\mathrm{m}} \sim Pe^{\alpha}$ with the value of $\alpha = 1.2$[179]) when such a correlation was not given (see Table 1.2).

NMR measurements of Seymour and Callaghan[176] shown in Figure 1.11 (red crosses) were performed in a confined cylindrical packing with a cylinder-to-particle diameter ratio of ~ 21 and porosity of 0.44. As it is shown in Chapter 5, cylinders with such lateral dimensions have several times larger *close-to-asymptotic* dispersion coefficient than a bulk packing of similar porosity, whereas the time required to reach close-to-asymptotic values of the dispersion coefficient for this cylindrical packing is two orders of magnitude larger than for the bulk one. Seymour and Callaghan presented data from two NMR measurements, with $\Delta = 10$ ms and $\Delta = 30$ ms (where Δ is the measurement time). In Figure 1.11, we present dispersion coefficients measured after a time of $\Delta = 30$ ms which corresponds to the convective time of $\tau_{\mathrm{C}} \approx 0.8$ for $Pe = 100$ and $\tau_{\mathrm{C}} \approx 4.0$ for

[172] R. S. Maier et al. *Water Resour. Res.*, **44**: W06S03, 2008.
[173] A. A. Khrapitchev and P. T. Callaghan. *Phys. Fluids*, **15**: 2649–2660, 2003.
[174] D. S. Grebenkov. *Rev. Mod. Phys.*, **79**: 1077–1137, 2007.
[175] D. S. Grebenkov. *Concepts Magn. Reson. Part A*, **36A**: 24–35, 2010.
[176] J. D. Seymour and P. T. Callaghan. *AIChE J.*, **43**: 2096–2111, 1997.
[177] F. Augier, F. Idoux, and J. Y. Delenne. *Chem. Eng. Sci.*, **65**: 1055–1064, 2010.
[178] U. M. Scheven, R. Harris, and M. L. Johns. *Phys. Rev. Lett.*, **99**: 054502, 2007.
[179] M. Sahimi. *Flow and transport in porous media and fractured rock: From classical methods to modern approaches*. Wiley-VCH, 1995.

Table 1.2: Original data on the dispersion coefficients digitized from literature, and the scaled values of the dispersion coefficients corresponding to $Pe = 100, 500$.

Original study	Porosity	Pe		D_{ax}/D_m		Scaling law
		original	scaled	original	scaled	
Seymour and Callaghan[176]	0.44	68	100	22.5	38.6	$D_{ax}/D_m \sim Pe^{1.37}$
		99	100	32.8	33.5	
		134	100	43.4	29.1	
		340	500	221	375	
		400	500	257	349	
		811	500	732	377	
Augier et al.[177]	0.37	70	100	31.4	44.3	$D_{ax}/D_m \sim Pe^{1.0}$
		1464	500	630	219	
Maier et al.[123]	0.44	95	100	28	29	$D_{ax}/D_m \sim Pe^{1.2}$
		476	500	191	203	
Maier et al.[172]	0.36	476	500	222	235	$D_{ax}/D_m \sim Pe^{1.2}$
	0.40	476	500	197	208	
	0.45	476	500	200	212	
Scheven et al.[178]	0.367	85.9	100	29.1	34.9	$D_{ax}/D_m \sim Pe^{1.2}$
	0.374	87.0	100	30.0	35.5	
		130.9	100	48.5	35.1	

$Pe = 500$. These values of convective time and Péclet number result in underdeveloped values of the dispersion coefficient of a *bulk* packing for $Pe = 100$ and $Pe = 500$ (for the corresponding time scales see, for example, Figure 13 in Reference [123]). As it was demonstrated in the study of Maier et al.,[180] dispersion coefficients at such short times in confined packing are close to the value of a bulk packing with similar properties, which are defined by the packing protocol and average porosity. Hence, the data of Seymour and Callaghan[176] with $\Delta = 30$ ms correspond to the dispersion values of the bulk region of their packing, and dispersion at lower Péclet number is underdeveloped compared to its higher Péclet number counterpart.

Dispersion coefficients in the study of Augier et al.[177] (Figure 1.11, green crosses) were simulated in a bulk packing extracted from the central region of a confined cylindrical packing with the aspect ratio of ~ 24. Generation of the confined polydisperse sphere packing was performed with discrete element method.[181] Large aspect ratio (~ 24) of the cylindrical packing and polydispersity of spheres resulted in a relatively low packing porosity of 0.33. Flow and mass transport problems were solved using traditional computational approaches based on the numerical solution of Navier–Stokes and advection–diffusion equations. Employed numerical methods require tessellation of the interparticle void space and sphere surfaces into a set of irregular space elements. The authors reported an inability of their numerical approach to perform the space tessellation for the case of touching spheres. Therefore, each sphere of the generated packing was contracted by 2% of its diameter what resulted in a final packing porosity of 0.37. On the one hand, our simulation results

[180] R. S. Maier, D. M. Kroll, and H. T. Davis. *AIChE J.*, **53**: 527–530, 2007.
[181] P. A. Cundall and O. D. L. Strack. *Geotechnique*, **29**: 47–65, 1979.

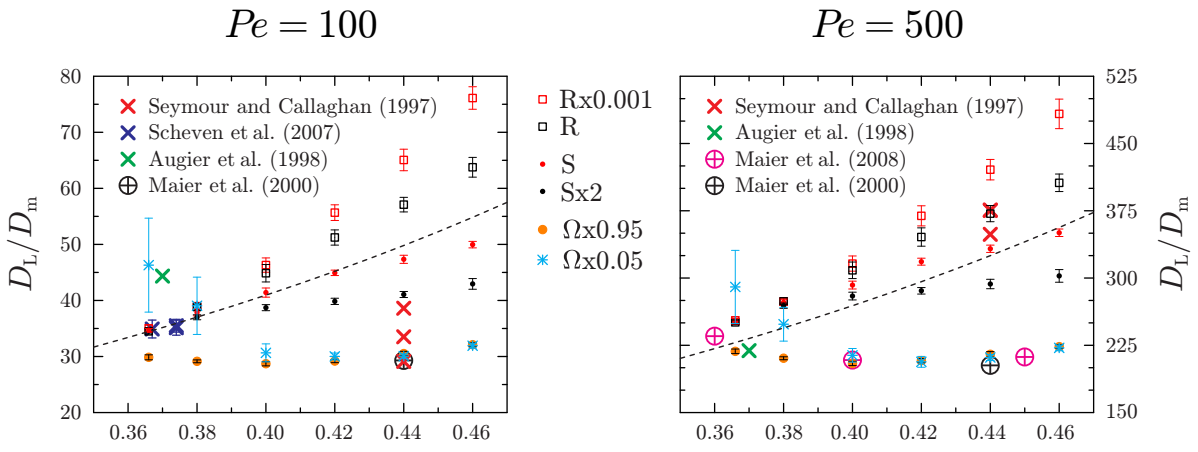

Figure 1.11: Close-to-asymptotic values of the hydrodynamic dispersion coefficient of i) bulk packings generated with JT (R- and S-packings) and MC (Ω- packings) algorithms, ii) NMR measurements of Seymour and Callaghan,[176] iii) NMR measurements of Scheven et al.,[178] iv) LBM and RWPT simulations of Maier et al.[123,172] in sphere packings generated with MC algorithm, and v) simulations of Augier et al.[177] based on the solution of ADE in a packing generated with discrete element method.[181] Results are shown for a) $Pe = 100$ and b) $Pe = 500$. Dashed line denotes corellation proposed by Scheven et al.[178] (equation (1.36)). Error bars for our simulations indicate 95% confidence intervals calculated using dispersion values of 10 random realizations of each packing with a fixed porosity and packing generation protocol. Error bars for the data of Scheven et al.[178] were digitized from their publication.

agree well with the dispersion coefficients simulated by Augier et al.[177] On the other hand, D_L/D_m simulated at $Pe = 100$ corresponds to the Ωx0.05 packings while D_L/D_m at $Pe = 500$ to the Ωx0.95 ones. This could not be attributed to one of the possible numerical artefacts of ADE solvers, numerical dispersion (because it increases the dispersion coefficient as Péclet number grows), but can be explained by the following differences between our simulations and the computational approach of Augier et al.[177]: i) monosized spheres contrary to the wide distribution of sphere diameters, ii) truly periodic packing with corresponding periodic boundary conditions against cut bulk packing with "symmetric planes" lateral boundary conditions, and iii) low Reynolds number ($Re \ll 1$) contrary to moderate Reynolds number ($1 < Re < 100$) flow.

Maier et al.[123,172] performed simulations of hydrodynamic dispersion in bulk packings generated with MC algorithm (corresponding dispersion coefficients are shown in Figure 1.11 by black and magenta crosses). Low Reynolds number flow and mass transport were simulated using LBM and RWPT approaches. The authors took care to observe close-to-asymptotic time behavior of the dispersion coefficient, which is free from most of the finite size or numerical artifacts. The similarity of our and Maier's packing generation algorithms allows us to perform a comparison of the dispersion coefficients in the bulk packings with similar microstructures. We note that the authors reported independence of the dispersion coefficients on the compression rate Ω (see Subsection 1.1.2 for the description of MC algorithm) over a wide porosity range of $0.36–0.50$. Contrary to their results, Figure 1.11 demonstrates such a dependence: at low porosities and $Pe = 100$ dispersion coefficients of Ωx0.95 and Ωx0.05 packings have a difference of about 50%. The difference in the microstructures (and corresponding dispersion coefficients) of our and Maier's packings generated with MC algorithm can be explained by the different amount of iterations (N) before

compression of the simulation box is applied. In our study $N = 5000$ while Maier et al.[123,172] did not specify the value of N in their study. To summarize, Figure 1.11 shows an excellent agreement for the hydrodynamic dispersion coefficients of our Ωx0.95 packings and dispersion data of Maier et al.[123,172]

Blue crosses in Figure 1.11a denote NMR data from the work of Scheven et al.[178] The NMR measurements were done in cylindrical columns with the cylinder-to-particle diameter ratio of ~ 375 and porosity of 0.367 and 0.374. Measurement time was long enough ($\tau_{\mathrm{C}} > 20$) to observe close-to-asymptotic behavior of the dispersion coefficients for the *bulk* region of the packings. As can be seen in Figure 1.11a, our simulation results agree very well with the authors data.

In their studies, Scheven et al.[178,182] suggested the existence of an *intrinsic* value of the dispersion coefficient for the bulk sphere packings. They stated that dispersion in an unconfined sphere packing is defined solely by Péclet number and hydrodynamic radius of a packing ($r_{\mathrm{h}} = 1/6\, d_{\mathrm{p}}\, \varepsilon/(1-\varepsilon)$), and proposed the following equation (dashed lines in Figure 1.11):

$$\frac{D_{\mathrm{L}}}{D_{\mathrm{m}}} = Pe_{\mathrm{eff}}(A \ln(Pe_{\mathrm{eff}}) + B), \tag{1.36}$$

where $Pe_{\mathrm{eff}} = 6u_{\mathrm{av}} r_{\mathrm{h}}/D_{\mathrm{m}} = Pe\, \varepsilon/(1-\varepsilon)$, $A = 0.12 \pm 0.007$, and $B = 0.11 \pm 0.03$ (in later work[182] Scheven suggested $A = 0.131 \pm 0.007$ and $B = 0.07 \pm 0.03$ for $10 \leq Pe_{\mathrm{eff}} \leq 2100$). According to the authors, equation (1.36) specifies the lower bound of the dispersion values, and higher dispersion coefficients, if they are observed, are caused by factors not related to the packing microstructure like nonuniform flow injection or faster flow near the confining wall. However, our results demonstrate the existence of *bulk* sphere packings with dispersion coefficients significantly lower or higher compared to the predictions of equation (1.36). Figure 1.11 also suggests that any correlation in a form of $D_{\mathrm{ax}}/D_{\mathrm{m}} = f(Pe, \varepsilon)$ for the random sphere packings will fail to provide precise results if it does not take microstructural disorder of the packings into account.

It is interesting to note that Scheven et al.[178] confirmed the validity of equation (1.36) by comparison of the dispersion coefficients calculated using (1.36) with their NMR data, theoretical predictions of Saffman[183,184] (which are based on the capillary model), and simulations of Maier et al.[123] As can be seen in Figure 1.11, Maier's data are approximately $3/2$ times lower that the predictions of (1.36). Probably, this fact led the authors to assume the hydrodynamic radius r_{h} of Maier's packings to be $3/2$ times lower than r_{h} of "smoothed" spheres (due to the discrete representation of the packing spheres on a cubic lattice), and to upscale Maier's data accordingly. Maier and Bernard[85] in their later study introduced the smooth representation of the sphere surfaces and found that such a representation results in *lower* values of the dispersion coefficient, which contradicts the assumption of Scheven et al.[178] It should be noted that uniform microstructure of MC packings used in the simulations of Maier et al.[42,123,180,185] resulted in probably the lowest dispersion coefficients for bulk sphere packings available in the literature.[118,178,186]

[182] U. M. Scheven. *AIChE J.*, **56**: 289–297, 2010.
[183] P. G. Saffman. *J. Fluid Mech.*, **6**: 321–349, 1959.
[184] P. G. Saffman. *J. Fluid Mech.*, **7**: 194–208, 1960.
[185] R. S. Maier et al. *Philos. Trans. R. Soc. A*, **360**: 497–506, 2002.
[186] P. Magnico. *Chem. Eng. Sci.*, **58**: 5005–5024, 2003.

Hydrodynamic dispersion in a pillar array with top and bottom walls

As it was mentioned, the comparison of our simulation results with dispersion coefficients measured experimentally in the random sphere packs is hindered by the lack of the description of the real packing microstructure. Therefore, on the last validation step we simulated hydrodynamic dispersion in a system presented by a hexagonal array of cylinders bounded at the top and bottom by two planes (see Figure 1.12a). We have chosen this system for simulations because of i) the availability of precise experimental data on the hydrodynamic dispersion coefficients and ii) the possibility to reproduce the microstructure of the system exactly. The geometry of the system enables optical visualization of the concentration profiles and corresponding estimation of the hydrodynamic dispersion despite the material of the stationary phase (i.e, cylinders) is not optically transparent.

Different views of the simulation domain are shown in Figures 1.12a,b. The simulation domain represented by the hexagonal array of cylinders, which are bounded at the top and bottom by two planes, is an approximation of the *ordered micropillar array* produced experimentally in the work of Eghbali et al.[187] For the applications of chromatography, micropillar arrays provide an alternative concept[188] to the traditional columns packed with spherical particles. Figure 1.12b provides details on the studied geometry: parallel cylinders of height b and diameter d are located between two parallel plates; the axes of the cylinders go through the vertices of the touching equilateral triangles with the side length a. The corresponding simulation domain has spatial dimensions of $\sqrt{3}\,a$ (length, x-direction), a (width, y-direction), and b (height, z-direction). This system was discretized with a high spatial resolution of $n = 200$ grid nodes per cylinder diameter to minimize possible finite size effects. The pressure gradient was applied along the domain resulting in the flow direction as indicated by the arrows in Figures 1.12a,b, and the mean flow velocity u_{av} corresponded to the Reynolds number of $Re \approx 0.002$ (experimental Reynolds numbers numbers were within the range of $0.002–0.05$).

Time evolution of the hydrodynamic dispersion coefficients simulated at Péclet numbers $Pe = u_{\mathrm{av}} d / D_{\mathrm{m}}$ of 10.3 (dashed lines) and 31.6 (solid lines) in the simulation domain with $b = 2.59\,d$ (see text below) are shown in Figure 1.12c. Figure 1.12c reveals qualitatively different time behavior of the dispersion coefficients calculated along three spatial directions. The dispersion coefficient $D_z(t)/D_{\mathrm{m}}$ decays monotonously towards zero value, which is related to the limitation of z-displacement of the tracers by the top and bottom planes. The decay rate is independent on the Péclet number due to the presence of only diffusion mixing along the z-direction (the flow field has zero z-components).

The dispersion coefficient $D_y(t)/D_{\mathrm{m}}$ oscillates at short times ($\tau_{\mathrm{D}} < 0.25$ here) and converges to a finite value afterwards. The oscillations are related to the correlation in the motion of tracers around the cylinders, and oscillations decay is caused by the mixing of the tracers due to molecular diffusion (consequently, oscillations are more pronounced at high Péclet numbers). The origin of the initial peak in the development of the transverse dispersion coefficient in random sphere packs (cf. Figure 5.3) is the same as of the oscillations observed here. However, in random sphere

[187] H. Eghbali et al. *Anal. Chem.*, **81**: 705–715, 2009.
[188] B. He, N. Tait, and F. Regnier. *Anal. Chem.*, **70**: 3790–3797, 1998.

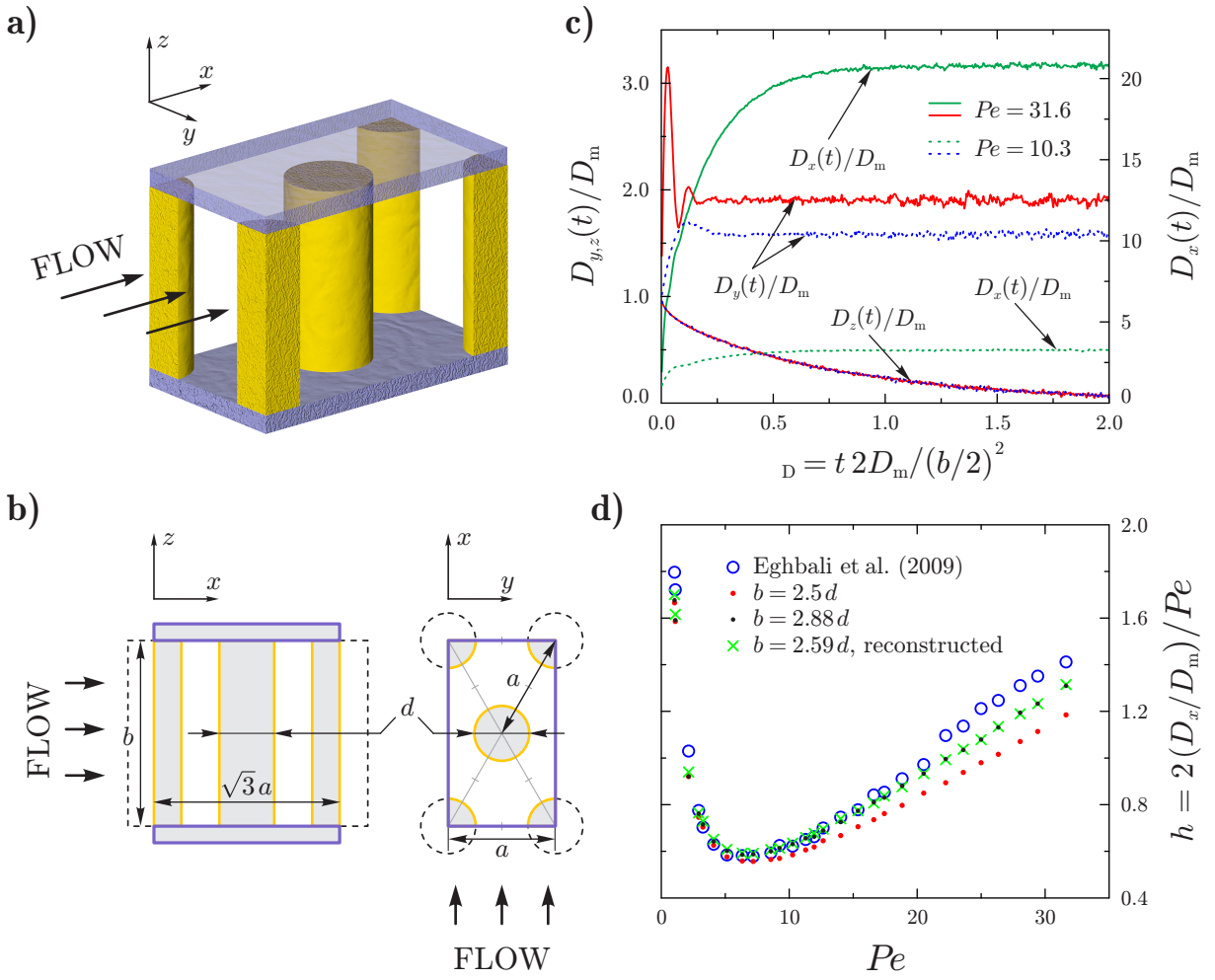

Figure 1.12: a) Side view of the periodic cell of the hexagonal array of cylinders bounded at the top and bottom by two planes. Shown is the periodic cell with porosity of $\varepsilon = 0.78$. b) Projections of the periodic cell on xz- and yx-planes; in the figure, d denotes cylinder diameter, a is the width of the periodic cell and the distance between the axes of nearest cylinders, b is the cylinder height, and $\sqrt{3}\,a$ is the cell length. c) Time development of longitudinal ($D_{\mathrm{x}}(t)/D_{\mathrm{m}}$) and transverse ($D_{\mathrm{y,z}}(t)/D_{\mathrm{m}}$) dispersion coefficients as a function of the diffusive time $\tau_{\mathrm{D}} = 2D_{\mathrm{m}}t/(b/2)^2$. d) Close-to-asymptotic values of longitudinal dispersion coefficient expressed in terms of plate height $h = 2D_{\mathrm{x}}/(D_{\mathrm{m}}Pe)$ as a function of Péclet number Pe.

packings only one peak is observed because mixing due to molecular diffusion is accelerated by the macroscopic randomness of the flow paths. The oscillations of the dispersion coefficient were observed in simulations (for example, see Figure 7 in the study of Acharya et al,[76] oscillations in their work are weakly pronounced probably due to a poorly resolved simulation domain) and experiments.[189]

Dispersion coefficient $D_x(t)/D_{\mathrm{m}}$, shown in Figure 1.12c, grows monotonously and reaches its close-to-asymptotic value after $\tau_{\mathrm{D}} \approx 1.2$. This time translates to the diffusion displacement of $l_{\mathrm{D}} = \sqrt{1.2}\,b/2 \approx 1.1\,b/2$. The time to reach close-to-asymptotic behavior is determined by the time

[189] P. T. Callaghan and S. L. Codd. *Phys. Fluids*, **13**: 421–427, 2001.

to cover the longest distance between different (longitudinal) velocities (see Chapters 2 and 5). In the studied system, maximum velocity of the parabolic-like flow profile in the array void space and zero velocity at the cylinder–plane contact can be assumed as different velocities located on the maximal distance (see, for example, Figures 1 and 2 in the work of De Smet et al.[190]). Due to the symmetry of the flow profile, the maximal distance between different velocities is roughly equal to $b/2$, which agrees very well with $l_{\mathrm{D}} \approx 1.1\, b/2$ estimated from the time behavior of $D_x(t)/D_{\mathrm{m}}$ above.

In Figure 1.12d we compare close-to-asymptotic values of the dispersion coefficient $D_x(t)/D_{\mathrm{m}}$, expressed in the terms of plate height $h = 2\,(D_x/D_{\mathrm{m}})/Pe$, with experimental values from the work of Eghbali et al.[187] Comparison is performed over the whole Péclet number range $(1.0–31.6)$ of the available experimental data. In their study,[187] the authors describe characteristic dimensions of the micropillar array as $b = 10\,\mu\mathrm{m}$ and $d = 4\,\mu\mathrm{m}$, which translates to the cylinder height-to-diameter ratio of $b/d = 2.5$. The result of our simulations performed with $b/d = 2.5$ (Figure 1.12d, red dots) demonstrates an underestimation of the experimental data. Eghbali et al.[187] commented their procedure of the fabrication of the micropillar array as "*... The fabrication of the pillar channels and the concomitant injection system was performed using the methods described in refs [191–195]...*" We found that fabrication procedures very similar to the work of Eghbali et al.[187] were used in works of Eghbali et al.[191] and De Malsche et al.[193] In Reference [191] the authors reported the pillar height as $10\,\mu\mathrm{m}$; however, according to Figure 2 in [191] (high resolution SEM image of a micropillar array with the specified length scale), micropillars have the height of $11.5\,\mu\mathrm{m}$. The same height of $11.5\,\mu\mathrm{m}$ was reported in Reference [193]. Therefore, we performed an additional set of simulations for $b/d = 11.5/4 \approx 2.88$ (black dots in Figure 1.12d) which demonstrated better agreement with experimental data.

High resolution SEM image of pillars in Reference [191] (Figure 2) reveals indentations on the pillar walls originating from the preparation process, which could result in a dispersion increase compared to the pillars with flat walls assumed before. In an attempt to find even better agreement with the experimental data of Eghbali et al,[187] we reproduced irregularities of the pillar walls and the average pillar diameter ($\approx 4.44\,\mu\mathrm{m}$; $b/d \approx 2.59$) from the SEM image in [191] with a resolution of 502 pixels per pillar height and 193.5 pixels per average pillar diameter. Note, we do not perform a direct comparison with the experimental data on dispersion available in Reference [191] due to their large scatter. As can be seen in Figure 1.12d (green crosses), the shape and the average diameter of the pillars extracted from the SEM image resulted in the dispersion values very close to our previous simulations with $b/d = 2.88$. The maximal (average) difference between dispersion values of Eghbali et al,[187] and our simulations in the system with reconstructed geometry is 5% (1%) for $Pe < 20$ and 12% (10%) for higher Péclet numbers. The quite significant difference for $Pe > 20$ (Figure 1.12d) can be attributed to the anomalous shift of experimental data for

[190] J. De Smet et al. *J. Chromatogr. A*, **1154**: 189–197, 2007.
[191] H. Eghbali et al. *J. Sep. Sci.*, **30**: 2605–2613, 2007.
[192] H. Eghbali et al. *LC-GC Eur.*, **20**: 208–222, 2007.
[193] W. De Malsche et al. *Anal. Chem.*, **79**: 5915–5926, 2007.
[194] W. De Malsche et al. *Lab Chip*, **7**: 1705–1711, 2007.
[195] M. De Pra et al. *Anal. Chem.*, **78**: 6519–6525, 2006.

$20 < Pe < 31.6$. Taking into account this shift and also some uncertainty in the spatial dimensions of the experimental system, we conclude that our model demonstrates excellent agreement with the experimental data when the microstructural disorder of the geometry of interest is known.

1.5 Program implementation

As it was mentioned before, our simulation approach includes the following sequential steps:

- generation of the random packing of solid impermeable spheres using Jodrey–Tory or Monte Carlo algorithms (Section 1.1),
- spatial discretization of the generated packing (Section 1.2),
- simulation of the fluid flow in the void space of the generated packing using the lattice Boltzmann method (LBM, Section 1.3),
- simulation of advective–diffusive transport in the packing void space with the random walk particle tracking method (RWPT) using the fluid velocity filed obtained on the previous simulation step (Section 1.4).

Most of the computational time ($> 99\%$) is spent during simulations with LBM and RWPT methods, and in this subsection we describe some aspects of our program implementation and performance of these two methods methods.

The majority of the simulations in this thesis were performed on the Blue Gene/P[196,197] system, hence information given in this subsection is mostly related to our experience with this system. Blue Gene/P is a system equipped with a large amount of low-power PowerPC 450 chips. A chip has four processor cores operating at a clock speed of 850 MHz and delivering a theoretical performance of 3.4 GFLOP/s per core (here FLOP is an acronym for FLoating point OPeration). Each chip is soldered to a small card together with a random access memory (RAM) of 2 GB (memory bandwidth is 13.6 GB/s per chip or 3.4 GB/s per core), forming a *compute card*. 32 compute cards are plugged in a *node card*. 32 node cards form a *rack* with 4096 processor cores and 2 TB of RAM. Chips within a rack and racks are interconnected with several networks including a three-dimensional torus network for point-to-point and collective communications.

To date (2010) the largest Blue Gene/P system is installed at Forschungszentrum Jülich (FZJ), has 72 racks or $294\,912$ processor cores (which is the world-largest amount of cores in one system), and a peak performance of 1 PFLOP/s. The size of the studied problems and computational approach used in this study allowed us to effectively utilize the whole Blue Gene/P system at FZJ.[198]

Lattice Boltzmann method

Iterative calculation of the distribution functions f_α according to equation (1.21) forms the basis for the program implementation of LBM. Equation (1.21) can be formally split into "collision" and

[196] C. Sosa and B. Knudson. *IBM system Blue Gene solution: Blue Gene/P application development*. 4th ed. IBM, International Technical Support Organization, 2009.
[197] B. R. de Supinski et al. *Int. J. High Perform. Comput. Appl.*, **22**: 33–51, 2008.
[198] S. Khirevich, A. Daneyko, and U. Tallarek. "Simulation of fluid flow and mass transport at extreme scale" in: *Jülich Blue Gene/P Extreme Scaling Workshop 2010* ed. by B. Mohr and W. Frings. Forschungszentrum Jülich, Jülich Supercomputing Centre, 2010.

"propagation" steps:

$$\text{collision:} \qquad f_\alpha^*(\vec{x},t) = f_\alpha(\vec{x},t) - \frac{\Delta t}{\tau}\left(f_\alpha(\vec{x},t) - f_\alpha^{\mathrm{eq}}(\vec{x},t)\right), \tag{1.37a}$$

$$\text{propagation:} \qquad f_\alpha(\vec{x}+\vec{e}_\alpha\Delta t, t+\Delta t) = f_\alpha^*(\vec{x},t). \tag{1.37b}$$

From the program point of view, the former step is computationally intensive (about 200 floating point operations per node update) and requires data from a single lattice node only, while the latter step is a copy of data from one memory location (a node) to another (node neighbors). Four dimensional array $N_x \times N_y \times N_z \times 19$ (where $N_{x,y,z}$ are the lattice dimensions and 19 is the amount of lattice links in the D3Q19 model) containing the lattice links is stored in a continuous block of computer memory, and selection of the data layout of this four dimensional array can greatly affect the program performance.[199] We used $lxyz$ layout, i.e. 19 links of the lattice node (x,y,z) are stored *continuously* in memory, followed by 19 links of the next node $(x+1,y,z)$ and so on. The size of z dimension was selected to be smaller than the sizes of y and z dimensions.

The performance of LBM is assumed to be limited by the memory bandwidth.[199] Computationally, PowerPC 450 processor core can deliver a theoretical performance of $3.4\cdot 10^9/200 = 17\cdot 10^6 = 17$ MLUP/s (here 200 is the FLOP amount and LUP is an acronym for Lattice node UPdate). To update a lattice node, $19\cdot 4$ bytes (here 19 is the amount of lattice links and 4 is the size of `float` variable) must be loaded and then stored from/to the RAM. On modern CPUs (also on PowerPC 450) data is fetched from RAM by the groups of bytes called *cache lines*.[200] PowerPC 450 has a cache line size of 128 bytes[196] resulting in 128 bytes to be read to load *continuously* stored 76 bytes containing information on 19 lattice links. After the collision step is performed, 19 updated links have to be stored in *different* locations in memory, and in the worst case scenario $19\cdot 128 = 2432$ bytes must be transferred to the memory. Hence, the performance of LBM is limited by the memory bandwidth as $3.4\cdot 10^9/((1+19)\cdot 128) \approx 1.33$ MLUP/s. Our program implementation of LBM, written in C programming language[201,202] and compiled with IBM xlC compiler had a performance of 0.6–1.1 MLUP/s depending on the system geometrical parameters (like the shape of the simulation domain and average porosity), which agrees well with the performance results reported in the literature.[203]

Parallel implementation of the LBM code was done using the Message Passing Interface[204] (MPI) which is *de facto* standard for the communication between the computational nodes of the distributed memory systems (like Blue Gene/P). Simulations in this thesis are mainly concerned with "long" computational domains, i.e. one dimension of the domain is significantly larger than two others. Therefore it is straightforward to use one-dimensional domain decomposition: the

[199] G. Wellein et al. *Comput. Fluids*, **35**: 910–919, 2006.
[200] J. Handy. *The cache memory book*. 2nd ed. Academic Press, 1998.
[201] B. W. Kernighan and D. M. Ritchie. *C programming language*. 2nd ed. Prentice Hall, 1988.
[202] *ISO/IEC 9899:1999: Programming languages — C*. International Organization for Standardization, 1999.
[203] J. Götz et al. "Direct numerical simulation of particulate flows on 294 912 processor cores" in: *ACM/IEEE International Conference for High Performance Computing, Networking, Storage and Analysis*. Los Alamitos, CA, USA, 2010.
[204] *MPI: A Message-Passing Interface Standard, Version 2.2*. Message Passing Interface Forum, 2009.

computational domain is split into "slices" which are distributed among MPI processes. Because an update of each lattice node requires information from its neighbors, each slice is then extended by two "ghost layers," from left and right of the slice. During the execution of the propagation step a memory buffer corresponding to the ghost layer is updated, and after the step is complete, each MPI process performs `MPI_Sendrecv()` operation to send and receive contents of the ghost layers of the neighboring processes.

Random walk particle tracking method

RWPT iteratively displaces infinitely small particles (tracers) according to equation (1.32) using normally distributed random numbers and a flow field calculated by the LBM. RWPT requires small amount of computations (compared to LBM) and its performance is mainly limited by i) the time to access memory elements containing information on the velocity field, which is needed to calculate the advective displacement of a tracer, ii) generation of the normally distributed random numbers to calculate the diffusive displacement of a tracer, and iii) float-to-integer truncation (i.e., rounding of a floating point number towards zero) required to calculate coordinates of the lattice voxel where the tracer is currently located. Further we give a short overview of our approach to speed up the aforementioned performance-limiting factors.

The maximal tracer displacement is limited approximately to one lattice space step h. Hence, the use of the slice decomposition (as in the LBM implementation) with one ghost layer results in the communication between MPI processes on every RWPT iteration. Extension of the ghost layer length (in lattice nodes) allowed us to increase the amount i of RWPT iterations between two subsequent MPI communications. Moreover, this extension enabled continuous displacement of each tracer during multiple iterations i increasing locality of the memory access and RWPT performance.

Generation of the normally distributed random numbers was performed using highly optimized routines from the IBM ESSL library;[205] and resulted in a performance gain of up to 20 times compared to our C-implementation of the random generator.

Despite its apparent simplicity, float-to-integer truncation can greatly slow down the performance of the code execution. Modern processor architectures use pipeline technique to process instructions, and maximum performance is achieved when all stages of the pipeline are filled with instructions which can be processed simultaneously.[206] In some situations, dependencies between instructions or instructions by itself may cause pipeline flush and, therefore, performance degradation.[207] Assembly instructions `frsp`[208] and `bl`, which were part of our default float-to-integer conversion implementation, would cause pipeline flushing: an optimized implementation (i.e., without `frsp` and `bl`) resulted in approximately twofold performance increase of the overall RWPT performance.

[205] *Engineering and Scientific Subroutine Library for Linux on POWER, Version 4 Release 2.2*. 4th ed. IBM Corporation, 2005.
[206] R. Hyde. *Write great code, volume 1: Understanding the machine*. No Starch Press, 2004.
[207] R. Hyde. *Write great code, volume 2: Thinking low-level, writing high-level*. No Starch Press, 2006.
[208] S. Weiss and A. Goldstein. *J. Syst. Archit.*, **45**: 15–29, 1998.

LBM and RWPT parallel performance

Figure 1.13a shows results on the performance scaling benchmarks[198] performed on JUGENE system (Blue Gene/P installed at Forschungszentrum Jülich) for a cylindrical sphere packing with diameter of $\sim 21\ d_\mathrm{p}$ and length of $9830.4\ d_\mathrm{p}$ (where d_p is the sphere diameter). The packing was discretized (see Section 1.2) with a spatial resolution of 30 lattice nodes per sphere diameter resulting in the lattice dimension of $632 \times 632 \times 294\,912$ lattice nodes. Such a lattice dimension required 12 TB for LBM and 6 TB for RWPT programs. Due to the memory limitations, we selected the performance at 32k and 16k processor cores (8 and 4 Blue Gene/P racks, respectively) as the baseline for LBM and RWPT, respectively. Both LBM and RWPT demonstrate an identical strong scaling behavior (Figure 1.13a), which is related to the similar decomposition techniques used in both of the methods and, consequently, similar distribution of fluid nodes (n_fl) among processor cores. In case of LBM, n_fl defines the number of lattice links to be processed while for RWPT n_fl specifies the number of tracer particles associated with a given processor (assuming uniform concentration of tracer particles in the fluid phase of the packing). Non-uniformity of n_fl distribution among processors leads to workload imbalance, caused by two factors:

- The smallest indivisible data chunk for the implemented decomposition procedure and a given problem size is a two dimensional layer with dimensions of $632 \times 632 \times 1$ lattice nodes. The whole simulation domain consists of $L_z = 294\,912$ silces, which may or may not be evenly divisible by the number of allocated processor cores n. The remainder of the L_z/n slices, if present, is distributed among some of the processes, which yields a non-uniform distribution of n_fl.
- Non-uniform distribution of n_fl on the lattice is an inherent property of the random porous media model (for the packing used in simulations, the ratio between maximal $n_\mathrm{fl,max}$ and minimal $n_\mathrm{fl,min}$ numbers of fluid nodes per lattice layer is 1.27).

Depending on whether L_z is a multiple of the current processor number n or not, only the second or both factors cause workload imbalance. More efficient scaling of RWPT can be explained by the larger ratio of computation (CPU time spent out of communication) to communication times compared to LBM.

Input/output operations

After the LBM has performed the calculation of the flow field, the simulated velocity field must be written into a file, and later this file must be read into the memory by the RWPT program. Operations of reading/writing of the file to the file system are often referred to as input/ouput operations (I/O). Time requirements to perform I/O can become prohibitive with the growth of the size of the simulation domain. For example, an optimized single-core I/O on Blue Gene/P results in a performance of 100 MB/s; our last simulations were performed for systems with a velocity field file size of ~ 2.5 TB. The time needed to calculate the velocity field was about 40 minutes and single-core I/O would take about 7.5 hours to write such a file. A possible solution is to use MPI I/O routines which allow to execute parallel I/O operations.[204] However, a system setup on supercomputers we used in earlier runs had a flag `MP_SINGLE_THREAD` set to `yes` disabling MPI I/O.[209]

[209] *Parallel Environment for AIX and Linux: MPI Subroutine Reference*. IBM Corporation, 2010.

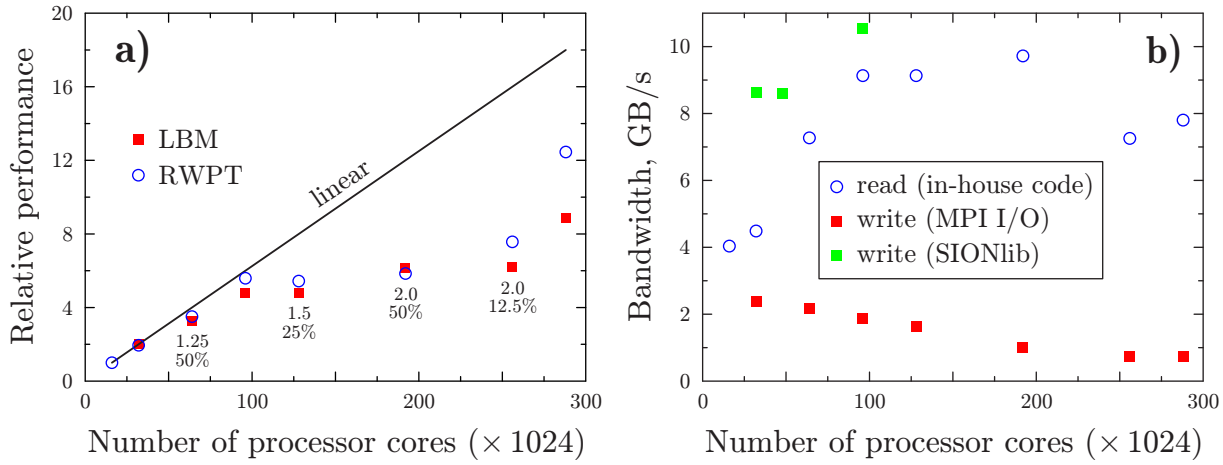

Figure 1.13: a) Performance scaling on the JUGENE system. The upper number in each pair indicates the ratio of the longitudinal dimensions of the longest to the shortest decomposed subdomains. The lower number is the fraction of the processes with the longest domain length. b) I/O performance of LBM (file write) and RWPT (file read).

Hence we implemented our own routines to speed up the I/O. The idea was to perform parallel writing in groups of p processes, where p is greater than unity (to increase I/O performance) and less than the total amount n of the allocated processes (to avoid overload or even crash of the file system, when n is on the order of thousands).

Our programm implementation allowed us to reach ~ 1 GB/s of I/O performance for both reading and writing on the 8192 processor cores (2 Blue Gene/P racks with GPFS file system[210,211] installed at Rechenzentrum Garching, Germany). On the JUGENE system (Blue Gene/P with GPFS) our I/O implementation demonstrated a good performance for the file reading (see Figure 1.13b, blue circles; file size is 1.3 TB). File writing on JUGENE using our I/O approach and MPI I/O implementation showed similar behavior: maximum performance was about 2 GB/s on $32\,768$ cores (8 racks) and further increase of the allocated processor cores led to I/O performance degradation (Figure 1.13b, red squares). File writing performance was greatly improved by the utilization of the SIONlib library[212] available on JUGENE (Figure 1.13b, green squares). However, the default use of SIONlib resulted in only half of the performance indicated in Figure 1.13b; maximum performance was achieved with allocation of the disk space (for example, using `dd if=/dev/zero of=velocity.file` unix command) for the file to be written by LBM before the LBM program run.

[210] S. Fadden. *An Introduction to GPFS Version 3.3*. IBM Corporation, 2010.
[211] J. Borrill et al. *Parallel Comput.*, **35**: 358–373, 2009.
[212] W. Frings, F. Wolf, and V. Petkov. "Scalable massively parallel I/O to task-local files" in: *Proceedings of the Conference on High Performance Computing Networking, Storage and Analysis*. New York, NY, USA, 2009.

Chapter 2

Packings of basic cross sections

In this chapter, the hydrodynamic dispersion in packings of different porosities and different cross sections (circular, quadratic, rectangular, and semicircular) is discussed. The obtained results were published in the journal *Analytical Chemistry* in 2007.[213]

2.1 Introduction

With the advent of the "-omics" era in the life sciences, there has been an ongoing pursuit for miniaturized and integrated analysis systems.[214] The comprehensive analysis of whole biological systems as well as large-scale screening projects in medicine and the pharmaceutical industry relies on the analysis of a huge number of complex samples available only in minute quantities. The answers to this problem are miniaturization, integration, parallelization, and automation. The current microfabrication techniques and materials enable integrated and highly multiplexed systems in chip format, along with the possibility of batch production to provide cost-effective, disposable devices for highthroughput operation.[215,216] Micro total analysis systems, which ideally integrate a complete analytical process in a microfluidic chip — from sample preparation and injection via analyte separation to the final identification and characterization of the components — are particularly attractive tools for applications in the life sciences and medical diagnostics.[217–221]

While LC–MS/MS (liquid chromatography–tandem mass spectrometry) is the standard analytical technique in proteomics and many other research areas, the development of microchip-LC systems has not enjoyed the success of electrokinetically based separation techniques. Voltage-controlled processes are relatively easily implemented in microfluidic platforms, whereas the integration of pressure-driven flow, especially high-pressure operation required for true HPLC, is challenging. Specific problems of microchip-HPLC development are as follows: i) integration of high-pressure pumps, ii) formation of solvent gradients with short cycle times, iii) integration of high-pressure sample injection, iv) fabrication of high-pressure-rating channels, v) microchip

[213] S. Khirevich et al. *Anal. Chem.*, **79**: 9340–9349, 2007.
[214] N. Lion et al. *Electrophoresis*, **24**: 3533–3562, 2003.
[215] M. J. Madou. *Fundamentals of microfabrication: the science of miniaturization*. 2nd ed. CRC Press, 2002.
[216] O. Geschke, H. Klank, and P. Tellemann. *Microsystem engineering of lab-on-a-chip devices*. John Wiley & Sons, 2004.
[217] S. C. Jakeway, A. J. de Mello, and E. L. Russell. *Fresenius' J. Anal. Chem.*, **366**: 525–539, 2000.
[218] D. R. Reyes et al. *Anal. Chem.*, **74**: 2623–2636, 2002.
[219] P.-A. Auroux et al. *Anal. Chem.*, **74**: 2637–2652, 2002.
[220] T. Vilkner, D. Janasek, and A. Manz. *Anal. Chem.*, **76**: 3373–3386, 2004.
[221] P. S. Dittrich, K. Tachikawa, and A. Manz. *Anal. Chem.*, **78**: 3887–3908, 2006.

column packing, and vi) world-to-chip interfacing. The extent of integration of the current LC-microchips varies considerably. Fully integrated, so-called "stand-alone," LC-microchips were recently introduced,[222,223] but the majority of LC-microchips are semi-integrated devices; i.e., only some of the system components (with the separation column(s) as key element) are seemlessly integrated on a microchip that is interfaced to desktop equipment.[5,9,10,12,224–230] For specific applications, microchip-LC systems have demonstrated results comparable or even superior to benchtop instrumentation, but their range of operation modes and general performance is still limited. For specific applications, microchip-LC systems have demonstrated results comparable or even superior to benchtop instrumentation, but their range of operation modes and general performance is still limited.

With the research focus on integration and multipexing, little attention has been given to the performance of the microchip separation columns. Microfluidic channels have been fabricated in silicon, glass, quartz, diamond, and a variety of polymeric materials. The channel geometry is mainly determined by the fabrication methods used and is inherently noncylindrical. The cross sections of LC-microchip separation columns include semicircular, quadratic, rectangular, trapezoidal, and elliptical geometries, often with irregularly angled corners and curved sides. Solid supports used in microfluidic analytical systems include beads, membranes, fabricated silicon microstructures, gels, and monoliths.[231] The separation columns of more recent LC-microchips[5,9,10,12,222–225,227–230] contain either porous monoliths[232] or slurry-packed particulate beds.[233] The former have the advantage of easy fabrication by polymerization of the monolithic column directly in microfluidic channels, while the latter are desirable because the wide variety of available chromatographic media and the knowledge gained from conventional HPLC could be utilized. Particle-packed microchip columns have a low channel-to-particle size ratio, as the reduction of column dimensions is not accompanied by a corresponding reduction in the particle diameter. Microchip column packing is not a firmly established procedure but still retains an experimental character. The microchannels are filled manually with a syringe or with the help of pumps at low to moderate pressure. Microchip columns, fittings, and packaging can usually not tolerate the high packing pressures used in conventional column packing, and the application of ultrasonication that is often crucial to achieve good packing structure can be detrimental to the microfluidic devices. It is therefore to be expected that bed

[222] J. Xie et al. *Anal. Chem.*, **77**: 6947–6953, 2005.
[223] I. M. Lazar, P. Trisiripisal, and H. A. Sarvaiya. *Anal. Chem.*, **78**: 5513–5524, 2006.
[5] H. Yin et al. *Anal. Chem.*, **77**: 527–533, 2005.
[9] K. W. Ro, J. Liu, and D. R. Knapp. *J. Chromatogr. A*, **1111**: 40–47, 2006.
[10] D. S. Reichmuth, T. J. Shepodd, and B. J. Kirby. *Anal. Chem.*, **77**: 2997–3000, 2005.
[12] C.-Y. Shih et al. *J. Chromatogr. A*, **1111**: 272–278, 2006.
[224] J. Carlier et al. *J. Chromatogr. A*, **1071**: 213–222, 2005.
[225] Y. Yang et al. *Lab Chip*, **5**: 869–876, 2005.
[226] M.-H. Fortier et al. *Anal. Chem.*, **77**: 1631–1640, 2005.
[227] A. Ishida et al. *J. Chromatogr. A*, **1132**: 90–98, 2006.
[228] D. A. Mair et al. *Lab Chip*, **6**: 1346–1354, 2006.
[229] J. Liu et al. *Int. J. Mass Spectrom.*, **259**: 65–72, 2007.
[230] Nanostream. *Brio Cartridges*.
[231] D. S. Peterson. *Lab Chip*, **5**: 132–139, 2005.
[232] K. W. Ro, R. Nayak, and D. R. Knapp. *Electrophoresis*, **27**: 3547–3558, 2006.
[233] G. Ocvirk et al. *Anal. Methods Instrum.*, **2**: 74–82, 1995.

porosities of microchip separation columns are higher than those of their conventional counterparts, cylindrical nanobore HPLC columns.

The analysis of dispersion in confined cylindrical packings at low column-to-particle diameter ratio is a topic with a long tradition in the chemical engineering literature.[166] It is generally accepted that the asymptotic axial dispersion coefficient under these conditions depends on the flow maldistribution due to a geometrical wall effect characterized by damped oscillations of the interparticle porosity, which exist over a few particle diameters from the cylinder inner surface toward the bulk of the packing.[234–237] These oscillations are influenced by the size distribution and shape of the particles and are most pronounced in packings of uniform spheres. The geometrical wall effect is a direct result of the inability of the particles to form a close packing against the flat and hard surface of the column wall. This effect in the immediate vicinity of the column wall is distinct from a second and more extended wall effect caused by friction between the bed and the column wall. Compared to the geometrical wall effect, the latter is traditionally discussed in chromatography in connection with relatively large column-to-particle diameter ratios.[238] Although a systematic dependence of axial dispersion in confined cylindrical packings on the column-to-particle diameter ratio is still controversially discussed,[180,239–241] the geometrical wall effect becomes important again for the fabrication of cylindrical nanobore and also noncylindrical microchip HPLC columns. In addition, axial dispersion in noncylindrical packed beds is expected to be affected by the corners of the various conduit geometries, which are absent in the classical cylinder format.

The influence of the conduit geometry on the chromatographic performance of packed beds has rarely been addressed;[14] whereas velocity distributions and hydrodynamic dispersion in open (micro)channels have been extensively investigated for various cross-sectional geometries, mostly by numerical analysis methods.[150,242–245] The results from these studies have limited implication for the situation in packed beds, where the packing microstructure determines time and length scales governing flow and dispersion. In this work, we utilize quantitative numerical analysis to resolve the velocity field and axial hydrodynamic dispersion in pressure-driven flow through fixed beds of solid (impermeable), spherical particles in conduits with four different container geometries and analyze the impact of inherent channel corners and cross-sectional symmetry on flow heterogeneity and resulting dispersion in dependence of the bed porosity.

[166] J. M. P. Q. Delgado. *Heat Mass Transfer*, **42**: 279–310, 2006.
[234] A. J. Sederman, P. Alexander, and L. F. Gladden. *Powder Technol.*, **117**: 255–269, 2001.
[235] A. de Klerk. *AIChE J.*, **49**: 2022–2029, 2003.
[236] D. Tang et al. *Chem. Eng. Technol.*, **27**: 866–873, 2004.
[237] J. Theuerkauf, P. Witt, and D. Schwesig. *Powder Technol.*, **165**: 92–99, 2006.
[238] R. A. Shalliker, B. S. Broyles, and G. Guiochon. *J. Chromatogr. A*, **888**: 1–12, 2000.
[180] R. S. Maier, D. M. Kroll, and H. T. Davis. *AIChE J.*, **53**: 527–530, 2007.
[239] R. T. Kennedy and J. W. Jorgenson. *Anal. Chem.*, **61**: 1128–1135, 1989.
[240] S. Hsieh and J. W. Jorgenson. *Anal. Chem.*, **68**: 1212–1217, 1996.
[241] S. Eeltink et al. *J. Chromatogr. A*, **1044**: 311–316, 2004.
[14] G. P. Rozing et al. *J. Sep. Sci.*, **27**: 1391–1401, 2004.
[150] D. Dutta, A. Ramachandran, and D. T. Leighton. *Microfluid. Nanofluid.*, **2**: 275–290, 2006.
[242] H. Poppe. *J. Chromatogr. A*, **948**: 3–17, 2002.
[243] A. Ajdari, N. Bontoux, and H. A. Stone. *Anal. Chem.*, **78**: 387–392, 2006.
[244] N. Bontoux et al. *Lab Chip*, **6**: 930–935, 2006.
[245] H. Eghbali and G. Desmet. *J. Sep. Sci.*, **30**: 1377–1397, 2007.

2.2 Numerical section

The analysis of hydrodynamic dispersion in channels containing fixed beds of nonporous spherical particles of uniform diameter involved three distinct stages: i) the generation of confined sphere packings in various geometries, ii) simulation of interparticle fluid flow, and iii) modeling of advective–diffusive solute transport. A parallel collective-rearrangement algorithm was used to generate the packings, while a lattice-Boltzmann (LB) algorithm served to calculate the velocity field for single-phase, isothermal, low-Mach number flows in the pore spaces of the packings. A regular grid (or lattice) is superimposed on the fixed beds, and fluid flow is simulated using only the grid cells in the interparticle pore space. Solute transport was approached by a random walk particle tracking method modeling the motion of an inert tracer in the LB-generated velocity field. No assumptions about transport coefficients or average properties of the fixed beds are required, except for the coefficients of solvent kinematic viscosity and solute molecular diffusion.

Using the Jodrey–Tory algorithm (see Section 1.1), a collection of sphere packings with fixed bed porosities (average interparticle void volume fractions) in the range of $0.40 \leq \varepsilon \leq 0.50$ was realized for containers with four different cross-sectional geometries: circular, quadratic, rectangular, and semicircular (Table 2.1). The cross-sectional area of all packings was kept constant at a value of $25\,\pi d_\mathrm{p}^2$. Periodic boundary conditions were used along the z-axis (axial dimension and direction of macroscopic flow) in all packings. The length of the packings was $300\,d_\mathrm{p}$ for containers with circular, quadratic, or rectangular cross section, and $500\,d_\mathrm{p}$ for semicircular containers, sufficient to eliminate possible recorrelation effects, which could lead to an overestimation of the dispersion coefficient.[123]

Table 2.1: Characteristic data of the confined sphere packings.

	circular	quadratic	rectangular	semicircular
area of cross section, d_p^2	$A_\mathrm{c} = A_\mathrm{q} = A_\mathrm{r} = A_\mathrm{s} = 25\pi$			
axial dimension, d_p	$L_\mathrm{c} = L_\mathrm{q} = L_\mathrm{r} = 300$			$L_\mathrm{s} = 500$
perimeter length, d_p	31.42	35.45	36.18	36.36
volume/surface ratio of container, d_p	0.796	0.705	0.691	0.688
lateral dimension, in d_p	diameter, $d_\mathrm{c} = 10$	edge length, $a_\mathrm{q} = 8.86$	edge lengths $a_\mathrm{r}/b_\mathrm{r} = 1.5$, $a_\mathrm{r} = 10.85$, $b_\mathrm{r} = 7.24$	radius, $r_\mathrm{s} = 7.07$
characteristic transverse length, d_p	$d_\mathrm{c}/2 = 5$	$a_\mathrm{q}/\sqrt{2} \approx 6.27$	$\sqrt{13}a_\mathrm{r}/6 \approx 6.52$	$r_\mathrm{s}\sqrt{2} = 10$
bed porosity	$0.40 \leq \varepsilon \leq 0.50$		$\varepsilon = 0.42, 0.48$	

The packings were discretized (Section 1.2) using a uniform grid with a spatial resolution of 30 lattice nodes per sphere diameter, resulting, for example, for the cylindrical packings in a lattice of $300 \times 300 \times 9000$ points in the x, y, and z directions, respectively. Fluid flow in a discretized packing was simulated by the means of Lattice-Boltzmann method (Section 1.3), employing the no-slip boundary condition at the solid–liquid interface. To define the hydrodynamic dispersion

[123] R. S. Maier et al. *Phys. Fluids*, **12**: 2065–2079, 2000.

coefficient, $N = 10^6$ tracer particles were randomly distributed in the whole interparticle pore space of a sphere packing and advective–diffusive mass transport was simulated with the random walk particle tracking approach (see Section 1.4).

With the numerical approach used in this work, it is possible to obtain complete information on the three-dimensional velocity field and address quantitatively structure–transport relations for pressure driven flow through sphere packings confined by a container of arbitrary shape. It includes the detailed analysis of time and length scales underlying transient dispersion, or the dependence of asymptotic dispersion on bed porosity and the average velocity through a packing. All simulations were run on a Hewlett-Packard Superdome at the Otto-von-Guericke-Universität Magdeburg. Calculations typically took 48 h for one velocity field and another 36 h for one dispersion coefficient using 64 processors.

2.3 Results and discussion

For our investigation on the influence of the conduit geometry on the flow velocity field and hydrodynamic dispersion in fixed beds of spherical, nonporous particles, we selected four basic cross-sectional geometries: circular (c), quadratic (q), rectangular (r), and semicircular (s). In miniaturized separation systems employing particulate beds, e.g., nano-HPLC, typical column inner diameters and particle diameters are 75 and 5 µm, respectively, i.e., column-to-particle diameter ratios of $10–20$ are prevalent. A diameter of $d_\mathrm{c} = 10\,d_\mathrm{p}$ was chosen for the cylindrical column as a representative value that would also allow the numerical simulations to be carried out with reasonable computational efforts. For the quantitative comparison between cylindrical and noncylindrical packings, the lateral dimensions of the noncylindrical conduits were chosen to yield the same cross-sectional area as the cylindrical column, i.e., $A = 25\,\pi d_\mathrm{p}^2$. An aspect ratio (channel width to channel depth) of 1.5 was used for the rectangular cross section (Table 2.1). Fixed beds with average porosities of $0.40 \leq \varepsilon \leq 0.50$ were generated. The lower limit of $\varepsilon = 0.40$ reflects a relatively dense packing for the investigated low channel-to-particle size ratios. The upper limit was chosen because packings with $\varepsilon > 0.50$ become too dilute, heterogeneous, and unstable in practice. Thus, the chosen range of $0.40 \leq \varepsilon \leq 0.50$ appears to be the most relevant for investigating structure–transport relations in packed microchannels in order to optimize the hydrodynamics for improved HPLC performance. Sphere packings with seven different bed porosities (from 0.40 to 0.50 in step of 0.02, and 0.43) were generated for columns with circular or quadratic cross section (main set of geometries), while for the columns with rectangular or semicircular cross section (additional set of geometries), two representative porosities were selected, $\varepsilon = 0.42$ and $\varepsilon = 0.48$, one near each end of the investigated range of porosities (Table 2.1).

2.3.1 Porosity distributions

Figure 2.1 shows the front view of the generated packings for two selected porosities (top row in Figure 2.1a ($\varepsilon = 0.42$) and Figure 2.1b ($\varepsilon = 0.48$)) as well as a side view of a packing with quadratic cross section (Figure 2.1c). All packings have axial dimensions of $L \geq 300\,d_\mathrm{p}$, which is demanding in terms of computational resources, but ensures the elimination of recorrelation

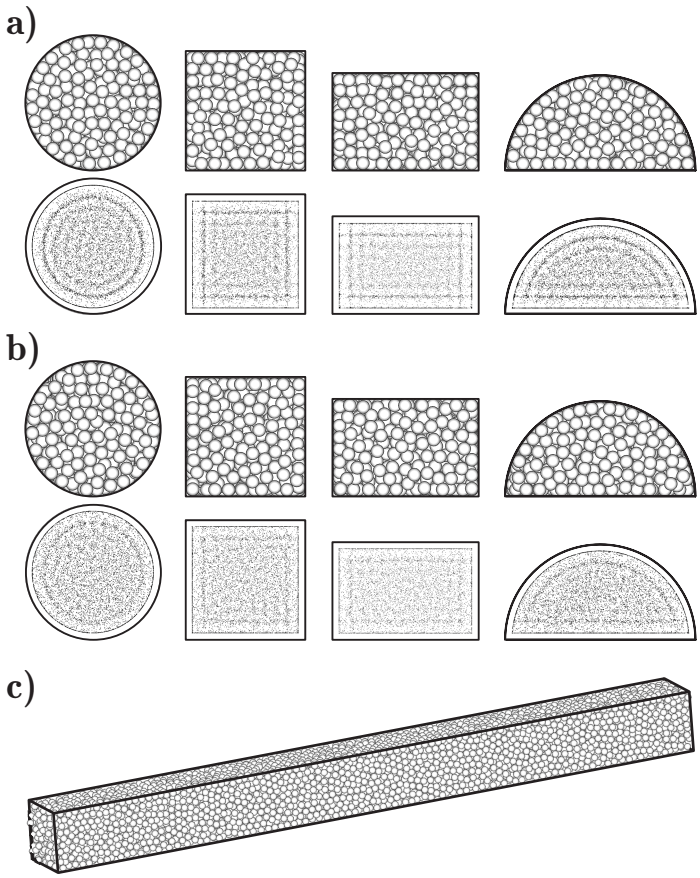

Figure 2.1: Fixed beds (confined sphere packings) simulated for containers with four different cross-sectional geometries: circular, quadratic, rectangular, and semicircular. Packings with two different bed porosities were generated for each container geometry: $\varepsilon = 0.42$ (a) and $\varepsilon = 0.48$ (b). Shown are the front of the generated packings (top rows in a and b) and projections of all particle centers in a packing onto the front plane (bottom rows). (c) depicts a side view of a packing with quadratic cross section. All packings have an identical cross-sectional area. Characteristic data of the sphere packings are given in Table 2.1.

effects that originate in the repeated experience of macroscopic flow features by tracer particles traversing the length of the packing more than once.[123] The porosity distribution in the generated packings is reflected in the bottom rows of Figure 2.1a and Figure 2.1b, which display projections of all particle centers in a packing onto the front plane. It is evident from these projections that particles are generally highly ordered in the near-wall region. The particle centers of the first layer next to the container wall form a sharply defined line in all packing projections shown. But the effect of ordering with regard to both, intensity and extension, is visibly less pronounced in packings of higher bed porosity ($\varepsilon = 0.48$). The porosity differences cannot be discerned visually in the pictures showing the complete sphere packings (top rows in Figure 2.1a and Figure 2.1b). This implies that a simple optical inspection, e.g., of a sliced packing, is insufficient to provide reliable information on the packing density, particularly in the critical wall region.

The porosity distribution in the packings is analyzed in more detail in Figure 2.2 for circular and quadratic cross-sectional geometries. The lateral porosity distribution of a packing was

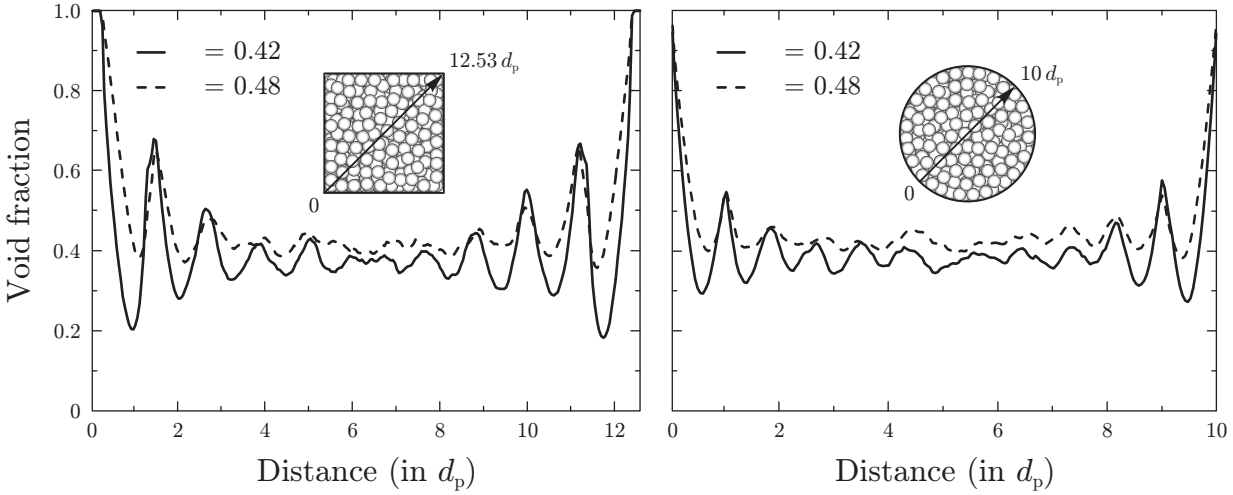

Figure 2.2: Distribution of the local porosity (or interparticle void fraction) for sphere packings in containers with quadratic cross section (left) and in cylindrical containers (right), with bed porosities of $\varepsilon = 0.42$ and $\varepsilon = 0.48$. Porosity distributions were calculated along the indicated arrows over the whole length of the packings, covering two of the corners in the quadratic geometry (diagonal profile).

calculated by recording the interparticle void fraction along the indicated arrow over the whole length of a packing. Significant fluctuations of local porosity are present over a distance of $2–3\,d_\mathrm{p}$ from the wall for both conduit geometries. The arrow along which the porosities were taken in the packings with quadratic cross section is longer than the diameter of the cylindrical packings (Table 2.1), which accounts for the observed difference in damping range. As expected, the fluctuations of porosity are for both geometries more pronounced in packings with lower average porosity ($\varepsilon = 0.42$), because the particles have to fill the available space more densely. The main difference between the cylindrical and noncylindrical packings here lies in the amplitudes of the observed porosity fluctuations, which are decidedly larger for the quadratic cross section, and in the porosity distribution in the near-wall region, i.e., within a distance of one d_p from the container wall. Figure 2.3 shows the enlarged near-wall region of Figure 2.2. In comparison to the cylindrical packings, the first minimums in the porosity distribution functions of the packings with quadratic cross section are shifted by $\sim 0.3\,d_\mathrm{p}$ to positions further inside the packing, which means that the exclusion volume (i.e., a region where no particle centers are found) adjacent to the wall is larger in the noncyclindrical packings. While the porosity distribution functions of the cylindrical packings start with an instant decline from the high porosity at the wall, there is a region of maximum porosity extended over nearly $0.2\,d_\mathrm{p}$ for the packings with the quadratic cross section.

The observed differences in the porosity distribution functions between packings with circular and quadratic cross section are the consequence of the reduced symmetry of a square compared to a circle. The presence of corners places geometric restrictions upon the particle positions. Particles occupying positions near the corners (“near-angle particles”) have a semifixed position due to the constrictions of the $90°$-angled corners. It may be imagined that a packing is generated by layering slices of particle-packed cross sections of one d_p thickness (“monolayers”) up to the desired packing length. The relative orientation of these layers is restricted in the case of quadratic

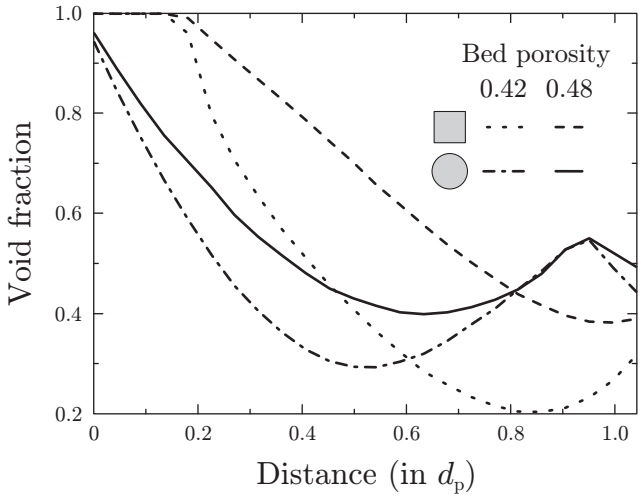

Figure 2.3: Comparison of the interparticle void fraction distribution in the near-wall region between packings with circular and quadratic cross section at the two selected bed porosities (from Figure 2.2). Noticeable is an extended region of maximum porosity on the order $0.2\,d_\mathrm{p}$ in the corner of the packings with quadratic cross section. These regions translate to channels of advanced flow velocity as shown in Figure 2.4

cross sections because the number of corner positions is limited and so are the possible positions of near-angle particles. Because of the limited possibilities of orientation of the layers to each other, the distribution of particle positions is more uniform in packings with quadratic cross section; i.e., the maximums and minimums of the periodic porosity distribution function are more pronounced than in cylindrical packings. The effect of the container corners on the packing porosity can also be seen by revisiting the particle projections in Figure 2.1a ($\varepsilon = 0.42$). All noncylindrical packings display distinct porosity oscillations near the corners within a distance of $3\,d_\mathrm{p}$ from the wall, while toward the packing center, the particle distributions are more random. The regions of high porosity in and near the corners of the noncylindrical packings are expected to become channels of advanced velocity in pressure-driven flow.

2.3.2 Fluid flow fields

Figure 2.4 shows velocity profiles calculated for all packing geometries and the two selected bed porosities at a reduced velocity or Péclet number $Pe = \bar{v}d_\mathrm{p}/D_\mathrm{m}$ (where $\bar{v}$ is the average velocity through the packings and D_m is the bulk molecular diffusion coefficient) of $Pe = 10$. These profiles correlate well with the particle center projections of Figure 2.1 and the porosity distribution functions of Figure 2.2. Regions of higher and lower than average velocity match the maximums and minimums, respectively, of the porosity distribution functions. As anticipated, regions of advanced velocity appear in the corners of the noncylindrical packings. A comparison between packings of higher and lower bed porosity reveals two facts: first, a higher bed porosity translates to a more pronounced flow heterogeneity between the near-wall region and the inner region of a packing for all cross-sectional geometries. Second, the impact of a higher bed porosity on the flow heterogeneity is much larger for noncylindrical packings, because the corner channels

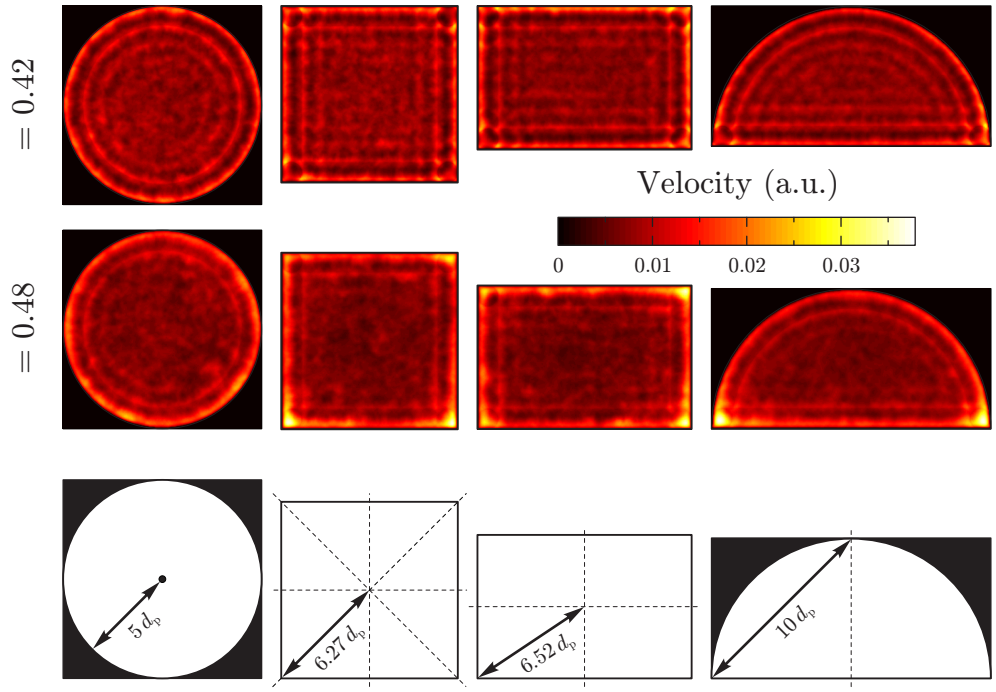

Figure 2.4: Velocity profiles for packings with the four different cross-sectional geometries at two selected bed porosities, $\varepsilon = 0.42$ (top row) and $\varepsilon = 0.48$ (center row). The reduced velocity or Péclet number $Pe = \bar{v}d_\mathrm{p}/D_\mathrm{m}$ (where $\bar{v}$ is the average velocity through the packings and D_m the bulk molecular diffusion coefficient) is $Pe = 10$. The schematic (bottom row) illustrates the characteristic transverse length for each velocity field (conduit geometry). It corresponds to the distance that needs to be covered in order to realize a complete exchange (equilibration) between different velocities (see also bottom row in Table 2.1).

of advanced fluid flow are not only more extended but the velocity in these channels is also higher than in packings of lower bed porosity.

Figure 2.4 is helpful in analyzing the characteristic transverse length of the computed velocity fields for each container geometry. Based on the underlying porosity distribution, which is intimately related to a particular container geometry, this length characterizes the straight distance transverse through a packing that needs to be covered to realize equilibration, i.e., a complete exchange between different velocities of the resulting three-dimensional velocity field ("flow equalization"). Under explicit consideration of the symmetry of the velocity fields, it refers to the longest distance between different velocities, as illustrated by the arrows in the schematic of Figure 2.4 (see also bottom row in Table 2.1). In cylindrical columns, the highest velocities are found along the wall, while they are located in the corners of the noncylindrical conduits investigated in this work. For the cylindrical packing, the complete exchange between velocity extremes in the mobile phase is achieved by covering the lateral distance from the wall of the cylinder to its center. Consequently, the characteristic transverse length on the macroscopic (conduit cross-sectional) scale is the radius of the cylindrical packing, while — due to the prevailing symmetry — it is the half-diagonal of the quadratic and rectangular geometries, i.e., the distance from each corner to the center of the packings (see arrows in Figure 2.4). Lateral exchange in the quadratic and rectangular geometries along the median is always faster than along the diagonal and, thus, not limiting concerning the

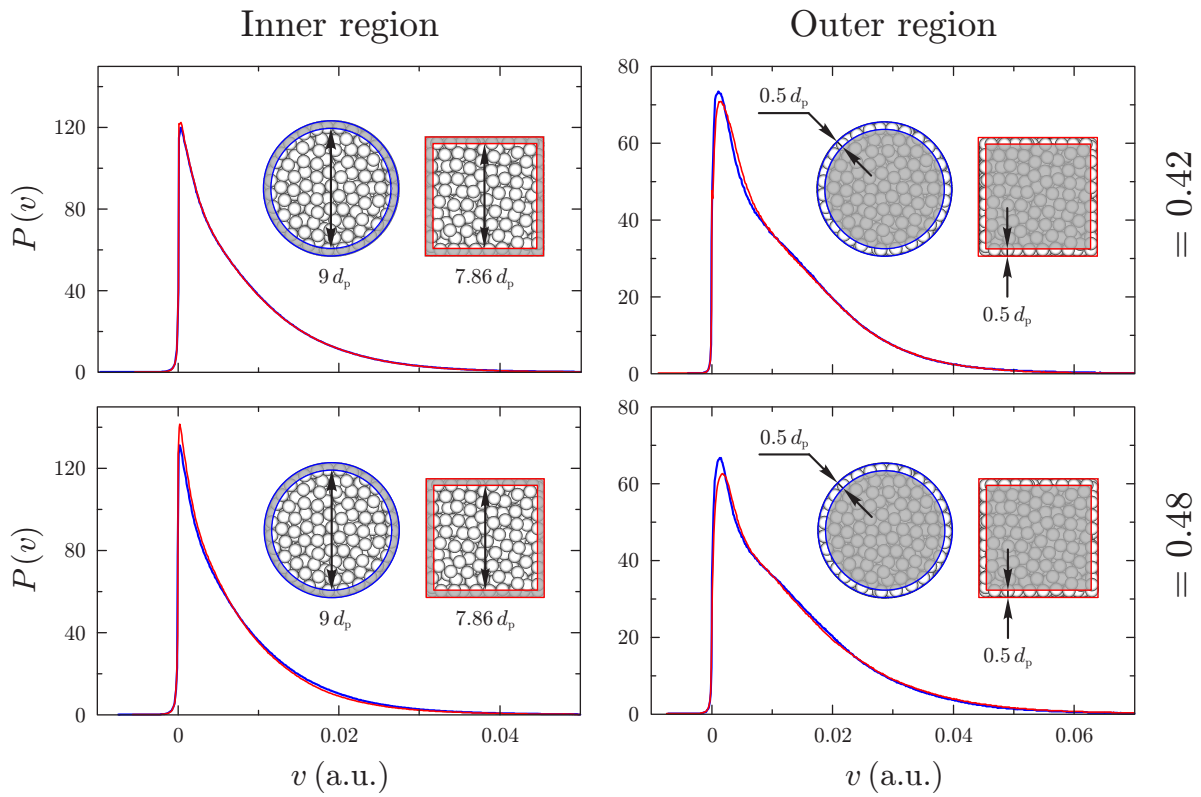

Figure 2.5: Velocity probability distribution functions at $Pe = 10$ for packings with circular (blue lines) and quadratic (red lines) cross section at two different bed porosities, $\varepsilon = 0.42$ (top row) and $\varepsilon = 0.48$ (bottom row). For better visualization of the differences, the distribution functions for the inner packing (left column) are plotted separately from the distribution functions obtained for the near-wall regions (within a distance of less than $0.5\ d_\mathrm{p}$, right column).

dynamics of this equilibration (attainment of asymptotic dispersion behavior). The semicircular geometry presents the longest characteristic transverse length, namely, the distance between a corner and the apex of the semicircle. We will return to that important aspect with Figure 2.7. For the geometries considered in this work, a reduced cross-sectional symmetry (from left to right in Figure 2.4) results in an increased characteristic transverse length of the velocity field given the constant cross-sectional area. This is also reflected in the perimeter length of the containers, which increases from the cylindrical to the semicircular geometry, as well as in the volume-to-surface ratio, which shows a corresponding decrease (Table 2.1).

The impact of the bed porosity on flow heterogeneity for noncylindrical packings is analyzed in more detail in Figure 2.5, which compares the velocity probability distribution functions of circular and quadratic packings for the two selected bed porosities, $\varepsilon = 0.42$ (top row) and $\varepsilon = 0.48$ (bottom row), at $Pe = 10$. The distributions for the near-wall region (less than $0.5\ d_\mathrm{p}$ distance from the wall) are plotted separately from the functions for the inner core of the packing for a clearer visualization of the differences. The velocity probability functions for the near-wall region have a form different from those for the inner core. The former comprise a shoulder that appears at higher flow velocities, reflecting a higher percentage of advanced flow velocities in the near-wall region. The maximums of the near-wall region functions are also shifted slightly to higher velocities

compared to the inner core functions because the fluid channels in the near-wall region are larger and less tortuous than those of the inner core. This behavior is observed for both cross-sectional geometries and bed porosities, but is more pronounced in the quadratic packings and at higher bed porosity. While the velocity probability functions for the inner core are practically identical for both cross-sectional geometries at $\varepsilon = 0.42$, one can observe a difference between the two geometries in the near-wall velocity probability functions, with the quadratic packing exhibiting a higher percentage of advanced flow velocities. This is more aggravated at $\varepsilon = 0.48$, where the difference between the cross-sectional geometries is also visible in the inner core. The presence of more locations of higher flow velocities in the near-wall region causes a decrease of higher flow velocity regions in the inner core; i.e., the average velocity in the inner core is decreasing, because the average velocity in the whole packing is kept constant. In all probability functions shown in Figure 2.5, there is a small but finite probability for negative arguments translating to fluid flow in the opposite direction of the applied pressure gradient. This stems from the fact that fluid motion in a curved path around a spherical particle contains velocity vector components with opposite orientation to the main direction of flow.[246,247]

2.3.3 Hydrodynamic dispersion

The differences between cylindrical and noncylindrical packed beds appear to be subtle from the velocity probability distribution functions shown in Figure 2.6, but they critically affect the hydrodynamic axial dispersion coefficient of the packings as evidenced in Figure 2.6 and Figure 2.7. Figure 2.6 shows the effective (asymptotic) axial dispersion coefficient normalized by D_{m} as a function of the average porosity for $Pe = \bar{v} d_{\mathrm{p}} / D_{\mathrm{m}} = 10$ (left) and $Pe = 20$ (right; this value is realized by doubling the average velocity $\bar{v}$ through the packings with respect to $Pe = 10$). Curves are drawn for circular and quadratic geometries for which packings with seven bed porosities in the range of $0.40 \leq \varepsilon \leq 0.50$ were generated. Dispersion coefficients for the additional set of packing geometries are also shown at the selected bed porosities of $\varepsilon = 0.42$ and $\varepsilon = 0.48$. Generally, the dispersion coefficient grows monotonically with increasing average porosity and Pe. But the slope of the curve for the quadratic geometry is decidedly steeper than the slope for the cylindrical packings. While at a bed porosity of $\varepsilon = 0.40$ the hydrodynamic dispersion coefficient for the quadratic packing geometry differs little from that of the cylindrical packing, the situation becomes more acute at higher bed porosity. For example, an increase in ε from 0.40 to 0.50 at $Pe = 10$ (20) results in an increase in D_{ax} by a factor of 3.1 (3.4) and 4.6 (5.2), respectively, for packings with circular and quadratic cross sections.

The corners of the container with quadratic cross section favor the formation of channels of advanced fluid flow velocity. The extension of these channels as well as the actual velocity in these channels increases with increasing bed porosity. The dispersion coefficients for the rectangular and semicircular geometries seem to follow a similar relationship with the bed porosity as the quadratic packing geometry. Their actual coefficients are, however, always larger than the corresponding coefficient for the quadratic geometry. But while the difference in the dispersion coefficients between

[246] R. S. Maier et al. *Phys. Fluids*, **10**: 60–74, 1998.
[247] D. Hlushkou, A. Seidel-Morgenstern, and U. Tallarek. *Langmuir*, **21**: 6097–6112, 2005.

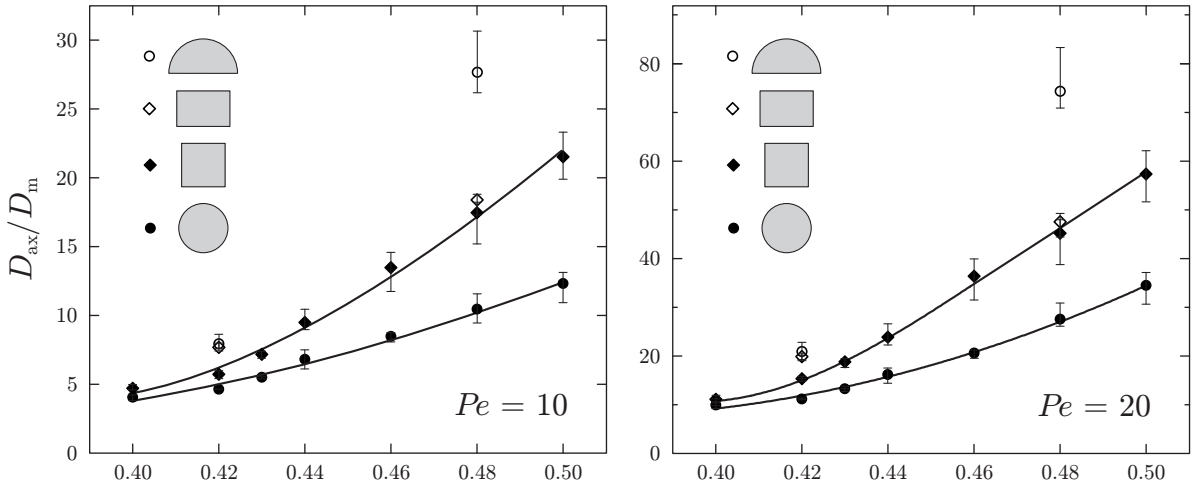

Figure 2.6: Effective axial dispersion coefficient D_{ax} (normalized by the bulk molecular diffusion coefficient D_m) as a function of the bed porosity simulated for an inert tracer at $Pe = 10$ (left) and $Pe = 20$ (right). For the circular and quadratic packing geometries, seven values in the range of $0.40 \leq \varepsilon \leq 0.50$ were computed, while for the packed rectangular and semicircular geometries values at two selected bed porosities of $\varepsilon = 0.42$ and $\varepsilon = 0.48$ were calculated.

quadratic and rectangular geometries is relatively small at both, the lower and higher bed porosity, the hydrodynamic dispersion coefficient for the semicircular geometry seems to be genuinely affected by higher bed porosities.

This leads us to another important aspect of the noncylindrical packings, already addressed in Figure 2.4, which is related to the reduced symmetry of noncylindrical compared to cylindrical geometries. The different conduit geometries differ with respect to the characteristic transverse length for the tracer molecules to achieve lateral equilibration between different flow velocities in a packing (see arrows in the schematic of Figure 2.4 and Table 2.1). The associated transient behavior is intimately coupled to the conduit geometry. Figure 2.7 shows the development of normalized axial dispersion coefficients as a function of the dimensionsless diffusive time $t_d = 2D_m t/d_p^2$, calculated for a bed porosity of $\varepsilon = 0.48$. Two curves are shown for each cross-sectional geometry, one calculated for $Pe = 10$ and one for $Pe = 20$ (that is, for twice the average velocity through the packings). Each curve represents an average of three independent calculations starting with the generation of the packings from three different seeds. Values for t_d in Figure 2.7 represent the time for each geometry and value of Pe after which asymptotic behavior in D_{ax}/D_m is observed.

We notice two trends: first, the time needed for reaching asymptotic behavior increases from the circular through the quadratic and rectangular to the semicircular geometry for both values of Pe. Second, this time is smaller for $Pe = 20$ than for $Pe = 10$, for all geometries. The characteristic diffusive times needed for reaching asymptotic behavior are longest for the semicircular geometry, which negatively affects hydrodynamic dispersion in these packings (cf. Figure 2.6; $\varepsilon = 0.48$). At high bed porosity, the channels in the corners of the semicircular containers are also more extended and display higher flow velocity than the channels in the corners of the quadratic and rectangular containers (Figure 2.4). The presence and characteristics of these channels as well as

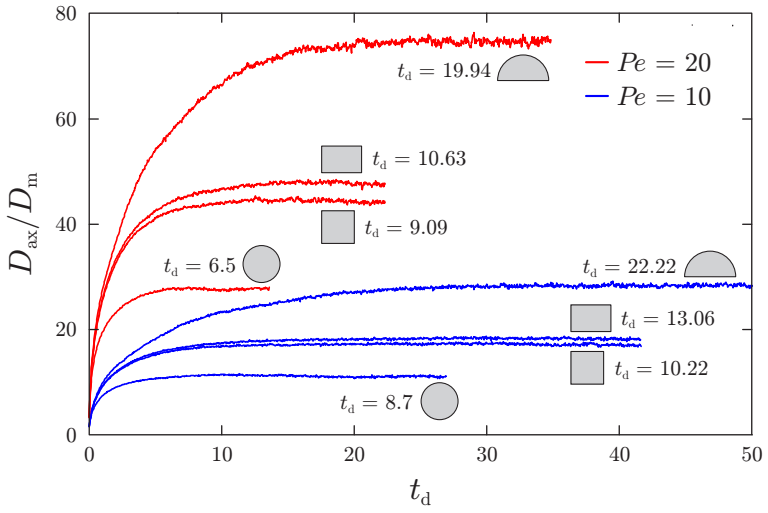

Figure 2.7: Normalized axial dispersion coefficient of an inert tracer as a function of the dimensionless diffusive time $t_d = 2D_m t/d_p^2$ for fixed beds with a porosity of $\varepsilon = 0.48$. For each container geometry, two curves are shown, one calculated at $Pe = 10$ (blue lines) and one at $Pe = 20$ (red lines). Each curve represents an average of three independent calculations starting with the generation of packings from three different seeds. The actual values for t_d provided in the figure represent the time for each geometry (and value of Pe) after which asymptotic behavior in D_{ax}/D_m is observed.

the required time (or corresponding spatial dimension) for lateral equilibration cause the relatively high dispersion coefficient of the semicircular packings (Figures 2.6 and 2.7).

The values of the diffusion times needed for reaching asymptotic behavior reported in Figure 2.7 can be expressed as distances in units of d_p. For example, with the cylindrical packing at $Pe = 10$, we find $t_d = 2D_m t/d_p^2 = 8.87$, from analysis of the corresponding curve for D_{ax}/D_m. This dimensionless time translates to a distance of $(2D_m t)^{1/2} = (8.7^{1/2})\, d_p \approx 3\, d_p$. A comparison of the distances calculated accordingly from the t_d-values in Figure 2.7 with the characteristic transverse length for each cross-sectional geometry deduced in Figure 2.4 from the symmetry of the velocity fields (cylinder radius, $r_c = 5\, d_p$ in the above example for the cylindrical packing) shows that the former are generally smaller and also flow rate dependent.

This finding may originate in the fact that lateral equilibration between different velocities in a packing is not determined by purely diffusive behavior, as reflected by the values for $t_d = 2D_m t/d_p^2$ in Figure 2.7, but is actually accelerated by a combination of lateral diffusion and convective motion (eddy dispersion).[248] For example, while the time scale for asymptotic development of axial dispersion in an unpacked cylinder is $t \sim r_c^2/D_m$, from Taylor dispersion, the time scale for packed cylinders expected by analogy is $t \sim r_c^2/D_{tr}$ (where D_{tr} is the transverse dispersion coefficient). In other words, D_{ax}/D_m in Figure 2.7 converges toward its asymptotic limit on a time scale that is proportional to the ratio of the characteristic transverse dimension squared and the transverse dispersion rate (not the purely diffusive one). Thus, within a given time needed to reach asymptotic dispersion, a larger distance can be sampled by the tracer molecules based on the transverse dispersion coefficient (D_{tr}) than by assuming purely diffusive behavior D_m.

[248] U. Tallarek et al. *AIChE J.*, **42**: 3041–3054, 1996.

This conclusion finds support in the velocity dependence of the transverse dispersion rate, which can explain the shorter times required to realize asymptotic dispersion at $Pe = 20$ compared to $Pe = 10$ (Figure 2.7). It also agrees with data reported recently by Maier et al.;[180,185] who have shown that the time scale for attaining asymptotic dispersion in cylindrical packings is neither the convective nor the diffusive time scale, but related to r_c^2/D_{tr}. Similar effects have been predicted for packed beds confined in conduits of any cross-sectional geometry;[185] which is confirmed with the selected noncylindrical packings in this work.

2.4 Conclusions

The presented numerical approach allows the simulation of fluid flow and solute dispersion in three-dimensional fixed beds confined in containers of arbitrary shape. It provides quantitative information on the spatial distribution of the simulated velocities and the resulting transient as well as asymptotic hydrodynamic dispersion. This feature was utilized to analyze the velocity profile and axial dispersion in pressure-driven flow through packings of uniform, solid spheres in conduits with four different cross-sectional geometries, namely, circular, quadratic, rectangular, and semicircular, over a range of bed porosities of $0.40 \leq \varepsilon \leq 0.50$.

The analysis of our data revealed two important aspects that influence the hydrodynamic dispersion in noncylindrical compared to cylindrical packed beds: i) the presence of corners gives rise to the formation of channels of advanced fluid flow velocity, and ii) the reduced symmetry of noncylindrical packings effects a longer characteristic length of the solute molecules for lateral equilibration between different velocities. These aspects effect that the axial hydrodynamic dispersion in noncylindrical packed beds is always larger than in cylindrical packed beds of equal cross-sectional area. Among the different noncylindrical geometries, the quadratic geometry shows the best performance, followed by the rectangular geometry. The semicircular geometry displays the worst dispersion characteristics, partly because the semicircle corners allow for extended channels of advanced fluid flow velocity, partly because the semicircle has the lowest symmetry among the investigated geometries and a decidedly longer characteristic transverse length. Of particular importance is the strong dependence of the hydrodynamic dispersion coefficient on the bed porosity of the noncylindrical packings. Noncylindrical packings are more strongly affected by higher bed porosities than cylindrical packings, while at low bed porosities, hydrodynamic dispersion comes close to those of the cylindrical packings.

It is therefore advisable to consider the symmetry of the channel cross section in the design and fabrication of separation columns for LC-microchips, but of prime importance for chromatographic performance is the porosity of the packing. To achieve a dense packing in microchip separation columns, it is necessary to optimize packing procedures, and in this respect, the development of high-pressure rating microchannels and fittings is particularly desirable.

[185] R. S. Maier et al. *Philos. Trans. R. Soc. A*, **360**: 497–506, 2002.

Chapter 3

Packings of trapezoidal cross sections

This chapter is concerned with hydrodynamic dispersion in the packings of trapezoidal cross sections; trapezoidal packings are derived from "ideal" rectangular geometries and packings of both types are compared. Results presented here were published in the journal *Lab on a Chip* in 2008.[249]

3.1 Introduction

In the quest for miniaturized analytical systems,[221] nano-HPLC and microchip-HPLC are of great interest.[250] Beside the advantages of increased speed and sensitivity as well as reduced sample and consumables volumes that come with miniaturization, the flow rates involved are well suited to ESI-MS, the detector-of-choice for screening and proteomics applications.[8] Nano-HPLC utilizes cylindrical fused-silica capillaries with internal diameters between 30 and $100\,\mu\text{m}$. Although open-tubular and monolithic columns are in use, the predominating stationary support are fixed beds of spherical porous silica-based particles of 3 to $5\,\mu\text{m}$ diameter. Their popularity is mainly due to the wide range of surface modifications available for these particles.[251] In microchip-HPLC, by contrast, the separation medium is confined in a microchannel of noncylindrical shape. From the limited number of recent publications on HPLC-microchips using fixed beds, a definite preference for monolithic[9,10,224,225,227–229,252] or particulate[5,12,222,223,253,254] stationary supports has not emerged yet.

[249] S. Khirevich et al. *Lab Chip*, **8**: 1801–1808, 2008.
[221] P. S. Dittrich, K. Tachikawa, and A. Manz. *Anal. Chem.*, **78**: 3887–3908, 2006.
[250] J. Hernández-Borges et al. *J. Sep. Sci.*, **30**: 1589–1610, 2007.
[8] S. Koster and E. Verpoorte. *Lab Chip*, **7**: 1394–1412, 2007.
[251] U. D. Neue. *HPLC columns: theory, technology, and practice*. Wiley-VCH, 1997.
[9] K. W. Ro, J. Liu, and D. R. Knapp. *J. Chromatogr. A*, **1111**: 40–47, 2006.
[10] D. S. Reichmuth, T. J. Shepodd, and B. J. Kirby. *Anal. Chem.*, **77**: 2997–3000, 2005.
[224] J. Carlier et al. *J. Chromatogr. A*, **1071**: 213–222, 2005.
[225] Y. Yang et al. *Lab Chip*, **5**: 869–876, 2005.
[227] A. Ishida et al. *J. Chromatogr. A*, **1132**: 90–98, 2006.
[228] D. A. Mair et al. *Lab Chip*, **6**: 1346–1354, 2006.
[229] J. Liu et al. *Int. J. Mass Spectrom.*, **259**: 65–72, 2007.
[252] P. A. Levkin et al. *J. Chromatogr. A*, **1200**: 55–61, 2008.
[5] H. Yin et al. *Anal. Chem.*, **77**: 527–533, 2005.
[12] C.-Y. Shih et al. *J. Chromatogr. A*, **1111**: 272–278, 2006.
[222] J. Xie et al. *Anal. Chem.*, **77**: 6947–6953, 2005.
[223] I. M. Lazar, P. Trisiripisal, and H. A. Sarvaiya. *Anal. Chem.*, **78**: 5513–5524, 2006.
[253] A. Gaspar, M. E. Piyasena, and F. A. Gomez. *Anal. Chem.*, **79**: 7906–7909, 2007.
[254] S. Ehlert et al. *Anal. Chem.*, **80**: 5945–5950, 2008.

While the wide selection of surface-modified particles is still desirable, particle packing inmicrofluidic channels is more difficult than in fused-silica capillaries. On the other hand, monolithic beds can be prepared *in situ* in the channels and chemically anchored to the channel walls.[231,232,255,256]

Microchannel fabrication on chips can be carried out by a number of techniques,[8] but inherently results in noncylindrical shapes with corners. "Cornerless" channels have been made by the bonding of two wafers with hemi-elliptical channels,[9,10] and Abate et al.[257] recently achieved the fabrication of a cylindrical channel by coating the inside of a rectangular PDMS channel with a glass-like layer using sol–gel chemistry. This channel was however not subjected to high pressure applications. The cross-sectional geometry of a microchannel is mainly determined by the specific materials and methods used for its fabrication. Quadrilateral channels are prevalent, but although channel dimensions are usually described in terms of width and height, the cross-sections are in fact more often trapezoidal than regular rectangles.[258]

The effect of the conduit shape on flow and dispersion in open microchannels with trapezoidal cross section has been investigated for pressure-driven, electrokinetically-driven, and mixed flows.[150,243,258–260] It was found that trapezoidal channels differ significantly from rectangular channels with respect to the resulting fluid flow profiles and axial dispersion. In rectangular open microchannels, axial dispersion is governed by the smaller of the lateral dimensions of the channel (referred to as the height or depth of the channel), whereas in trapezoidal channels fluid flow in the triangular side-regions dominates overall axial dispersion.

In packed beds, where the packing microstructure determines time and lengths scales governing flow and dispersion,[166,235,261,262] the effect of noncylindrical conduit geometry has rarely been addressed.[14,213] We recently investigated the impact of corners in noncylindrical conduits on the axial dispersion in particulate beds for quadratic, rectangular, and semicircular cross-sectional geometries by quantitative numerical simulation methods (Chapter 2). This analysis revealed that regions of advanced fluid flow are present in the corners of noncylindrical packings, leading to larger axial dispersion coefficients as compared to cylindrical packings of equal cross-sectional area. The dimensions of the corner channels are determined by the specific conduit geometry and the average bed porosity of the packing. In densely packed beds, i.e., at low bed porosity, these regions

[231] D. S. Peterson. *Lab Chip*, **5**: 132–139, 2005.
[232] K. W. Ro, R. Nayak, and D. R. Knapp. *Electrophoresis*, **27**: 3547–3558, 2006.
[255] J. Billen and G. Desmet. *J. Chromatogr. A*, **1168**: 73–99, 2007.
[256] M. De Pra, W. Th. Kok, and P. J. Schoenmakers. *J. Chromatogr. A*, **1184**: 560–572, 2008.
[257] A. R. Abate et al. *Lab Chip*, **8**: 516–518, 2008.
[258] K. Horiuchi, P. Dutta, and C. D. Richards. *Microfluid. Nanofluid.*, **3**: 347–358, 2007.
[150] D. Dutta, A. Ramachandran, and D. T. Leighton. *Microfluid. Nanofluid.*, **2**: 275–290, 2006.
[243] A. Ajdari, N. Bontoux, and H. A. Stone. *Anal. Chem.*, **78**: 387–392, 2006.
[259] E. K. Zholkovskij and J. H. Masliyah. *Chem. Eng. Sci.*, **61**: 4155–4164, 2006.
[260] M. Bahrami, M. M. Yovanovich, and J. R. Culham. *Int. J. Heat Mass Transfer*, **50**: 2492–2502, 2007.
[166] J. M. P. Q. Delgado. *Heat Mass Transfer*, **42**: 279–310, 2006.
[235] A. de Klerk. *AIChE J.*, **49**: 2022–2029, 2003.
[261] U. Tallarek, E. Bayer, and G. Guiochon. *J. Am. Chem. Soc.*, **120**: 1494–1505, 1998.
[262] D. Kandhai et al. *Phys. Rev. Lett.*, **88**: 234501, 2002.
[14] G. P. Rozing et al. *J. Sep. Sci.*, **27**: 1391–1401, 2004.
[213] S. Khirevich et al. *Anal. Chem.*, **79**: 9340–9349, 2007.

Table 3.1: Characteristic data of the generated quadrilateral sphere packings[a]

Cross-sectional geometry	Basic geometry	Height, d_p	Base angle	Width, d_p	Side-aspect ratio	Bottom base length, d_p	Top base length, d_p	Base-aspect ratio	Characteristic length for lateral equilibration[b], d_p
Quadratic			90°	10	1				7.071
Trapezoidal			85°			10.875	9.125	1.192	11.383
Trapezoidal			80°			11.763	8.237	1.428	11.601
Trapezoidal	Quadratic	10	75°			12.679	7.321	1.732	11.840
Trapezoidal			70°			13.640	6.360	2.145	12.104
Trapezoidal			65°			14.663	5.337	2.747	12.400
Rectangular			90°	14.142	2				7.906
Trapezoidal			85°			14.761	13.523	1.092	10.221
Trapezoidal			80°			15.389	12.895	1.193	10.450
Trapezoidal	Rectangular	7.071	75°			16.037	12.247	1.309	10.691
Trapezoidal			70°			16.716	11.568	1.445	10.945
Trapezoidal			65°			17.439	10.845	1.608	11.226
Rectangular			90°	22.361	5				11.402
Trapezoidal			85°			22.752	21.969	1.036	12.223
Trapezoidal			80°			23.149	21.572	1.073	12.408
Trapezoidal	Rectangular	4.472	75°			23.559	21.162	1.113	12.600
Trapezoidal			70°			23.988	20.732	1.157	12.801
Trapezoidal			65°			24.446	20.275	1.206	13.015

[a] All conduits have a cross-sectional area of $100\,d_\mathrm{p}^2$ and a length of $1200\,d_\mathrm{p}$. The bed porosity of all packings is $\varepsilon = 0.48$.

[b] For the regular orthogonal geometries the characteristic length corresponds to half the diagonal of the cross section. For trapezoidal packings, the distance between the mid-point of the top base and the bottom base corner was calculated.

are smaller than at higher bed porosity and hydrodynamic dispersion comes close to that observed for cylindrical packings. It was also found that the reduced symmetry of noncylindrical conduits translates to a longer characteristic length for lateral equilibration of solute molecules between different velocities.

We investigate the efficiency of trapezoidal particulate beds in terms of hydrodynamic dispersion. We present lateral porosity distributions, fluid flow velocity fields, and axial dispersion coefficients simulated for random-close packings of spherical particles confined in quadratic, rectangular, and trapezoidal conduits of equal cross-sectional area, and analyze the results with respect to the base angles and respective (side and base) aspect ratios of the conduits.

3.2 Numerical section

The numerical simulations involved three distinct steps for each investigated conduit geometry: i) generation of a sphere packing, ii) calculation of the accompanying fluid flow velocity field, and iii) simulation of axial hydrodynamic dispersion at various Péclet numbers $Pe = u_\mathrm{av} d_\mathrm{p} / D_\mathrm{m}$ (where u_av is the average velocity through the interstitial space of a packing and D_m is the bulk molecular diffusion coefficient).

Packings of uniform, solid (impermeable), spherical particles of diameter d_p with average bed porosities (interparticle void fractions) of $\varepsilon = 0.48$ were generated in conduits with quadrilateral cross section (Table 3.1). Fifteen isosceles trapezoids were derived from quadratic and rectangular geometries by varying the base angle from $85°$ to $65°$ in steps of $5°$ while maintaining the height of the basic geometry (Figure 3.1) to express a slight to moderate deviation of the trapezoidal

channels from the respective regular orthogonal conduits. We utilized the Jodrey–Tory algorithm (see Section 1.1), which allows the generation of unconfined random packings of low bed porosity. Periodic boundary conditions were used in the axial direction (direction of macroscopic fluid flow). All packings had a cross-sectional area of $100\,d_\mathrm{p}^2$, a length of $1200\,d_\mathrm{p}$, and contained about 1.0–1.3×10^5 particles. The extended length of the packings is necessary to eliminate recorrelation effects due to the periodic boundary conditions, which could lead to an overestimation of the actual dispersion coefficient.[123] After generation, the packings were discretized using a uniform grid with a spatial resolution of 30 lattice nodes per sphere diameter (Section 1.2).

For the calculation of low Mach-number, single-phase, isothermal fluid flow in the interparticle pore space of the generated packings we utilized the lattice Boltzmann method (LBM), specifically the lattice BGK-model and the D3Q19 lattice (Section 1.3). The no-slip boundary condition was applied at the solid–liquid interfaces and a constant pressure gradient was enforced in the axial direction. For each generated packing simulations were performed over a range of Péclet numbers from $Pe = 5$ to $Pe = 30$, by calculating the velocity field at a certain value of Pe and afterwards scaling the field by multiplication of the fluid velocity at each node of the lattice to get the desired value of Pe. Using velocity field, calculated with LBM, advective–diffusive mass transport was simulated by the means of random walk particle tracking method (Section 1.4) with the number of tracer particles $N = 1.2 \times 10^6$.

3.3 Results and discussion

3.3.1 Porosity distribution of particulate beds in quadrilateral conduits

Random-close packings of uniform, solid (impermeable), spherical particles of diameter d_p were generated in eighteen conduits with different quadrilateral cross section (Table 3.1). The investigated conduit shapes were comprised of three basic and fifteen trapezoidal geometries. Basic geometries included i) quadratic, ii) rectangular with a side-aspect ratio (ratio of width to height) of 2, and iii) rectangular with a side-aspect ratio of 5. From each of these basic geometries five isosceles trapezoids were derived by varying the base angle from $85°$ to $65°$ in steps of $5°$ while maintaining the height of the respective basic geometry (Figure 3.1). All conduits had the same cross-sectional area of $100\,d_\mathrm{p}^2$ to enable quantitative comparisons between the packings. This results in a channel diagonal-to-particle size ratio of ~ 14 for the quadratic conduit, reflecting a typical value for particulate beds in miniaturized HPLC systems.[254,263] The average bed porosity of all packings was chosen as $\varepsilon = 0.48$, a larger value than usually encountered in densely-packed cylindrical fused-silica columns,[263] to account for the fact that column packing in microchip separation channels is not an optimized procedure yet. Most microfluidic chips cannot tolerate high pressure and ultrasonication, both of which are crucial factors to achieve densely packed beds.[254] All packings had a length of $1200\,d_\mathrm{p}$ to exclude the occurrence of recorrelation effects during transient dispersion. Recorrelation effects originate in the repeated experience of macroscopic flow features by tracer molecules traversing the length of the packing more than once. Lateral dimensions and other data of the generated packings are summarized in Table 3.1.

[123] R. S. Maier et al. *Phys. Fluids*, **12**: 2065–2079, 2000.
[263] S. Ehlert, T. Rösler, and U. Tallarek. *J. Sep. Sci.*, **31**: 1719–1728, 2008.

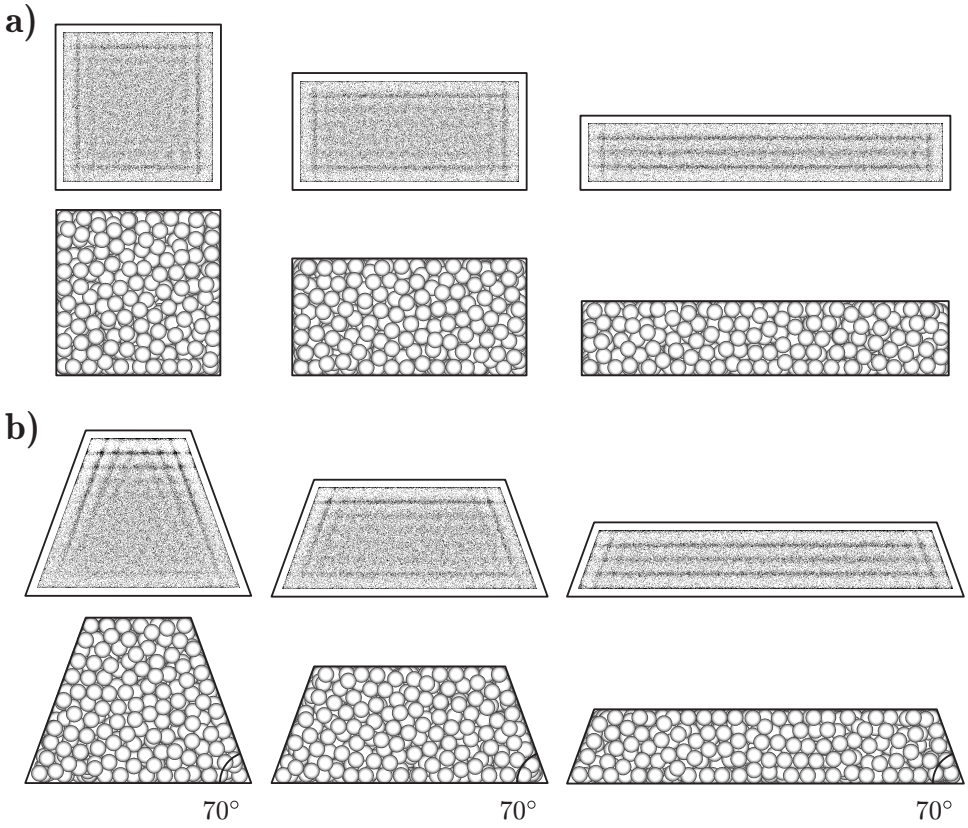

Figure 3.1: Packings of uniform, solid (impermeable), spherical particles confined in quadrilateral conduits. Shown are the front view of the generated packings (bottom rows) and projections of particle centers in a packing onto its front plane (top rows). (a) Basic quadrilateral geometries: quadratic (left), rectangular with side-aspect ratio of 2 (middle), and rectangular with side-aspect ratio of 5 (right). (b) Trapezoidal conduits derived from the basic geometries above by varying the base angle, here set to 70°, while maintaining the height of the basic geometry. All packings have a cross-sectional area of $100\ d_\mathrm{p}^2$, a length of $1200\ d_\mathrm{p}$, and an average bed porosity of $\varepsilon = 0.48$. Details and data for further trapezoidal packings are given in Table 3.1.

Figure 3.1 shows the front view and particle center projections (a) for packings with basic cross-sectional geometry and (b) for trapezoidal packings derived from these geometries by setting the base angle to 70°. The particle center projections (top rows) visualize that particles near the container walls, within a distance of $2\ d_\mathrm{p}$ are highly ordered in all packings. The location of maximum order (corresponding to the highest density of particle centers) is found at a distance of $0.5\ d_\mathrm{p}$ or $1.5\ d_\mathrm{p}$ from the container wall.[213,235] No significant differences are apparent between the particle center projections of the packings with the basic cross-sectional geometries (Figure 3.1a). The observed patterns of the particle centers repeat the shape of the confining conduit.

The rectangular packing with the side-aspect ratio of 5 (Figure 3.1a, right) is distinguished by a higher degree of order along the median, and the same behavior is observed for the trapezoidal packing based on this geometry (Figure 3.1b, right). The particle center projections of the two other trapezoidal packings reveal differences between the top and bottom part of the packings. In the trapezoidal packing based on the rectangle with a side-aspect ratio of 2 (Figure 3.1b, middle), this is indicated by a slightly higher degree of order in the top part of the packing. The trapezoidal packing

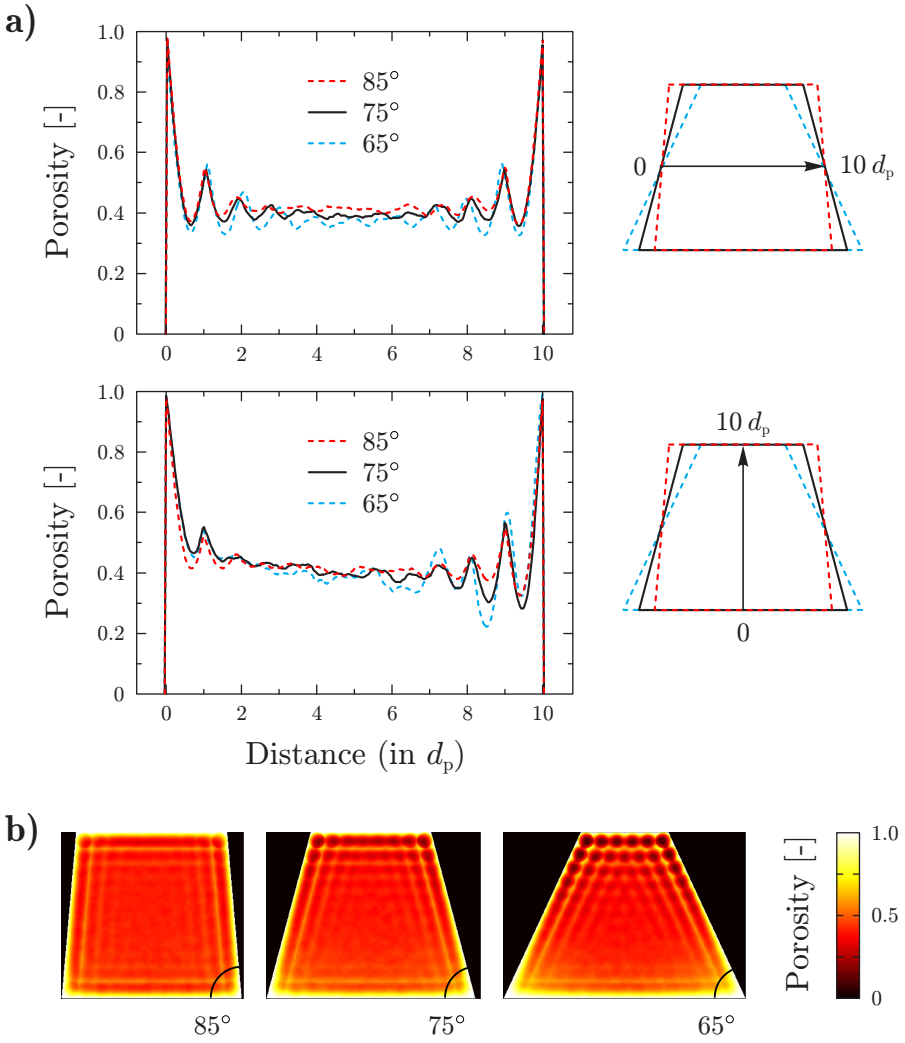

Figure 3.2: Lateral porosity distributions of three trapezoidal packings derived from the quadratic geometry by setting the base angle to 85°, 75° or 65°. (a) Lateral porosity distributions along the median (top) and the symmetry axis (bottom) of the trapezoids, calculated along the indicated arrows over the whole length of a packing. (b) Length-wise averaged two-dimensional representation of the lateral porosity distribution in the packings.

derived from the quadratic geometry (Figure 3.1b, left) not only features a clearly higher order in the top part of the packing, but also a larger extension of this highly ordered area. Comparing the quadratic with its derived trapezoidal packing, it is immediately apparent that the loss of the symmetry axis along the median in the trapezoidal conduit corresponds to a loss of symmetry in the particle center distribution of the packing. The front views of all sphere packings appear similar, regardless of conduit shape, and bear no relation to the respective particle center distributions. This illustrates the fact that cross-sectional images of packings, e.g., obtained by scanning electron microscopy, do not convey information about the porosity distribution or general quality of a packing.

Figure 3.2 analyzes the lateral porosity distribution of trapezoidal packings derived from quadratic geometry for three different base angles. Figure 3.2a shows porosity distribution func-

tions along the median (top) and along the symmetry axis through the mid-points of the bases (central symmetry axis, bottom), calculated by averaging the porosity distribution along the indicated arrows over the whole length of a packing. The porosity distribution along the median is very similar with respect to the central symmetry axis and shows the expected oscillatory behavior with maximal amplitude of the interparticle void fraction close to unity near the container wall that is damped over a range of $3–4\,d_\mathrm{p}$ to a value of ~ 0.4 in the center of the packing.[213,235] With decreasing base angle $85° \rightarrow 65°$ the porosity distribution exhibits more pronounced minima and in general indicates a denser packing. The reason for this trend becomes evident after analyzing the porosity distribution along the central symmetry axis (Figure 3.2a, bottom). There is no symmetry about the median. The porosity at the top of the packing undergoes stronger fluctuations than at the bottom of the packing, with decidedly lower minima, reflecting a more ordered, denser packing of particles in the top part of the conduit compared to the bottom. Thus, there exists a gradient in packing order and bed density along the central symmetry axis. This behavior is apparent in all three packings, but becomes more pronounced with decreasing base angle of the conduit. In Figure 3.2b the length-wise averaged lateral porosity distributions of the packings are shown as color-coded projections. Regions of high porosity are present in the bottom base corners, and their extension and local porosity increase with decreasing base angle of the conduit. The occurrence of these high-porosity regions in and near the bottom corners of the conduit is counterbalanced by a lower local porosity (higher bed density) in the top part of the packing to maintain the average bed porosity of $\varepsilon = 0.48$ common to all packings.

As analyzed previously for quadratic and rectangular cross-sectional geometries (Chapter 2), the corners of a conduit reduce the number of possible particle positions close to the corners which effects a stronger porosity fluctuation in the corner areas compared to the rest of the packing. The presence of corners was thus the main influence on the porosity distribution of noncylindrical compared to cylindrical packings. In this chapter, all conduit geometries are quadrilateral and have the same number of corners. An isosceles trapezoid contains two different pairs of corners, the top corners with an angle $> 90°$ and the bottom corners with an angle $< 90°$ (cf. Figure 3.1 and Figure 3.2), but the porosity distribution does not seem to be influenced so much from the non-orthogonal corners but from the limitation of available space near the top of the trapezoidal conduits. The reduced available space in the top part of a packing imposes restrictions on the possible location of particles which results in a locally higher ordering reflected by stronger fluctuations in the porosity distribution.

3.3.2 Fluid flow velocity fields

Figure 3.3 presents color-coded fluid flow velocity profiles for nine trapezoidal packings calculated at a Péclet number (Pe) or reduced velocity of $Pe = u_\mathrm{av} d_\mathrm{p} / D_\mathrm{m} = 10$, where u_av is the average velocity through a packing and D_m is the bulk molecular diffusion coefficient. The images of the left column which represent trapezoidal packings based on quadratic geometry closely correspond to the lateral porosity distributions of Figure 3.2b. We have already shown for quadratic, rectangular, and semicircular conduits that regions of high local porosity in a packing become channels of advanced fluid flow (Chapter 2). All nine investigated trapezoidal packings exhibit these rapid-

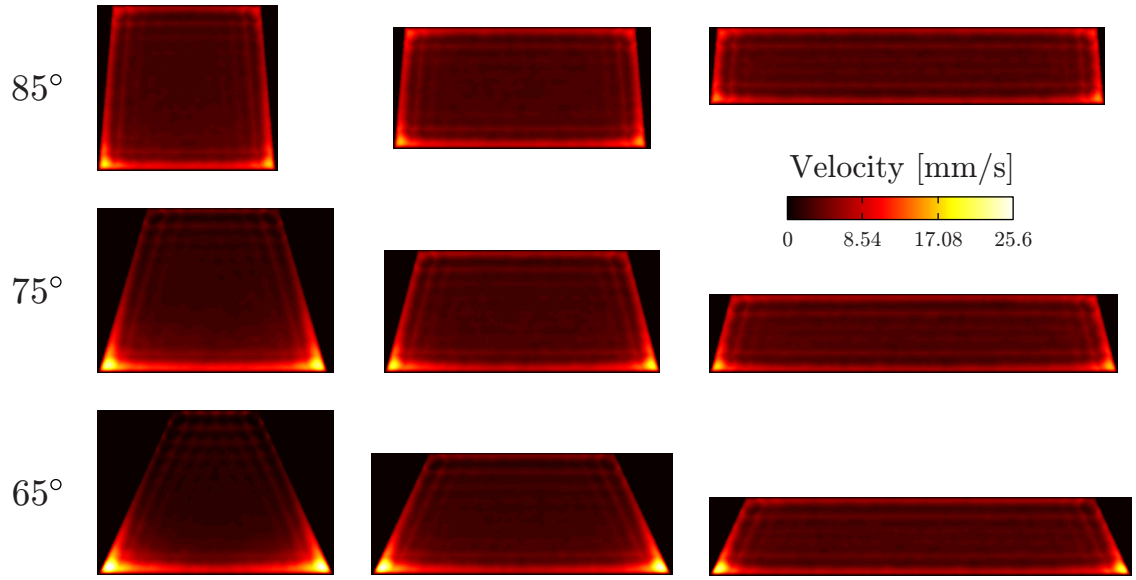

Figure 3.3: Fluid flow velocity profiles at $Pe = 10$ for nine trapezoidal sphere packings with average bed porosity of $\varepsilon = 0.48$. The trapezoidal conduit shapes were derived from quadratic (left) and rectangular geometries with a side-aspect ratio of 2 (middle) or 5 (right). Base angles of the trapezoidal cross sections are given on the far left.

flow channels in bottom corners of the conduits (base angle $< 90°$), but both, the actual velocity in these channels as well as their extension, increase with decreasing base angle ($85° \rightarrow 65°$) and with decreasing side-aspect ratio ($5 \rightarrow 1$) of the basic geometry (from top to bottom and right to left in Figure 3.3). While the area of maximum velocity resides in the bottom base corners, the area of minimum velocity is not as easily located. Cylindrical, quadratic, and rectangular packings all have their area of minimum velocity around the packing center with an extension that depends on the actual channel-to-particle size ratio, but this is not the case for the presented trapezoidal packings. Here, due to the locally increased density and order in the top part of the packing (Figure 3.2) the lowest velocities are observed at about $0.5\,d_\mathrm{p}$ from the top base of the trapezoidal conduits, however, their exact location depends on a particular geometry.

The dependence of the velocity distributions on the base angle of the conduit and the side-aspect ratio of the basic geometry the respective trapezoidal cross section was derived from is analyzed in more detail in Figure 3.4. Figure 3.4a depicts velocity probability distribution functions at $Pe = 10$ for trapezoidal packings based on the quadratic geometry. These functions represent the probability of finding a certain axial velocity inside the whole packing (black), the top part of the packing (red), and the bottom part of the packing (blue). At first glance, the velocity distributions for the top and bottom part of the trapezoidal packing with a base angle of $85°$ (Figure 3.4a, top) seem to differ very little from each other, but they already show the characteristics that are becoming more pronounced with decreasing conduit base angle. There is a higher probability of finding higher fluid velocities in the bottom part of the packings, and the differences in the velocity distributions of top and bottom part increase with decreasing base angle ($85° \rightarrow 65°$) of the trapezoidal conduit and decreasing side-aspect ratio ($5 \rightarrow 1$) of the basic geometry (Figure 3.4b). If we compare the differences between top and bottom part velocity distributions of all nine

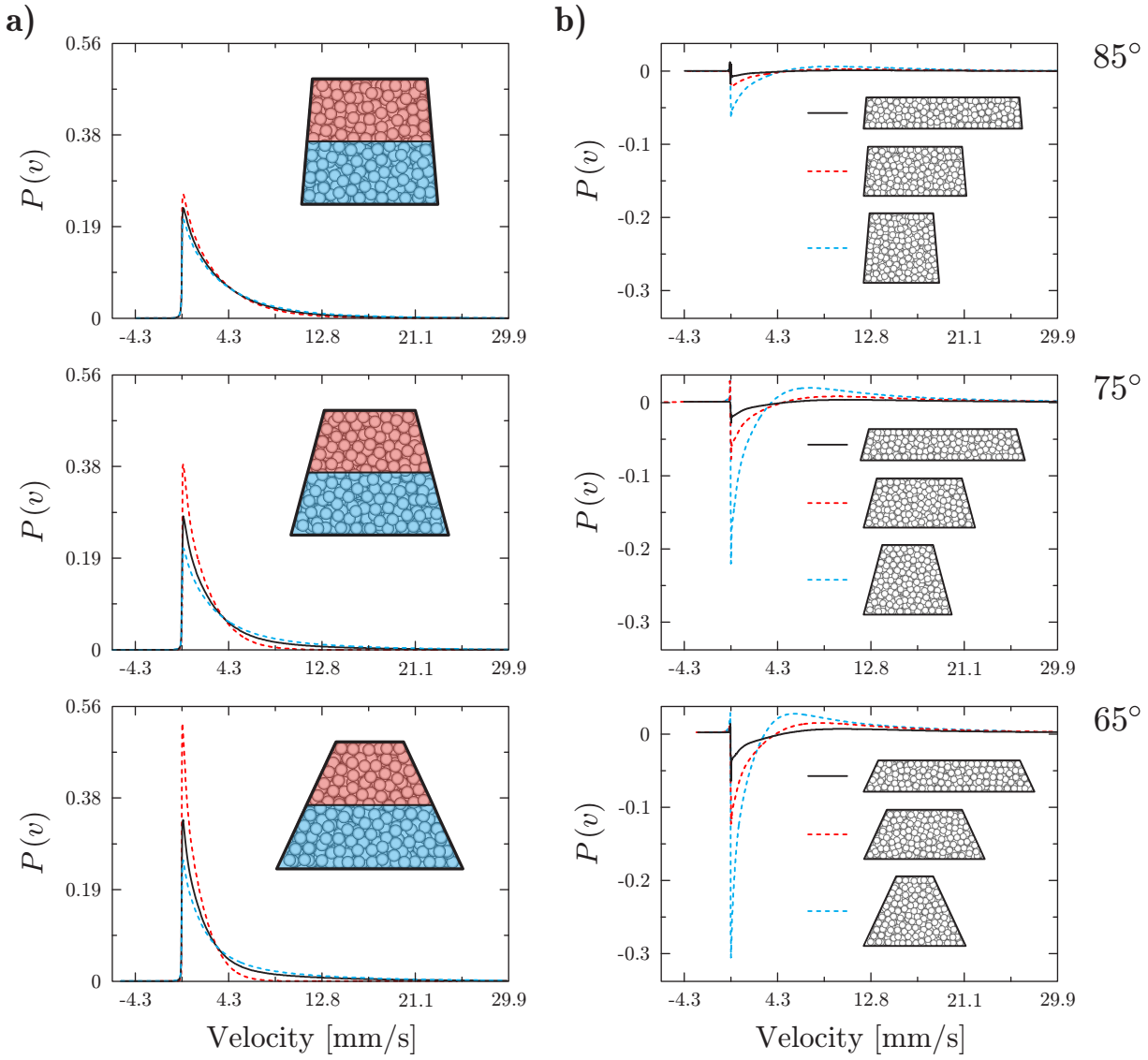

Figure 3.4: (a) Velocity probability distribution functions at $Pe = 10$ for three trapezoidal packings derived from the quadratic geometry by setting the base angle to $85°$ (top), $75°$ (middle), or $65°$ (bottom). Functions representing the whole packing (black), the top part of the packing (red), and the bottom part of the packing (blue) are plotted separately. It is evident that the velocity probability functions of the top part and the bottom part of the packings increasingly deviate from each other with decreasing base angle of the trapezoidal conduit, i.e., with increasing deviation of the conduit shape from quadratic geometry. (b) Differences in velocity probability distribution functions between the top and bottom part of the trapezoidal packings with a conduit base angle of $85°$ (top), $75°$ (middle), and $65°$ (bottom). Packings whose conduit shape was derived from quadratic geometry show larger differences between top and bottom part distribution functions than trapezoidal packings derived from rectangular geometries.

investigated trapezoidal packings, it is apparent that the side aspect ratio of the basic geometry the trapezoid was derived from has a larger influence than the base angle of the conduit.

3.3.3 Hydrodynamic dispersion

In Figures 3.5 and 3.6 we investigate the efficiencies of the generated packings in terms of hydrodynamic dispersion. Normalized axial dispersion coefficients $D_{\mathrm{ax}}/D_{\mathrm{m}}$ were calculated from the displacement of inert tracer molecules at reduced velocities ranging from $Pe = 5$ to $Pe = 30$. For all nine trapezoidal packings depicted in Figure 3.5 axial dispersion grows monotonically with Pe, but the slope of the curves depends on the base angle of the conduit and the side-aspect ratio of the basic geometry the trapezoid was derived from. Trapezoidal conduits based on rectangular geometries show not only a weaker dependence of $D_{\mathrm{ax}}/D_{\mathrm{m}}$ on Pe, but this dependence is also less influenced by the base angle of the conduit. Basing the cross-sectional geometry of a trapezoidal conduit on a larger rather than on a lower side-aspect ratio rectangle is obviously advantageous. Trapezoidal conduits derived from quadratic geometry differ clearly from their rectangular-based counterparts. While a small deviation from orthogonality results in similar dispersion for the investigated rectangular-based packings, axial dispersion in quadratic based trapezoidal packings is strongly affected by increasing deviation of the conduit base angle from orthogonality.

In our comparison of trapezoidal packings with constant cross-sectional area, both geometric factors, base angle and side aspect ratio of the basic geometry, can be jointly expressed by the base-aspect ratio a/c (a: bottom or longer base length, c: top or shorter base length). This parameter is a measure for the deviation of a trapezoidal shape from regular rectangular geometry, or for the inequality between top base and bottom base length. With increasing base-aspect ratio, i.e., with increasing difference between top and bottom base length, porosity and velocity inhomogeneities between the top and bottom part of the packing increase (Figures 3.2–3.4), resulting in larger axial dispersion coefficients compared to regular rectangular conduits (Figure 3.5).

In Figure 3.6, we finally present normalized axial dispersion coefficients for all generated eighteen packings in dependence of the base angle (Figure 3.6a) and as a function of the base-aspect ratio (Figure 3.6b). $D_{\mathrm{ax}}/D_{\mathrm{m}}$ was calculated at a reduced average velocity of $Pe = 10$. If we first compare the regular orthogonal conduits, we find that the quadratic geometry has a slight advantage over the rectangle with a side-aspect ratio of 2, and both geometries result in smaller axial dispersion coefficients for packed beds than the rectangular conduit with a side-aspect ratio of 5. For regular orthogonal conduits axial dispersion can be conclusively analyzed by the "equilibration length" of a flow field. Based on the underlying porosity distribution which is intimately related to a particular conduit geometry, this length characterizes the lateral distance through a packing that needs to be covered to realize equilibration, i.e., a complete exchange between different velocities of the resulting flow field. With consideration of the actual symmetry it refers to the longest distance between different velocities, and is thus equal to half the diagonal of the regular orthogonal conduits, where maximum velocities are found in the corners and the minimum velocity is located around the center of a conduit (Chapter 2). The larger axial dispersion coefficient of the rectangular packing with larger side-aspect ratio reflects the longer half-diagonal distance of this conduit (Table 3.1).

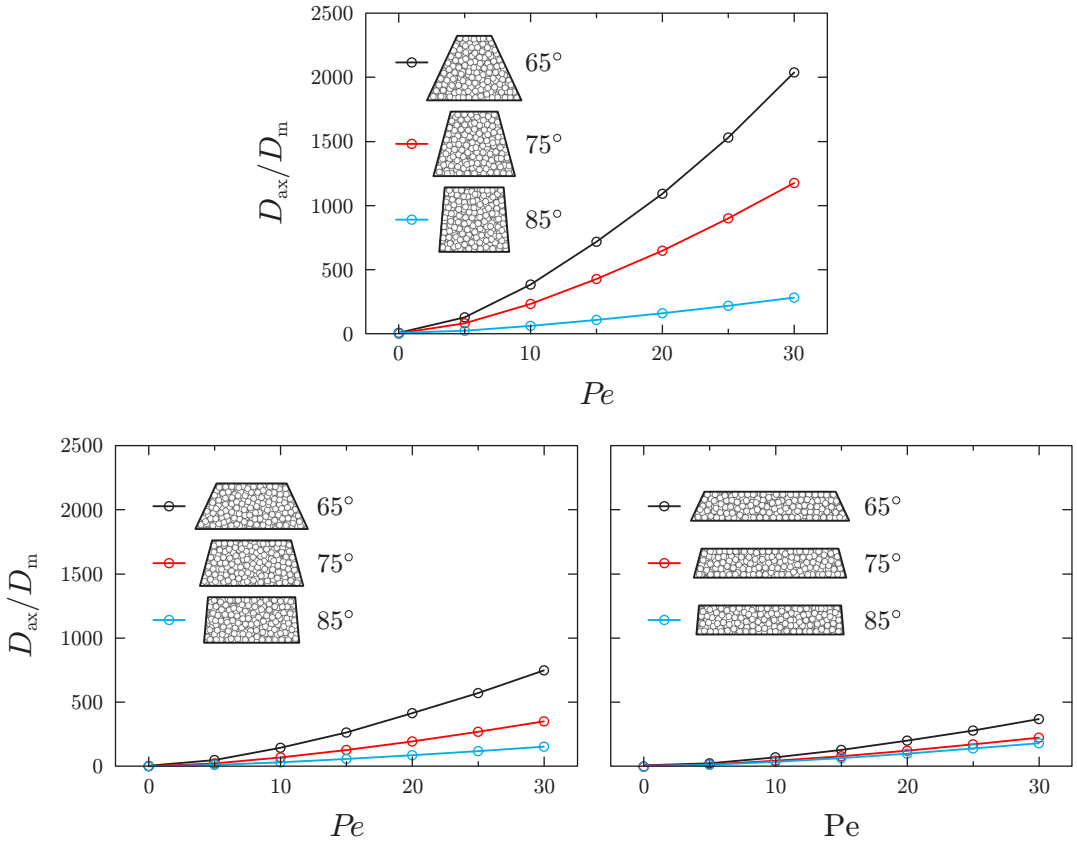

Figure 3.5: Normalized axial dispersion coefficients of an inert tracer as a function of the Péclet number (Pe) or reduced velocity $Pe = u_{av} d_p / D_m$ (where $u_a v$ is the average velocity through a packing and D_m is the bulk molecular diffusion coefficient) for nine trapezoidal sphere packings derived from quadratic (top) or rectangular geometries (bottom left: side-aspect ratio 2, bottom right: side-aspect ratio 5).

With the deviation from orthogonality of the conduit corners and the beginning of differing top and bottom base lengths the characteristic lateral equilibration length of a packing geometry becomes only a side issue. At a bottom base angle of 85° it is the reason why the trapezoidal packing derived from the large side-aspect ratio rectangle still has a slightly larger axial dispersion coefficient than the trapezoidal packing based on the rectangle with a side-aspect ratio of 2. It is to be noted that the characteristic length scale for lateral equilibration in the trapezoidal conduits differs from those of the regular orthogonal conduits. We have seen in Figure 3.3 that the location of maximum flow velocity is found in the bottom base corners, but the location of minimum flow velocity is near the top base. Therefore the characteristic length for lateral equilibration, i.e., the longest distance between different velocities in the smallest geometrical subunit of the packing cross section, which in trapezoidal packings is obtained by cutting the bed along the central symmetry axis from top to bottom base, is equal to the distance between the mid-point of the top base and the bottom base corner (Table 3.1). The quadratic-based trapezoidal packing exhibits a decidedly larger axial dispersion coefficient than its rectangular-based counterparts at a bottom base angle of 85° despite the fact that its characteristic lateral equilibration length is smaller than that of the trapezoidal packing based on the large side-aspect ratio rectangle. It demonstrates that in this case

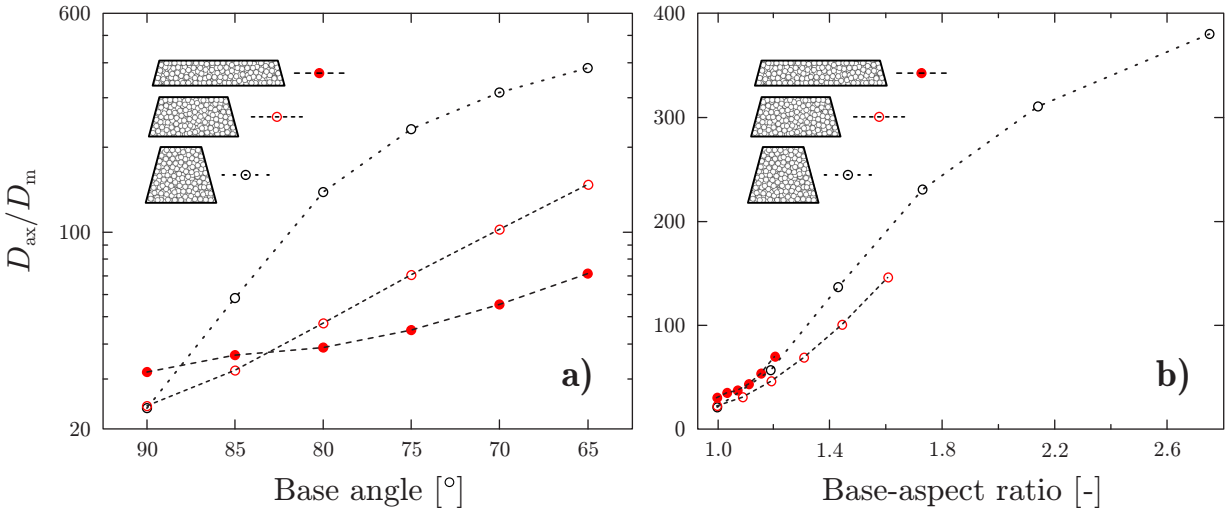

Figure 3.6: Normalized axial dispersion coefficients of an inert tracer at $Pe = 10$ for all investigated sphere packings (a) as a function of the base angle of the quadrilateral conduits and (b) as a function of their base-aspect ratio (ratio of bottom base to top base length).

the actual amplitude of heterogeneities (intensity of dissimilarity between top part and bottom part of a trapezoidal packing), expressed by the relatively high base-aspect ratio of the quadratic-based trapezoidal packing (Table 3.1), and not the length over which disequilibrium exists, becomes the dominating factor for dispersion.

For trapezoidal packings the dominating influence of the conduit shape on packing homogeneity is the ratio of the bottom base length to the top base length. With increasing value of this base-aspect ratio, i.e., with increasing inequality between top base and bottom base length, there is less space available for the positioning of particles near the top base than near the bottom base. The column-to-particle diameter ratio (particle-aspect ratio) of conventional cylindrical columns would have to be replaced in quadrilateral conduits with the ratio of the conduit wall-to-wall-distance to the particle diameter. Contrary to regular rectangular geometries, this ratio is not a constant in trapezoidal conduits, but a series of values increasing from the smaller top base to the larger bottom base. Limited space for particle packing results in more ordered regions with higher fluctuations of local porosity. This is known for cylindrical packings with small column-to-particle diameter ratio,[235] but equally applies to regions of trapezoidal packings with a small conduit wall-to-wall–distance-to-particle diameter ratio (Figures 3.1 and 3.2). Compared to the basic quadratic packing with a particle-aspect ratio of 10 over the whole height of the packing, we find for the derived trapezoidal packing with base angle of $65°$ a particle aspect ratio of only ~ 5 at the top and of ~ 15 at the bottom of the packing. The particle-aspect ratio in the rectangular packing with large side-aspect ratio is $\sim$22, and in the derived trapezoidal packing with base angle of $65°$, the particle-aspect ratio is $\sim$20 at the top and $\sim$24 at the bottom. The efficiency of packings in quadrilateral conduits with large side-aspect ratio is much less affected by deviations from orthogonality of the conduit corners, because the base-aspect ratio of this conduit geometry increases slowly with decreasing base angle.

Figure 3.6 visualizes that axial dispersion in all investigated quadrilateral particulate packings grows monotonically with decreasing bottom base angle (increasing base-aspect ratio) of the

conduit, but that the slope of the curve becomes larger with decreasing side-aspect ratio of the basic geometry. It therefore appears advantageous with regard to the efficiency of particle-packed trapezoidal microchannels to base the cross-sectional geometry of the channel on a rectangle with large side-aspect ratio and to limit the deviation of the corner angles from orthogonality to a maximum of 10°. If, on the other hand, geometries with regular orthogonal conduits can be manufactured, the quadratic geometry gains a slight advantage and rectangular conduits become increasingly unfavorable as their side-aspect ratio increases. However, a high degree of precision is required in manufacturing a regular quadratic conduit because already a 5° deviation from orthogonality makes the resulting trapezoid less favorable than trapezoidal channels derived from rectangular geometries (Figure 3.6).

3.4 Conclusions

We have presented a quantitative numerical analysis approach to investigate the lateral porosity distribution, fluid flow field, and axial hydrodynamic dispersion in particulate beds fixed in conduits with quadrilateral shape, with emphasis on trapezoidal geometries. We have shown that trapezoidal packings differ significantly from quadratic or rectangular packings. The dominating influence of the trapezoidal conduit geometry is the inequality between top and bottom base length, resulting in a decreasing number of possible particle positions from the larger bottom base to the smaller top base of the conduit. The limitations of restricted space in the top part of the trapezoidal conduits effect a more ordered, denser packing structure with stronger fluctuations of local porosity, while the packing structure in the bottom part of the conduit is less ordered with regions of maximum porosity in the bottom base corners. The loss of a symmetry axis in going from a regular rectangular to a trapezoidal conduit is immediately reflected in the lateral porosity distribution and the accompanying fluid flow field. In all investigated quadrilateral packings, channels of advanced fluid flow reside in the high-porosity corners of the conduit. In the bottom base corners (base angle $< 90^{\circ}$) of trapezoidal packings, however, these channels are more extended than in regular orthogonal packings, while the channels in the top corners are much less developed. Axial dispersion in packings with regular orthogonal cross-sectional geometries is affected by the channels of advanced fluid flow in the conduit corners and reflects the different characteristic lengths of the conduits for lateral equilibration (equal to half their diagonal). In trapezoidal packings axial dispersion is primarily influenced by the base-aspect ratio of the conduit. An increasing base-aspect ratio of the conduit increases the porosity difference between the more ordered, denser packed top part and the less-ordered bottom part as well as the extension of and flow velocity in the bottom base corners, resulting in increased axial dispersion. The presented data lead to the conclusion that for trapezoidal packings composed of uniform, solid (impermeable), spherical particles, a channel design with a small base-aspect ratio, i.e., with its cross section as close as possible to a large side-aspect ratio rectangle, is with regard to efficiency preferable over a trapezoidal channel of comparable height and width.

Chapter 4

Reconstructed HPLC Microchip

This chapter is dedicated to the hydrodynamic dispersion in packings of "real life" cross-sectional shape: sphere packings are generated in containers with the cross section reconstructed from a high-resolution SEM image of a real HPLC-microchip. In addition, average packing porosity and particle-size distribution were estimated from experimentally determined values. Results presented in this chapter were published in the journal *Analytical Chemistry* in 2009.[39]

4.1 Introduction

In recent years, the miniaturization of analytical techniques and their implementation on microfabricated devices (chips) has been a focus of research, triggered particularly by the requirements of small sample volumes and high throughput in the "omics" era.[8,264,265] Liquid chromatography has been successfully miniaturized in the form of micro- and nanoflow HPLC,[250,266,267] but the implementation on the chip has proven to be tedious, mostly for reasons related to pressure: the difficulty of generating high pressure with on-chip integrated pumps as well as of fabricating high-pressure rating microchips. Consequently, on-chip liquid chromatography is underdeveloped, not only compared to other chip-based analytical techniques but also in view of the importance of HPLC as an analytical technique. The existing LC-microchips differ widely in i) the materials and methods used for their fabrication, ii) their grade of integration, i.e., in the number and kind of instrumental elements contained on the chip, and iii) their chromatographic separation elements which encompass particulate and monolithic packed beds, open tubulars, and microfabricated pillar arrays.[231,256] Contrary to the cylindrical stainless-steel columns or fused-silica capillaries of analytical and miniaturized HPLC, microchips contain noncylindrical separation channels whose cross-sectional shapes depend on the material and method used for their fabrication. Separation

[39] S. Khirevich et al. *Anal. Chem.*, **81**: 4937–4945, 2009.
[8] S. Koster and E. Verpoorte. *Lab Chip*, **7**: 1394–1412, 2007.
[264] P. S. Dittrich and A. Manz. *Nat. Rev. Drug Discovery*, **5**: 210–218, 2006.
[265] K. Ohno, K. Tachikawa, and M. Manz. *Electrophoresis*, **29**: 4443–4453, 2008.
[250] J. Hernández-Borges et al. *J. Sep. Sci.*, **30**: 1589–1610, 2007.
[266] G. P. Rozing. *LC-GC Eur.*, **16**: 14–19, 2003.
[267] J. M. Saz and M. L. Marina. *J. Sep. Sci.*, **31**: 446–458, 2008.
[231] D. S. Peterson. *Lab Chip*, **5**: 132–139, 2005.
[256] M. De Pra, W. Th. Kok, and P. J. Schoenmakers. *J. Chromatogr. A*, **1184**: 560–572, 2008.

channels on recent LC-microchips have approximately semicircular,[9,223] elliptical,[10] quadratic,[225] rectangular,[11,268] or trapezoidal cross sections[5,12,227,229,269,270] which deviate from the ideal geometries with features such as, e.g., curved sides, rough edges, and irregularly angled corners. The pressure sensitivity of most microchips prohibits the use of high pressure and ultrasound for particle packing, so that packing densities comparable to those of capillary HPLC columns cannot be expected. The noncylindrical and nonideal cross-sectional geometry as well as the relatively high interparticle porosities should affect the quality of particulate microchip packings, but the subject has not received much attention.[14] This is partly due to the fact that the majority of existing LC-microchips is still experimental in character and that the aim is more often set toward integration rather than performance.

Previously, our group has addressed the question of how the noncylindrical conduit geometry of particulate HPLC-microchip packings influences axial dispersion, and thus the efficiency of the chromatographic separation, through numerical simulation (see Chapters 2 and 3) as well as experimental studies.[103,254] The issues investigated up to now were the presence of corners in the conduit, the symmetry of the conduit cross section (Chapter 2), the base angle and base-aspect ratio (i.e., the ratio of the longer base length to the shorter base length) in isosceles trapezoidal conduits (Chapter 3), the average interparticle porosity of the packings and the optimal packing conditions,[254] the particle-aspect ratio (ratio of conduit cross-sectional size to particle size),[103] and the particle-size distribution of the packing material.[103]

In our previous numerical simulation studies (Chapters 2 and 3), the modeled packings consisted of hard, impermeable spheres of uniform diameter (monodisperse packings) confined in conduits with regular cross-sectional geometries. To approach real-life conditions, the confined sphere packings generated in this study were modeled after real-life HPLC-microchip packings,[103,254] by reconstructing i) the actual cross-sectional geometry of the microchannel, ii) the particle-size distribution of the packing material, and iii) the average interparticle porosity of the packings (packing density).

Figure 4.1 is a schematic representation of the basic elements and flow of information in this work. Our study is based on a prototype HPLC/UV-microchip that integrates sample injection, chromatographic separation, and UV detection. Figure 4.1 (top right) shows the experimental setup in which the sample injection end of the microchip is placed between the stator and rotor of

[9] K. W. Ro, J. Liu, and D. R. Knapp. *J. Chromatogr. A*, **1111**: 40–47, 2006.
[223] I. M. Lazar, P. Trisiripisal, and H. A. Sarvaiya. *Anal. Chem.*, **78**: 5513–5524, 2006.
[10] D. S. Reichmuth, T. J. Shepodd, and B. J. Kirby. *Anal. Chem.*, **77**: 2997–3000, 2005.
[225] Y. Yang et al. *Lab Chip*, **5**: 869–876, 2005.
[11] J. Liu et al. *Anal. Chem.*, **81**: 2545–2554, 2009.
[268] A. Bhattacharyya and C. M. Klapperich. *Anal. Chem.*, **78**: 788–792, 2006.
[5] H. Yin et al. *Anal. Chem.*, **77**: 527–533, 2005.
[12] C.-Y. Shih et al. *J. Chromatogr. A*, **1111**: 272–278, 2006.
[227] A. Ishida et al. *J. Chromatogr. A*, **1132**: 90–98, 2006.
[229] J. Liu et al. *Int. J. Mass Spectrom.*, **259**: 65–72, 2007.
[269] J. F. Borowsky et al. *Anal. Chem.*, **80**: 8287–8292, 2008.
[270] M. T. Koesdjojo, C. R. Koch, and V. T. Remcho. *Anal. Chem.*, **81**: 1652–1659, 2009.
[14] G. P. Rozing et al. *J. Sep. Sci.*, **27**: 1391–1401, 2004.
[103] S. Jung et al. *J. Chromatogr. A*, **1216**: 264–273, 2009.
[254] S. Ehlert et al. *Anal. Chem.*, **80**: 5945–5950, 2008.

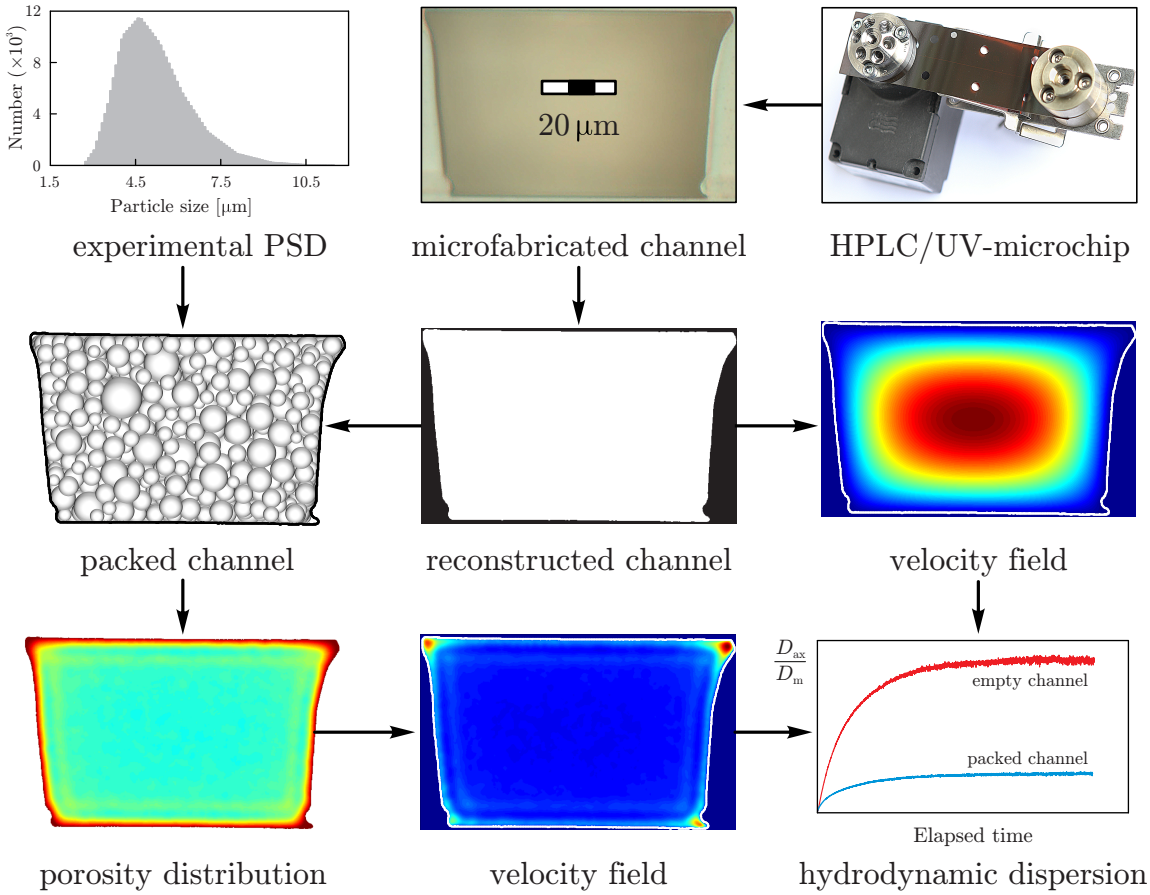

Figure 4.1: Schematic representation of the basic elements and flow of information in this study. Top row (from right to left): prototype HPLC/UV-microchip placed between the stator and rotor of a Rheodyne valve (left) and a special holder (right) for connection to a diode array UV-detector; high-resolution image of the unpacked separation channel on this microchip; number-based particle-size distribution of the packing material. Middle row: reconstructed cross section of the microchannel (middle); lateral velocity distribution in the empty reconstructed microchannel (right); cross section of a reconstructed microchip packing (left). Bottom row: lateral porosity (left) and velocity distribution (middle) in a reconstructed microchip packing; time-dependent axial dispersion in the empty and particle-packed reconstructed microchannel (right).

a Rheodyne valve (left), and the end containing the UV-detection cell is fixed by a holder (right) for connection to a diode array UV detector. The cross-sectional geometry of the microchip separation channel (top row, middle) was reconstructed for the simulations (middle row, middle) and packed with particles whose diameters matched the experimentally determined particle-size distribution of the packing material (top row, left). Several packings at bed porosities (average interstitial void volume or interparticle porosity) between $\varepsilon = 0.42$ and $\varepsilon = 0.48$ were generated (middle row, left) and analyzed with regard to their lateral porosity distributions (bottom row, left). The lateral velocity distribution in the generated packings (bottom row, middle) as well as in the empty channel (middle row, right) was calculated from the respective 3D velocity fields. Evolution of the axial dispersion coefficient over time was studied in packed and empty channels (bottom row, right), and simulated dispersion data were compared to experimental separation efficiencies of the HPLC/UV-microchips.

4.2 Experimental section

All details concerning the prototype HPLC/UV-microchips are described in previous publications of our group.[103,254] The term prototype refers to the fact that these microchips were specially fabricated for our research with a UV-detection cell. They are, however, very similar to the commercially available HPLC/MS-microchips which contain an emitter needle for coupling to ESI-MS (electrospray ionization mass spectrometry).[5] For convenience, the salient points are briefly described here.

The separation channels on these prototype HPLC/UV-microchips (Agilent Technologies, Waldbronn, Germany) were slurry-packed by applying pressures between 150 and 300 bar, with or without the assistance of ultrasound. The packing material was $5\,\mu$m Zorbax SB-C18 (Agilent Technologies, Waldbronn, Germany) with a mean intraparticle pore size of 80 Å and a Sauter mean diameter of $5.51\,\mu$m.[263] Dry particles were suspended in tetrahydrofuran, and methanol was used as the pushing solvent. Interparticle porosities were determined by inverse size-exclusion chromatography of a suitable polystyrene standard in methylene chloride with UV detection at 230 nm.[103,254,263] Separation efficiencies were analyzed by isocratic elution of a mixture of five alkylbenzenes (containing uracil as the dead-time marker) with $80/20$ (v/v) acetonitrile/water and UV detection at 210 nm. Plate heights for the pentylbenzene peak ($k' = 3.5$) were calculated with the Agilent ChemStation software and found, not at least due to the high symmetry of the peaks, to be practically identical to those obtained by the independently applied method of moments (via the second central moment). Axial dispersion coefficients (D_{ax}) were calculated from plate heights (H) and the average mobile phase velocity (u_{av}) through $D_{\mathrm{ax}} = H u_{\mathrm{av}}/2$ and were normalized by D_{m}, the diffusion coefficient of the tracer in the bulk mobile phase. For pentylbenzene in $80/20$ (v/v) acetonitrile/water, we used $D_{\mathrm{ax}} = 1.5 \times 10^{-9}$ m^2/s.[271] All data were acquired at 298 ± 1 K with an Agilent 1200 liquid chromatograph, including degasser, nanopump, and a diode array UV detector.

4.3 Numerical section

Simulation of hydrodynamic dispersion in the reconstructed microchip packings involved three successive steps: i) generation of confined, polydisperse random sphere packings, ii) calculation of the 3D fluid flow field in the generated packings, and iii) simulation of advective–diffusive mass transport in the generated packings and corresponding flow fields. Simulation methods are described in Chapter 1. In the following, we report only the specific alterations and adjustments made for this work.

The cross-sectional shape of the conduit was reconstructed from a high-resolution optical microscope image (15 pixels/μm) of the cross section of an empty HPLC-microchip separation channel (Figure 4.1). Each pixel in the image was assigned to either one wall or one void node of the lattice, followed by downsizing the lattice to a lateral resolution of ~ 8 pixels/μm. Downsizing was necessary to fit the lattice into the memory of the available supercomputers, but sufficient grid

[263] S. Ehlert, T. Rösler, and U. Tallarek. *J. Sep. Sci.*, **31**: 1719–1728, 2008.
[271] J. Li and P. W. Carr. *Anal. Chem.*, **69**: 2530–2536, 1997.

resolution for the accurate simulation of fluid flow was maintained.[272] The number-based particle-size distribution of $5\,\mu m$ Zorbax SB-C18, the material used for slurry-packing of the HPLC/UV-microchip separation channels, is also shown in Figure 4.1 (top row, left). This experimentally determined log-normal distribution was discretized for the simulations with a step size of $0.10\,\mu m$. The grid resolution was 19.8 nodes for $d_{p,min} = 2.72\,\mu m$ (smallest particles in the distribution) and 34.1 nodes per $d_p(N_{max}) = 4.69\,\mu m$ (maximum of the distribution). Final dimensions of the lattice (computational domain containing the packing) were $617 \times 378 \times 99\,000$ nodes (in the x, y, and z-directions, respectively), corresponding to $18.1\ d_p(N_{max}) \times 11.1\ d_p(N_{max}) \times 2903\ d_p(N_{max})$.

Confined random sphere packings were generated with bed porosities of $\varepsilon = 0.42$, 0.44, 0.46, and 0.48. The necessary amount of solid spheres for each packing of a certain bed porosity ε was calculated, and a corresponding set of particle diameters was generated from the experimentally determined particle-size distribution. For each bed porosity, five packings were generated from five different initial random positions of particle centers (seeds), resulting in a total of 20 generated sphere packings. Lateral porosity distributions presented in the figures refer to one specific packing at the indicated bed porosity, while axial dispersion coefficients represent the average value calculated from all five packings of a given bed porosity.

The lattice Boltzmann method (Section 1.3) was used for the simulation of low Reynolds-number flow of an incompressible fluid within the interparticle space of the generated packings. For the computational domain described above, we employed a 3D lattice with 19 links at each lattice node resulting in a lattice size of ~ 2 TB. The no-slip boundary condition (realized by the "bounce-back" scheme) at solid–liquid interfaces and periodic boundary conditions along the z-axis were applied to the lattice nodes.

The simulation of one fluid flow velocity field in a reconstructed microchip packing required 3000 LBM iterations, 3 TB memory space, and took ~ 1.5 h on 8192 processor cores of an IBM Blue Gene/P system. For each packing, the velocity field was first calculated at a low Péclet number, $Pe = u_{av} d_p / D_m$ (where u_{av} is the average fluid flow velocity through a packing and D_m is the bulk diffusion coefficient of the tracer particles, see below), and velocity fields at average velocities of up to $Pe = 140$ were subsequently received by linear rescaling. For calculating Pe, we used the Sauter mean diameter of the packing material ($d_p = 5.51\,\mu m$).

Mass transport in the generated packings and fluid flow velocity fields was simulated by a random walk particle tracking technique, which is described in Section 1.4. Hydrodynamic dispersion coefficient was calculated as described in Subsection 1.4.3.

4.4 Results and discussion

4.4.1 Unpacked microchip

Figure 4.2 shows the cross section of the unpacked separation channel on the HPLC/UV-microchip (top left) and its reconstruction for the simulations (white circumference, top right). The HPLC/UV-microchip is fabricated from three layers of polyimide film using direct laser ablation to define

[272] D. Kandhai et al. *Philos. Trans. R. Soc. A*, **360**: 521–534, 2002.

channels and holes followed by thermal pressure lamination of the three films. The side-walls of the separation channel originate from the middle polyimide layer (of $50\,\mu m$ thickness), while the bottom and top of the channel originate from two polyimide layers of $125\,\mu m$ thickness each. The separation channel (Figure 4.2, top left) has a length of ~ 75 mm and an approximately trapezoidal cross section with dimensions of $68\,\mu m$ (bottom base) $\times$ $82\,\mu m$ (top base) $\times$ $50\,\mu m$ (height) resulting in a cross-sectional area of $3750\,\mu m^2$. Deviations from regular trapezoidal geometry are the result of the fabrication process. Laser defocusing effects produce slanted walls and curved sides (Gaussian profile of the spatial energy distribution of the laser) and the deposition of ablated and laminated material leads to irregularly angled corners. Each corner in the microfabricated channel is different, so that the symmetry of an isosceles trapezoid (around the middle axis) is lost.

As a starting point, flow and transport were simulated in the empty reconstructed microchannel. The lateral distribution of axial velocity (simulated at an average velocity of 3 mm/s) reflects the parabolic profile of laminar flow (Figure 4.2, top right). Normalized axial dispersion coefficients D_{ax}/D_m were calculated as a function of the average microchannel velocity (u_{av}) and compared to experimental data collected with several unpacked HPLC/UV-microchips, using pentylbenzene as a nonadsorbing tracer (with respect to the channel walls) in a $80/20$ (v/v) acetonitrile/water mobile phase (Figure 4.2, bottom). Simulated data were fitted to the following equation based on Taylor–Aris dispersion in pressure-driven flow between two parallel plates[150]

$$\frac{D_{ax}}{D_m} = 1 + \left(\frac{f}{210}\right) Pe^2, \tag{4.1}$$

where Pe is the Péclet number or reduced velocity here defined for the empty channel, $Pe = u_{av}L/D_m$ (with L, a characteristic transverse dimension). f is a function of the exact cross-sectional geometry of the channel, which for a trapezoid depends on the ratio h/w_l of its height h over the larger base width w_l (top base in Figure 4.2) and the base angle; it is unity for the parallel-plate geometry.

We obtained a value of 2.62 for f from fitting our simulated data to equation (4.1) (see Figure 4.2, bottom) using the channel height ($h = 50\,\mu m$) as the characteristic transverse dimension. According to Dutta et al.,[150] a conduit with ideal trapezoidal cross-sectional geometry, a base angle of 82°, and a ratio w_s/h of the smaller base width (w_s) to its height of 1.00 would give a value of 2.01 for f (cf. Figure 6 in Reference [150]). Assuming an idealized isosceles trapezoidal geometry for the reconstructed channel cross section, the ratio w_s/h would be 1.36 ($68\,\mu m/50\,\mu m$), which would increase the value for f only slightly. The increased f-value of the reconstructed channel can be explained by the presence of four different, irregularly angled corners, which not only reduces the symmetry of the conduit cross section but introduces additional regions of fluid velocity slow-down compared to a channel with ideal trapezoidal cross section. While the maximum of the velocity profile is determined by the smallest dimension of a channel's cross section, in our case, the channel height, axial dispersion is determined by the distance and actual velocity difference between high flow velocity and low flow velocity regions. In a trapezoidal channel, the corner regions are the locations of low velocity and the channel center is the location of maximum

[150] D. Dutta, A. Ramachandran, and D. T. Leighton. *Microfluid. Nanofluid.*, **2**: 275–290, 2006.

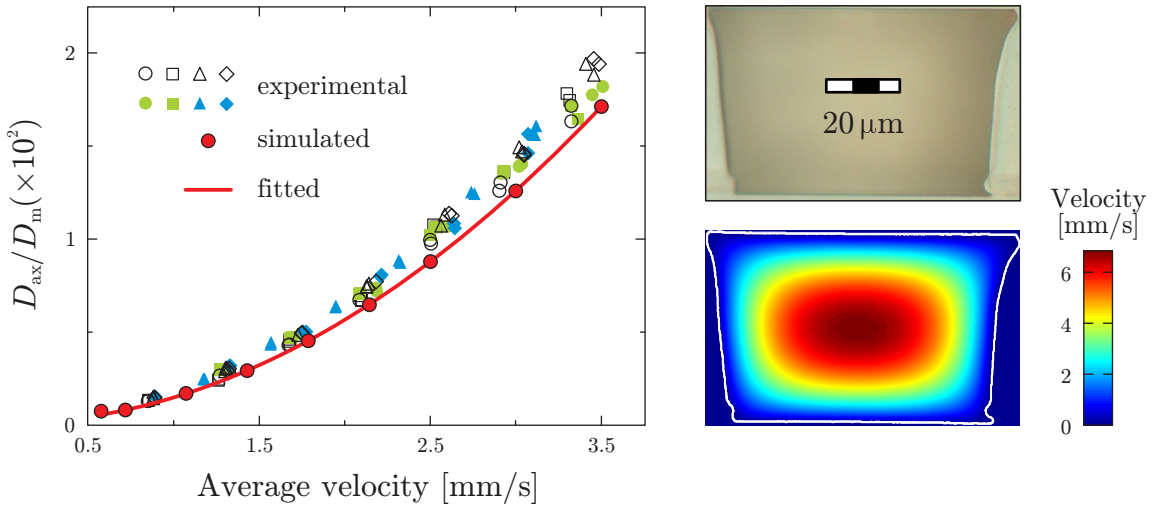

Figure 4.2: Lateral velocity distribution (averaged over the whole channel length) at an average velocity of 3 mm/s and normalized asymptotic axial dispersion coefficients D_{ax}/D_m in the unpacked reconstructed microchannel. Simulated data are fitted to equation (4.1) Experimental data were collected with several prototype HPLC/UV-microchips (each symbol refers to one microchip).

velocity. The irregularly shaped corner regions of the microfabricated channel thus increase the low-flow velocity regions, where mass transport becomes diffusion-limited, as well as the distance between low- and high-flow velocity regions, resulting in an increased Taylor-Aris dispersivity in the reconstructed microchannel.

Experimental dispersion data (Figure 4.2, bottom) fit the simulated data at low velocities and then diverge slowly from the simulated values with increasing velocity, because small, yet finite extra-column effects[103,254] contribute increasingly to the overall dispersion at higher velocities. Still, even at a velocity of 3.5 mm/s (translating to $Pe = u_{av}h/D_m \approx 117$, using $h = 50\,\mu m$ and $D_m = 1.5 \times 10^{-9}$ m^2/s), the maximum difference between simulated and experimental data amounts to only 12%. In summary, simulation results for the unpacked reconstructed microchannel agree very well with both the theoretical predictions and experimental data, validating our reconstruction and numerical analysis approach for this problem.

4.4.2 Porosity distributions

Figure 4.3 evaluates the porosity distribution in two of the reconstructed microchip packings, one from each end of the investigated range of bed porosities, i.e., at $\varepsilon = 0.42$ and high $\varepsilon = 0.48$. Figure 4.3a depicts the front view onto the packings (left), the particle center projections (middle), and the lateral porosity distributions averaged over the whole packing length (right). A geometrical wall effect, i.e., a higher packing order near the channel wall reflected in a repetition of the channel cross-sectional geometry by the particle centers adjacent to the high porosity region near the channel wall (Chapters 2 and 3), can be observed in the particle center projections and lateral porosity distributions of both packings. The lateral porosity distributions further reveal differences between packings of different bed porosity. There is generally a region of medium-to-high local

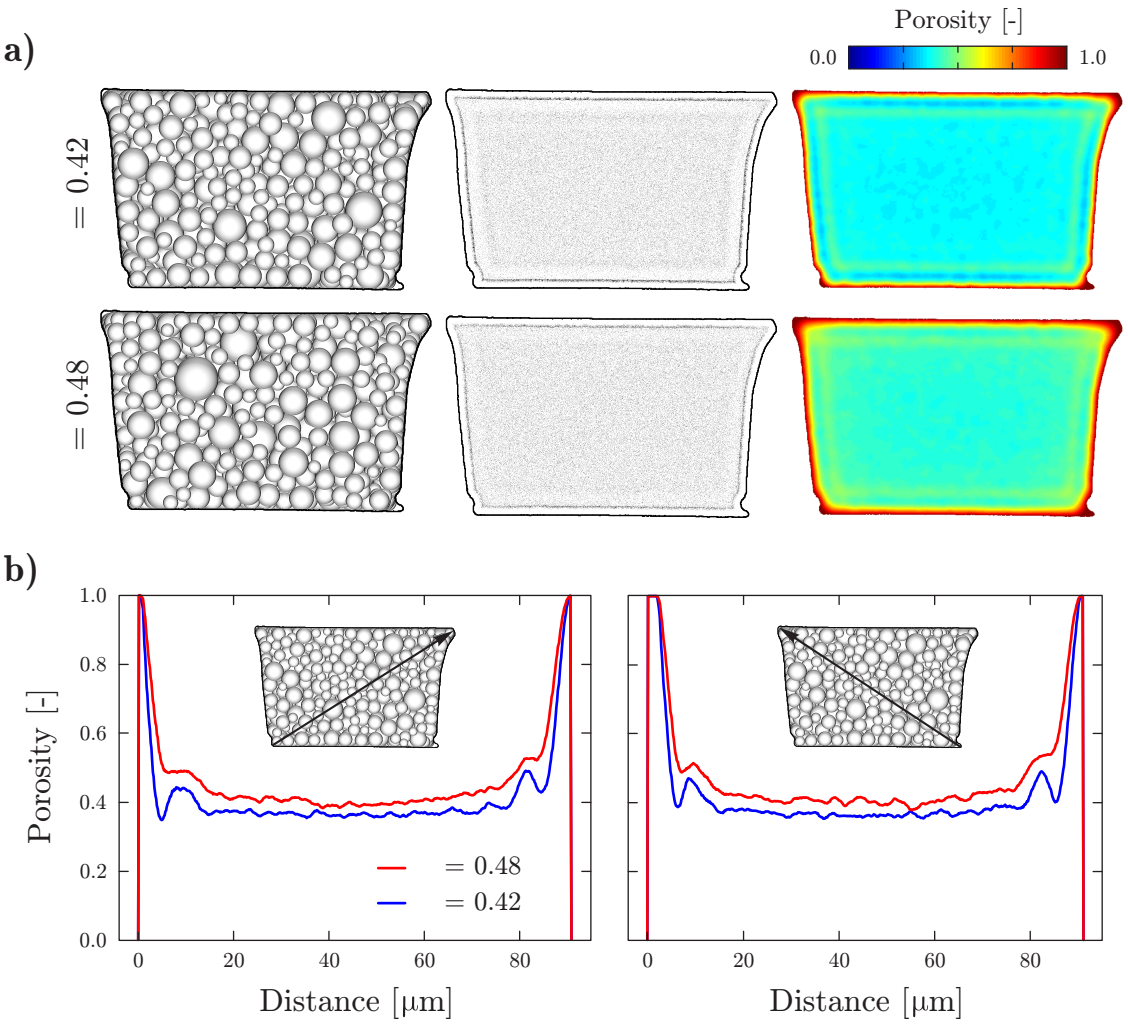

Figure 4.3: Reconstructed microchip packings of low ($\varepsilon = 0.42$) and high ($\varepsilon = 0.48$) bed porosity. (a) Frontview onto the packing cross section (left), projection of particle centers (of the 110 000 particles in the front third) onto the front plane (middle), and lateral porosity distribution averaged over the whole packing length (right). (b) Porosity distribution along both diagonals of the channel cross section (averaged over the whole packing length).

porosity close to the channel walls with maximum porosity in the four channel corners. A second region of medium porosity whose shape repeats the channel geometry can be found at some distance from the channel wall. In the higher bed porosity packing ($\varepsilon = 0.48$), the region of medium-to-high local porosity is more extended. The situation is further analyzed in Figure 4.3b which depicts the lateral porosity distributions along the channel's diagonals. The two diagonal porosity profiles differ slightly from another because of the channel cross section's asymmetry. Oscillations of porosity occur only up to a distance of 17 μm from the channel corners, with the maximum in the channel corners and a second, much lower, local maximum at a distance of ~ 9 μm. This contrasts strongly with the porosity distributions of the monodisperse packings in our previous simulations, where regardless of conduit geometry, the damping range extended over a distance of $5–6\, d_\mathrm{p}$ from the conduit corners to the core and where differences between

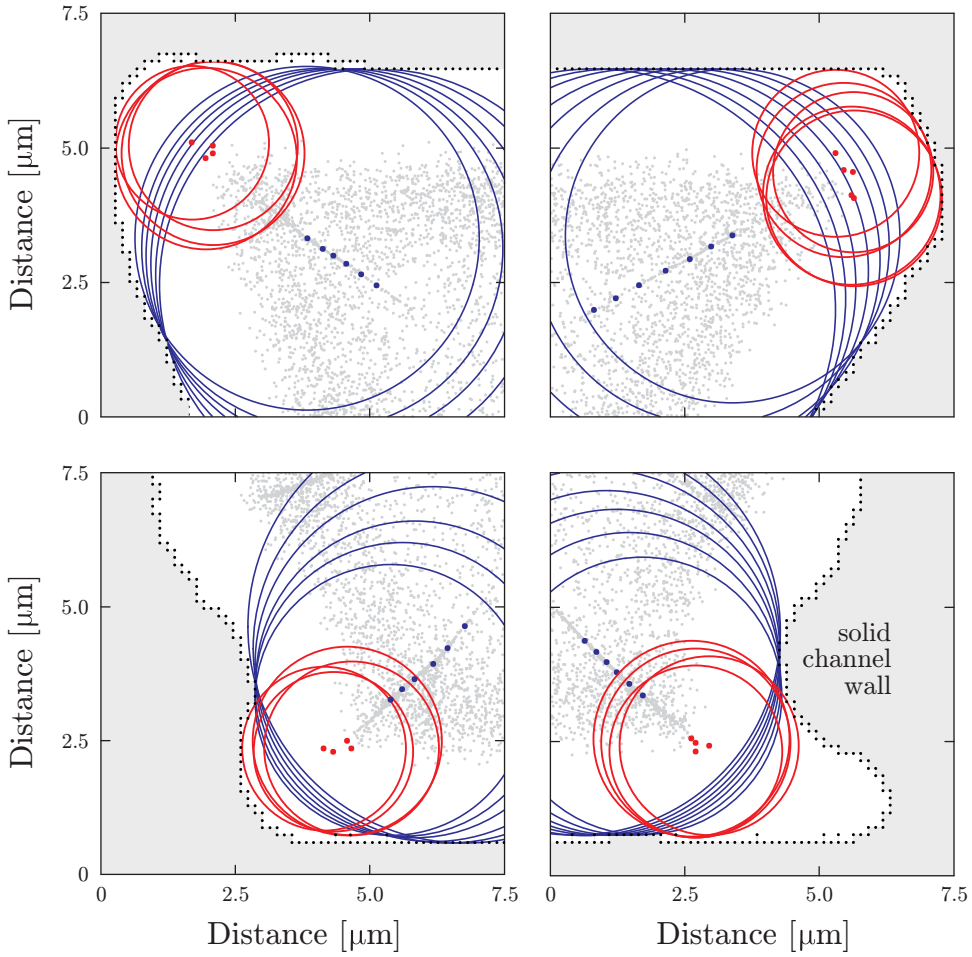

Figure 4.4: Packing structure in the corner regions of a reconstructed microchip packing of low bed porosity ($\varepsilon = 0.42$). The enlarged view of the channel corners shows a projection of all particle centers in this part of the packing onto the front plane (gray dots). The accumulation of particle centers along the channel's diagonals is underlined by the blue dots and circles, which represent centers and circumferences, respectively, of particles positioned along these diagonal lines. Red dots and circles represent the particles closest to the channel corners.

packings of equal conduit geometry, but different bed porosity, were more emphasized (Chapter 2). Compared to monodisperse packings, the wall effect is not only damped in its spatial extension but also in the amplitude of porosity fluctuations. Note that at decreased bed porosity ($\varepsilon = 0.42$), the local minimum porosity in three of the corners is still higher than the core porosity. Only the lower left corner displays a local porosity minimum below that of the core, the same as observed for monodisperse noncylindrical packings. Obviously, this corner shows the least deviations from regular geometry and can therefore be more effectively packed than the other three corners.

The corner regions of a channel were identified in our previous simulations of noncylindrical, monodisperse packings as the location of maximum porosity and fluid flow velocity as well as high porosity oscillations (Chapters 2 and 3). In the present study, the polydispersity of the particles and the irregular shape of the channel corners particularly affect the packing structure in the corner regions. Figure 4.4 provides a closer look at the corner regions of a low bed porosity packing

($\varepsilon = 0.42$). The particle centers in the corner regions accumulate along the channel's diagonals, whereas in monodisperse packings, particle centers near a conduit corner accumulate in a single point (cf. Chapters 2 and 3). Particles near the channel corners whose diameters are too large to fit closer into the actual corner (blue in Figure 4.4) effectively block smaller-diameter particles (red) from access to this region, so that only a tiny fraction of particles actually occupies the channel corners. Each channel corner deviates in a different way from the ideal trapezoidal geometry and displays a unique constriction on the packing of particles, an effect whose degree can be observed in the particle center distributions of the four corner regions (Figure 4.4). The two upper corners are rather similar, but the lower corners differ strongly from each other. While the lower left corner exhibits the least void distance between particles and channel wall, the "tail" of the lower right corner is inaccessible to even the smallest particles and therefore constitutes an isolated void volume in the confined packing.

4.4.3 Fluid flow field

As expected from the lateral porosity distributions shown in Figure 4.3 and 4.4, the loose packing structure in the channel corners enables advanced fluid flow in these regions that can be detected in the lateral velocity distributions of Figure 4.5. The enlargements show lateral velocity distributions in the top right and bottom left corners of the channel for a low bed porosity ($\varepsilon = 0.42$) and a high bed porosity packing ($\varepsilon = 0.48$). As observed before, the four channel corners differ in their shape and so, consequently, in their local porosity and flow velocity. The extension of the highvelocity region as well as the maximum fluid velocity in this region increases with the amount of available void space in a corner region. Thus, the maximum fluid velocity over the channel cross section can be found in the top right corner which has the largest total amount of void space. The maximum fluid velocity as well as the extension of the high velocity region in the conduit corners of noncylindrical monodisperse packings increases with increasing bed porosity, simply because with decreasing bed porosity the local porosity in the corners also decreases (Chapter 2). Similar behavior can be observed for the bottom left corner of the reconstructed microchannel when comparing the low bed porosity with the high bed porosity packing. At decreased bed porosity, this channel corner is packed more densely, as was also observed in the diagonal porosity distribution of Figure 4.3b. The other three corners, however, display a different behavior. While the extension of the high-velocity region decreases at decreasing bed porosity, as expected, the maximum fluid velocity in these three corners increases (Figure 4.5b). This seemingly divergent behavior can be explained by considering the effect of a decrease in bed porosity on the local porosity in the corner and the core regions of the channel. At decreasing bed porosity, the local porosity in the corner regions does decrease (Figure 4.3b), but the relative change is small, because the corner regions are difficult to access for most particles and much of the actual corner space is practically empty. The corners are isolated void volumes. The core of the channel, however, can be packed more tightly, so the void volume in the channel core of the low bed porosity packing with ($\varepsilon = 0.42$) is smaller (cf. Figure 4.3b), and consequently the hydraulic permeability in this region is lower than in the higher bed porosity packing ($\varepsilon = 0.48$). Because the velocity averaged over the channel cross section is kept constant in our simulations ($Pe = u_{\mathrm{av}} d_{\mathrm{p}} / D_{\mathrm{m}} = 12$ in Figure 4.5), the maximum

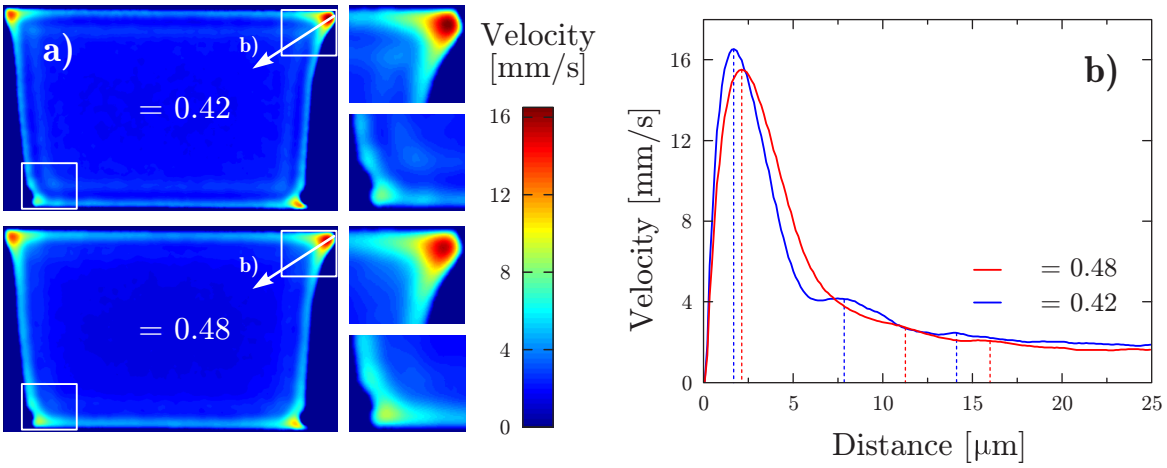

Figure 4.5: (a) Lateral velocity distribution (averaged over the whole packing length) in reconstructed microchip packings of low ($\varepsilon = 0.42$) and high ($\varepsilon = 0.48$) bed porosity at a reduced velocity of $Pe = u_{\mathrm{av}} d_{\mathrm{p}} / D_{\mathrm{m}} = 12$. The top right and bottom left corner regions are shown as enlargements. (b) One-dimensional velocity distribution in the top right channel corner for both packings taken along the arrow indicated in the images above. Dashed vertical lines denote maxima in the velocity distributions.

fluid velocity in the high-porosity corners increases accordingly to maintain the average velocity across the channel. The relative increase is highest where the most void space is available, i.e., in the upper right corner of the reconstructed channel. Local velocity oscillations are analyzed in Figure 4.5b which shows the one-dimensional velocity distribution (averaged over the whole packing length) along the channel's diagonal in the upper right corner region for both packings. Oscillations in local velocity in the polydisperse packings are restricted mainly to the actual corner region, while second and third maxima are very weakly pronounced.

4.4.4 Hydrodynamic dispersion

Figure 4.6a shows the efficiency of the reconstructed microchip packings as the dependence of the normalized axial dispersion coefficient from the average velocity for up to $Pe = 140$. The slope of the curves increases with increasing bed porosity, most notably at higher flow velocities, but the relative increase in the slope at increasing bed porosity decreases. The packings with bed porosities of $\varepsilon = 0.46$ and $\varepsilon = 0.48$ differ only slightly in their slope, while the slope of the curve representing the lowest bed porosity packing ($\varepsilon = 0.42$) is decidedly smaller than that of the other curves. This behavior is expected for at least two reasons. First, Taylor dispersion on the interparticle pore level is higher in a less densely packed bed, simply because the average interparticle pore size in the core region increases (cf. Figure 4.3). Second, and most important for the reconstructed conduit cross section of this work, the critical corner regions are expanding as the packing density decreases. It includes not only the immediate void space directly in the corners which is unaccessed by the packing particles but rather covers a region in the corner and along the adjoining walls in which a porosity and velocity heterogeneity with respect to the core region persists (Figures 4.3 and 4.5). The corner and wall regions act as more permeable flow paths parallel to the more densely packed core region (parallel combination of unequal resistances) over the entire length of the bed.

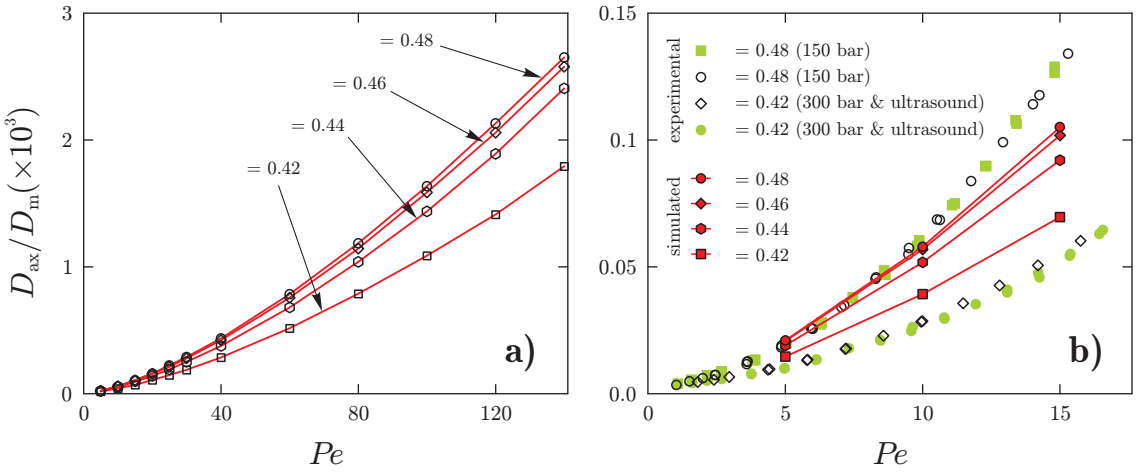

Figure 4.6: (a) Normalized asymptotic axial dispersion coefficients D_{ax}/D_m as a function of the Péclet number ($Pe = u_{av}d_p/D_m$) for the reconstructed microchip packings. Average values of D_{ax}/D_m were calculated from all five packings of a given bed porosity. (b) Comparison of axial dispersion in the reconstructed microchip packings with experimental data from HPLC/UV-microchips. Experimental data were duplicated with microchips slurry-packed under the indicated conditions, and each value of D_{ax}/D_m is the average of three measurements. Relative standard deviations of simulated and experimental data are between 3 and 5%.

Therefore, this macroscopic flow heterogeneity engenders mass transport resistance in the mobile phase, in dependence of the packing density, over relatively long distances (covering the whole conduit cross section), see Chapter 2 and works of Ehlert et al.[254] and Broeckhoven et al.[273]

The ratio between the nomalized axial dispersion coefficients of the highest ($\varepsilon = 0.48$) and lowest bed porosity packings ($\varepsilon = 0.42$) is $\sim$1.5 and nearly independent of Pe (Figure 4.6a). The value for this ratio is significantly smaller than the corresponding values calculated previously for monodisperse packings in all investigated (cylindrical and noncylindrical) geometries (Chapter 2). Several factors contribute to the observed decrease in the efficiency ratio between high and low bed porosity packings: i) the particle-aspect (channel-to-particle size) ratio, ii) monodisperse vs polydisperse packings, and iii) the irregular angles present in the microchip channel. The first two issues concern the geometrical wall effect. In particulate packings, the confining wall exerts an ordering effect on the particles positioned in the vicinity of the wall.[42,235] Monodisperse packings (regardless of conduit shape) consist of a highly ordered wall region, with high porosity fluctuations over a distance of $4-5\ d_p$ from the wall, and a random, densely packed core region. The first particle layer of the bed in contact with the wall is not only highly ordered but differs from subsequent layers, because the interstitial space between the wall and the first layer cannot be partially occupied by other particles. Subsequent particle layers toward the center of the packing do not retain this level of order, so that the degree of randomness increases with the distance from the wall.

In monodisperse packings with a particle-aspect ratio ≤ 10, the relative extension of the wall region is much larger than the core size, so that porosity fluctuations persist over the whole cross section (Chapters 2 and 3). As we have already seen in Figure 4.3, the geometrical wall

[273] K. Broeckhoven and G. Desmet. *J. Chromatogr. A*, **1172**: 25–39, 2007.
[42] R. S. Maier et al. *Phys. Fluids*, **15**: 3795–3815, 2003.
[235] A. de Klerk. *AIChE J.*, **49**: 2022–2029, 2003.

effect in the presented polydisperse packings is limited to a distance of $\sim 3.5\, d_{\mathrm{p}}(N_{\max})$ from the corner, because the sizevariation of the particles strongly damps the porosity oscillations.[247] The relative extension of the random, densely packed core is here much larger as in the previously simulated monodisperse packings (Chapters 2 and 3). A third factor is the irregular shape of the channel corners, which allows only a tiny fraction of particles to occupy corner positions, as seen in Figure 4.4. The inequality of the four channel corners also introduces a divergent behavior of the local fluid velocity, i.e., the high velocity regions in all of the channel corners expand at increased bed porosity, but the maximum fluid velocity decreases in three of the corners. In summary, both the polydispersity of the particles and the actual cross-sectional shape of the channel contribute to a lessened influence of the bed porosity on the efficiency of the packing. Nevertheless, the improved efficiency of a packing with low bed porosity, particularly at higher flow velocities, is still so significant as to necessitate the effort of achieving high-quality, dense microchip packings.

Figure 4.6b compares simulated axial dispersion coefficients for the reconstructed microchip packings with experimental data from HPLC/UV-microchip packings for $Pe < 20$. Experimental data were determined with microchip packings fabricated under the indicated conditions and resulting in the given interparticle porosities (see Experimental Section and References [254] and [103] for further details). Simulated dispersion data genuinely reflect the general form of the experimental curves as well as the influence of interparticle porosity (packing density). In absolute values, experimental dispersion coefficients are generally higher than simulated data for the high bed porosity packings ($\varepsilon = 0.48$). This is to be expected, because experimental separation efficiencies contain additional mass transfer resistances absent in the simulated packings. First, the porosity of the real-life particles contributes to axial dispersion because transport of analytes in the intraparticle stagnant mobile phase is diffusion-limited. Second, the pentylbenzene tracer is moderately retained on the real-life microchip packings under the experimental conditions. While these intraparticle mass transfer resistances add only little dispersion to the processes occurring within the flowing mobile phase outside the particles at the low velocities analyzed in Figure 4.6b ($Pe < 20$),[262,274,275] experimental dispersion should nevertheless be higher than simulated dispersion.

For the low bed porosity packings ($\varepsilon = 0.42$), however, experimental dispersion coefficients are lower than simulated data. A clue for the explanation of this surprising result is given in Figure 4.7, which contains SEM images of random vertical cuts through HPLC/UV-microchip packings with interparticle porosities of $\varepsilon = 0.42$ alongside random vertical slices through the reconstructed microchip packing with $\varepsilon = 0.42$. Shown is the upper right corner region of the packed microchannel. Although the inevitable distortions from the cutting process, like additional surface roughness of the channel wall or displacement of particles, are visible in the SEM images, it is obvious that particles do actually occupy corner positions, in contrast to the simulated packings, where only very rarely a particle is situated directly in the corner. As the nearly empty channel corners and adjacent loosely packed regions are the main source of axial dispersion in the simulated packings,

[247] D. Hlushkou, A. Seidel-Morgenstern, and U. Tallarek. *Langmuir*, **21**: 6097–6112, 2005.
[262] D. Kandhai et al. *Phys. Rev. Lett.*, **88**: 234501, 2002.
[274] J. H. Knox. *J. Chromatogr. A*, **831**: 3–15, 1999.
[275] J. H. Knox. *J. Chromatogr. A*, **960**: 7–18, 2002.

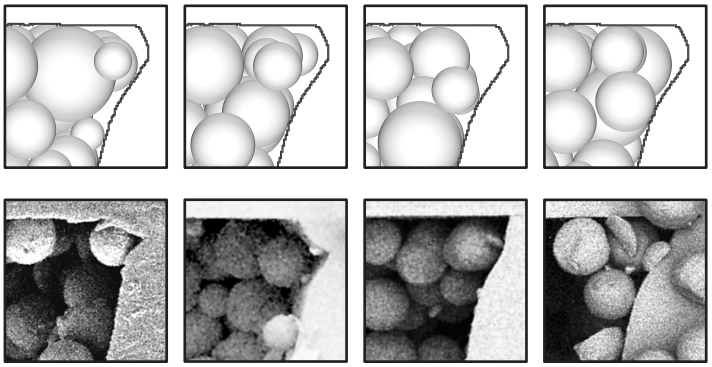

Figure 4.7: Comparison of packing structure in the upper right channel corner of reconstructed and HPLC/UV-microchip packings ($\varepsilon = 0.42$). Reconstructed packings are represented by slices of $\sim 2d_{\mathrm{p}}(N_{\max})$ thickness, taken at random intervals along the packing length. SEM images of HPLC/UV-microchip packings were obtained from cutting orthogonally to the separation channel length. Note that the cutting process introduces additional surface roughness to the channel walls.

band broadening in the real-life microchip packings is lower because of their more densely packed channel corners.

This is probably enabled by a certain flexibility of the relatively soft polymeric channel walls (compared to glass or stainless steel) under the enforced packing conditions. While the pressure drop over even the most densely packed HPLC/UV-microchip channels did not exceed 70 bar for the range of velocities in Figure 4.6b and we did not observe any sign of microchannel deformation ("column breathing") during operation, e.g., in the pressure drop–flow rate characteristics, the residence times of the deadtime marker, or in separation efficiencies, the application of much higher pressure (300 bar) and ultrasound required for the best microchip packings ($\varepsilon = 0.42$) may induce channel deformation during the packing process, which in turn allows particles better access to the channel corners.[103,254] Unfortunately, conduit wall flexibility and the influence of ultrasound on the packing process are not incorporated into the current packing generation algorithms. Also, the simulation of the comprehensive slurry packing process including interparticle forces remains a future challenge. Despite these limitations, the simulated data genuinely reflect the general dispersion behavior of the real-life HPLC-microchip packings.

4.5 Conclusions

In this study, flow and transport in reconstructed microchip packings were analyzed with quantitative numerical simulation methods. The presented work is a succession and an advancement of previous numerical simulation studies of hydrodynamic dispersion in noncylindrical sphere packings at low particle-aspect ratios (Chapters 2 and 3). Novel aspects were introduced by reconstructing real-life HPLC-microchip packings with regard to the exact cross-sectional geometry of the separation channel, including the irregularly shaped corners that result from the fabrication process, the particle-size distribution of the packing material, and the average interparticle porosity of the packings (packing density).

Calculation of asymptotic axial dispersion coefficients at reduced velocities of up to $Pe = 140$ translated to a large-scale simulation of packings containing $\sim 330\,000$ polydisperse spherical particles at bed porosities between $\varepsilon = 0.42$ and $\varepsilon = 0.48$. The lateral porosity distribution in the reconstructed microchip packings reveals a highly ordered, high porosity wall region and a random, densely packed core. Compared to monodisperse packings regardless of conduit geometry, however, the geometrical wall effect is strongly damped, i.e., the porosity oscillations near the channel wall are smaller in amplitude and decay over a shorter distance and differences in the lateral porosity distribution between packings of different bed porosity are less enhanced.

The restricted, irregularly shaped space in the channel corners exercises an ordering effect on the position of particles in the corner region. The higher the restriction of corner space, the higher the ordering effect. Particle centers in the near-corner regions accumulate along the cross-sectional diagonals, while the actual corner space is nearly empty. Only a handful of particles with smaller than average diameter can be found in the corners, despite the fact that more small-diameter particles would be available to occupy the corner positions. The channel corners are locations of advanced fluid flow, and these high porosity and high velocity corner regions expand with increasing bed porosity of the packing, just as in noncylindrical monodisperse packings. However, at decreasing bed porosity, the largest change in local porosity occurs in the core region, because the irregularly shaped channel corners cannot be packed as densely as the orthogonal corners of, e.g., rectangular conduits, and so there is a lower limit for the local porosity in the corner regions. Accordingly, the fluid velocity in the core region decreases in a larger amount at decreasing bed porosity, and to maintain the constant fluid velocity averaged over the whole cross section, the maximum fluid velocity in the corners increases. Only the lower left corner (cf. Figure 4.3–4.5), which has the smallest aberration from regular shape and can be packed better than the other three corners, displays a decrease of maximum fluid velocity at decreased bed porosity (increasing packing density).

Axial dispersion coefficients were calculated for reduced velocities of up to $Pe = 140$. The efficiencies of the reconstructed microchip packings reflect the reduced influence of bed porosity in polydisperse compared to noncylindrical monodisperse packings but at the same time indicate the superior performance of the low-bed porosity packing ($\varepsilon = 0.42$) at higher flow velocities. This underlines the importance of achieving high-quality, dense microchip packings. The comparison of simulated dispersion data with experimental separation efficiencies of HPLC/UV-microchip packings has shown good agreement. Surprisingly, axial dispersion in the best HPLC/UV-microchip packings ($\varepsilon = 0.42$) was lower than in the comparable reconstructed packings. Because dispersion in the simulated packings is mainly caused by the highporosity and high-velocity corner regions, it was assumed that the local porosity in the corners of the HPLC/UV-microchip packings is lower than in the reconstructed packings. SEM images of cuts through HPLC/UV-microchip packings indeed revealed densely packed channel corners. A possible explanation is the side-wall flexibility of the polyimide channel at the applied packing pressure. Ultrasound, which has been demonstrated to be a crucial factor in achieving dense packings,[254] will also contribute toward a denser packing in the corner regions. This observation underlines the importance of developing advanced packing algorithms as well as of reconstructing real-life packings in detail by suitable microscopic methods.

Chapter 5

Time and length scales of hydrodynamic dispersion

This chapter discusses length scales of heterogeneity persisting in periodic (bulk) and confined cylindrical sphere packings. The length scales are studied by the analysis of time evolution of the hydrodynamic dispersion coefficient. Hydrodynamic dispersion is simulated within the broad range of Péclet numbers (reduced velocities) until the close-to-asymptotic behavior is observed, and resulting dispersion values are fitted to the generalized Giddings equation; the value of fitted coefficients of each individual term of the Giddings equation demonstrate good agreement with the Giddings' estimates. To our knowledge, this is the first systematic resolving of the individual contributions of generalized Giddings equation derived more than fifty years ago. Results presented in this chapter were published in the journal *Analytical Chemistry* in 2009.[40]

5.1 Introduction

An analyte zone migrating through a chromatographic bed is dispersed in longitudinal and transverse directions (parallel and perpendicular, respectively, with respect to the macroscopic flow direction) by a combination of diffusive and convective processes. When a streamlet of the mobile phase hits a solid obstacle, e.g., a support particle of the chromatographic bed, it splits into several, unequal streamlets which flow around the obstacle and merge with other streamlets coming from neighboring obstacles. Convective dispersion in transverse direction in a particulate bed is caused by this stream splitting mechanism, whereas longitudinal dispersion originates in the point-to-point differences of the flow velocity that exist over the column cross section.[166] The flow pattern of a fluid undergoing laminar flow in a particulate bed depends on the morphology (i.e., the topology and geometry) of the pore space available for the flow so that the inherent structural heterogeneity of the packed bed sensitively influences time and length scales which characterize velocity fluctuations in the mobile phase.[89,131,145,276]

[40] S. Khirevich et al. *Anal. Chem.*, **81**: 7057–7066, 2009.
[166] J. M. P. Q. Delgado. *Heat Mass Transfer*, **42**: 279–310, 2006.
[89] J. Bear. *Dynamics of fluids in porous media*. Dover Publications, 1988.
[131] J. C. Giddings. *Dynamics of chromatography: principles and theory*. Marcel Dekker, 1965.
[145] D. L. Koch and J. F. Brady. *J. Fluid Mech.*, **154**: 399–427, 1985.
[276] S. G. Weber and P. W. Carr. In: *High Performance Liquid Chromatography*. P. R. Brown and R. A. Hartwick, eds. Chap. 1. John Wiley & Sons, 1989.

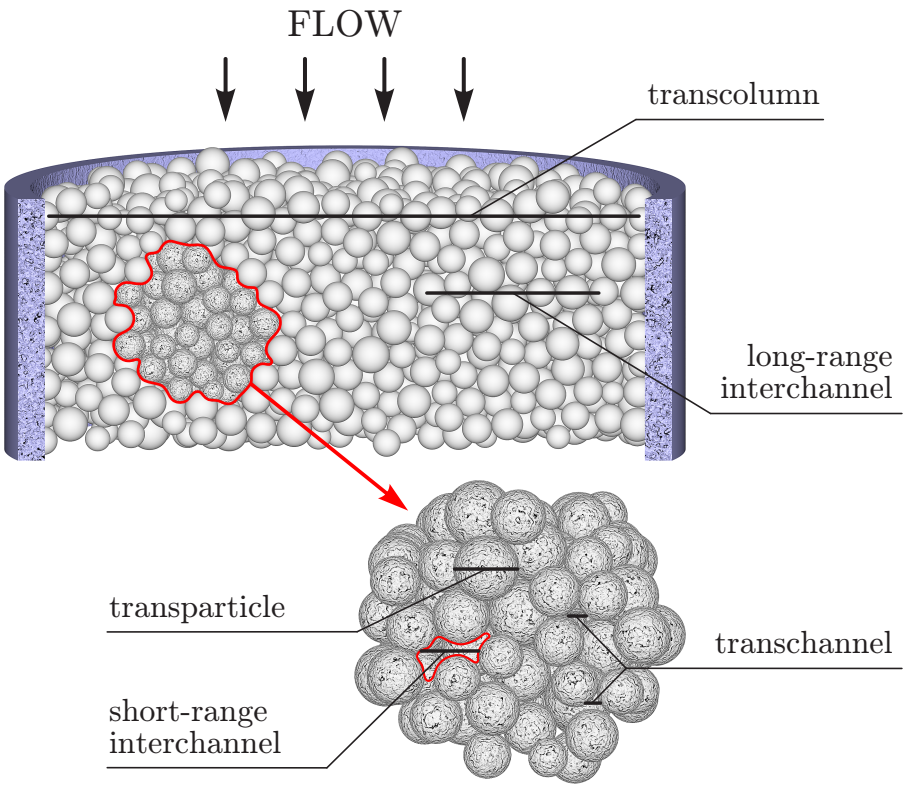

Figure 5.1: Definitions, locations, and scales of the different velocity inhomogeneities contributing to eddy dispersion according to Giddings.[131]

In a chromatographic bed the anastomosis of the pore space causes important and rapid changes in the mobile phase velocity. An analyte molecule caught in a fast stream path (i.e., moving at a local velocity higher than the average mobile phase velocity) literally takes a step forward with respect to the center of the zone. This can change either because the velocity of the particular stream path decreases (due to the complexity of the pore network, velocities at different positions along a given stream path are unrelated) or because the molecule transfers by diffusion to another stream path. Thus, diffusion relaxes transverse concentration gradients that arise from inequalities in the local flow velocity. Lateral diffusion in the new streamlets and a succession of similar events at each particle encountered promote transverse dispersion. The average width of streamlets in a packed particulate bed is much smaller than one particle diameter so that local transverse homogenization of the mobile phase composition takes place quickly. Homogenization at the scale of the column diameter, however, is much slower. This implies that at least two fundamental length and time scales exist for eddy dispersion and the associated transverse equilibration between different velocities of the flow field in a confined chromatographic bed: the pore (shorttime) scale and the confinement or transcolumn (long-time) scale.[42]

Giddings[131] has divided the local velocity inequalities inside a confined particulate bed that contribute to eddy dispersion into the following categories illustrated in Figure 5.1: (1) The

[42] R. S. Maier et al. *Phys. Fluids*, **15**: 3795–3815, 2003.

transchannel contribution arises from the transverse distribution of velocities inside each individual channel between particles. It resembles the Hagen–Poiseuille flow profile in a cylindrical tube, though channels in a packed bed have a much more complicated geometry and flow velocity distribution. (2) The *short-range interchannel* contribution is due to the existence of small groups of tightly packed particles between which more loosely packed regions are found. (3) Fluctuations of local packing density cause this pattern of tightly packed groups of particles interspersed by loosely packed regions to be erratic, which results in the *long-range interchannel* contribution. (4) The existence of systematic variations of the mobile phase velocity between different regions of the column, i.e., in the core and the wall regions, is responsible for the *transcolumn* contribution. A fifth contribution mentioned by Giddings[131] as a source of velocity bias is the *transparticle* contribution, which exists in beds of porous particles. This effect should not be taken into account as an eddy dispersion term, however, as it is actually the strict equivalent of the pore diffusion mechanism.[277] The flowing mobile phase does not affect pore diffusion inside the particles. The intraparticle fluid velocity is zero (stagnant mobile phase), as only transfer by diffusion allows the solute molecules to penetrate or leave the particles.[278]

The influence of transcolumn velocity gradients of various origins on the separation efficiency in liquid chromatography is well-known,[279,280] but the precise nature of how the microstructure of a packed bed and the geometry of the confinement affect the flow heterogeneity, transverse equilibration as well as the macroscopically resulting longitudinal dispersion, and how it interrelates with the velocity-dependent transverse rate of mass transport is still largely unresolved. This topic has been addressed over the past decades in the engineering[166] and chromatographic communities[261,281–283] which operate with packed beds. There is a general consensus that measurements of transverse dispersion are moredifficult to perform than the analysis of the far easier accessible longitudinal dispersion data.

Numerical simulations of flow and transport in sphere packings are particularly suited to the challenge of investigating the central structure–transport relationships in chromatographic media, because this approach allows us to systematically study relevant parameters such as the shape and average size of the particles, the particle size distribution, inter- and intraparticle porosities, as well as the column dimensions and cross-sectional geometry.[19,42,99,180,262,284] Longitudinal and transverse dispersion can be studied simultaneously in the same packings, thereby quantifying time and length scales required for the attainment of asymptotic dispersion behavior and providing

[277] F. Gritti and G. Guiochon. *Anal. Chem.*, **78**: 5329–5347, 2006.
[278] U. Tallarek, F. J. Vergeldt, and H. Van As. *J. Phys. Chem. B*, **103**: 7654–7664, 1999.
[279] G. Guiochon. *J. Chromatogr. A*, **1126**: 6–49, 2006.
[280] K. Broeckhoven and G. Desmet. *J. Chromatogr. A*, **1216**: 1325–1337, 2009.
[261] U. Tallarek, E. Bayer, and G. Guiochon. *J. Am. Chem. Soc.*, **120**: 1494–1505, 1998.
[281] J. H. Knox, G. R. Laird, and P. A. Raven. *J. Chromatogr.*, **122**: 129–145, 1976.
[282] C. H. Eon. *J. Chromatogr.*, **149**: 29–42, 1978.
[283] R. A. Shalliker, B. S. Broyles, and G. Guiochon. *J. Chromatogr. A*, **994**: 1–12, 2003.
[19] B. Manz, L. F. Gladden, and P. B. Warren. *AIChE J.*, **45**: 1845–1854, 1999.
[99] D. Coelho, J.-F. Thovert, and P. M. Adler. *Phys. Rev. E*, **55**: 1959–1978, 1997.
[180] R. S. Maier, D. M. Kroll, and H. T. Davis. *AIChE J.*, **53**: 527–530, 2007.
[262] D. Kandhai et al. *Phys. Rev. Lett.*, **88**: 234501, 2002.
[284] S. Stapf et al. *Phys. Rev. E*, **58**: 6206–6221, 1998.

correlations for the dependence of dispersion coefficients on the average mobile phase velocity. Because all dispersion data are referenced to a particular type of packing and are unbiased by extracolumn contributions, the numerical simulations approach establishes a systematic route toward quantitative structure–transport relationships.

In this work we resolve time and length scales as well as the magnitude of *individual* contributions to eddy dispersion in chromatographic beds. We address this issue by a high-resolution numerical analysis of flow and mass transport in computer-generated bulk (unconfined) and complementary confined cylindrical packings of monosized, nonporous, incompressible, spherical particles. The complementary analysis of bulk packings (which mimic infinitely wide, randomly packed beds without walls) and packings confined in the conventional cylindrical column format is of high diagnostic value, because contributions to eddy dispersion associated with widely differing time and length scales, from the individual pore (transchannel) scale in a bulk packing to the transcolumn equilibration in confined packings, can be approached individually with the best possible precision.

5.2 Analysis of dispersion

In chromatography the height equivalent to a theoretical plate (HETP, H) is defined as the slope of the dependence of the variance of a band (σ) on the migration distance. In a first approximation, assuming a homogeneous column and an incompressible mobile phase, this slope, and hence the HETP, is constant along the column. A similar definition applies to band broadening in the longitudinal (z) direction, i.e., parallel to the macroscopic flow velocity and in the transverse direction. The longitudinal and transverse dispersion coefficients (D_L and D_T, respectively) usually discussed in the engineering literature[166] are related to the corresponding chromatographic plate heights H_L and H_T by[131]

$$D_\mathrm{L} = \frac{H_\mathrm{L} u_\mathrm{av}}{2} = \frac{h_\mathrm{L} \nu D_\mathrm{m}}{2} = \frac{u_\mathrm{av}}{2} \frac{\partial \sigma_\mathrm{L}^2}{\partial z}, \tag{5.1a}$$

$$D_\mathrm{T} = \frac{H_\mathrm{T} u_\mathrm{av}}{2} = \frac{h_\mathrm{T} \nu D_\mathrm{m}}{2} = \frac{u_\mathrm{av}}{2} \frac{\partial \sigma_\mathrm{T}^2}{\partial z}. \tag{5.1b}$$

Here, $h = H/d_\mathrm{p}$ denotes the reduced plate height and ν is the reduced velocity (or particle Péclet number, Pe) defined as $\nu \equiv Pe = u_\mathrm{av} d_\mathrm{p}/D_\mathrm{m}$, where u_av is the average mobile phase velocity through the packed bed, D_m the solute diffusivity in the mobile phase, and d_p the average diameter of the spherical support particles.

By applying the random walk relationship to a model of eddy dispersion incorporating the coupling between transverse diffusion and spatial velocity fluctuations, Giddings[131] developed a plate height equation by analogy to parallel conductors. The comprehensive equation for $h_\mathrm{L} = f(\nu)$ is

$$h_\mathrm{L} = \frac{H_\mathrm{L}}{d_\mathrm{p}} = \frac{b}{\nu} + \sum_{i=1}^{4} \frac{2\lambda_i}{1 + (2\lambda_i/\omega_i)\nu^{-1}} + c\nu. \tag{5.2}$$

The first term on the right-hand side of equation (5.2) (b/ν) accounts for the effect of longitudinal molecular diffusion in the packed bed driven by the concentration gradient along the zone profile.[277,285] The second term in equation (5.2) describes eddy dispersion as the sum of the four contributions (Figure 5.1) used to model the erratic mass transfer by flow and diffusion between the interparticle pores of the packing on different length scales (transchannel, short-range interchannel, long-range interchannel, transcolumn), where λ_i and ω_i are universal structural parameters characteristic of each contribution and the ratio $\nu_{1/2} = 2\lambda_i/\omega_i$ is a reduced transition velocity for each type of velocity disparity.[131] It is the velocity at which the corresponding plate height term reaches half of its limiting value and thereafter begins to flatten noticeably.[286] The last term in equation (5.2) ($c\nu$) accounts for the mass transfer kinetics from the bulk solution into and across the particles.[287,288]

In an attempt to find a simple equivalent to the generalized Giddings equation (5.2), Knox has derived the most popular plate height equation,[274] in which the different contributions to eddy dispersion as proposed by Giddings are pooled into one *empirical* term. Considering a number of experimental data sets, the following equation was found to provide a good empirical correlation:

$$h_{\mathrm{L}} = \frac{b}{\nu} + a\nu^n + c\nu, \tag{5.3}$$

where n is between 0.2 and 0.35 and most often taken as one-third in the chromatographic literature. The famous van Deemter equation[289] corresponds to equation (5.3) with $n = 0$; hence, the eddy dispersion term is constant. The Knox equation (5.3) has been widely used in the literature. It explains reasonably well most experimental data around the plate height minimum, which is in part due to the narrow range of reduced velocities within which most of these data have been acquired. In most cases, experimental correlations were studied in the range of $1 \leq \nu \leq 20{-}40$, which is barely sufficient for an accurate estimate of the eddy dispersion coefficient (a in equation (5.3)). Further, estimates obtained for b and/or c are often poorly precise.

While Knox has focused on the *magnitude* of eddy dispersion,[274] a deeper understanding of that phenomenon aiding in the systematic optimization of packing processes and particle characteristics can only be gained as the details of its origin are analyzed and broken down into its component parts. In this respect, Giddings' coupling theory of eddy dispersion is the most rigorous approach available and provides *physical* insight into the parameters involved in the description of the eddy dispersion term (λ_i and ω_i in equation (5.2)). However, his division of the column on the basis of the average size of a few selected subdomains is empirical. Although the transchannel and a more or less complex transcolumn equilibration are certainly intrinsic to the morphology of any confined packing, the short-range and long-range interchannel contributions are difficult to assess or quantify even. The latter two contributions will be highly dependent on the particle

[285] K. Broeckhoven et al. *J. Chromatogr. A*, **1188**: 189–198, 2008.
[286] J. C. Giddings. *Nature*, **184**: 357–358, 1959.
[287] K. Miyabe and G. Guiochon. *J. Sep. Sci.*, **26**: 155–173, 2003.
[288] G. Desmet and K. Broeckhoven. *Anal. Chem.*, **80**: 8076–8088, 2008.
[274] J. H. Knox. *J. Chromatogr. A*, **831**: 3–15, 1999.
[289] J. J. van Deemter, F. J. Zuiderweg, and A. Klinkenberg. *Chem. Eng. Sci.*, **5**: 271–289, 1956.

shape and size distribution and the specific column packing procedure used. Wall effects from the confinement which strongly influence the transcolumn contribution are similarly sensitive to the packing method and particle characteristics and also depend on the column-to-particle diameter ratio.[238] It is therefore not clear which of the four biases of the eddy dispersion term in equation (5.2) should be omitted depending on the experimental conditions or under what conditions the contribution of eddy dispersion to band broadening can be reduced to one term.

To our knowledge the challenge of resolving systematically, either experimentally or by means of suitable simulations, the different structural parameters characteristic of each contribution to the eddy dispersion term of the *comprehensive* Giddings equation ((5.2)) has never been undertaken. Investigations which have been conducted in this direction in the past with packed beds[132,261,275,290] are all in favor of Giddings' coupling theory of eddy dispersion, but the analysis remained limited to the "simple" Giddings equation, i.e., equation (5.2) with $i = 1$.

The choice of packings and operating conditions in our numerical analysis approach facilitates the focus on eddy dispersion and its precise dependence on the morphology of the packed bed. The selection of perfectly monosized, spherical particles allows the strict operation with reduced parameters ($h_{\mathrm{L}} = H_{\mathrm{L}}/d_{\mathrm{p}}$ and $\nu = u_{\mathrm{av}} d_{\mathrm{p}}/D_{\mathrm{m}}$) without the influence of the particle size distribution and particle shape. The use of nonporous support particles and inert conditions (nonadsorbing, nonreacting tracer particles) eliminates mass transfer resistance contributions ($c = 0$ in equation (5.2)).[275,290] Although it has sometimes been claimed that even with solid particles and unretained tracers a remaining c-term in equation (5.2) is needed (to account for pore-scale Taylor dispersion), we like to emphasize that this contribution is contained in the eddy dispersion term of equation (5.2) as the transchannel contribution. In deriving equation (5.2) under most general conditions, Giddings has absorbed all mass transfer resistances in the mobile phase (as distinguished from the diffusion and adsorption/desorption in the stationary phase) into the coupling expression of equation (5.2) (cf. derivation of equation 2.11-1 on page 62 of Reference [131] and the transition to equation 2.11-2). For the packings and conditions considered in our analysis, the coefficient accounting for the contribution of longitudinal diffusion to the reduced plate height in equation (5.2) is $b = 2\gamma$, where γ is the obstruction factor often used in chromatography.[131,274] It is the inverse of the tortuosity factor (τ) of the interconnected pore space usually used in the engineering literature[166] and is defined as

$$\gamma = \frac{1}{\tau} = \frac{D_{\mathrm{eff}}}{D_{\mathrm{m}}}, \tag{5.4}$$

where D_{eff} is the effective diffusion coefficient in the sphere packing, i.e., its asymptotic value observed in the long-time limit for $\nu = 0$.

[238] R. A. Shalliker, B. S. Broyles, and G. Guiochon. *J. Chromatogr. A*, **888**: 1–12, 2000.
[132] M. R. Schure et al. *Anal. Chem.*, **74**: 6006–6016, 2002.
[275] J. H. Knox. *J. Chromatogr. A*, **960**: 7–18, 2002.
[290] P. Magnico and M. Martin. *J. Chromatogr.*, **517**: 31–49, 1990.

5.3 Numerical section

Our simulation approach consists of three consequent steps: random packing generation (and its discretization), simulation of flow in the packing void space, and simulation of hydrodynamic dispersion using information on the packing geometry and corresponding flow field from two previous steps. Detailed description of the employed methods is given in Chapter 1.

Packings of solid, impermeable, spherical particles were generated by a modified Jodrey–Tory algorithm (Section 1.1) at bed porosities (average interstitial void fraction or interparticle porosity) of $\varepsilon = 0.40$ for the confined cylindrical packings and of $\varepsilon = 0.378$ for the bulk packings. The value of $\varepsilon = 0.378$ for the bulk packings, which represents *random-close* packing, matches the bed porosity in the randomly packed core region of the confined cylindrical packings. Confined packings are characterized by a cylinder-to-particle diameter ratio of $d_\mathrm{c}/d_\mathrm{p} = 20$. Bulk packings contained 8300 spheres and had a dimension of $10 \times 10 \times 68.27\ d_\mathrm{p}^3$ (in x-, y-, and z-direction, respectively), whereas confined cylindrical packings contained 2.4×10^6 spheres and had a dimension of $20 \times 20 \times 6553.6\ d_\mathrm{p}^3$. The grid resolution was chosen as 30 nodes per d_p, sufficient for the accurate simulation of fluid flow and dispersion (see Subsections 1.3.5 and 1.4.6). Final dimensions of the lattice (computational domain containing the packings) were $300 \times 300 \times 2048$ nodes for the bulk packings and $600 \times 600 \times 196\,608$ for the confined cylindrical packings. For each type of packing five different initial random positions of particle centers (seeds) were used, resulting in a total of 10 generated random sphere packings. The transient dispersion curves (Figures 5.3 and 5.5) and plots of $h_\mathrm{L} = f(\nu)$ in Figures 5.4 and 5.6 represent the average values calculated from all five packings of a given type.

The lattice Boltzmann method (Section 1.3) was used for the simulation of low Reynolds-number flow of an incompressible fluid within the interparticle pore space of the generated packings. For the computational domain described above, we employed a D3Q19 model, resulting in lattice sizes of ~ 13 GB for a bulk packing and ~ 5 TB for a confined cylindrical packing. The no-slip boundary condition at the solid–liquid interfaces of the cylinder inner surface and the solid particles was realized by the "bounce-back" scheme. Periodic boundary conditions were used along the z-axis of the confined cylindrical packings and in all directions for the bulk packings.

The simulation of one fluid flow velocity field in a confined cylindrical packing required 1500 LBM iterations, 7.2 TB memory space, and took ~ 0.8 h on 16384 processor cores of an IBM Blue Gene/P system, while for a bulk packing the simulation required 1500 LBM iterations, 31 GB of memory space, and took ~ 0.1 h on 512 processor cores. For each packing, the velocity field was first calculated at a low reduced velocity ($\nu \approx 1$), from which velocity fields at values of up to $\nu = 500$ were then received by linear rescaling.[132,291]

Mass transport in the generated packings and fluid flow velocity fields was simulated by a random walk particle tracking method (Section 1.4). Time-dependent longitudinal ($D_\mathrm{L}(t)$) and transverse ($D_\mathrm{T}(t)$) dispersion coefficients were calculated as described in Subsection 1.4.3. Simulation of dispersion in all five bulk packings (over the whole velocity range) required ~ 24 h on 1024 processor cores. Dispersion in confined cylindrical packings was simulated using 8192 processor cores and took 256 h.

[291] O. Bey and G. Eigenberger. *Chem. Eng. Sci.*, **52**: 1365–1376, 1997.

5.4 Results and discussion

Figure 5.2 shows a front view onto both types of packings investigated and illustrates the differences in their respective lateral porosity profiles. Confined packings of monosized spheres consist of a highly ordered wall region, with high porosity fluctuations over a distance of $4–5\ d_\mathrm{p}$ from the wall, and a random, densely packed core region.[42,234–237,247] These porosity oscillations result from the inability of the hard spheres to form a close packing against the hard surface of the cylindrical column as particles can touch, but not penetrate, the wall. The first particle layer of the bed in

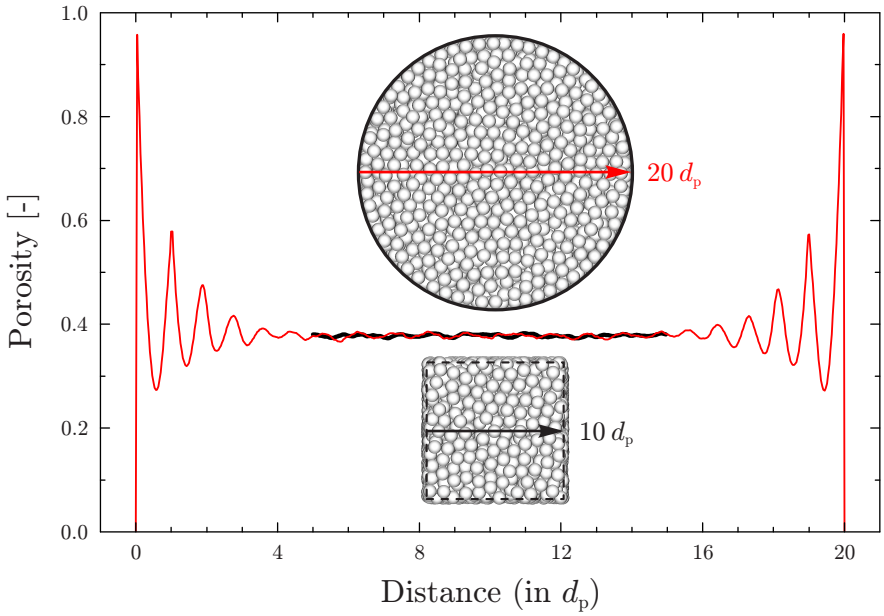

Figure 5.2: Front view onto the two types of monodisperse sphere packings studied in this chapter, together with representative lateral porosity distributions (taken along the arrows and averaged over the whole length of the packings). Confined packings have a cylinder-to-particle diameter ratio of $d_\mathrm{c}/d_\mathrm{p} = 20$, a length of $6553.6\ d_\mathrm{p}$, and a bed porosity of $\varepsilon = 0.40$. Bulk (unconfined) packings have dimensions of $10\ d_\mathrm{p} \times 10\ d_\mathrm{p} \times 68.27\ d_\mathrm{p}$ with periodic boundary conditions in all directions and a bed porosity of $\varepsilon = 0.378$ which, as indicated by the overlaid porosity profiles, matches the porosity of the random-close *core region* of the confined packings.

contact with the wall is not only highly ordered, but differs from subsequent layers, because the interstitial space between the wall and the first layer cannot be partially occupied by other particles. Subsequent particle layers toward the center of the column do not retain this level of order and the degree of randomness increases with the distance from the wall. Lacking the ordering effect of a confining wall, bulk packings show only low-level random porosity fluctuations. As visualized by the overlaid lateral porosity profiles in Figure 5.2 (bulk, black; confined cylindrical, red), the bed porosity of the generated bulk packings ($\varepsilon = 0.378$) matches the bed porosity in the core region of the confined cylindrical packings.

[234] A. J. Sederman, P. Alexander, and L. F. Gladden. *Powder Technol.*, **117**: 255–269, 2001.
[235] A. de Klerk. *AIChE J.*, **49**: 2022–2029, 2003.
[236] D. Tang et al. *Chem. Eng. Technol.*, **27**: 866–873, 2004.
[237] J. Theuerkauf, P. Witt, and D. Schwesig. *Powder Technol.*, **165**: 92–99, 2006.
[247] D. Hlushkou, A. Seidel-Morgenstern, and U. Tallarek. *Langmuir*, **21**: 6097–6112, 2005.

We note here for clarity that the above-described wall effect is a purely geometrical effect existing in immediate vicinity of the column wall. This geometrical wall effect is distinct from a second and more extended wall effect caused by friction between the particles of the bed and the column wall,[238,292,293] The latter effect is traditionally discussed in chromatography in connection with relatively large column-to-particle diameter ratios. Here, the packing density near the wall is *higher* than in the core region. The effect is related to the relatively high compressibility of pulverulent materials and the complex distribution of axial and radial stress during compression of the bed. The extent of this effect strongly depends on the packing procedure and operational conditions.

The *geometrical* wall effect (Figure 5.2) was envisioned early in the chromatographic literature[274,294] and later carefully studied by Jorgenson and co-workers with packed capillaries.[239,240,295] For example, Kennedy and Jorgenson[239] and subsequently Hsieh and Jorgenson[240] have demonstrated that the performance of fused silica capillaries packed with $5\,\mu$m sized porous C18-silica particles improves significantly with decreasing capillary inner diameter between 12 and $50\,\mu$m. At these low aspect ratios of $d_\mathrm{c}/d_\mathrm{p} \leq 10$,[239,240] the core region ultimately disappears and the packing structure is dominated by the wall region, i.e., the packing structure becomes effectively more ordered and homogeneous over the whole cross section. In this respect, the analysis of longitudinal dispersion in confined cylindrical sphere packings at *low* cylinder-to-particle diameter ratios is a topic with a long tradition in the engineering literature,[166] although the precise dependence of dispersion on the aspect ratio and the packing length has found renewed attention.[42,180,296] A closely related diameter-dependent dispersion has also been observed in numerical studies which suggest that the adverse influence of the geometrical wall effect on longitudinal dispersion remains significant even at aspect ratios on the order of $d_\mathrm{c}/d_\mathrm{p} = 100$.[180,297] In the present study, we selected an intermediate aspect ratio ($d_\mathrm{c}/d_\mathrm{p} = 20$) for which the more ordered wall region and the random–close-packed core region both have significant volume fractions. In addition, we took great care to generate packings long enough $L_\mathrm{bed} = L_z = 6553.6\,d_\mathrm{p}$ to enable *complete* transcolumn equilibration. The truncation of dispersion data due to insufficient packed-bed length in chromatography is known to result in artificially strong tapering-off of plate height data at higher velocities[130] which, in turn, affects the values of both λ_i and ω_i.

5.4.1 Bulk packings

The generated bulk packings mimic infinitely wide, unconfined random sphere packings to study hydrodynamics and eddy dispersion without the complex influence of wall effects.[238] To quantify

[292] G. Guiochon, E. Drumm, and D. Cherrak. *J. Chromatogr. A*, **835**: 41–58, 1999.
[293] R. A. Shalliker et al. *J. Chromatogr. A*, **977**: 213–223, 2002.
[294] J. H. Knox and J. F. Parcher. *Anal. Chem.*, **41**: 1599–1606, 1969.
[239] R. T. Kennedy and J. W. Jorgenson. *Anal. Chem.*, **61**: 1128–1135, 1989.
[240] S. Hsieh and J. W. Jorgenson. *Anal. Chem.*, **68**: 1212–1217, 1996.
[295] K. D. Patel et al. *Anal. Chem.*, **76**: 5777–5786, 2004.
[296] E. Vandre et al. *AIChE J.*, **54**: 2024–2028, 2008.
[297] J. Tobis' and D. Vortmeyer. *Chem. Eng. Process.*, **29**: 147–153, 1991.
[130] D. Hlushkou and U. Tallarek. *J. Chromatogr. A*, **1126**: 70–85, 2006.

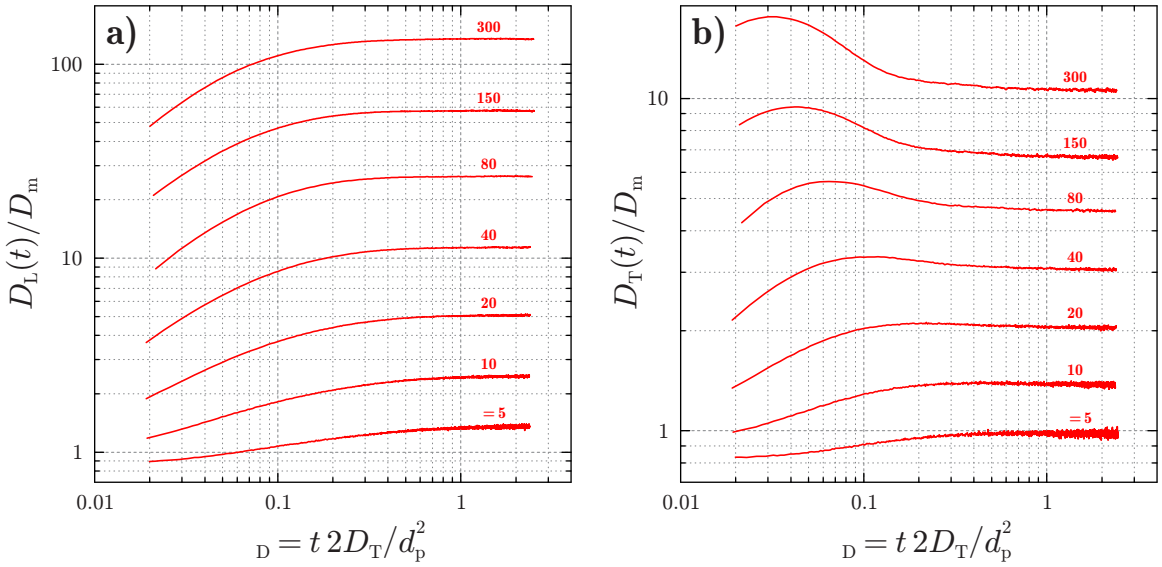

Figure 5.3: Development of longitudinal (a) and transverse (b) dispersion coefficients vs dimensionless transverse dispersive time $\tau_D = 2D_T t/d_p^2$ in bulk packings ($\varepsilon = 0.378$). Reduced velocities $\nu = u_{av} d_p/D_m$ ($d_p = 5\,\mu$m, $D_m = 1.5 \times 10^{-9}$ m^2/s) are given for each curve. Note that the values covered by $D_L(t)/D_m$ and $D_T(t)/D_m$ for the displayed range of reduced velocities differ by one order of magnitude.

time and length scales behind the velocity heterogeneities in bulk packings we analyze the development of longitudinal and transverse dispersion coefficients. Transient values are denoted as $D_L(t)$ and $D_T(t)$, while the absence of the time parameter denotes time independence. Monitoring the transient behavior of the dispersion process toward asymptotic values allows us to distinguish between individual contributions to eddy dispersion, especially with regard to the *upper* limit of the involved time and length scales. This will help to condense, where physically meaningful, the number of scales of velocity disparity in the packing proposed by Giddings[131] (cf. Figure 5.1). In the investigated bulk packings, we expect only the transchannel and a (yet not closer defined) short-range interchannel effect to contribute to eddy dispersion.

Parts (a) and (b) of Figure 5.3 show the development of longitudinal and transverse dispersion coefficients, respectively, for selected values of $\nu = u_{av} d_p/D_m$ from the investigated range of reduced velocities ($0.5 \leq \nu \leq 500$). Elapsed time in Figure 5.3 has been normalized through the transverse dispersive time $\tau_D = 2D_T t/d_p^2$ to reveal general trends. The dispersive time unit $2D_T t/d_p^2$ corresponds to the time span after which tracer particles are dispersed laterally by one sphere diameter. The use of a transverse dispersive time scale is important here, because neither pure diffusion nor pure convection determines the lateral equilibration between different velocities, which instead would have resulted in a diffusive ($\tau_D = 2D_T t/d_p^2$) or a convective ($\tau_C = u_{av} t/d_p$) time scale. The use of $D_T(\nu)$ in the dimensionless dispersive time scale τ_D reflects the *combination* of flow and diffusion which is also the essence of Giddings' coupling theory.[131]

Throughout the range of reduced velocities both $D_L(t)/D_m$ (Figure 5.3a) and $D_T(t)/D_m$ (Figure 5.3b) demonstrate the attainment of asymptotic values after $\tau_D \approx 2$. First, this unique behavior shows that the time scale for asymptotic behavior in a bulk random sphere packing is

indeed adequately characterized by normalization with respect to the value of $D_{\mathrm{T}}(\nu)$, as done in Figure 5.3. Second, the asymptotic time scale of $\tau_{\mathrm{D}} = 2D_{\mathrm{T}}t/d_{\mathrm{p}}^2 \approx 2$ translates to a characteristic average transverse dispersion length in the bulk packings $\langle l_{\mathrm{T}} \rangle_{\mathrm{bulk}}$ of

$$\langle l_{\mathrm{T}} \rangle_{\mathrm{bulk}} = \sqrt{2D_{\mathrm{T}}(\nu)t} \approx \sqrt{2}\, d_{\mathrm{p}}. \tag{5.5}$$

Thus, dispersion in the bulk packings becomes asymptotic after a distance of approximately $1.4\, d_{\mathrm{p}}$ has been sampled laterally by the tracer molecules. However, the *absolute* time required for this process decreases with increasing velocity due to the concomitant increase of $D_{\mathrm{T}}(\nu)$. For example, at $\nu = 10$ the asymptotic value for $D_{\mathrm{T}}(t)/D_{\mathrm{m}}$ is 1.38, whereas at $\nu = 150$ this ratio has already grown to 6.72 (Figure 5.3).

The analysis of longitudinal and transverse dispersion asymptotic time and length scales confirms our surmise that a shortscale heterogeneity is responsible for the *upper* limit in the time and length scales of eddy dispersion in the bulk packings. Although transchannel equilibration is required in any packed bed, ordered or random, the short-scale heterogeneity observed here on the order of $1\text{–}2\, d_{\mathrm{p}}$ (equation (5.5)) is probably associated with the disorder introduced in a random sphere packing compared to a crystal-like structure, e.g., an ordered array of spheres. For the short-range interchannel contribution Giddings estimated a distance of $\sim 1.25\, d_{\mathrm{p}}$ to be required for exchanging molecules between the involved velocity extremes (page 45 in Reference [131]) This estimate compares favorably with our own characterization of a short-scale heterogeneity over a distance of $\sim 1.4\, d_{\mathrm{p}}$ associated with packing randomness.

Figure 5.3 also displays the difference between longitudinal and transverse dispersion curves. Whereas longitudinal dispersion curves (Figure 5.3a) increase monotonically up to their asymptotic values for all selected reduced velocities, transverse dispersion curves (Figure 5.3b) show a peak for fluid velocities of $\nu > 10$, i.e., as convection begins to dominate over diffusion. With increasing fluid velocity the peak is shifted toward very short times τ_{D}.[42,123] The form of the transverse dispersion curves is caused by longitudinal convection which initially forces the average tracer to make a transverse displacement on the order of $d_{\mathrm{p}}/2$ around a sphere (the obstacle). Afterward, the tracer may either move back toward its initial transverse position or further increase its transverse displacement, yielding a net reduction in the rate of spreading.

To summarize, the analysis of transient dispersion in the bulk packings reveals a short-range interchannel contribution on the single-particle scale ($1\text{–}2\, d_{\mathrm{p}}$) in addition to the transchannel contribution, which intrinsically exists in any packed bed on the scale of an *individual channel* between the particles ($\ll d_{\mathrm{p}}$). Thus, the investigated bulk packings of monosized spheres can be characterized as random, dense ($\varepsilon = 0.378$), and relatively homogeneous. Structural and flow heterogeneities beyond the documented short-range scale (cf. Figure 5.3 and equation (5.5)) cannot be resolved. This knowledge is extremely helpful in analyzing the dependence of reduced longitudinal plate heights on the reduced velocity, $h_{\mathrm{L}} = f(\nu)$, using the comprehensive Giddings equation (5.2), as it allows us to reduce the number of contributions to eddy dispersion to the transchannel and a short-range interchannel effect (equation (5.2) with $i = 2$).

[123] R. S. Maier et al. *Phys. Fluids*, **12**: 2065–2079, 2000.

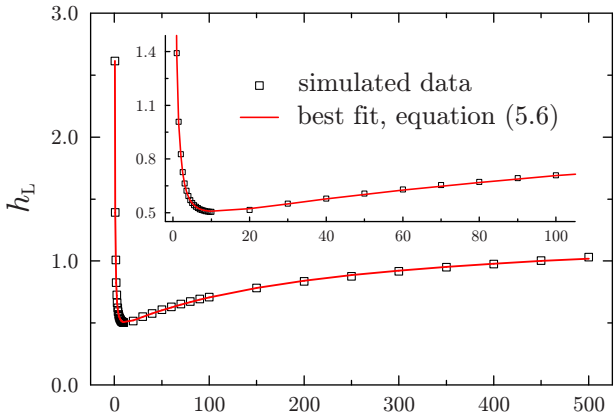

Figure 5.4: Reduced longitudinal plate height $h_L = H_L/d_p$ vs reduced velocity $\nu = u_{av}d_p/D_m$ in the range of $0.5 \leq \nu \leq 500$ for bulk packings. Each data point represents the average from five generated packings ($\varepsilon = 0.378$). The inset shows a selected velocity range $1 \leq \nu \leq 100$ of plate height data.

Thus, we use the following form of equation (5.2) to fit the dependence of reduced longitudinal plate heights (calculated from the asymptotic values of $D_L(t)/D_m$ — see Figure 5.3 — via equation (5.1a)) on the reduced velocity for the bulk packings (cf. equation 2.11-6 on page 63 of Reference [131]):

$$h_L = \frac{2\gamma}{\nu} + \underbrace{\frac{2\lambda_1}{1 + (2\lambda_1/\omega_1)\nu^{-1}}}_{\text{transchannel}} + \underbrace{\frac{2\lambda_2}{1 + (2\lambda_2/\omega_2)\nu^{-1}}}_{\text{short-range interchannel}}, \tag{5.6}$$

where index 1 refers to the transchannel contribution and index 2 to the short-range interchannel contribution to eddy dispersion.

The dependence of h_L on ν for the bulk packings (with a total of 37 values of h_L over the range of $0.5 \leq \nu \leq 500$ where each value of h_L represents the average from five bulk packings obtained from different initial seeds, but with the same final interparticle porosity of $\varepsilon = 0.378$) is shown in Figure 5.4, together with the best fit of these data to equation (5.6). The condensed Giddings equation for bulk packings (5.6) excellently fits simulated plate heights over the whole range of reduced velocities ($R^2 = 0.9998$). The parameters obtained from that fitting are $\gamma = 0.64$, $\lambda_1 = 0.41$, $\omega_1 = 0.0038$, $\lambda_2 = 0.223$, and $\omega_2 = 0.15$. These values agree reasonably well with Giddings' estimation for the transchannel and short-range interchannel parameters: $\lambda_1 \sim 0.5$, $\omega_1 \sim 0.01$, $\lambda_2 \sim 0.5$, and $\omega_2 \sim 0.5$.[131] Concerning the remaining differences in the "universal" structural parameters (λ_i and ω_i) it should be noted that the exact geometrical and topological differences between packed beds analyzed by Giddings and those studied in this work (and particularly those encountered in chromatographic practice) are hardly known with sufficient accuracy to allow for meaningful *quantitative* distinctions. distinctions. Thus, we conclude our analysis of eddy dispersion in bulk random sphere packings with a physically consistent restraint to the transchannel and a short-scale interchannel heterogeneity in the cross-sectional velocity distribution, as well as with a reasonable agreement to the values of the structural parameters estimated by Giddings for these

two contributions. Before continuing and comparing the results with those for confined cylindrical packings, several aspects should be mentioned about the analysis conducted so far.

First, the value of $\gamma = D_{\mathrm{eff}}(t)/D_{\mathrm{m}} = 0.64$ for fixed beds of monosized spheres with an interparticle porosity of $\varepsilon = 0.378$, obtained by fitting the $h_{\mathrm{L}} = f(\nu)$ data in Figure 5.4 to equation (5.6), agrees very well with data reported for similar systems.[298,299] Further, we observed a value of $\gamma = 0.64$ also independently by monitoring the long-time (tortuosity) limit of the diffusion coefficient D_{eff} in the bulk packings (equation (5.4)), analogous to $D_{\mathrm{L}}(t)/D_{\mathrm{m}}$ in Figure 5.3a but for $\gamma = 0$. This demonstrates that sufficient plate height data were simulated at low velocities (20 values of h_{L} in the range of $0.5 \leq \nu \leq 10$, cf. inset in Figure 5.4) where the contribution of molecular diffusion to longitudinal dispersion is important.

Second, by examining the above-determined structural parameters (λ_i and ω_i) we identify the short-range interchannel effect as being responsible for a convex bending of the eddy dispersion curve at low velocities, whereas the transchannel effect causes the eddy dispersion curve (and overall plate height data) to taper off at high velocities. This can easily be understood by calculating the transition velocities $\nu_{1/2} = 2\lambda_i/\omega_i$ for each contribution to eddy dispersion at which the plate height term reaches half of its limiting value and thereafter begins to flatten noticeably.[286] We obtain $\nu_{1/2} = 215$ for the transchannel effect and $\nu_{1/2} = 3$ for the short-range interchannel effect. The values provided by Giddings are 100 and 2, respectively.[131] Where $\nu_{1/2}$ is large (transchannel effect) the contribution to the reduced plate height continues to increase with the velocity over a significant range of the plot in Figure 5.4, the same as for an ordinary kinetics or mass transfer velocity proportional term, whereas the plate height contribution of the short-range interchannel effect reaches its plateau at relatively low velocities. We will return to the consequences of the widely disparate transition velocities for the individual contributions to eddy dispersion with the analysis of the plate height data for the confined packings.

5.4.2 Confined cylindrical packings

The transient behavior of longitudinal and transverse dispersion coefficients toward asymptotic values was monitored for the confined cylindrical packings, expecting an additional transcolumn contribution to eddy dispersion. Figure 5.5 shows the development of $D_{\mathrm{L}}/D_{\mathrm{m}}$ and $D_{\mathrm{T}}/D_{\mathrm{m}}$ (Figure 5.5, parts (a) and (b), respectively) for a few selected values of $\nu = u_{\mathrm{av}} d_{\mathrm{p}}/D_{\mathrm{m}}$ from the investigated range of reduced velocities (here $0.1 \leq \nu \leq 500$). Elapsed time in Figure 5.5 has again been normalized through the transverse dispersive time $\tau_{\mathrm{D}} = 2D_{\mathrm{T}}t/d_{\mathrm{p}}^2$, with the value for $D_{\mathrm{T}}(\nu)$ taken from the *bulk* packings. Several aspects are immediately apparent when comparing Figure 5.5 (confined cylindrical packings) to Figure 5.3 (bulk packings). First, the longitudinal dispersion curves have the same form, but the time scale for asymptotic longitudinal dispersion in the confined packings is significantly larger than for the bulk packings. Second, transverse dispersion curves in the confined packings decrease to *zero*, on a time scale ca. 4 times longer than it takes to reach asymptotic longitudinal dispersion.

[298] L. L. Latour et al. *J. Magn. Reson., Ser. A*, **101**: 342–346, 1993.
[299] J. M. Zalc, S. C. Reyes, and E. Iglesia. *Chem. Eng. Sci.*, **59**: 2947–2960, 2004.

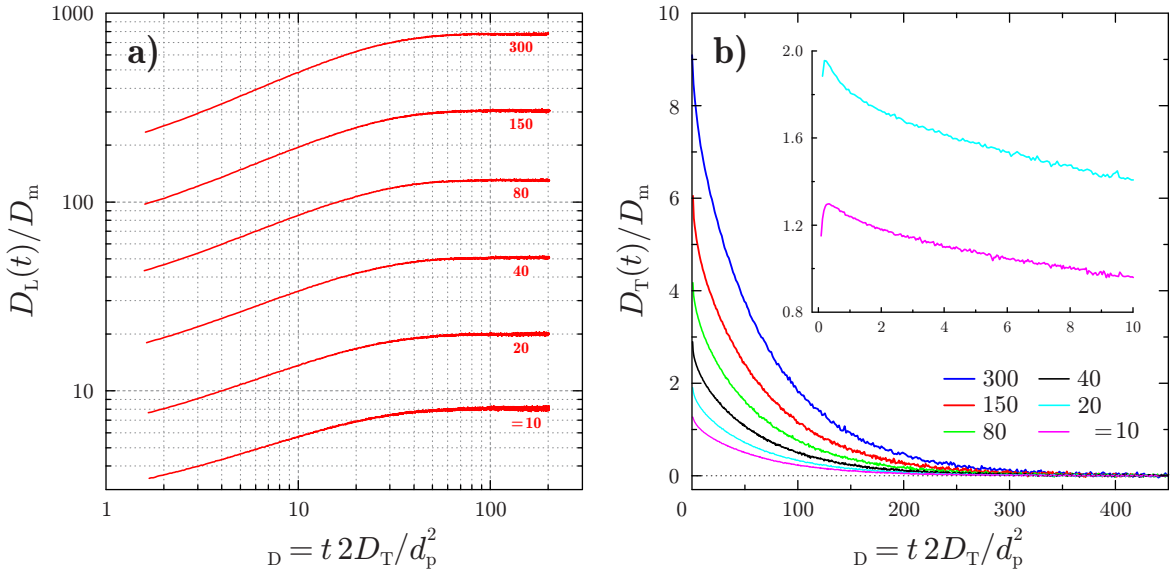

Figure 5.5: Development of longitudinal (a) and transverse (b) dispersion coefficients vs dimensionless transverse dispersive time $\tau_D = 2D_T t/d_p^2$ in confined cylindrical packings (cf. Figure 5.2) with $\varepsilon = 0.40$. Reduced velocities $\nu = u_{av} d_p/D_m$ ($d_p = 5\,\mu$m, $D_m = 1.5 \times 10^{-9}$ m^2/s) are given for each curve. The inset shows D_T/D_m for $\nu = 10$ and 20 at short times.

Throughout the covered range of reduced velocities the longitudinal dispersion data D_T/D_m (Figure 5.5a) demonstrate the attainment of asymptotic values at $\tau_D \sim 100$, corresponding to a characteristic average transverse dispersion length in the confined packings $\langle l_T \rangle_{\text{confined,L}}$ of

$$\langle l_T \rangle_{\text{confined,L}} = \sqrt{2D_T(\nu)t} \approx 10 d_p \equiv \frac{d_c}{2}. \tag{5.7}$$

This result clearly demonstrates that the macroscopic flow heterogeneity caused by the cylindrical confinement of the sphere packing adds a transcolumn contribution to eddy dispersion, which — due to the cylindrical symmetry — requires a lateral equilibration on the scale of the cylinder radius $(d_c/2)$. The observed asymptotic time scale of $t \approx (d_c/2)^2/2D_T(\nu)$ for longitudinal dispersion is reminiscent of classical Taylor–Aris dispersion in laminar (Poiseuille) flow through an *unpacked* cylindrical column (open tube), where the asymptotic time scale is proportional to $t \approx (d_c/2)^2/2D_m$.[276]

Transverse asymptotic dispersion is observed after $\tau_D = 2D_T t/d_p^2 \approx 400$ (Figure 5.5b) which translates to a characteristic average transverse dispersion length in the confined cylindrical packings $\langle l_T \rangle_{\text{confined,T}}$ of

$$\langle l_T \rangle_{\text{confined,T}} = \sqrt{2D_T(\nu)t} \approx 20 d_p \equiv d_c. \tag{5.8}$$

This result is not surprising because the cylindrical confinement of the sphere packing imposes limits on the lateral displacements of the tracer particles. Tracer particles on their journey laterally through the sphere packings are bounced back from the cylinder wall. This implies that transverse dispersion has decayed to zero after the time $t \approx (d_c)^2/2D_T(\nu)$ has elapsed (Figure 5.5b), i.e., the

asymptotic time scale for the confined cylindrical packings is 2^2 times larger in transverse than in longitudinal direction. It should be mentioned here that compared to the work of Jorgenson and co-workers[239,240,295] with packed capillaries and to the situation in nano-HPLC in general, where the ratio of packed bed length to column diameter is typically on the order of thousands, most HPLC separations which involve larger column diameters, but also analytical and narrow-bore HPLC separations, are carried out under nonequilibrium conditions where the analyte residence times in a column are insufficient to *fully* relax transcolumn contributions to eddy dispersion. Thus, the complete dynamic process illustrated in detail in Figure 5.5 is usually truncated (i.e., the asymptotic longitudinal dispersion coefficient or plate height cannot be achieved) and it may be incorrectly concluded that wall effects are absent.

The preceding analysis of transient dispersion (Figures 5.3 and 5.5) demonstrates that, in addition to the transchannel and the short-range interchannel contributions to eddy dispersion identified for the bulk packings, a transcolumn contribution term needs to be added to the reduced plate height equation $h_L = f(\nu)$ for the confined packings:

$$h_L = \frac{2\gamma}{\nu} + \underbrace{\frac{2\lambda_1}{1+(2\lambda_1/\omega_1)\nu^{-1}}}_{\text{transchannel}} + \underbrace{\frac{2\lambda_2}{1+(2\lambda_2/\omega_2)\nu^{-1}}}_{\text{short-range interchannel}} + \underbrace{\frac{2\lambda_1}{1+(2\lambda_1/\omega_1)\nu^{-1}}}_{\text{transcolumn}} . \tag{5.9}$$

The dependence of h_L on ν for the confined packings (with a total of 41 values of h_L over the range of $0.1 \leq \nu \leq 500$, where each value of h_L represents the average from five confined packings obtained from different initial seeds, but with the same final interparticle porosity of $\varepsilon = 0.40$) is shown in Figure 5.6, together with the best fit of these data to equation (5.9). For a better analysis of the wall effect in the confined packings, we limited the number of unknown parameters in equation (5.9) by using the values λ_1 and ω_1 for the transchannel contribution as obtained for the bulk packings. This is a valid first approximation because the transchannel contribution appears to be the most "universal" eddy dispersion contribution which is expected to show the least variations between different packings of similar packing density and composed of identical particles. The short-range interchannel and transcolumn contributions, by contrast, are far more difficult, if possible at all, to generalize.

As seen in Figure 5.6, the comprehensive Giddings equation for the confined packings (5.9) excellently fits simulated plate heights over the whole range of reduced velocities ($R^2 = 0.9996$). The parameters obtained from that fitting are $\gamma = 0.67$, $\lambda_1 \equiv 0.41$, $\omega_1 \equiv 0.0038$, $\lambda_2 = 0.86$, $\omega_2 = 0.436$, $\lambda_3 = 2.61$, and $\omega_3 = 0.023$. The value obtained for γ can be explained by the slightly higher bed porosity of the confined ($\varepsilon = 0.40$, $\gamma = 0.67$) compared to the bulk packings ($\varepsilon = 0.378$, $\gamma = 0.64$). A very similar value of $\gamma = 0.66$ was obtained independently via equation (5.4) by monitoring the long-time (tortuosity) limit of the diffusion coefficient D_{eff} in the confined packings, analogous to $D_L(t)/D_m$ in Figure 5.5a but for $\nu = 0$. In comparison to the bulk packings the dramatic influence of the cylindrical confinement on packing microstructure (Figure 5.2), the resulting macroscopic flow heterogeneity, and the associated transcolumn equilibration behind the overall eddy dispersion (Figure 5.5) are immediately recognized in the comparatively large value of $\lambda_3 = 2.61$ (with respect to the transchannel and short-range interchannel contributions) as well

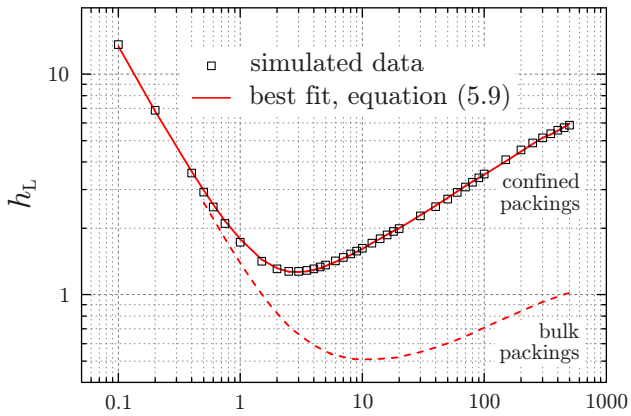

Figure 5.6: Reduced longitudinal plate height (h_L) vs reduced velocity (ν) in the range of $0.1 \leq \nu \leq 500$ for confined cylindrical packings. Each data point represents the average of five generated packings ($\varepsilon = 0.40$). Plate height data for the bulk packings (dashed line) are shown as well for comparison.

as in the coordinates characterizing the plate height minimum in the h_L–ν space in Figure 5.6: $h_{L,bulk} = 1.27$ at $\nu_{min} = 2.5$–3.0 for the confined packings versus $h_{L,bulk} = 0.5$ at $\nu_{min} = 10$–12 for the bulk packings. This result *demonstrates* that the impressive performance of the bulk packings is largely obscured by the geometrical wall effect arising from the cylindrical packing confinement, here illustrated for a cylinder-to-particle diameter ratio of $d_c/d_p = 20$. At $\nu = 500$, for example, the minimum plate height in the confined cylindrical packings ($h_L = 5.96$) is nearly 6 times larger than in the bulk packings ($h_L = 1.03$). In HPLC practice the favorable bulk performance is usually further obscured by extracolumn band broadening, and plate heights generally increase for *porous* particles due to diffusion and adsorption/desorption in the stationary phase.

We return to the reduced transition velocities $\nu_{1/2} = 2\lambda_i/\omega_i$ which characterize the individual contributions to eddy dispersion. From the analysis of the data for the confined cylindrical packings in Figure 5.6 we obtain $\nu_{1/2} = 215$, 3.9, and 227 for the transchannel, short-range interchannel, and transcolumn contributions, respectively. The reduced transition velocity is a rough dividing point between the dominance of diffusive and flow mechanisms of lateral exchange in a packing at lower and higher velocities, respectively. The high transition velocities of the transchannel and transcolumn contributions indicate that in a practical range of chromatographic operation, at reduced velocities of about $5 \leq \nu \leq 20$, these effects reduce to simple mass transfer velocity-proportional terms, while only the short-range interchannel contribution retains its coupling characteristics, i.e., with $(2\lambda_i/\omega_i \gg \nu)$, the transchannel and transcolumn contributions can be expressed just as $\omega_i\nu$. The total effect of the component plate height curves to eddy dispersion can then be written in the form

$$h_{L,eddy} = (\omega_1 + \omega_3)\nu + \frac{2\lambda_1}{1 + (2\lambda_1/\omega_1)\nu^{-1}}, \tag{5.10}$$

where $i = 1$, 2, and 3 denote the transchannel, short-range interchannel, and transcolumn contributions, respectively. This result agrees well with the scale analysis presented by Giddings for these

three contributions.[131] The relatively low impact of coupling between diffusive and flow mechanisms of eddy dispersion in this limited range of velocities ($5 \leq \nu \leq 20$) also explains why the van Deemter equation (equation (5.3) with $n = 0$) remains an accurate description of plate height data in that case, particularly with porous particles, when the mass transfer terms associated with the stationary phase are added.[261,300] Our study demonstrates that the geometrical wall effect,[42,235] here illustrated at an aspect ratio of $d_c/d_p = 20$, adds a transcolumn contribution to eddy dispersion which, over a substantial range of reduced velocities (but certainly within a practical range of chromatographic operation), can be adequately represented by a conventional mass transfer term giving rise to a nearly linear dependence of h_L on ν. This conclusion, however, is strictly valid only for the studied packing where only the geometrical wall effect which is an intrinsic property of confined hard sphere packings exists. In real-life HPLC columns, however, issues are complicated by the fact that wall effects can vary widely from column to column, not only because the values of λ_3 and ω_3 for the transcolumn contribution vary with the aspect ratio, but also because these parameters are a sensitive function of the packing procedure and particle characteristics like shape and size distribution or surface roughness. For example, the "size-separation effect" originally analyzed by Giddings in the context of wall effects[131,301] is caused by a very special packing procedure. Thus, the wall of an HPLC column can interact with the packing in different ways which are simple to understand individually but whose consequences for eddy dispersion and dependence from d_c/d_p. are much more difficult to predict and analyze.

5.5 Conclusions

A carefully conducted numerical analysis of longitudinal and transverse dispersion in computer-generated bulk and confined cylindrical packings of monosized, nonporous, spherical particles has allowed us to identify time and length scales as well as the magnitude of individual contributions to eddy dispersion in each type of packing. For the bulk (unconfined) random-close packings with interparticle porosities of $\varepsilon = 0.378$ only transchannel and short-range interchannel contributions (on a length scale of $1–2\ d_p$ to eddy dispersion were identified from the transient dispersion behavior. These two contributions, in turn, were used in the analysis of the dependence of the reduced longitudinal plate height on the reduced velocity for $0.5 \leq \nu \leq 500$ (equation (5.6)). Reasonable agreement of the "universal" structural parameters (λ_i and ω_i) and the transition velocities $\nu_{1/2}$ for transchannel and short-range interchannel contributions with the values estimated by Giddings for these effects was observed.

A similar analysis was subsequently conducted for the confined cylindrical packings with an aspect ratio of $d_c/d_p = 20$ and $\varepsilon = 0.40$. This analysis revealed a dominating influence of the geometrical wall effect in the transient dispersion behavior in the much larger time and length scales for asymptotic longitudinal and transverse dispersion than observed for the bulk packings. Whereas asymptotic longitudinal dispersion is achieved on a time scale proportional to the square of the column radius, transverse dispersion decays to zero on a time scale proportional to the square of the column diameter, i.e., 4 times more slowly. The influence of the geometrical wall

[300] K. M. Usher, C. R. Simmons, and J. G. Dorsey. *J. Chromatogr. A*, **1200**: 122–128, 2008.
[301] J. C. Giddings and E. N. Fuller. *J. Chromatogr.*, **7**: 255–258, 1962.

effect on the dispersion behavior is also apparent in the dependence of the reduced plate height data on the reduced velocity for $0.1 \leq \nu \leq 500$. In particular, the coordinates in the h_{L}–ν space characterizing the plate height minimum demonstrated a shift from $h_{\mathrm{L,min}} = 0.5$ at $\nu_{\mathrm{min}} = 10$–12 for the bulk packings to $h_{\mathrm{L,min}} = 1.27$ at $\nu_{\mathrm{min}} = 2.5$–3.0 for the confined cylindrical packings (Figure 5.6). As a consequence of the geometrical wall effect (manifested in damped porosity oscillations over a distance of 4–$5\,d_{\mathrm{p}}$ from the cylinder wall) in the confined cylindrical packings, a relatively large eddy dispersion parameter λ_3 was observed for the transcolumn contribution in the comprehensive Giddings equation. The latter had been carefully adapted to the actual packing morphology (equation (5.9)), using insight gained from the bulk packings. Given the approximate nature of the classification of eddy dispersion contributions and the estimation of the actual numerical magnitude of the involved parameters, the agreement between the well-defined sets of transient and asymptotic dispersion data presented in this work and the physicochemical–hydrodynamic nature of eddy dispersion contributions according to Giddings is favorable. In the velocity range typically used in operating chromatographic columns the comprehensive Giddings equation for the studied packing can be reduced to a composite expression in which only the short-range interchannel contribution retains its coupling characteristics, while transchannel and transcolumn contributions (due to their relatively high transition velocities) appear as simple mass transfer velocity-proportional terms (equation (5.10)). This also demonstrates that, in order to resolve the Giddings equation comprehensively, plate height data have to be acquired carefully, e.g., without extracolumn effects or contributions from intraparticle diffusion and adsorption. In addition, a relatively wide range of velocities needs to be covered because the individual eddy dispersion contributions taper off in different flow regimes. Other effects (particle shape and size distribution, intraparticle porosity and adsorption) can be incorporated and addressed progressively in future work to refine the current picture.

Chapter 6

Influence of packing heterogeneity on hydrodynamic dispersion

Microstructure of the random sphere packings can be classified as more or less heterogeneous, or, in other words, packings can have different *Degree of Heterogeneity* (DoH). In this chapter, hydrodynamic dispersion is studied in the bulk packings with systematically varied values of porosity and DoH. DoH was successfully quantified and correlated with the values of the dispersion coefficient. To our knowledge, this study is the first systematic analysis of the influence of DoH on the hydrodynamic dispersion, presented in the literature. The results of this chapter were published in *Journal of Chromatography A* in 2010.[302]

6.1 Introduction

The properties of a wide variety of materials, including liquids, glasses, crystals, and granular media, depend on the way particles pack and arrange.[303] One of the scientists who first investigated the microscopic nature of granular media was Bernal,[304–306] who in a series of papers about the "structure of liquids" reported some of the most important features of the structural organization of disordered sphere packings. Bernal originally used random packings of ball bearings to study the structure of liquids and he coined the term 'random-close packing' to describe the densest random arrangement of spheres. Indeed, the filling of containers with balls is among the oldest physical puzzles known to scientists.[307] Apart from its mathematical significance, this problem has found applications in modern science related, e.g., to jamming in granular media, compaction of colloids, the structure of liquids, and the glass transition.[308] Despite the progress made in developing a statistical mechanics for such systems,[309] the definition of jammed states and the characterization

[302] S. Khirevich et al. *J. Chromatogr. A*, **1217**: 4713–4722, 2010.
[303] S. Torquato. *Random heterogeneous materials: microstructure and macroscopic properties*. Springer, 2002.
[304] J. D. Bernal. *Nature*, **183**: 141–147, 1959.
[305] J. D. Bernal and J. Mason. *Nature*, **188**: 910–911, 1960.
[306] J. D. Bernal. *Philos. Trans. R. Soc. A*, **280**: 299–322, 1964.
[307] T. Aste and D. L. Weaire. *The pursuit of perfect packing*. Taylor & Francis, 2000.
[308] A. Coniglio et al., eds. *Unifying concepts in granular media and glasses*. Elsevier, 2004.
[309] S. F. Edwards and R. B. S. Oakeshott. *Physica A*, **157**: 1080–1090, 1989.

of their randomness are still intensively discussed.[171,310–314]

In chromatography we have accepted to "jam-pack" columns by a slurry packing process that experience has told us to be most appropriate in terms of the traditionally measured (post-column) separation efficiency.[279,315] The packing process involves several, often strongly interrelated, parameters, among them the physicochemical properties of the stationary-phase particles, interparticle forces, slurry preparation, the application of pressure and ultrasound, as well as the coupled stress–strain-flow behavior.[316] Owing to the difficulty in probing the packing microstructure systematically as a function of all relevant process parameters, column packing and consolidation are largely treated phenomenologically and considered an art rather than a science. Although at present the packing process cannot be approached comprehensively by simulations, recent progress in our understanding and modeling of the dynamic behavior of particulate systems originates from discrete particle simulation.[317,318]

The density or particle volume fraction ρ of random sphere packings falls between $\rho \sim 0.55$ and $\rho \sim 0.64$, values which are commonly referred to as the random-loose-packing (RLP) and random-close packing (RCP) limit, respectively.[15,171,319–321] In chromatography, the density of a column packing is more often described by the interparticle void fraction or interparticle porosity $\varepsilon = 1 - \rho$. Stable column packings can vary up to 15% in their interparticle porosities, depending on the packing parameters. Moreover, a given interparticle porosity is just a macroscopic value that may apply to a large number of columns with very different packing microstructures. The latter, however, determine the individual structure–transport relationships that govern hydrodynamic dispersion in and ultimately the separation efficiency of any packed column.

Packing microstructures are commonly classified as "more homogeneous" or "more heterogeneous." These intuitive, qualitative labels are usually based on column performance. Experimentally, it would be desirable to generate packings with a known and controllable degree of heterogeneity. However, this requires a sound scientific quantification of the degree of heterogeneity of the underlying, individual packing microstructure. An adequate quantification of the disorder (or microstructural degree of heterogeneity) in different packings, which could have the same packing density ρ or interparticle porosity ε, and a strong and sensitive correlation to the experimentally observable dispersion, has not yet been demonstrated.

[171] C. Song, P. Wang, and H. A. Makse. *Nature*, **453**: 629–632, 2008.
[310] S. Torquato, T. M. Truskett, and P. G. Debenedetti. *Phys. Rev. Lett.*, **84**: 2064–2067, 2000.
[311] S. Torquato and F. H. Stillinger. *J. Phys. Chem. B*, **105**: 11849–11853, 2001.
[312] K. Bagi. *Granular Matter*, **9**: 109–134, 2007.
[313] C. Briscoe et al. *Phys. Rev. Lett.*, **101**: 188001, 2008.
[314] N. C. Karayiannis, K. Foteinopoulou, and M. Laso. *Phys. Rev. E*, **80**: 011307, 2009.
[279] G. Guiochon. *J. Chromatogr. A*, **1126**: 6–49, 2006.
[315] K. K. Unger, R. Skudas, and M. M. Schulte. *J. Chromatogr. A*, **1184**: 393–415, 2008.
[316] B. G. Yew et al. *AIChE J.*, **49**: 642–664, 2003.
[317] H. P. Zhu et al. *Chem. Eng. Sci.*, **62**: 3378–3396, 2007.
[318] H. P. Zhu et al. *Chem. Eng. Sci.*, **63**: 5728–5770, 2008.
[15] T. Aste, M. Saadatfar, and T. J. Senden. *Phys. Rev. E*, **71**: 061302, 2005.
[319] R. D. Kamien and A. J. Liu. *Phys. Rev. Lett.*, **99**: 155501, 2007.
[320] A. V. Anikeenko, N. N. Medvedev, and T. Aste. *Phys. Rev. E*, **77**: 031101, 2008.
[321] T. Aste and T. Di Matteo. *Eur. Phys. J. B*, **64**: 511–517, 2008.

Detailed three-dimensional numerical simulations of flow and transport in sphere packings are particularly suited to the challenge of investigating the central structure–transport relationships in chromatographic media, because this approach allows to systematically study relevant parameters, such as the shape and average size of the particles, the particle size distribution, inter- and intraparticle porosities, as well as the column dimensions and cross-sectional geometry.[99,172,185,186,247,284,322–325] Transient dispersion can be recorded easily, thereby quantifying time and length scales required for the attainment of asymptotic dispersion behavior and providing correlations for the dependence of dispersion on the mobile phase velocity. Because all dispersion data are referenced to a particular packing microstructure and are unbiased by extra-column contributions, the numerical simulations approach establishes a systematic route towards quantitative structure–transport relationships. Further, statistical information about the structure of the simulated packings can be collected, because position, size, and usually also the shape of the particles are known. However, the microstructures of computer-generated idealized random packings are protocol-dependent, just as packing density and column performance depend on the precise packing protocol in chromatographic practice.[172,310] Thus, any structure–transport analysis should be accompanied by a suitable statistical analysis of the employed packed beds. This will allow to compare and optimize the protocols for simulated as well as experimental packings, e.g., with respect to dispersion.

In the present study we apply a statistical and hydrodynamic analysis to packed beds to correlate disorder with dispersion. We employ Voronoi tessellation and use the distribution of Voronoi volumes to quantify the degree of heterogeneity of a packing. This method permits to explicitly capture the disorder of packed beds in the form of quantitative scalar measures. We demonstrate the great potential of this approach for a well-designed set of computer-generated bulk, random packings of monosized hard spheres with “more homogeneous” and “more heterogeneous” microstructures, covering packing densities from the RLP to the RCP limit, and their asymptotic longitudinal dispersion coefficients simulated over a wide range of mobile phase velocities. To our knowledge, this is the first report that sensitively correlates the actual disorder of packed beds with the measurable dispersion in packed beds, using Voronoi volume distributions as a suitable statistical measure.

6.2 Numerical section

Experience tells us that both packing density or porosity and packing procedure affect dispersion. We therefore generated a set of bulk packings (which mimic infinitely wide, randomly packed beds without walls) with packing (interparticle) porosities ε from the RCP to the RLP limit and a systematically varied degree of heterogeneity.

[99] D. Coelho, J.-F. Thovert, and P. M. Adler. *Phys. Rev. E*, **55**: 1959–1978, 1997.
[172] R. S. Maier et al. *Water Resour. Res.*, **44**: W06S03, 2008.
[185] R. S. Maier et al. *Philos. Trans. R. Soc. A*, **360**: 497–506, 2002.
[186] P. Magnico. *Chem. Eng. Sci.*, **58**: 5005–5024, 2003.
[247] D. Hlushkou, A. Seidel-Morgenstern, and U. Tallarek. *Langmuir*, **21**: 6097–6112, 2005.
[284] S. Stapf et al. *Phys. Rev. E*, **58**: 6206–6221, 1998.
[322] K. E. Thompson and H. S. Fogler. *AIChE J.*, **43**: 1377–1389, 1997.
[323] M. D. Mantle, A. J. Sederman, and L. F. Gladden. *Chem. Eng. Sci.*, **56**: 523–529, 2001.
[324] R. J. Hill, D. L. Koch, and A. J. C. Ladd. *J. Fluid Mech.*, **448**: 213–241, 2001.
[325] M. R. Schure and R. S. Maier. *J. Chromatogr. A*, **1126**: 58–69, 2006.

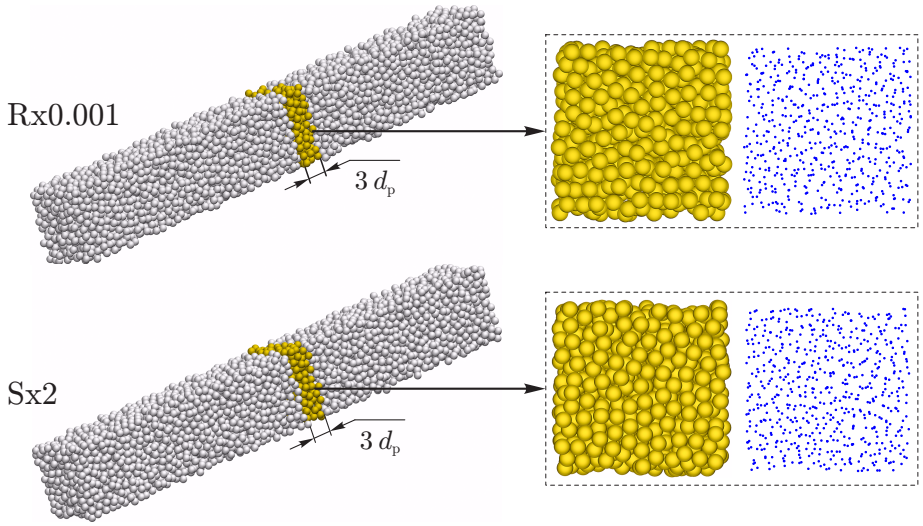

Figure 6.1: Bulk (unconfined) random packings of monosized hard spheres at the random-loose packing limit ($\varepsilon = 0.46$), generated with the Rx0.001 or Sx2 packing protocols. Shown are the generated packings (left) and three particle layers of the packings (right), as a front view and as the projection of particle centers onto the front plane.

Computationally, isotropic random monosized hard-sphere packings with periodic boundary conditions and dimensions of approximately $10\,d_\mathrm{p} \times 10\,d_\mathrm{p} \times 70\,d_\mathrm{p}$ (where d_p is the sphere diameter) were successfully reproduced using a modified Jodrey–Tory (JT) algorithm, which is described in the Section 1.1. The realized packing dimensions are sufficient for performing both statistical analysis of packing microstructure and simulations of hydrodynamic dispersion within the void space of a packing.

In this study we represent varying degrees of microstructural disorder by four different types of packings (see Subsection 1.1.1). So-called R-packings originate from a random uniform initial distribution of particle centers in the simulation box. To generate S-packings, the simulation box was initially divided into n equal cubic cells and each particle center was then placed in a random position into a cell. Here n denotes amount of spheres in the packing. Both types of initial distributions result in a uniform random distribution of particle centers within the simulation box. R-packings were generated with $\alpha = 1$ (R) or $\alpha = 0.001$ (Rx0.001), and S-packings with $\alpha = 1$ (S) or $\alpha = 2$ (Sx2). The meaning of the displacement parameter α is given in the Subsection 1.1.1, equation (1.3). With a small displacement value the particle centers tend to stay closer to their initial positions so that the final configuration reflects the randomness of the initial distribution of particle centers. A larger displacement value provides a more uniform distribution of particle centers in the final configuration. The four generated packing types therefore reflect a systematic decrease of heterogeneity (or disorder) in the sequence: Rx0.001 > R > S > Sx2.

Figure 6.1 shows a front view onto three particle layers as well as a projection of the particle centers for the most ordered and the least ordered of the generated packings (Sx2 and Rx0.001, respectively). Even to the experienced eye, differences between the two packing microstructures are not discernible in Figure 6.1. Therefore, we use two-dimensional views (disks instead of spheres) to illustrate the differences between the four different packing types and additionally

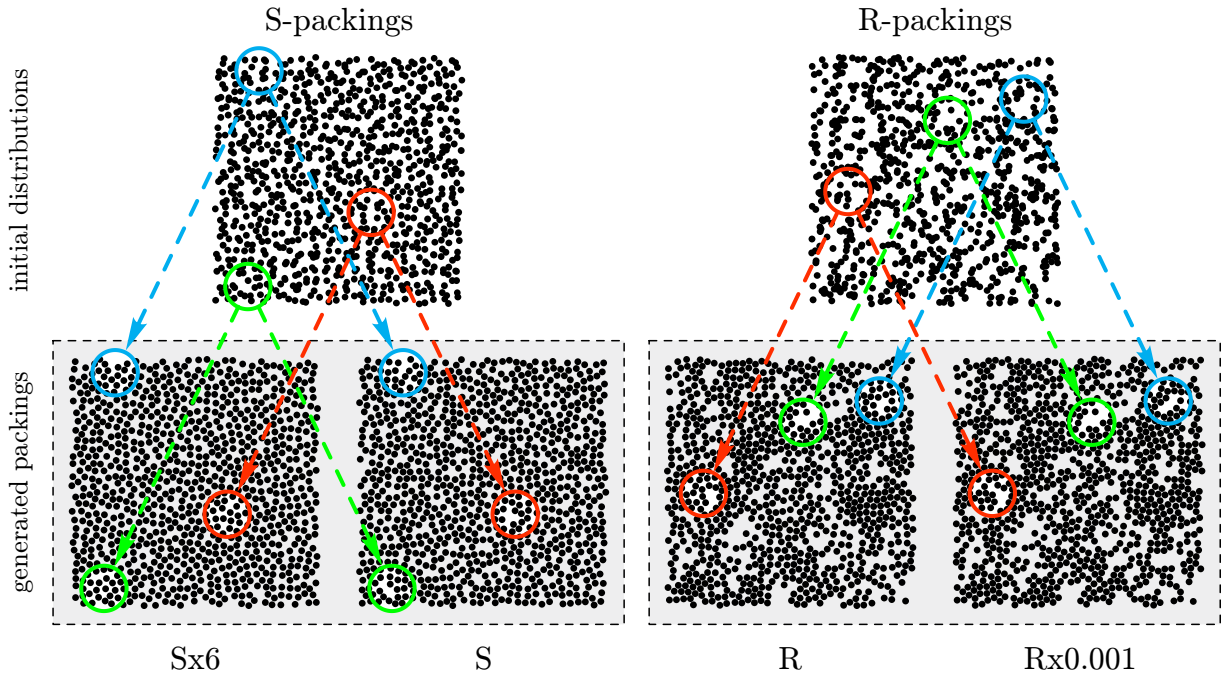

Figure 6.2: Bulk (unconfined) random packings of monosized hard disks at $\varepsilon = 0.46$ generated with different packing protocols. Shown are the initial distributions of the disks for S- and R-configurations (top) and the generated two-dimensional packings (Sx6, S, R, Rx0.001; bottom). Circles around several regions help to compare the microstructure in the initial distributions with that of the final packings.

replace the Sx2 packing by a Sx6 packing for a stronger effect (Figure 6.2). For selected regions the microstructure of the final packings is compared with the respective initial particle center distributions in Figure 6.2. The generated packings indeed reflect what was intended by their respective packing protocols: i) S-packings are more homogeneous than R-packings, owing to the initial, ordered distribution of the disks, and ii) initial nonuniformities are best balanced in the Sx6 configuration and least balanced in the Rx0.001 configuration.

Three-dimensional sphere packings of each type were generated at the following porosities: $\varepsilon = 0.366$, 0.38, 0.40, 0.42, 0.44, and 0.46. The border values ($\varepsilon = 0.366$ and 0.46) reflect the theoretical RCP and RLP limits reported by Song et al.[171] They have shown that random hard-sphere packings in three dimensions cannot exceed a density limit of $\rho = 0.634$ (or $\varepsilon = 0.366$). Similarly, they predicted a theoretical limit for the lowest stable volume fraction occupied by a sphere packing of $\rho = 0.536$ ($\varepsilon = 0.464$).

For each packing protocol and porosity 10 individual packings were generated from 10 different initial positions of particle centers (seeds). We were not able to generate Sx2 packings at the RCP limit ($\varepsilon = 0.366$). The total of all generated packings amounts to 230. Each packing was discretized with a relatively high spatial resolution of 60 nodes per d_p resulting in a space grid with dimensions of approximately $600 \times 600 \times 4300$ nodes.

The lattice-Boltzmann method (LBM) was used for the simulation of low-Reynolds number flow of an incompressible fluid in the interparticle void space of the bulk packings (Subsection 1.3.2).

For each packing, the velocity field was first calculated at a low Reynolds number (~ 0.1), and the calculated velocity field was then linearly rescaled[132] to cover the whole velocity range used in the dispersion simulations.

All simulations were performed on IBM Blue Gene/P systems installed at RZG (Rechenzentrum Garching, Germany) and FZJ (Forschungszentrum Jülich, Germany). A typical simulation of one velocity field required ~ 0.5 h on 2048 processor cores and around 420 GB of memory. After its simulation, the calculated velocity field was written into an output file with a size of ~ 17 GB.

Mass transport in the bulk packings was simulated by a random walk particle tracking (RWPT) technique (Subsection 1.4.2) and time-dependent longitudinal dispersion coefficients $D_{\mathrm{L}}(t)$ and $D_{\mathrm{T}}(t)$ were calculated from the tracer displacements as described in Subsection 1.4.3.

Hydrodynamic dispersion in the packings was simulated at reduced velocities (ν) or particle Péclet numbers (Pe), defined as $\nu \equiv Pe = u_{\mathrm{av}} d_{\mathrm{p}} / D_{\mathrm{m}}$ (where u_{av} is the average mobile phase velocity through the packed bed), ranging from 0.5 to 750. The total simulation time of hydrodynamic dispersion for all generated packings was ~ 460 h on 2048 Blue Gene/P processor cores.

6.3 Results and discussion

6.3.1 Statistical analysis of packed beds

A sensitive analysis tool for probing the local packing density and disorder in packed beds is the determination of Voronoi cells.[41,44,45,326] This method, initiated by Finney,[327] has found increasing use for the characterization of the morphology of random sphere packings, including the study of, e.g., structural transitions upon compaction or the formation of coagulated colloids.[319,328–336] In particular, Schenker et al.[336] recently investigated and compared different methods to quantify and classify the disorder of particulate packings (in the context of stability and microstructure of coagulated colloids) based on i) pore size distribution, ii) density-fluctuation, and iii) Voronoi volume distribution. Each of these methods provides a scalar measure, either via a parameter in a fit function or an integral, that correlates with the heterogeneity of the microstructure and thus allows to quantitatively capture the degree of heterogeneity of a granular material. They found that

[132] M. R. Schure et al. *Anal. Chem.*, **74**: 6006–6016, 2002.
[41] A. Okabe. *Spatial tessellations: concepts and applications of Voronoi diagrams*. 2nd ed. John Wiley & Sons, 2000.
[44] G. Voronoi. *J. Reine Angew. Math.*, **133**: 97–102, 1908.
[45] G. Voronoi. *J. Reine Angew. Math.*, **134**: 198–287, 1908.
[326] G. Voronoi. *J. Reine Angew. Math.*, **136**: 67–182, 1909.
[327] J. L. Finney. *Philos. Trans. R. Soc. A*, **319**: 479–493, 1970.
[328] R. Jullien et al. *Phys. Rev. E*, **54**: 6035–6041, 1996.
[329] L. Oger et al. *Philos. Mag.*, **74**: 177–197, 1996.
[330] P. L. Spedding and R. M. Spencer. *Comput. Chem. Eng.*, **22**: 247–257, 1998.
[331] P. Richard et al. *Granular Matter*, **1**: 203–211, 1999.
[332] R. Y. Yang, R. P. Zou, and A. B. Yu. *Phys. Rev. E*, **65**: 041302, 2002.
[333] J. Q. Xu, R. P. Zou, and A. B. Yu. *Granular Matter*, **9**: 455–463, 2007.
[334] A. V. Anikeenko and N. N. Medvedev. *Phys. Rev. Lett.*, **98**: 235504, 2007.
[335] T. Aste and T. Di Matteo. *Phys. Rev. E*, **77**: 021309, 2008.
[336] I. Schenker et al. *Phys. Rev. E*, **80**: 021302, 2009.

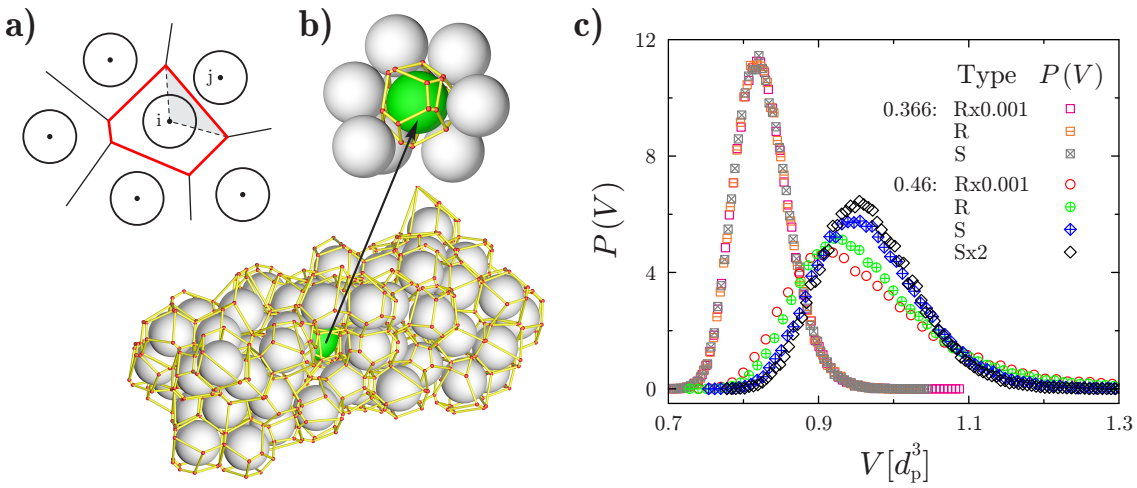

Figure 6.3: a) Voronoi cells in a two-dimensional array of disks. The Voronoi cell of disk i is encased by the bold red lines. The gray-shaded area indicates the contribution of disk j to the Voronoi area of disk i. b) Three-dimensional Voronoi tessellation of a sphere packing (bottom); Voronoi cell of a sphere (highlighted in green) and some of the sphere neighbors contributing to the volume of the cell (top). c) Voronoi volume distributions for the generated bulk sphere packings at the limiting porosities ($\varepsilon = 0.366$ and 0.46).

among the three methods, analysis of the Voronoi volume distributions reflected differences in the degree of microstructural heterogeneity most sensitively.[336] We therefore expect this method to be an excellent diagnostic tool for establishing a strong correlation between disorder and dispersion in packed beds.

A Voronoi cell is the generalization of a Wigner–Seitz cell for disordered structures. For a packing of monosized spheres it is the polyhedron that contains all points closer to a given sphere center than to any other[41,44,45,326] (as illustrated in Figure 6.3a for a set of monosized disks; cf. the area encased by the bold red lines around disk center i). Voronoi tessellation partitions the whole space of a sphere packing into a set of non-overlapping Voronoi volumes V, which are inherently associated with the local packing density. The packing is represented quantitatively by the Voronoi volume distribution $P(V)$. The distribution function is defined such that $P(V)\mathrm{d}V$ is the fraction of cells with a volume between V and $V + \mathrm{d}V$. We used the QUICKHULL algorithm[337] to compute the volume V of the Voronoi cells.

Figure 6.3c shows the Voronoi volume distributions for the generated packings at the limiting porosities, $\varepsilon = 0.366$ and 0.46. At the RCP limit ($\varepsilon = 0.366$), all Voronoi volume distributions are relatively narrow and symmetric, irrespective of the underlying packing protocol. They are nearly perfectly collapsed onto a single "universal" distribution. At the RLP limit ($\varepsilon = 0.46$) the distributions are shifted towards larger Voronoi volumes, as expected from the "dilution" of the packings at increasing porosity, and differences between the packing protocols emerge. Importantly, Voronoi volume distributions become wider and more asymmetric (skewed) with increasing microstructural heterogeneity in a packing. Thus, the Sx2 packing has the narrowest and most symmetric Voronoi volume distribution at $\varepsilon = 0.46$, and the Rx0.001 packing the broadest and most skewed, confirming the qualitative structural insight from Figure 6.2.

[337] C. B. Barber, D. P. Dobkin, and H. Huhdanpaa. *ACM Trans. Math. Software*, **22**: 469–483, 1996.

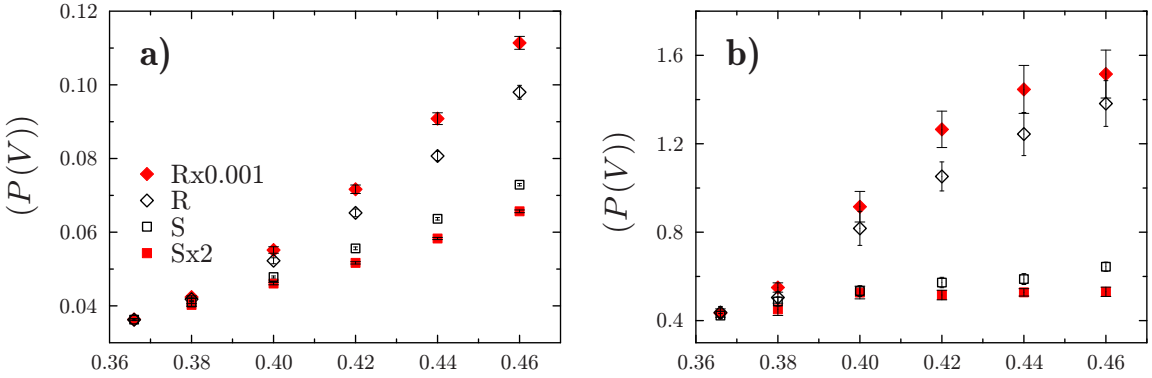

Figure 6.4: Statistical analysis of the Voronoi volume distributions $P(V)$ for the bulk sphere packings (cf. Figure 6.3c). a) Standard deviation σ and b) skewness γ as a function of packing protocol (Rx0.001, R, S, Sx2) and porosity ($0.366 \leq \varepsilon \leq 0.46$). Error bars indicate upper and lower bounds of 95% confidence intervals.

Figure 6.4 summarizes the statistical properties of the Voronoi volume distributions for the generated packings in terms of the standard deviation σ (Figure 6.4a) and the skewness γ (Figure 6.4b). These data quantify the effect of packing protocol and porosity as we move from the RCP ($\varepsilon = 0.366$) to the RLP limit ($\varepsilon = 0.46$) on the microstructural heterogeneity of a packing, already qualitatively discussed for Figure 6.3c. At the RCP limit ($\varepsilon = 0.366$), the standard deviations $\sigma(P(V))$ are practically identical for all generated packings (Figure 6.4a). With increasing porosity $\sigma(P(V))$ increases monotonically, and differences in $\sigma(P(V))$ between the packing types are visible from $\varepsilon = 0.40$. The skewness of the distribution $\gamma(P(V))$ is little affected by increasing porosity for the S-packings (Figure 6.4b). Differentiation between R- and S-packings by $\gamma(P(V))$ starts already at $\varepsilon = 0.38$, and $\gamma(P(V))$ for the R-packings is rather sensitive towards increasing porosity. The strongest effect on the statistical parameters $\sigma(P(V))$ and $\gamma(P(V))$ in Figure 6.4 comes from the principal difference between R- and S-packings, i.e., the random or ordered initial distribution of particle centers. Variation of the rate constant in the packing protocols (i.e., varying the distance over which particle centers can move away from their initial positions) affects the statistical parameters moderately and in the expected direction. Figure 6.4 augments the qualitative picture of Figure 6.2 by a thorough statistical analysis, demonstrating that the S-packings retain relatively narrow and symmetric Voronoi volume distributions even at increasing porosity (as opposed to the R-packings), and that the four generated packing types are indeed characterized by a systematic decrease of disorder in the sequence: Rx0.001 > R > S > Sx2.

The Voronoi volume distributions in Figure 6.4 describe the degree of deviation of a given packing type from a perfectly crystalline packing. All spheres in a crystal are associated with the same Voronoi volume, so that the Voronoi volume distribution is a delta function. For the studied random bulk packings the Voronoi volume distributions become wider and more asymmetric as we move from the RCP ($\varepsilon = 0.366$) to the RLP limit ($\varepsilon = 0.46$). Their standard deviation and skewness can then be used to express and quantify the heterogeneity of a packing (Figure 6.4), analogous to the familiar analysis of separation efficiency from the width and skewness of peaks in a chromatogram.

For completeness we mention that Aste and Di Matteo[335] deduced by statistical mechanics that the Voronoi volume distributions for monodisperse random sphere packings follow a so-called two-parameter 'k-Gamma' function, in which k, the shape parameter of the curve, depends sensitively on the packing microstructure. Furthermore, we also conducted a Delaunay tessellation[41,320] of the generated packings, but found a stronger correlation between dispersion and disorder with the statistical moments of the Voronoi volume distributions.

Our findings (Figure 6.4) agree with those of closely related investigations,[328,332,335] where the dilution of particle packings was always accompanied by broadening and increasing asymmetry of the Voronoi volume distributions. Packings at the RCP limit show merely statistical variations in standard deviation and skewness of their Voronoi volume distributions (Figures 6.3 and 6.4), because the constraints of the RCP limit on the placement of particles allow for so little variation in packing microstructure that the different protocols used in this study will nonetheless yield very similar packings.[171,310,319–321] At the other extreme of stable packings, the RLP limit, the spheres experience more freedom of placement and differences between the packing types are clearly reflected in their Voronoi volume distributions. This behavior can be visualized with a formal analogy between the statistical mechanics of granular jammed matter and classical statistical mechanics: the microcanonical ensemble, defined by all microstates with fixed energy, is replaced by the ensemble of all jammed microstates with fixed volume.[309] Within this notion, the RCP limit of spheres can be interpreted as the ground state of the ensemble of jammed matter for a given friction (see, e.g., the volume landscape of jammed matter, Figure 2 in Reference [171]).

6.3.2 Transient and asymptotic dispersion

We simulated eddy dispersion in the generated packings to correlate the quantified microstructural disorder with the transport properties most relevant to chromatography. The longitudinal dispersion coefficient D_L usually discussed in the engineering literature[166] is related to chromatographic plate height H by[131]

$$D_\mathrm{L} = \frac{u_\mathrm{av} H}{2} = \frac{\nu D_\mathrm{m} h}{2}, \tag{6.1}$$

where $h = H/d_\mathrm{p}$ denotes reduced plate height and ν is the reduced velocity introduced earlier. The flow pattern of a fluid depends critically on the morphology of the pore space available for the flow, so that the inherent structural heterogeneities of the packed beds investigated in this work determine time and length scales that characterize velocity fluctuations in the mobile phase.[89,131,145,276,277,338]

[166] J. M. P. Q. Delgado. *Heat Mass Transfer*, **42**: 279–310, 2006.
[131] J. C. Giddings. *Dynamics of chromatography: principles and theory*. Marcel Dekker, 1965.
[89] J. Bear. *Dynamics of fluids in porous media*. Dover Publications, 1988.
[145] D. L. Koch and J. F. Brady. *J. Fluid Mech.*, **154**: 399–427, 1985.
[276] S. G. Weber and P. W. Carr. In: *High Performance Liquid Chromatography*. P. R. Brown and R. A. Hartwick, eds. Chap. 1. John Wiley & Sons, 1989.
[277] F. Gritti and G. Guiochon. *Anal. Chem.*, **78**: 5329–5347, 2006.
[338] A. L. Berdichevsky and U. D. Neue. *J. Chromatogr.*, **535**: 189–198, 1990.

By applying the random walk relationship to a model of eddy dispersion incorporating the coupling between transverse diffusion and spatial velocity fluctuations, Giddings[131] developed a plate height equation by analogy to parallel conductors. The comprehensive equation for $h = f(\nu)$ is

$$h_{\mathrm{L}} = \frac{H_{\mathrm{L}}}{d_{\mathrm{p}}} = \frac{b}{\nu} + \sum_{i=1}^{4} \frac{2\lambda_i}{1 + (2\lambda_i/\omega_i)\nu^{-1}} + c\nu. \tag{6.2}$$

The first term on the right-hand side of equation (6.2), b/ν, accounts for the effect of longitudinal molecular diffusion in the packed bed driven by the concentration gradient along the zone profile.[277] The second term in equation (6.2) describes eddy dispersion as the sum of four contributions used to model the erratic mass transfer by flow and diffusion in the interparticle pore space of a packing on different length scales (transchannel, short-range interchannel, long-range interchannel, and transcolumn), where λ_i and ω_i are universal structural parameters characteristic of each contribution, and the ratio $\nu_{1/2} = 2\lambda_i/\omega_i$ is a reduced transition velocity for each type of velocity disparity. It is the velocity at which the corresponding plate height term reaches half of its limiting value and thereafter begins to flatten noticeably.[286] The last term in equation (6.2), $c\nu$, accounts for the mass transfer kinetics from the bulk solution into and across the particles.[287]

To our knowledge the challenge of resolving systematically, either by experiment or simulation, the different structural parameters characteristic of each contribution to the eddy dispersion term of the comprehensive Giddings equation (equation (6.2)) has never been undertaken. Past investigations in this direction[132,261,275,290] are all in favor of Giddings' coupling theory of eddy dispersion, but the analysis remained limited to the "simple" Giddings equation, i.e., equation (6.2) with $i = 1$.

Recent progress in our understanding of the time and length scales as well as the magnitude of individual contributions to eddy dispersion in chromatographic beds stems from a high-resolution numerical analysis of flow and mass transport in computer-generated bulk packings of spherical particles and complementary confined cylindrical packings with a cylinder-to-particle diameter ratio of 20 (Chapter 5).

In Chapter 5 as well as in the present chapter, the choice of packing protocols, porosities, and operating conditions in our numerical analysis approach facilitates the focus on eddy dispersion and its precise dependence on the morphology of the packed beds. The selection of perfectly monosized, spherical particles allows the strict operation with reduced parameters ($h = H/d_{\mathrm{p}}$ and $\nu = u_{\mathrm{av}} d_{\mathrm{p}}/D_{\mathrm{m}}$) without influence from the particle size distribution and particle shape. The use of nonporous support particles and inert conditions (unretained tracer particles) eliminates mass transfer resistance contributions ($c = 0$ in equation (6.2)).[275,290] Although it has sometimes been claimed that even with solid particles and unretained tracers a remaining c-term in equation (6.2) is needed to account for pore-scale Taylor dispersion, we like to emphasize that this contribution is

[286] J. C. Giddings. *Nature*, **184**: 357–358, 1959.
[287] K. Miyabe and G. Guiochon. *J. Sep. Sci.*, **26**: 155–173, 2003.
[261] U. Tallarek, E. Bayer, and G. Guiochon. *J. Am. Chem. Soc.*, **120**: 1494–1505, 1998.
[275] J. H. Knox. *J. Chromatogr. A*, **960**: 7–18, 2002.
[290] P. Magnico and M. Martin. *J. Chromatogr.*, **517**: 31–49, 1990.

already contained in the eddy dispersion term of equation (6.2) as the transchannel contribution. In deriving equation (6.2) under most general conditions, Giddings has pooled all mass transfer resistances in the mobile phase (as distinguished from diffusion and adsorption/desorption in the stationary phase) into the coupling expression of equation (6.2) (cf. derivation of equation (2.11-1) on page 62 in Reference [131] and the transition to equation (2.11-2)).

For the packings and conditions considered in our analysis, the coefficient accounting for the contribution of longitudinal diffusion to the reduced plate height in equation (6.2) $b = 2\gamma$, where γ is the obstruction factor often used in chromatography.[131,274] It is the inverse of the tortuosity factor (τ) of the interconnected pore space usually used in the engineering literature[166] and is defined as

$$\gamma = \lim_{t\to\infty} \frac{D(t)}{D_\mathrm{m}} = \frac{1}{\tau} = \frac{D_\mathrm{eff}}{D_\mathrm{m}}, \tag{6.3}$$

where D_eff is the effective diffusion coefficient in the sphere packing, i.e., its asymptotic value observed in the long-time limit for $\nu = 0$.

The packed beds in this work mimic infinitely wide, unconfined random sphere packings, suitable for the study of eddy dispersion as related to bulk microstructural properties without the complex influence of wall effects.[18,32,42,180,185,235,238,325] To quantify the time and length scales behind the velocity heterogeneities from different packing microstructures, we analyze the development of longitudinal dispersion coefficients $D_\mathrm{L}(t)$. Monitoring the transient behavior of the dispersion process towards asymptotic values allows to distinguish between individual contributions to eddy dispersion, especially with regard to the upper limit of the involved time and length scales. This helps to condense, where physically meaningful, the number of scales of velocity disparity in a packing proposed by Giddings.[131] In the investigated bulk packings, we expect only the transchannel and a short-range interchannel effect to contribute to eddy dispersion.

Figure 6.5a shows the development of normalized longitudinal dispersion coefficients $D_\mathrm{L}/D_\mathrm{m}$ at $\nu = 50$ for the Rx0.001 packings at three porosities ($\varepsilon = 0.366, 0.42$, and 0.46). Elapsed time here has been normalized through the transverse dispersive time $\tau_\mathrm{D} = 2D_\mathrm{T}t/d_\mathrm{p}^2$. The dispersive time unit $2D_\mathrm{T}t/d_\mathrm{p}^2$ corresponds to the time span after which tracer particles are dispersed laterally by one sphere diameter. The use of the transverse dispersive time scale is important here, because neither pure diffusion nor pure convection determines the lateral equilibration between different velocities, which instead would have resulted in a diffusive ($\tau_\mathrm{D} = 2D_\mathrm{m}t/d_\mathrm{p}^2$) or a convective ($\tau_\mathrm{C} = u_\mathrm{av}t/d_\mathrm{p}$) time scale. The use of $D_\mathrm{T}(\nu)$ in the dimensionless dispersive time scale τ_D (Figure 6.5a) reflects the actual combination of flow and diffusion, which is also the essence of Giddings' coupling theory.[131]

All generated packings, irrespective of their packing protocol, demonstrate asymptotic dispersion for $\tau_\mathrm{D} < 2$ throughout the whole porosity range ($\varepsilon = 0.366$–0.46), as shown exemplarily

[274] J. H. Knox. *J. Chromatogr. A*, **831**: 3–15, 1999.
[18] H. Freund et al. *Ind. Eng. Chem. Res.*, **44**: 6423–6434, 2005.
[32] G. E. Mueller. *Powder Technol.*, **159**: 105–110, 2005.
[42] R. S. Maier et al. *Phys. Fluids*, **15**: 3795–3815, 2003.
[180] R. S. Maier, D. M. Kroll, and H. T. Davis. *AIChE J.*, **53**: 527–530, 2007.
[235] A. de Klerk. *AIChE J.*, **49**: 2022–2029, 2003.
[238] R. A. Shalliker, B. S. Broyles, and G. Guiochon. *J. Chromatogr. A*, **888**: 1–12, 2000.

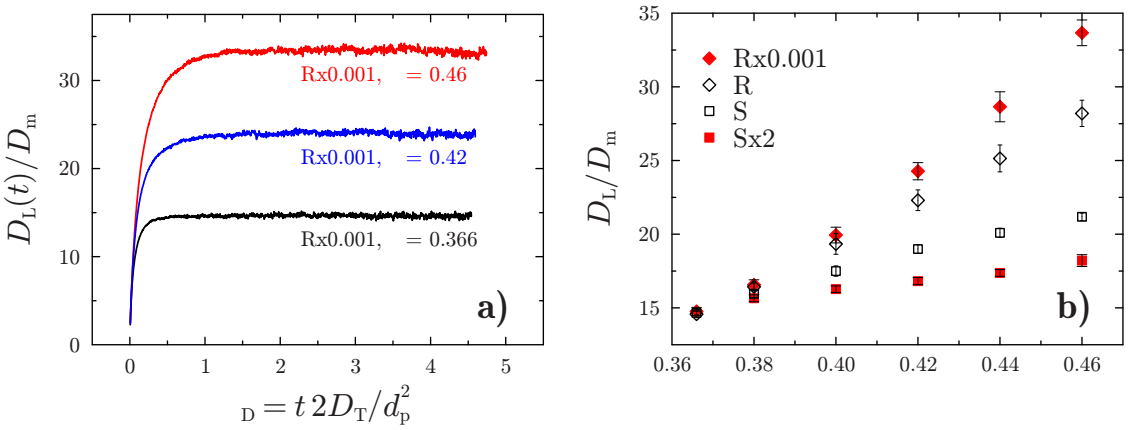

Figure 6.5: a) Time evolution of normalized longitudinal dispersion coefficients $D_L(t)/D_m$ at $\nu = u_{av} d_p/D_m = 50$ for Rx0.001 packings at porosities of $\varepsilon = 0.366$, 0.42, and 0.46. b) Normalized asymptotic dispersion coefficients D_L/D_m for all generated packings as a function of packing protocol and porosity. Error bars indicate upper and lower bounds of 95% confidence intervals.

for the Rx0.001 packings in Figure 6.5a. However, as the porosity decreases from $\varepsilon = 0.46$ to $\varepsilon = 0.366$, the transient dispersion domain shrinks, i.e., asymptotic dispersion is reached faster (cf. Figure 6.5a). This is readily explained by our previous analysis (Figure 6.4) to originate from the accompanying decrease of local disorder in the packing microstructures. The time scale of $\tau_D = 2D_T t/d_p^2 \approx 2$ translates to a characteristic average transverse dispersion length in the bulk packings $\langle l_T \rangle$ of

$$\langle l_T \rangle = \sqrt{2D_T(\nu)t} \approx \sqrt{2}\, d_p. \tag{6.4}$$

Thus, dispersion in the bulk packings is asymptotic after a distance of about $1.4\, d_p$ (or less, depending on the packing protocol and porosity) has been sampled laterally by the tracer particles.

The analysis of longitudinal dispersion confirms our surmise that a short-range disorder is responsible for the upper limit in the time and length scales of eddy dispersion in the bulk packings. Whereas transchannel equilibration (length scale $\ll d_p$) is required in any packed bed, ordered or random, the short-range heterogeneity observed here is associated with the disorder in a random sphere packing as compared with a crystalline packing. Our characterization of a short-scale heterogeneity on the order of $1\text{–}1.5\, d_p$ (Figure 6.5a, equation (6.4)) compares favorably with the distance of $\sim 1.25 d_p$ required for exchanging molecules between the involved velocity extremes estimated by Giddings (page 45 in Reference [131]).

Figure 6.5b contains the asymptotic longitudinal dispersion coefficients (D_L/D_m) for all generated packings at $\nu = 50$. The data are immediately reminiscent of those in Figure 6.4, i.e., the dispersion coefficients and (particularly) the standard deviations of the Voronoi volume distributions (Figure 6.4a) show highly similar dependencies on packing protocol and porosity. From this we conclude that the width of the Voronoi volume distribution of a packing is a sensitive measure for its disorder that closely correlates with the dispersion in the packing.

To summarize, our analysis of transient dispersion in the bulk sphere packings reveals a short-range interchannel contribution on the single-particle scale (1–$1.5\ d_\mathrm{p}$) in addition to the transchannel contribution, which naturally exists in any packed bed on the scale of an individual channel between the particles ($\ll d_\mathrm{p}$). Thus, all packings investigated in this work can be characterized as relatively homogeneous, even though they were generated to reflect individual local disorder (Figures 6.2–6.4). Structural and flow heterogeneities beyond the documented short-scale (cf. Figure 6.5a, equation (6.4)) cannot be resolved.

This knowledge is extremely helpful in analyzing the dependence of reduced plate heights on the reduced velocity, $h = f(\nu)$, by the comprehensive Giddings equation (6.2), as it allows to reduce the number of eddy dispersion contributions to the transchannel and the short-range interchannel effect (equation (6.2) with $i = 2$). Thus, we use the following form of equation (6.2) to fit the dependence of reduced plate heights (calculated from the asymptotic values of $D_\mathrm{L}/D_\mathrm{m}$ — see Figure 6.5a — via equation (6.1)) on the reduced velocity for the generated bulk packings (cf. equation (2.11-6) on page 63 in Reference [131])

$$h_\mathrm{L} = \frac{2\gamma}{\nu} + \underbrace{\frac{2\lambda_1}{1 + (2\lambda_1/\omega_1)\nu^{-1}}}_{\text{transchannel}} + \underbrace{\frac{2\lambda_2}{1 + (2\lambda_2/\omega_2)\nu^{-1}}}_{\text{short-range interchannel}}, \tag{6.5}$$

where indices 1 and 2 refer to the transchannel and the short-range interchannel contribution to eddy dispersion, respectively. As explained above, the use of nonporous support particles and unretained tracer particles gives $c = 0$ in equation (6.2).

The h–ν curves for the four different types of bulk packings are presented in Figure 6.6. Each curve contains 29 values for h over the range of $0.5 \leq \nu \leq 750$, with each h value representing the average from 10 individual packings of a given type and porosity. For packings at the limiting porosities ($\varepsilon = 0.366$ and $\varepsilon = 0.46$) the best fits of the h–ν data to the condensed Giddings equation for bulk packings (equation (6.5)) are also shown. Equation (6.5) fits excellently the simulated plate height data over the whole range of reduced velocities ($R^2 > 0.999$). The shift of the plate height curves as the porosity increases from $\varepsilon = 0.366$ and $\varepsilon = 0.46$ reveals the degree to which the porosity increases the disorder and therefore the dispersion in a particular packing type. The plate height curves for the most ordered packing type, the Sx2 packings, are hardly affected by a porosity increase, whereas those for the least ordered packing type, the Rx0.001 packings, span a relatively large range. For example, the curve minimum for the Rx0.001 packings shifts from the universal (to all packing types) minimum at the RCP limit at $h_\mathrm{min} = 0.5$ and $\nu_\mathrm{min} = 10$ to $h_\mathrm{min} = 1$ and $\nu_\mathrm{min} = 5$ at the RLP limit. The disparate sensitivities of the various packing types towards increased porosity underline the importance of the packing method for dispersion in (and ultimately the separation efficiency of) a packed bed.

The parameters for the transchannel (λ_1, ω_1) and the short-range interchannel contribution (λ_2, ω_2) obtained from the fitting of the comprehensive dataset of Figure 6.6 are summarized in Figure 6.7. Values for the obstruction factor $\gamma = D_\mathrm{eff}/D_\mathrm{m}$ (equation (6.3)) were obtained independently by monitoring the long-time (tortuosity) limit of the diffusion coefficient D_eff in the generated bulk packings, analogous to $D_\mathrm{L}(t)/D_\mathrm{m}$ in Figure 6.5a, but for $\nu = 0$. In this way,

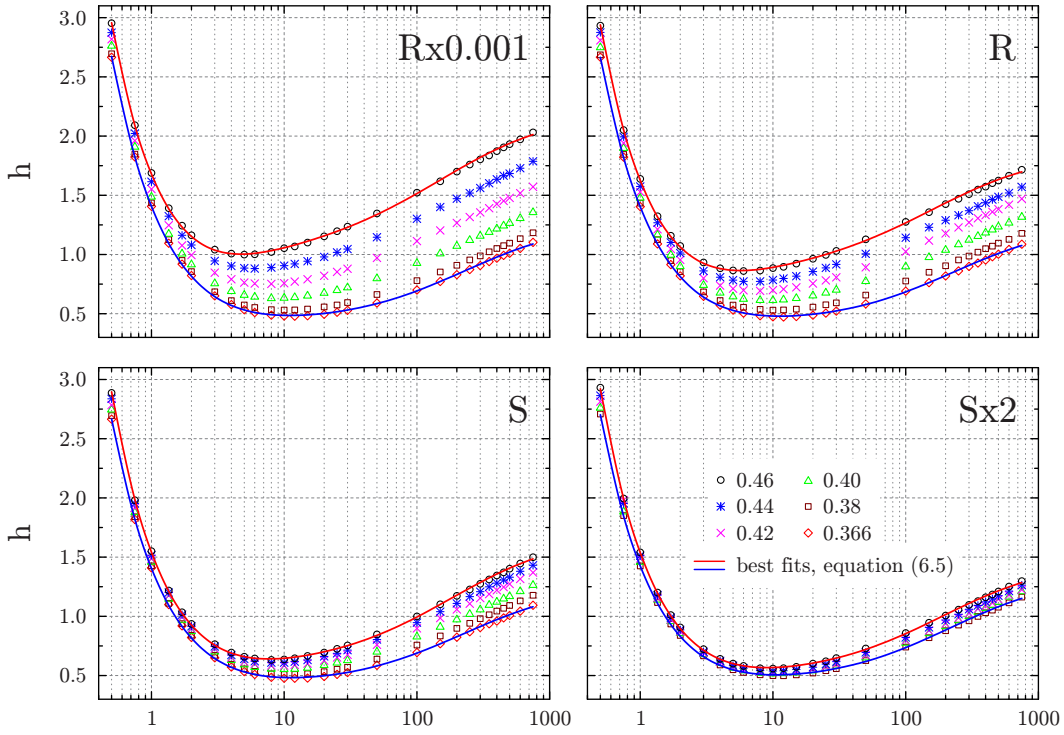

Figure 6.6: Dependence of the reduced plate height $h = H/d_\mathrm{p}$ on the reduced velocity $\nu = u_\mathrm{av} d_\mathrm{p}/D_\mathrm{m}$ ($0.5 \leq \nu \leq 750$) and the porosity ($0.366 \leq \varepsilon \leq 0.46$) for the four different types of bulk packings (Rx0.001, R, S, Sx2). Each value of h represents the average from 10 generated packings. Solid lines are the best fits of the data at $\varepsilon = 0.366$ and 0.46 to equation $\varepsilon = 0.366$ and 0.46 to equation (6.5).

the contribution of longitudinal diffusion to the dispersion (first term on the righthand side of equation (6.5)) can be determined separately and with high precision (Chapter 5). The values of γ range from ~ 0.65 (for all packings at the RCP limit) to ~ 0.71 (for the Sx2 packings at the RLP limit). The received value for each packing was then fixed during fitting of the h–ν data in Figure 6.6 to equation (6.5). The values of Figure 6.7 should now be compared with the estimates of Giddings,[131] who did not include their dependence on packing method or porosity, but was certainly well aware at his time that both factors influence the final packing microstructure. Giddings estimated values of $\lambda_1 \sim 0.5$, $\omega_1 \sim 0.01$, $\lambda_2 \sim 0.5$, and $\omega_2 \sim 0.5$.[131] We recognize that our values in Figure 6.7 genuinely reflect his estimates made more than forty years ago. Concerning the remaining differences in the "universal" structural parameters (λ_i and ω_i) it should be noted that the exact geometrical and topological differences between the packed beds analyzed by Giddings and those studied in this work (and particularly those encountered in chromatographic practice) are hardly known with sufficient accuracy to allow for meaningful quantitative distinctions. But exactly this missing link is provided in the current work by the complementary statistical analysis of the packed beds (Figures 6.3 and 6.4), which quantifies their disorder.

Comparison of Figure 6.7 with Figure 6.4 now rounds off our structure–transport analysis from packing generation via statistical mechanics to hydrodynamics and chromatography. We par-

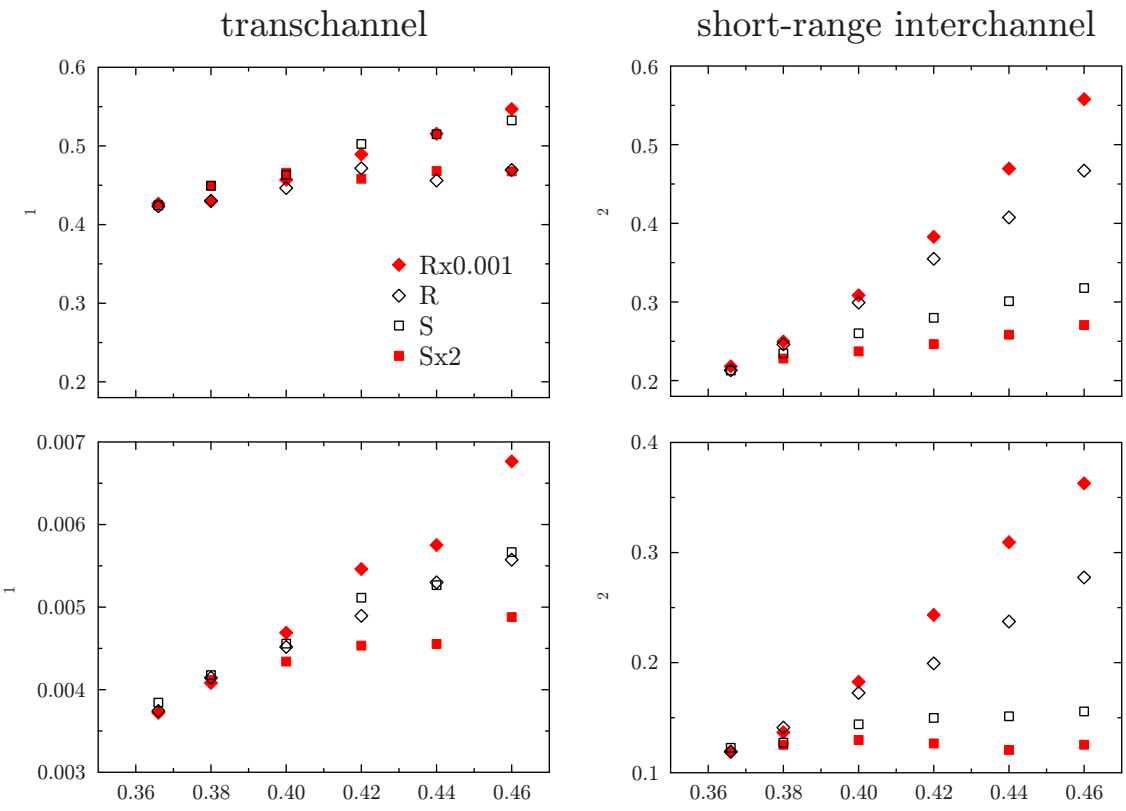

Figure 6.7: Dependence of the parameters for the transchannel contribution (λ_1 and ω_1; left column) and the short-range interchannel contribution (λ_2 and ω_2; right column) on packing protocol and porosity. Values were obtained from the best fits of the comprehensive dataset of Figure 6.6 to the condensed Giddings equation for bulk packings, equation (6.5).

ticularly note the strong correlation between the dependencies on generation protocol and porosity of the short-range interchannel effect (λ_2, ω_2) in Figure 6.7 and both the standard deviation (σ) and skewness (γ) of the Voronoi volume distributions reported in Figure 6.4. Thus, both statistical measures of the Voronoi volume distributions (σ, γ) are excellent, quantitative descriptors of the short-range disorder in the generated packings. This confirms that the deviation of the Voronoi volume distributions in Figure 6.3 from the delta function characterizing a crystalline packing describes the origin of short-range disorder, and the statistical measures in Figure 6.4 therefore represent particle packings with an individual, local randomness in their microstructure.

In addition to the strong correlation between our statistical measures (Figure 6.4) and the parameters λ_2 and ω_2 characterizing the short-range interchannel effect (right column in Figure 6.7), we also note a weaker correlation of the statistical measures with the parameter ω_1 for the transchannel effect in Figure 6.7. This is expected, because the value of ω_1 depends on the lateral dimensions of the interparticle pores in a packed bed (pp. 43–44 in Reference [131]), thus, also on the porosity and individual generation of a packing. Further, we observe little or no correlation between the statistical measures in Figure 6.4 and the parameter λ_1 for the transchannel effect

(Figure 6.7). The values of λ_1 scatter around ~ 0.48 (close to Giddings' value of 0.5[131]). In this respect, the velocity inequality between the center and the wall regions of a pore may be envisioned as lasting along the length of a single particle, after which the flow will split up into several subsequent pores (pp. 49–50 in Referencee [131]). Therefore, the value of λ_1 is little or not affected by the local disorder encountered in this work. To summarize, the analysis of short-range disorder based on the Voronoi volume distributions (Figure 6.4) shows the expected strong correlation with the short-range interchannel contribution to eddy dispersion in equation (6.5), whereas the transchannel contribution is relatively little affected.

Finally, by examining the above-determined structural parameters (λ_i, ω_i) we identify the short-range interchannel effect as being responsible for a convex upward bending of the eddy dispersion curve at low velocities. The transchannel effect causes the eddy dispersion curve (and overall plate height data) to taper off at high velocities. This is easily understood by calculating the transition velocities $\nu_{1/2} = 2\lambda_i/\omega_i$ for each contribution to eddy dispersion at which the plate height term reaches half of its limiting value and thereafter begins to flatten noticeably.[286] Where $\nu_{1/2}$ is large (~ 200 for the transchannel effect) the contribution to the reduced plate height continues to increase with velocity over a significant range of the plots in Figure 6.6, the same as for an ordinary kinetics or mass transfer velocity-proportional term, whereas the plate height contribution of the short-range interchannel effect ($\nu \sim 3$) reaches its plateau at relatively low velocities.

The high transition velocities of the transchannel contribution indicate that in a practical range of chromatographic operation, i.e., at reduced velocities of about $5 \leq \nu \leq 20$, this effect reduces to a simple mass transfer velocity-proportional term, i.e., for ($2\lambda_i/\omega_i \gg \nu$), the transchannel contribution can be expressed by $\omega_1\nu$. Only the short-range interchannel contribution retains its coupling characteristics. The total effect of the component plate height curves to eddy dispersion can then be written in the form

$$h_{\text{eddy}} = \omega_1\nu + \frac{2\lambda_2}{1 + (2\lambda_2/\omega_2)\nu^{-1}}. \tag{6.6}$$

This result agrees very well with the scale analysis for bulk packings in previous Chapter 5. The relatively low impact of coupling between diffusive and flow mechanisms of eddy dispersion in this limited range of velocities ($5 \leq \nu \leq 20$) also explains why the van Deemter equation[289] remains an accurate description of plate height data in that case, particularly with porous particles, when the mass transfer terms associated with the stationary phase are added.[261,300]

6.4 Conclusions

Statistical analysis of packed beds by the standard deviation and skewness of the Voronoi volume distributions (Figures 6.3c and 6.4) provides quantitative scalar measures for local disorder in packing microstructure that correlate strongly with the resulting eddy dispersion (Figures 6.5b and 6.6). Therefore, the presented approach defines a straight route to quantitative structure–transport

[289] J. J. van Deemter, F. J. Zuiderweg, and A. Klinkenberg. *Chem. Eng. Sci.*, **5**: 271–289, 1956.
[300] K. M. Usher, C. R. Simmons, and J. G. Dorsey. *J. Chromatogr. A*, **1200**: 122–128, 2008.

relationships, replacing popularized views based on heuristics.[161] Transport phenomena relevant to chromatography can be analyzed in detail by direct numerical simulations (realized on an efficient high-performance computing platform) and correlated, e.g., with the generalized Giddings equation (Figures 6.6 and 6.7). Complementary analysis of the transient dispersion domain allows to identify the spatial scales of disorder in the packings, which helps to condense the number of scales of velocity disparity in a packing proposed by Giddings.[131] In the investigated bulk packings, we identified only the transchannel and a short-range interchannel effect to contribute to eddy dispersion (Figure 6.5a). This result is in excellent agreement with our statistical analysis based on the Voronoi volume distributions, which revealed a packing porosity and protocol-dependent short-range disorder, in a strong correlation with the short-range interchannel contribution to eddy dispersion (Figures 6.4 and 6.6).

[161] J. Billen et al. *J. Chromatogr. A*, **1073**: 53–61, 2005.

Chapter 7

Influence of packing heterogeneity on effective diffusion

This chapter is concerned with diffusion in monodisperse random sphere packings. Using two algorithms, Monte Carlo and Jodrey–Troy, we generated monodisperse packings with six distinct types of the microstructural disorder and six porosity values between 0.366 and 0.46. Microstructure of the generated packings was analyzed using Delaunay tessellation and correlated with corresponding effective diffusion coefficients of the packings. Revised version of this chapter is planned to be submitted to *Journal of Chromatography A*.

7.1 Introduction

The transport properties of porous media are a central theme of research in physics, chemistry, geology, and engineering, affecting such diverse fields as molecular diffusion in supercooled liquids and glasses, separation of chemical compounds by chromatography, oil recovery and migration of soil pollutants, ground water engineering and dam building. The ability to predict the transport properties of a porous medium from the knowledge of its pore space architecture is of fundamental interest.[89,90] Traditionally, structure–transport correlations for porous media were established either by fitting experimental data or by using specific, simplified (often 2D) models to solve the fundamental transport equations. The structural properties of the porous medium were described by macroscopic, experimentally accessible parameters, such as the density or porosity (void volume fraction). Since the last quarter of the 19$^{\text{th}}$ century,[339] for example, scientists have sought the relation between obstructed diffusion in a porous medium and its porosity. Instead of the diffusion coefficient, the diffusive tortuosity τ is often used in equations. It is defined as:

$$\frac{1}{\tau} = \frac{D_{\text{eff}}}{D_{\text{m}}} = \lim_{t\to\infty} \frac{D(t)}{D_{\text{m}}}, \tag{7.1}$$

[89] J. Bear. *Dynamics of fluids in porous media*. Dover Publications, 1988.
[90] F. A. L. Dullien. *Porous media: fluid transport and pore structure*. 2$^{\text{nd}}$ ed. Academic Press, 1992.
[339] J. C. Maxwell. *A treatise on electricity and magnetism*. 2$^{\text{nd}}$ ed. Clarendon Press, 1881.

where $D(t)$ is the time-dependent diffusion coefficient of a tracer in the porous medium, D_{eff} its asymptotic (steady-state) limit, and D_{m} is the diffusion coefficient of the tracer in bulk solution.[166] Chromatographic literature uses the inverse of the diffusive tortuosity, the obstruction factor, which directly gives the extent to which free diffusion of a molecule in solution is hindered (obstructed) by the porous medium. Although we prefer the obstruction factor as an illustrative descriptor of effective diffusion in a porous medium over the diffusive tortuosity, which is usually imagined as the winding pathways through a porous medium, we will use the diffusive tortuosity in the following because of its tradition in the physics and engineering community.

Various tortuosity–porosity correlations, empirical as well as theoretical, are found in the literature.[340,341,†] Although it is acknowledged that the diversity of porous media precludes the existence of a universal tortuosity–porosity relation, the notion exists that it can be found for a well-defined porous medium, such as a random packing of hard objects of equal shape.[342] Indeed, the proposed correlations for such packings[339,342–348] do not account for the possibility that the individual arrangement of the obstacles in the packing, i.e., the packing microstructure, influences diffusion, and thus convey the expectation that the tortuosity of a random packing of uniform spheres is solely determined by the packing's porosity.

On the other hand it is known, e.g., from the common experience of packing and running chromatographic columns, which are packed beds of spherical particles, that random sphere packings of similar porosity may have rather different microstructures and transport properties, such as hydrodynamic dispersion coefficients.[6] The possibility to characterize random sphere packings by the heterogeneity of their microstructures was recently recognized and expounded in numerical simulation studies.[335,336] Aste and Di Matteo[335] have linked the structural organization of a packing to its Voronoi volume distribution (VVD), for which they deduced the functional form of a k-gamma distribution. The value of the shape parameter k of this distribution was then proposed by Schenker et al.[336] as a measure for the microstructural degree of heterogeneity (DoH) found in computer-generated packings of coagulated colloidal particles. And we have shown in an extensive numerical simulation study that standard deviation and skewness of the VVD are sensitive measures of hydrodynamic dispersion in unconfined, monodisperse, random sphere packings, establishing a correlation between disorder and dispersion in a packing (Chapter 6).

[166] J. M. P. Q. Delgado. *Heat Mass Transfer*, **42**: 279–310, 2006.
[340] B. P. Boudreau. *Geochim. Cosmochim. Acta*, **60**: 3139–3142, 1996.
[341] L. Shen and Z. Chen. *Chem. Eng. Sci.*, **62**: 3748–3755, 2007.
[†] There is no consensus on the definition of tortuosity in the literature. In fact several definitions of tortuosity, related to various experimentally accessible quantities or theoretical models, co-exist.
[342] M. Matyka, A. Khalili, and Z. Koza. *Phys. Rev. E*, **78**: 026306, 2008.
[343] H. L. Weissberg. *J. Appl. Phys.*, **34**: 2636–2639, 1963.
[344] E. Mauret and M. Renaud. *Chem. Eng. Sci.*, **52**: 1807–1817, 1997.
[345] J. P. du Plessis and J. H. Masliyah. *Transp. Porous Media*, **3**: 145–161, 1988.
[346] M.-J. Yun et al. *Chin. Phys. Lett.*, **22**: 1464–1467, 2005.
[347] P.-Y. Lanfrey, Z. V. Kuzeljevic, and M. P. Dudukovic. *Chem. Eng. Sci.*, **65**: 1891–1896, 2010.
[348] E. du Plessis, S. Woudberg, and J. P. du Plessis. *Chem. Eng. Sci.*, **65**: 2541–2551, 2010.
[6] G. Guiochon et al. *Fundamentals of preparative and nonlinear chromatography*. 2nd ed. Elsevier, 2006.
[335] T. Aste and T. Di Matteo. *Phys. Rev. E*, **77**: 021309, 2008.
[336] I. Schenker et al. *Phys. Rev. E*, **80**: 021302, 2009.

In this chapter, we challenge the expectation that the tortuosity of a random sphere packing is independent from its microstructure by a random walk simulation of diffusion in computer-generated packings of unconfined, uniform, impermeable spheres. The tortuosity–porosity scaling of random sphere packings has been compared with those of periodic packings,[138] but differences between random packings of different microstructures have so far not been explored. Six distinct packing types with different microstructures were generated in the porosity range between $\varepsilon = 0.366$ and $\varepsilon = 0.46$, commonly referred to as the random-close and the random-loose packing limit, respectively.[171] We compute and compare the effective diffusion coefficients for each packing type and porosity to investigate if and how the resulting tortuosity–porosity curves reflect the different packing types.

7.2 Numerical section

Isotropic, random, unconfined packings of monosized, hard, impermeable spheres with dimensions of ca. $10\,d_\mathrm{p} \times 10\,d_\mathrm{p} \times 70\,d_\mathrm{p}$ (where d_p is the sphere diameter) were generated computationally, applying periodic boundary conditions in all three dimensions. The chosen packing size was sufficient for statistical analysis of the packing microstructure and void space as well as for simulation of diffusion up to the asymptotic limit.

Six distinct packing types were generated by variation of the generation algorithm and its parameters. Four packing types (Rx0.001, R, S, Sx2) were generated with a modified Jodrey–Tory (JT) algorithm and two (Ωx0.05, Ωx0.95) with a Monte Carlo algorithms. Description of the generation algorithms and corresponding algorithm parameters is given in Subsections 1.1.1 and 1.1.2.

Each packing type was generated at six porosities ($\varepsilon = 0.366$, 0.38, 0.40, 0.42, 0.44, 0.46) between the random-close and the random-loose packing limit, with one exception: we were not able to generate Sx2-packings at $\varepsilon = 0.366$. To account for statistical variations, ten individual packings of each type and porosity, 350 packings in total, were generated. Results reported refer to the mean of the values from all ten individual packings of a given type and porosity.

For simulation of diffusion, the packings were discretized on a uniform cubic lattice, where each node was assigned as either “solid” or “fluid” according to its position within or outside the closest sphere, respectively. Two grid resolutions, 30 nodes/d_p and 60 nodes/d_p, were evaluated to test their influence on the simulated diffusion coefficients (Table 7.1). Respective grid sizes were approximately $300 \times 300 \times 2100$ (30 nodes/dp) and $600 \times 600 \times 4200$ (60 nodes/dp). Additionally, we used a smoothed spheres representation of the spheres' boundaries. Here, discretization is omitted and random walk takes place between spheres with smooth as opposed to stair-step contours. If not stated otherwise, results discussed were obtained with the smoothed spheres approach, for example as used by Maier and Bernard in simulations of hydrodynamic dispersion.[85]

Diffusion in the generated packings was simulated by a random walk particle tracking technique using $5 \cdot 10^6$ tracer particles (Subsection 1.4.2). Time-dependent diffusion coefficients $D(t)$

[138] A. S. Kim and H. Chen. *J. Membr. Sci.*, **279**: 129–139, 2006.
[171] C. Song, P. Wang, and H. A. Makse. *Nature*, **453**: 629–632, 2008.
[85] R. S. Maier and R. S. Bernard. *J. Comput. Phys.*, **229**: 233–255, 2010.

in a given direction were calculated from the tracer displacements as described in Subsection 1.4.3. $D(t)$ was calculated for thirteen different directions. Isotropic diffusion behavior was found for all packing types. Effective diffusion coefficients D_{eff} were determined from the asymptotes of the time-dependent diffusion curves, and the respective tortuosity τ was calculated with equation (7.1). Total simulation time for all 350 generated packings was $\sim$110 hours on 2048 Blue Gene/P processor cores.

For Voronoi and Delaunay tessellations of the generated packings we used MATLAB® 7.0 built-in routines, which are based on the QUICKHULL algorithm introduced by Barber et al.[337]

7.3 Results and discussion

7.3.1 Packing generation and microstructure

Depending on packing porosity, the six generated types of unconfined, monodisperse, random sphere packings possess different microstructural degrees of heterogeneity (DoH). The DoH or packing-scale disorder of the generated packings is described by the standard deviation and skewness of the respective Voronoi volume distributions (VVDs) (Figure 7.1). All packing types generated with the JT-algorithm exhibit the same DoH at $\varepsilon = 0.366$. The limited space available at the random-close packing limit restricts the possible placement of spheres, so that all JT-packing types have highly similar microstructures. As the DoH of the packings increases along with the porosity, differences between the packing types emerge and intensify towards the random-loose packing limit ($\varepsilon = 0.46$). The disorder–porosity dependence of the four JT-packing types reflects their designated homogeneity in the order: Rx0.001 < R < S < Sx2. Hydrodynamic dispersion in these packing types is correlated to their DoH or packing-scale disorder (Chapter 6).

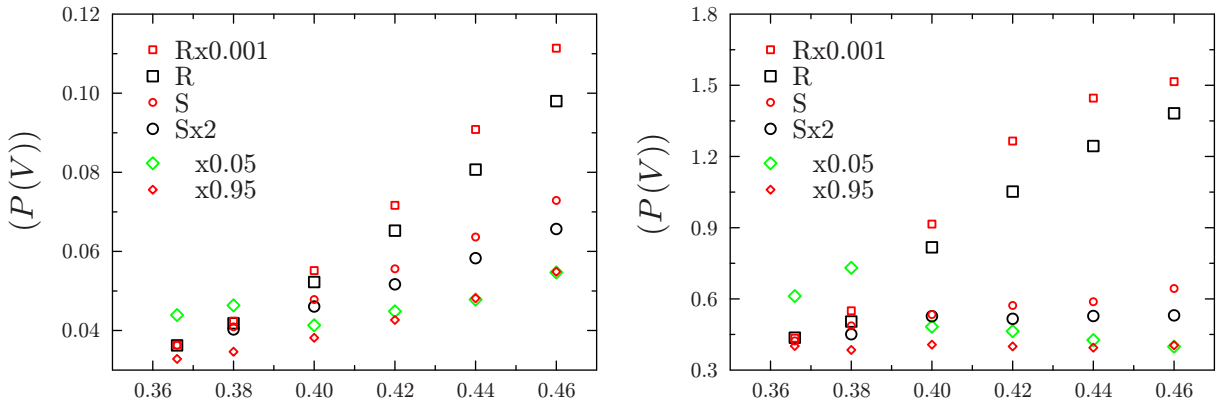

Figure 7.1: Standard deviation σ (left) and skewness γ (right) of the packing's Voronoi volume distributions as a function of porosity ε.

At $\varepsilon = 0.46$, both MC-packing types are more homogeneous than the least disordered JT-packing type (Sx2), and for the Ωx0.95-packing type this remains the case throughout the whole

[337] C. B. Barber, D. P. Dobkin, and H. Huhdanpaa. *ACM Trans. Math. Software*, **22**: 469–483, 1996.

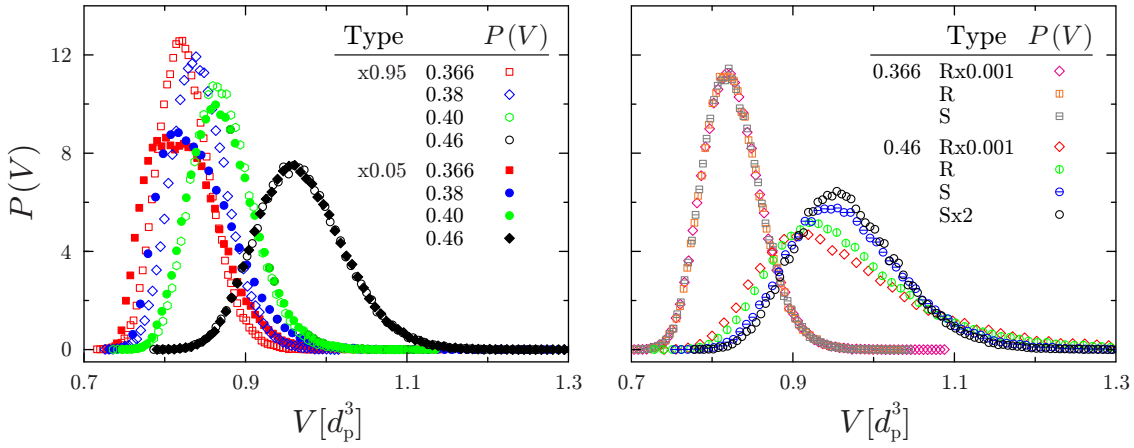

Figure 7.2: Voronoi volume distributions of the packing types generated with a) the Monte Carlo method and b) the Jodrey–Tory algorithm at selected porosities ε.

investigated porosity range (Figure 7.1). Considering that MC-packing generation starts from a lattice-based distribution of sphere centers, this is not unexpected. Ωx0.95-packings essentially show the same trend upon densification as the JT-packing types, i.e., a decrease of packing-scale disorder, only with a smaller slope. Ωx0.05-packings, however, behave differently: their DoH goes through a minimum at $\varepsilon = 0.40$, and then increases so that at $\varepsilon = 0.366$ the Ωx0.05-packing has the highest packing-scale disorder among all generated packing types. Why? The MC-algorithm is known to incorporate dense, highly ordered regions into the packings if slow compression rates and low porosity are combined?[29,325] The generic microstructural difference of the Ωx0.05-packings at lower porosities shows in the form of their VVDs (Figure 7.2). As opposed to the sharp, symmetrical VVDs of all other packing types at $\varepsilon < 0.40$, the VVDs of the Ωx0.05-packing type widen and skew. They are expanded towards smaller Voronoi volumes, which correspond to the more densely packed regions. The irregular occurrence of dense and more loosely packed regions in a packing translates to more disorder on the packing scale.

7.3.2 Packing-scale disorder and tortuosity

Figure 7.3a contains the results of simulating effective diffusion in the void space of the generated packings in the form of tortuosity–porosity data. At first glance, the tortuosity–porosity data of the JT-packing types reflect their relative packing-scale disorder as captured by the VVDs (Fig. 2): i) all JT-packing types have identical tortuosity ($\tau = 1.486$) at $\varepsilon = 0.366$, ii) differences between the packing types emerge and increase with porosity, and iii) at $\varepsilon = 0.46$, the most homogeneous JT-packing type, Sx2, has the lowest tortuosity ($\tau = 1.373$) and the most heterogeneous JT-packing type, Rx0.001, the highest tortuosity ($\tau = 1.403$). R- and S- packings, however, despite their different DoH, display identical tortuosities (within the limits of statistical variations) throughout the investigated porosity range. The varied JT-algorithm parameters, initial distribution of sphere

[29] A. Z. Zinchenko. *J. Comput. Phys.*, **114**: 298–307, 1994.
[325] M. R. Schure and R. S. Maier. *J. Chromatogr. A*, **1126**: 58–69, 2006.

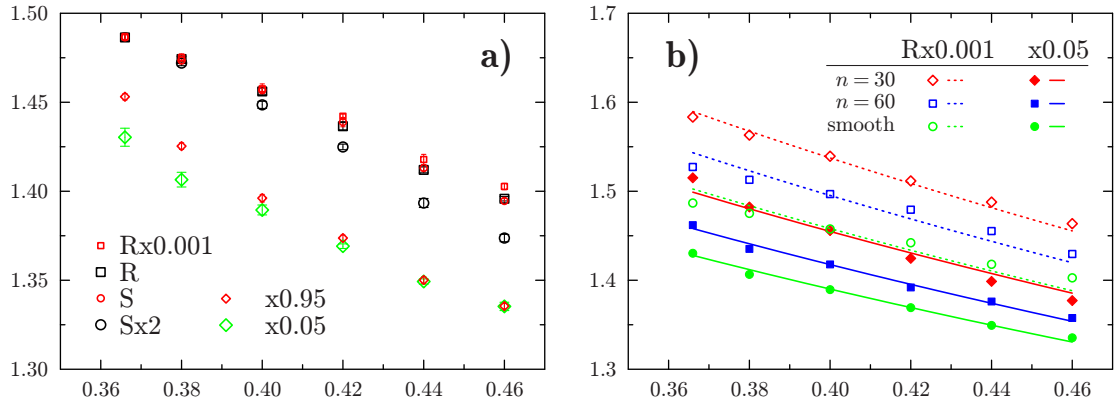

Figure 7.3: a) Tortuosity–porosity data for the generated packing types based on simulation of effective (asymptotic) diffusion with the smoothed spheres approach. Statistical variations among individual packings of a given type and porosity are expressed by 95% confidence intervals calculated using the standard error of the mean. b) Effect of grid resolution and representation of the spheres' surface on the simulated tortuosity–porosity data for Rx0.001- and Ωx0.05-packing types.

centers and displacement length scaling constant, introduce microstructural differences on two different length scales: the former influences the packing microstructure on the packing scale (S-type packings are more homogeneous than R-type packings), whereas the latter acts on a much smaller scale. Expressed in terms of the packing void space, the value of the displacement length scaling constant affects the pores and their connecting pathways to adjacent pores, the pore throats. Because the same value for the displacement length scaling constant was used in the generation of R- and S-packings, their identical tortuosity–porosity curves suggest that the influence of the packing heterogeneity on diffusion is restricted to the pore scale.

MC-packings are less tortuous than JT-packings, with tortuosity values between $\tau = 1.335$ at $\varepsilon = 0.46$ and $\tau = 1.430$ (Ωx0.05) or $\tau = 1.454$ (Ωx0.95) at $\varepsilon = 0.366$. Differences between the two MC-packing types emerge and increase upon densification as was observed for the DoH, but the Ωx0.05-packing type has the lowest tortuosity among all generated packing types throughout the whole porosity range. This is another indicator that packing-scale disorder is not the determining influence for diffusion.

Figure 7.3 demonstrates that the packing microstructure influences diffusion in monodisperse random sphere packings. A comparison with Figure 7.1 reveals that — contrary to hydrodynamic dispersion (Chapter 6) — the effective diffusion coefficient does not scale with the DoH or packing-scale disorder. The influence of the packing microstructure on diffusion is small, effecting merely a 2% difference at $\varepsilon = 0.46$ between the JT-packing types Sx2 and Rx0.001, and similarly a ca. 2% difference at $\varepsilon = 0.366$ between the two MC-packing types. However, the observed influence of the packing microstructure on diffusion is not due to statistical variations among individual packings of a given type and porosity, as the confidence intervals in Figure 7.3a prove.

7.3.3 Tortuosity–porosity relation and grid resolution

One of the earliest correlations was proposed on a theoretical basis by Weissberg[343] as a lower bound for the tortuosity in random arrangements of freely overlapping spheres:

$$\tau = 1 - 0.5 \ln \varepsilon. \tag{7.2}$$

In the modified form of

$$\tau = 1 - p \ln \varepsilon \tag{7.3}$$

Weissberg's correlation has found corroboration from experiments[340,344,349] and simulations.[342] For example, the coefficient was determined as $p = 0.49$;[344,349] $p = 0.77$;[342] or $p = 2$.[340] Although the restricted applicability of theoretical correlations is often stated as their weak point, the success of the modified Weissberg correlation proves that theoretical correlations may find a wider applicability than assumed from the underlying model.

Table 7.1: Fit of the tortuosity data to the modified Weissberg equation, equation (7.3), for different representations of the spheres' boundaries in the simulations.

	Stair-step (30 nodes/d_p)		Stair-step (60 nodes/d_p)		Smooth spheres	
Packing type	p	R^2	p	R^2	p	R^2
Rx0.001	0.587	0.983	0.541	0.959	0.500	0.877
R	0.582	0.996	0.538	0.981	0.496	0.943
S	0.583	0.997	0.537	0.986	0.497	0.938
Sx2	0.566	0.964	0.521	0.981	0.486	0.989
Ωx0.95	0.509	0.903	0.467	0.947	0.437	0.967
Ωx0.05	0.496	0.967	0.456	0.990	0.426	0.991

The simulated data of Figure 7.3 demonstrate that establishing a tortuosity–porosity relation for random sphere packings requires consideration of the packing microstructure. We fitted our simulated tortuosity data to equation (7.3) using p as an adjustable parameter to evaluate if the influence of the packing microstructure may simply be accounted for by a coefficient. The results along with the correlation coefficients R^2 for the fits are listed in Table 7.1. The coefficient for Rx0.001, R-, and S-packings is $p \approx 0.5$, the value predicted by Weissberg,[343] whereas the coefficient for the Sx2-packing type is closer to $p = 0.49$, the value introduced by Mauret and Renaud.[344] MC-packings are set apart by smaller p-values ($p = 0.43$–0.44). If we rank the six packing types according to the relative position of their tortuosity curves in Figure 7.3a as Ωx0.05 < Ωx0.95 < Sx2 < S < R < Rx0.001 and equate this sequence with an increasing degree of heterogeneity around individual pores in the packings, then the calculated p-values can be said to increase with the heterogeneity around the pores. Interestingly, the correlation coefficients show the opposite trend, i.e., adherence to the modified Weissberg equation appears to be better for packings with less pore-environment heterogeneity. In summary, however, the correlation coefficients are uncon-

[349] M. Barrande, R. Bouchet, and R. Denoyel. *Anal. Chem.*, **79**: 9115–9121, 2007.

vincing and lead to the conclusion that diffusion in monodisperse random sphere packings is not adequately represented by a modified Weissberg correlation. The heterogeneity around a packing's pores is expected to vary with porosity and therefore cannot be captured by a porosity-independent coefficient.

The simulated data discussed so far were received using an approach, where the packing's spheres have smooth as opposed to stair-step contours. The adequate geometrical representation of the spherical obstacles in the packing is important for modeling diffusion, because the path of a tracer around a ragged surface is longer than around a smooth one. Simulating diffusion around "ragged spheres," even with a comparatively high grid resolution of 60 nodes/d_p, yields not only exaggerated tortuosity values (as exemplarily shown for two selected packing types in Figure 7.3b), but also raised p-coefficients for the tortuosity–porosity dependence (Table 7.1).

7.3.4 Delaunay tessellation of the pore space

Spatial tessellation of a packing into Delaunay simplices has been shown to be especially suited to characterize the packing void space.[322,333,350–354] Delaunay tessellation divides monodisperse sphere packings into irregular tetrahedra, whose corners (vertices) are the centers of four closest (but not necessarily touching) spheres that enclose a pore. The packing space is completely filled with non-overlapping tetrahedra, each containing solid and void components: the void volume represents the pore volume, and the void areas of the tetrahedron's four faces correspond to the pore throats that form the connections to the four neighboring pores. The void face areas can therefore be considered as the entrance and exit ways for a tracer particle into or out of a given pore.

We evaluated several metric properties of Delaunay tetrahedra for their ability to represent the influence of the packing microstructure on diffusion: volume; maximum, minimum, and average void face areas; maximum, minimum, and average edge length; and the T-measure,[320] which quantifies the deviation of the Delaunay tetrahedra from regularity (Delaunay simplices of crystalline packings are quasi-regular tetrahedra or quartoctahedra); also the distances of the center of mass to the center of the faces, as well as various combinations of metric properties. The mean, standard variation, and skewness of each metric property was calculated and its porosity-scaling compared to those of the simulated diffusive tortuosity values. The mean of the maximum and the mean of the minimum void face area — but not that of the average void face area — gave close results, pointing to the limiting properties of a pore rather than its average properties as a possible measure. We found a good representation for the tortuosity–porosity scaling of all packing types by considering two limiting properties for each pore, namely the minimum and maximum void face areas, A_min and A_max, respectively, of each Delaunay tetrahedron. The standard deviation σ

[322] K. E. Thompson and H. S. Fogler. *AIChE J.*, **43**: 1377–1389, 1997.
[333] J. Q. Xu, R. P. Zou, and A. B. Yu. *Granular Matter*, **9**: 455–463, 2007.
[350] S. Bryant, G. Mason, and D. Mellor. *J. Colloid Interface Sci.*, **177**: 88–100, 1996.
[351] R. Al-Raoush, K. Thompson, and C. S. Willson. *Soil Sci. Soc. Am. J.*, **67**: 1687–1700, 2003.
[352] R. Y. Yang et al. *J. Colloid Interface Sci.*, **299**: 719–725, 2006.
[353] S. Rémond, J. L. Gallias, and A. Mizrahi. *Granular Matter*, **10**: 329–334, 2008.
[354] N. Reboul, Eric Vincens, and B. Cambou. *Granular Matter*, **10**: 457–468, 2008.
[320] A. V. Anikeenko, N. N. Medvedev, and T. Aste. *Phys. Rev. E*, **77**: 031101, 2008.

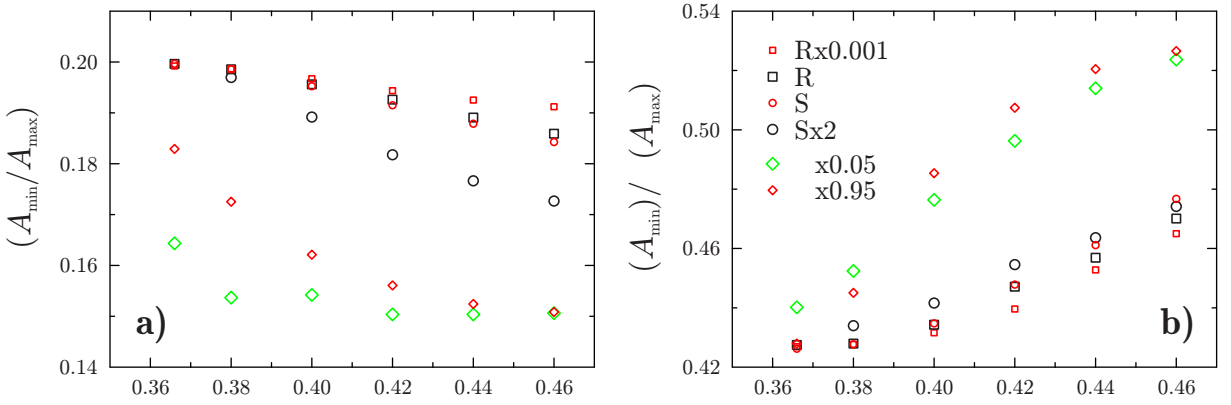

Figure 7.4: a) Porosity-scaling of $\sigma(A_{\min}/A_{\max})$, the standard deviation of the ratio between the minimum ($A_{\min}$) and the maximum void face area ($A_{\min}$) of each Delaunay tetrahedron around a pore. b) Porosity-scaling of $\sigma(A_{\min})/\sigma(A_{\max})$, the ratio of the standard deviations of $A_{\min}$ and $A_{\max}$.

of the ratio of $A_{\min}$ and $A_{\max}$ calculated for each tetrahedron, $\sigma(A_{\min}/A_{\max})$, over all pores in a packing, Figure 7.4a, mimics the porosity-scaling of the simulated diffusive tortuosity values for each of the six packing types, Figure 7.3a.

It is elucidating to compare the porosity-scaling of $\sigma(A_{\min}/A_{\max})$ with that of $\sigma(A_{\min})/\sigma(A_{\max})$, Figure 7.3b. The first measure considers the limitations of an individual pore first before summing over all pores in the packing, the second measure does not and fails to represent the influence of the packing microstructure on diffusion. Considering the process of diffusion in the packings and how this quantity is computed, Figure 7.3a reflects the independence of a tracer particle's motion from the rest of the tracer ensemble as well as from its own previous motions. The probability for

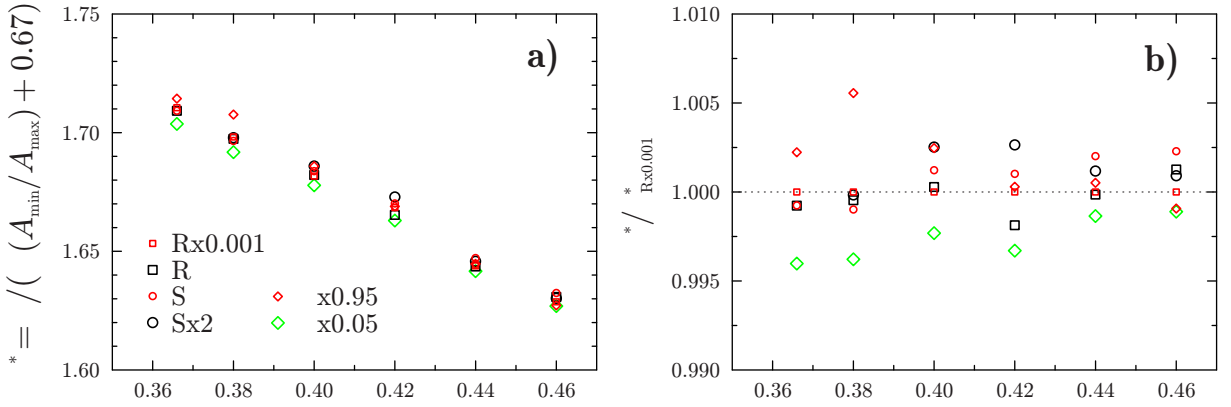

Figure 7.5: a) Collapsed tortuosity–porosity data for all packing types. b) Scatter of collapsed tortuosity–porosity data relative to the Rx0.001-packing type.

diffusion of a tracer particle into or out of a given pore is determined by the pathways connected to the pore, i.e., by the size of the pore throats, which are here represented by the void face areas of the Delaunay tetrahedron around the pore. The chance of a tracer to find a way out of a given

pore is maximal, if it encounters the pore throat with the largest cross section ($A_{\max}$), and minimal, if it encounters the smallest pore throat ($A_{\min}$). We interpret the ratio ($A_{\min}/A_{\max}$) as related to the probability for effective diffusion into or out of a given pore, and judge the standard deviation σ of this ratio as a suitable descriptor of the influence of the packing microstructure on effective diffusion.

To visualize the quality of the identified structural descriptor, we provide a unified representation of the tortuosity–porosity data for all packing types. If the simulated tortuosity data τ are divided by $[\sigma(A_{\min}/A_{\max}) + 0.67]$, the data points collapse onto a curve, which can be fitted as a linear function of ε with a correlation coefficient of $R^2 > 0.99$ (Figure 7.5a). Figure 7.5b plots the ratio of the collapsed tortuosity data of the different packing types normalized to the Rx0.001-packing type. The scatter is small (within 1%), underlining the quality of the found scaling factor. On the other hand, the scatter is not random for the Ωx0.05-packing type and the data points are more united at higher porosities. Also, the necessity of adding a constant number to $\sigma(A_{\min}/A_{\max})$ to receive collapsed tortuosity data reminds us that the identified structural descriptor is insufficient to describe fully the scaling of effective diffusion and that further research is required to achieve this goal.

7.4 Conclusions

We have shown that diffusion in monodisperse random sphere packings is not solely defined by the packing porosity, but also depends on the packing microstructure, which affects value and porosity-scaling of the effective diffusion coefficient. Diffusion is influenced by the degree of structural heterogeneity that exists around individual pores in a packing. We have proposed a suitable structural descriptor for this influence based on the metric properties of Delaunay tetrahedra, namely the standard deviation of the ratio of minimum to the maximum void face area for each Delaunay tetrahedron in the tessellation. The correlation to the limiting properties of individual pores (i.e., minimum to maximum pore throat cross-section) reflects the piecewise nature of diffusion, which is calculated from independent tracer motions, contrary to flow-field dependent (convective) dispersion, which is correlated to the disorder (or DoH as captured by the VVD) made up by the network of pore-scale heterogeneities in the packing.

In a previous study of the time and length scales of dispersion in unconfined, monodisperse, random sphere packings, we had shown that microstructural heterogeneities occur on the scale of $1–2\,d_{\mathrm{p}}$ (Chapter 6). Whereas for dispersion the pattern of this heterogeneity in the whole packing is relevant, for diffusion it is only the standard deviation of the pore-scale heterogeneity over the packing that counts. Packings with identical DoH (e.g., the JT-packing types at $\varepsilon = 0.366$) have the same hydrodynamic dispersion coefficient and the same effective diffusion coefficient. But two packings with different dispersion coefficient can nevertheless have an identical diffusion coefficient, if both packings have the same degree of heterogeneity as seen from the environment of individual pores (e.g., R- and S-packings). Also, a packing may have a homogeneous microstructure around individual pores and thus a high effective diffusion coefficient (low tortuosity), but a disordered microstructure on the packing scale and thus a high dispersion coefficient (e.g., the Ωx0.05-packing type).

Conclusion

In this thesis, mass transport processes (flow, diffusion, and hydrodynamic (eddy) dispersion) in random sphere packings were investigated by large-scale numerical simulations. Here "large-scale" denotes that the time and lengths scales, on which transport in the packings was simulated, ranged from the pore-scale ($\sim 0.1\, d_\mathrm{p}$, where d_p is the diameter of a spherical particle), over the particle-scale ($1-2\, d_\mathrm{p}$) up to the confinement-scale (e.g., column diameter, $\sim 20\, d_\mathrm{p}$). Combination of the lattice Boltzmann method and random walk particle tracking, making efficient use of the fastest supercomputers available today, enabled numerical solutions of the advection–diffusion problems in complex geometries over a wide range of Péclet numbers ($Pe \approx 10^{-1}-10^{3}$).

Chapters 2 to 4 form the first part of the thesis. They address the influence of the conduit cross-sectional geometry on hydrodynamic dispersion in confined random sphere packings. Circular, quadratic, rectangular, and semicircular (Chapter 2), as well as trapezoidal cross sections (Chapter 3) were studied, thus gradually approaching the irregular cross-sectional geometry of a real-life microchannel (Chapter 4). The simulations revealed a strong effect of the conduit cross-sectional geometry on hydrodynamic dispersion, such that the dispersion coefficient of a packing with non-optimal geometry may be up to 50 times higher than that of a cylindrical packing at the same bed porosity (cf. Figures 2.6 and 3.6). The time evolution of the hydrodynamic dispersion coefficients provided important information for the analysis: it was found that i) the time to reach a close-to-asymptotic value of the dispersion coefficient (lateral "equilibration" time) correlates with the maximal distance between different axial velocities specific to a particular conduit geometry, and ii) asymmetric conduit geometries with longer equilibration times are typically characterized by higher dispersion coefficients (a result that was confirmed experimentally[355]). It was demonstrated that the presence of corners in a conduit causes the formation of channels of advanced (with respect to the average) fluid flow velocity, and that the resulting maldistribution of the flow field significantly increases the equilibration time and the hydrodynamic dispersion coefficient of the packing. Finally, very good agreement with experimental data was found for the simulated dispersion coefficients in the packings, for which the cross-sectional geometry and the particle-size distribution of the adsorber particles in a microchip separation channel had been reconstructed (Chapter 4).

Whereas pre-asymptotic dispersion has been investigated by several research groups during the last decade,[18,42,177,180] pore-scale simulations to study close-to-asymptotic hydrodynamic dispersion

[355] S. Jung et al. *Anal. Chem.*, **81**: 10193–10200, 2009.
[18] H. Freund et al. *Ind. Eng. Chem. Res.*, **44**: 6423–6434, 2005.
[42] R. S. Maier et al. *Phys. Fluids*, **15**: 3795–3815, 2003.
[177] F. Augier, F. Idoux, and J. Y. Delenne. *Chem. Eng. Sci.*, **65**: 1055–1064, 2010.
[180] R. S. Maier, D. M. Kroll, and H. T. Davis. *AIChE J.*, **53**: 527–530, 2007.

in confined random sphere packings have never been undertaken before, probably due to the high computational requirements.

Part two of this thesis addresses fundamental issues of mass transport in random sphere packings. Chapter 5 is dedicated to the analysis of the different length scales of structural heterogeneity in bulk (periodic, unconfined) packings and in cylindrically confined packings. It was shown that the time to reach close-to-asymptotic dispersion behavior is defined neither by a diffusive nor a convective, but by a transverse-dispersive time scale. Analysis of the time evolution of the hydrodynamic dispersion coefficient based on the transverse-dispersive time scale revealed different length scales of heterogeneity (pore-, particle-, and packing-scale) and their *individual* contributions to the close-to-asymptotic value of the hydrodynamic dispersion coefficient. Compared with bulk packings, dispersion in confined packings is characterized by significantly higher values of the dispersion coefficient and a correspondingly longer time to reach close-to-asymptotic behavior. The results presented in Chapter 5 include an excellent fit of the simulated dispersion coefficients to the generalized Giddings' equation (see Figures 5.4 and 5.6), the most rigorous and accurate equation to describe hydrodynamic dispersion in packed, particulate beds. Such a fit has never been presented before for experimental or simulated data since the equation was proposed by Giddings in 1959.[286]

Chapters 6 and 7 study the influence of the packing microstructure on effective diffusion and hydrodynamic dispersion in unconfined, monodisperse random sphere packings. Packings generated with systematically different microstructure and bed porosities between the random-close and the random-loose packing limit were analyzed with respect to their packing microstructure applying spatial tessellation techniques (Delaunay and Voronoi tessellations). Mass transport in the generated packings was simulated and a unique, qualitative correlation found between *geometrical* descriptors of their pore structure and the transport coefficients for hydrodynamic dispersion and effective diffusion. Recent studies have addressed mass transport in an isolated pore[356,357] or in porous structures of a given microstructural disorder,[18,75,97,99,123,177,358–361] which for random sphere packings (experimental as well as simulated) is determined by the packing generation protocol. The numerical approach and spatial tessellation schemes used in this work are applicable to a variety of granular materials, and we believe it constitutes a systematic route towards quantitative structure–transport relationships for granular porous media.

[286] J. C. Giddings. *Nature*, **184**: 357–358, 1959.
[356] S. Blanco and R. Fournier. *EPL*, **61**: 168–173, 2003.
[357] O. Bénichou et al. *EPL*, **70**: 42–48, 2005.
[75] M. A. van der Hoef, R. Beetstra, and J. A. M. Kuipers. *J. Fluid Mech.*, **528**: 233–254, 2005.
[97] D. Vidal et al. *Comput. Chem. Eng.*, **33**: 256–266, 2009.
[99] D. Coelho, J.-F. Thovert, and P. M. Adler. *Phys. Rev. E*, **55**: 1959–1978, 1997.
[123] R. S. Maier et al. *Phys. Fluids*, **12**: 2065–2079, 2000.
[358] V. Mourzenko et al. *Phys. Rev. E*, **77**: 066306, 2008.
[359] A. G. Dixon and M. Nijemeisland. *Ind. Eng. Chem. Res.*, **40**: 5246–5254, 2001.
[360] A. V. Anikeenko et al. *J. Struct. Chem.*, **50**: 403–410, 2009.
[361] K. Schnitzlein. *Chem. Eng. Sci.*, **56**: 579–585, 2001.

Bibliography

[1] S. Succi. *The lattice Boltzmann equation for fluid dynamics and beyond*. Oxford University Press, 2001. (see pp. 1, 14)

[2] J. A. Rudnick and G. D. Gaspari. *Elements of the random walk: an introduction for advanced students and researchers*. Cambridge University Press, 2004. (see pp. 1, 25)

[3] D. G. Feitelson. The supercomputer industry in light of the Top500 data. *Computing in Science and Engineering*, **7**: 42–47, 2005. doi: 10.1109/MCSE.2005.24 (see p. 2)

[4] G. M. Whitesides. The origins and the future of microfluidics. *Nature*, **442**: 368–373, 2006. doi: 10.1038/nature05058 (see p. 2)

[5] H. Yin, K. Killeen, R. Brennen, D. Sobek, M. Werlich, and T. van de Goor. Microfluidic chip for peptide analysis with an integrated HPLC column, sample enrichment column, and nanoelectrospray tip. *Analytical Chemistry*, **77**: 527–533, 2005. doi: 10.1021/ac049068d (see pp. 2, 49, 62, 76, 78)

[6] G. Guiochon, A. Felinger, A. M. Katti, and D. G. Shirazi. *Fundamentals of preparative and nonlinear chromatography*. 2nd ed. Elsevier, 2006. (see pp. 2, 4, 126)

[7] J. W. Jorgenson. Capillary liquid chromatography at ultrahigh pressures. *Annual Review of Analytical Chemistry*, **3**: 129–150, 2010. doi: 10.1146/annurev.anchem.1.031207.113014 (see p. 2)

[8] S. Koster and E. Verpoorte. A decade of microfluidic analysis coupled with electrospray mass spectrometry: An overview. *Lab on a Chip*, **7**: 1394–1412, 2007. doi: 10.1039/b709706a (see pp. 2, 62, 63, 75)

[9] K. W. Ro, J. Liu, and D. R. Knapp. Plastic microchip liquid chromatography-matrix-assisted laser desorption/ionization mass spectrometry using monolithic columns. *Journal of Chromatography A*, **1111**: 40–47, 2006. doi: 10.1016/j.chroma.2006.01.105 (see pp. 2, 49, 62, 63, 76)

[10] D. S. Reichmuth, T. J. Shepodd, and B. J. Kirby. Microchip HPLC of peptides and proteins. *Analytical Chemistry*, **77**: 2997–3000, 2005. doi: 10.1021/ac048358r (see pp. 2, 49, 62, 63, 76)

[11] J. Liu, C.-F. Chen, C.-W. Tsao, C.-C. Chang, C.-C. Chu, and D. L. DeVoe. Polymer microchips integrating solid-phase extraction and high-performance liquid chromatography using reversed-phase polymethacrylate monoliths. *Analytical Chemistry*, **81**: 2545–2554, 2009. doi: 10.1021/ac802359e (see pp. 2, 76)

[12] C.-Y. Shih, Y. Chen, J. Xie, Q. He, and Y.-C. Tai. On-chip temperature gradient interaction chromatography. *Journal of Chromatography A*, **1111**: 272–278, 2006. doi: 10.1016/j.chroma.2005.08.075 (see pp. 2, 49, 62, 76)

[13] H. A. Stone, A. D. Stroock, and A. Ajdari. Engineering flows in small devices. *Annual Review of Fluid Mechanics*, **36**: 381–411, 2004. doi: 10.1146/annurev.fluid.36.050802.122124 (see p. 3)

[14] G. P. Rozing, T. van de Goor, H. Yin, K. Killeen, B. Glatz, K. Kraiczek, and H. H. Lauer. An experimental study of chromatographic dynamics in open and packed non-cylindrical conduits. *Journal of Separation Science*, **27**: 1391–1401, 2004. doi: 10.1002/jssc.200401856 (see pp. 3, 50, 63, 76)

[15] T. Aste, M. Saadatfar, and T. J. Senden. Geometrical structure of disordered sphere packings. *Physical Review E*, **71**: 061302, 2005. doi: 10.1103/PhysRevE.71.061302 (see pp. 4, 109)

[16] R. Mizutani, A. Takeuchi, R. Y. Osamura, S. Takekoshi, K. Uesugi, and Y. Suzuki. Submicrometer tomographic resolution examined using a micro-fabricated test object. *Micron*, **41**: 90–95, 2010. doi: 10.1016/j.micron.2009.09.001 (see p. 4)

[17] M. Piller, G. Schena, M. Nolich, S. Favretto, F. Radaelli, and E. Rossi. Analysis of hydraulic permeability in porous media: from high resolution X-ray tomography to direct numerical simulation. *Transport in Porous Media*, **80**: 57–78, 2009. doi: 10.1007/s11242-009-9338-9 (see p. 4)

[18] H. Freund, J. Bauer, T. Zeiser, and G. Emig. Detailed simulation of transport processes in fixed-beds. *Industrial & Engineering Chemistry Research*, **44**: 6423–6434, 2005. doi: 10.1021/ie0489453 (see pp. 4, 17, 25, 28, 29, 35, 118, 135, 136)

[19] B. Manz, L. F. Gladden, and P. B. Warren. Flow and dispersion in porous media: Lattice-Boltzmann and NMR studies. *AIChE Journal*, **45**: 1845–1854, 1999. doi: 10.1002/aic.690450902 (see pp. 4, 92)

[20] D. Hlushkou, S. Bruns, and U. Tallarek. High-performance computing of flow and transport in physically reconstructed silica monoliths. *Journal of Chromatography A*, **1217**: 3674–3682, 2010. doi: 10.1016/j.chroma.2010.04.004 (see p. 4)

[21] J. P. C. Vissers, M. A. Hoeben, J. Laven, H. A. Claessens, and C. A. Cramers. Hydrodynamic aspects of slurry packing processes in microcolumn liquid chromatography. *Journal of Chromatography A*, **883**: 11–25, 2000. doi: 10.1016/S0021-9673(00)00276-4 (see p. 4)

[22] L. A. Colón, T. D. Maloney, and A. M. Fermier. Packing columns for capillary electrochromatography. *Journal of Chromatography A*, **887**: 43–53, 2000. doi: 10.1016/S0021-9673(99)01328-X (see p. 4)

[23] S. S. Skiena. *The algorithm design manual*. 2nd ed. Springer-Verlag, 2008. (see pp. 5, 8)

[24] M. P. Allen and D. J. Tildesley. *Computer simulation of liquids*. Oxford University Press, 1989. (see pp. 5, 6, 9)

[25] B. D. Lubachevsky and F. H. Stillinger. Geometric properties of random disk packings. *Journal of Statistical Physics*, **60**: 561–583, 1990. doi: 10.1007/BF01025983 (see p. 5)

[26] B. D. Lubachevsky, F. H. Stillinger, and E. N. Pinson. Disks vs. spheres: Contrasting properties of random packings. *Journal of Statistical Physics*, **64**: 501–524, 1991. doi: 10.1007/BF01048304 (see p. 5)

[27] A. Donev, S. Torquato, and F. H. Stillinger. Neighbor list collision-driven molecular dynamics simulation for nonspherical hard particles. I. Algorithmic details. *Journal of Computational Physics*, **202**: 737–764, 2005. doi: 10.1016/j.jcp.2004.08.014 (see p. 5)

[28] G. T. Nolan and P. E. Kavanagh. Computer simulation of random packing of hard spheres. *Powder Technology*, **72**: 149–155, 1992. doi: 10.1016/0032-5910(92)88021-9 (see p. 5)

[29] A. Z. Zinchenko. Algorithm for random close packing of spheres with periodic boundary conditions. *Journal of Computational Physics*, **114**: 298–307, 1994. doi: 10.1006/jcph.1994.1168 (see pp. 5, 9, 129)

[30] D. He, N. N. Ekere, and L. Cai. Computer simulation of random packing of unequal particles. *Physical Review E*, **60**: 7098–7104, 1999. DOI: 10.1103/PhysRevE.60.7098 (see p. 5)

[31] C. S. O'Hern, S. A. Langer, A. J. Liu, and S. R. Nagel. Random packings of frictionless particles. *Physical Review Letters*, **88**: 075507, 2002. DOI: 10.1103/PhysRevLett.88.075507 (see p. 5)

[32] G. E. Mueller. Numerically packing spheres in cylinders. *Powder Technology*, **159**: 105–110, 2005. DOI: 10.1016/j.powtec.2005.06.002 (see pp. 5, 118)

[33] Z. Yao, J.-S. Wang, G.-R. Liu, and M. Cheng. Improved neighbor list algorithm in molecular simulations using cell decomposition and data sorting method. *Computer Physics Communications*, **161**: 27–35, 2004. DOI: 10.1016/j.cpc.2004.04.004 (see p. 5)

[34] W. S. Jodrey and E. M. Tory. Computer simulation of close random packing of equal spheres. *Physical Review A*, **32**: 2347–2351, 1985. DOI: 10.1103/PhysRevA.32.2347 (see p. 6)

[35] A. Bezrukov, M. Bargieł, and D. Stoyan. Statistical analysis of simulated random packings of spheres. *Particle & Particle Systems Characterization*, **19**: 111–118, 2002. DOI: 10.1002/1521-4117(200205)19:2%3C111::AID-PPSC111%3E3.0.CO;2-M (see p. 6)

[36] M. Bargieł and J. Mościński. C-language program for the irregular close packing of hard spheres. *Computer Physics Communications*, **64**: 183–192, 1991. DOI: 10.1016/0010-4655(91)90060-X (see pp. 8, 9)

[37] E. M. Tory, N. A. Cochrane, and S. R. Waddell. Anisotropy in simulated random packing of equal spheres. *Nature*, **220**: 1023–1024, 1968. DOI: 10.1038/2201023a0 (see p. 9)

[38] G. E. Schröder-Turk, W. Mickel, M. Schröter, G. W. Delaney, M. Saadatfar, T. J. Senden, K. Mecke, and T. Aste. Disordered spherical bead packs are anisotropic. *EPL*, **90**: 34001, 2010. DOI: 10.1209/0295-5075/90/34001 (see p. 9)

[39] S. Khirevich, A. Höltzel, S. Ehlert, A. Seidel-Morgenstern, and U. Tallarek. Large-scale simulation of flow and transport in reconstructed HPLC-microchip packings. *Analytical Chemistry*, **81**: 4937–4945, 2009. DOI: 10.1021/ac900631d (see pp. 9, 75)

[40] S. Khirevich, A. Höltzel, A. Seidel-Morgenstern, and U. Tallarek. Time and length scales of eddy dispersion in chromatographic beds. *Analytical Chemistry*, **81**: 7057–7066, 2009. DOI: 10.1021/ac901187d (see pp. 9, 90)

[41] A. Okabe. *Spatial tessellations: concepts and applications of Voronoi diagrams*. 2nd ed. John Wiley & Sons, 2000. (see pp. 10, 11, 113, 114, 116)

[42] R. S. Maier, D. M. Kroll, R. S. Bernard, S. E. Howington, J. F. Peters, and H. T. Davis. Hydrodynamic dispersion in confined packed beds. *Physics of Fluids*, **15**: 3795–3815, 2003. DOI: 10.1063/1.1624836 (see pp. 10, 17, 33, 39, 86, 91, 92, 97, 98, 100, 106, 118, 135)

[43] P. Wesseling. *Principles of computational fluid dynamics*. Springer-Verlag, 2001. (see p. 10)

[44] G. Voronoi. Nouvelles applications des paramètres continus à la théorie des formes quadratiques. Premier mémoire. Sur quelques propriétés des formes quadratiques positives parfaites. *Journal für die reine und angewandte Mathematik*, **133**: 97–102, 1908. DOI: 10.1515/crll.1908.133.97 (see pp. 11, 113, 114)

[45] G. Voronoi. Nouvelles applications des paramètres continus à la théorie des formes quadratiques. Deuxième mémoire. Recherches sur les paralléllòèdres primitifs. *Journal für die reine und angewandte Mathematik*, **134**: 198–287, 1908. DOI: 10.1515/crll.1908.134.198 (see pp. 11, 113, 114)

[46] V. A. Luchnikov, N. N. Medvedev, L. Oger, and J.-P. Troadec. Voronoi–Delaunay analysis of voids in systems of nonspherical particles. *Physical Review E*, **59**: 7205–7212, 1999. DOI: 10.1103/PhysRevE.59.7205 (see p. 11)

[47] N. N. Medvedev, V. P. Voloshin, V. A. Luchnikov, and M. L. Gavrilova. An algorithm for three-dimensional Voronoi S-network. *Journal of Computational Chemistry*, **27**: 1676–1692, 2006. DOI: 10.1002/jcc.20484 (see p. 11)

[48] L. D. Landau and E. M. Lifschitz. *Fluid mechanics*. 2nd ed. Butterworth–Heinemann, 2007. (see p. 12)

[49] K. Huang. *Statistical mechanics*. 2nd ed. John Wiley & Sons, 1987. (see p. 13)

[50] P. L. Bhatnagar, E. P. Gross, and M. Krook. A model for collision processes in gases. I. Small amplitude processes in charged and neutral one-component systems. *Physical Review*, **94**: 511–525, 1954. DOI: 10.1103/PhysRev.94.511 (see p. 14)

[51] S. Chapman and T. G. Cowling. *The mathematical theory of non-uniform gases*. 3rd ed. Cambridge University Press, 1990. (see p. 14)

[52] S. Chen, Z. Wang, X. Shan, and G. D. Doolen. Lattice Boltzmann computational fluid dynamics in three dimensions. *Journal of Statistical Physics*, **68**: 379–400, 1992. DOI: 10.1007/BF01341754 (see p. 14)

[53] S. Chen and G. D. Doolen. Lattice Boltzmann method for fluid flows. *Annual Review of Fluid Mechanics*, **30**: 329–364, 1998. DOI: 10.1146/annurev.fluid.30.1.329 (see p. 14)

[54] G. R. McNamara and G. Zanetti. Use of the Boltzmann equation to simulate lattice-gas automata. *Physical Review Letters*, **61**: 2332–2335, 1988. DOI: 10.1103/PhysRevLett.61.2332 (see p. 14)

[55] J. Hardy, Y. Pomeau, and O. de Pazzis. Time evolution of a two-dimensional model system. I. Invariant states and time correlation functions. *Journal of Mathematical Physics*, **14**: 1746–1759, 1973. DOI: 10.1063/1.1666248 (see p. 14)

[56] J. Hardy, O. de Pazzis, and Y. Pomeau. Molecular dynamics of a classical lattice gas: Transport properties and time correlation functions. *Physical Review A*, **13**: 1949–1961, 1976. DOI: 10.1103/PhysRevA.13.1949 (see p. 14)

[57] U. Frisch, B. Hasslacher, and Y. Pomeau. Lattice-gas automata for the Navier–Stokes equation. *Physical Review Letters*, **56**: 1505–1508, 1986. DOI: 10.1103/PhysRevLett.56.1505 (see p. 14)

[58] U. Frisch, D. d'Humières, B. Hasslacher, P. Lallemand, Y. Pomeau, and J.-P. Rivet. Lattice gas hydrodynamics in two and three dimensions. *Complex Systems*, **1**: 649–707, 1987. (see p. 14)

[59] S. Wolfram. Cellular automaton fluids 1: Basic theory. *Journal of Statistical Physics*, **45**: 471–526, 1986. DOI: 10.1007/BF01021083 (see p. 14)

[60] X. He and L.-S. Luo. Theory of the lattice Boltzmann method: From the Boltzmann equation to the lattice Boltzmann equation. *Physical Review E*, **56**: 6811–6817, 1997. DOI: 10.1103/PhysRevE.56.6811 (see pp. 14, 15)

[61] T. Abe. Derivation of the lattice Boltzmann method by means of the discrete ordinate method for the Boltzmann equation. *Journal of Computational Physics*, **131**: 241–246, 1997. DOI: 10.1006/jcph.1996.5595 (see p. 15)

[62] Y. H. Qian, D. d'Humières, and P. Lallemand. Lattice BGK models for Navier–Stokes equation. *EPL*, **17**: 479–484, 1992. DOI: 10.1209/0295-5075/17/6/001 (see p. 16)

[63] X. B. Nie, X. Shan, and H. Chen. Galilean invariance of lattice Boltzmann models. *EPL*, **81**: 34005, 2008. DOI: 10.1209/0295-5075/81/34005 (see p. 16)

[64] X. W. SHAN and X. HE. Discretization of the velocity space in the solution of the Boltzmann equation. *Physical Review Letters*, **80**: 65–68, 1998. DOI: 10.1103/PhysRevLett.80.65 (see p. 16)

[65] S. ANSUMALI, I. V. KARLIN, and H. C. ÖTTINGER. Minimal entropic kinetic models for hydrodynamics. *EPL*, **63**: 798–804, 2003. DOI: 10.1209/epl/i2003-00496-6 (see p. 16)

[66] W.-A. YONG and L.-S. LUO. Nonexistence of *H*-theorem for some lattice Boltzmann models. *Journal of Statistical Physics*, **121**: 91–103, 2005. DOI: 10.1007/s10955-005-5958-9 (see p. 16)

[67] X. SHAN, X.-F. YUAN, and H. CHEN. Kinetic theory representation of hydrodynamics: a way beyond the Navier–Stokes equation. *Journal of Fluid Mechanics*, **550**: 413–441, 2006. DOI: 10.1017/S0022112005008153 (see p. 16)

[68] S. ANSUMALI, I. V. KARLIN, S. ARCIDIACONO, A. ABBAS, and N. I. PRASIANAKIS. Hydrodynamics beyond Navier–Stokes: Exact solution to the lattice Boltzmann hierarchy. *Physical Review Letters*, **98**: 124502, 2007. DOI: 10.1103/PhysRevLett.98.124502 (see p. 16)

[69] S. S. CHIKATAMARLA and I. V. KARLIN. Lattices for the lattice Boltzmann method. *Physical Review E*, **79**: 046701, 2009. DOI: 10.1103/PhysRevE.79.046701 (see p. 16)

[70] X. SHAN. General solution of lattices for Cartesian lattice Bhatanagar–Gross–Krook models. *Physical Review E*, **81**: 036702, 2010. DOI: 10.1103/PhysRevE.81.036702 (see p. 16)

[71] M. B. REIDER and J. D. STERLING. Accuracy of discrete-velocity BGK models for the simulation of the incompressible Navier–Stokes equations. *Computers & Fluids*, **24**: 459–467, 1995. DOI: 10.1016/0045-7930(94)00037-Y (see p. 17)

[72] A. KOPONEN, D. KANDHAI, E. HELLÉN, M. ALAVA, A. G. HOEKSTRA, M. KATAJA, K. NISKANEN, P. M. A. SLOOT, and J. TIMONEN. Permeability of three-dimensional random fiber webs. *Physical Review Letters*, **80**: 716–719, 1998. DOI: 10.1103/PhysRevLett.80.716 (see p. 17)

[73] A. W. J. HEIJS and C. P. LOWE. Numerical evaluation of the permeability and the Kozeny constant for two types of porous media. *Physical Review E*, **51**: 4346–4352, 1995. DOI: 10.1103/PhysRevE.51.4346 (see pp. 17, 21)

[74] C. SUN and L. L. MUNN. Lattice-Boltzmann simulation of blood flow in digitized vessel networks. *Computers & Mathematics with Applications*, **55**: 1594–1600, 2008. DOI: 10.1016/j.camwa.2007.08.019 (see p. 17)

[75] M. A. VAN DER HOEF, R. BEETSTRA, and J. A. M. KUIPERS. Lattice-Boltzmann simulations of low-Reynolds-number flow past mono- and bidisperse arrays of spheres: results for the permeability and drag force. *Journal of Fluid Mechanics*, **528**: 233–254, 2005. DOI: 10.1017/S0022112004003295 (see pp. 17, 21, 22, 136)

[76] R. C. ACHARYA, A. J. VALOCCHI, C. J. WERTH, and T. W. WILLINGHAM. Pore-scale simulation of dispersion and reaction along a transverse mixing zone in two-dimensional porous media. *Water Resources Research*, **43**: W10435, 2007. DOI: 10.1029/2007WR005969 (see pp. 17, 35, 41)

[77] D. R. NOBLE, S. CHEN, J. G. GEORGIADIS, and R. O. BUCKIUS. A consistent hydrodynamic boundary condition for the lattice Boltzmann method. *Physics of Fluids*, **7**: 203–209, 1995. DOI: 10.1063/1.868767 (see p. 17)

[78] A. M. ARTOLI, A. G. HOEKSTRA, and P. M. A. SLOOT. Accelerated lattice BGK method for unsteady simulations through Mach number annealing. *International Journal of Modern Physics C: Computational Physics, Physical Computation*, **14**: 835–845, 2003. DOI: 10.1142/S012918310300498X (see p. 17)

[79] J. BOYD, J. M. BUICK, J. A. COSGROVE, and P. STANSELL. Application of the lattice Boltzmann method to arterial flow simulation: Investigation of boundary conditions for complex arterial ge-

ometries. *Australasian Physical & Engineering Science in Medicine*, **27**: 207–212, 2004. DOI: 10.1007/BF03178650 (see p. 17)

[80] S. GELLER, M. KRAFCZYK, J. TÖLKE, S. TUREK, and J. HRON. Benchmark computations based on lattice-Boltzmann, finite element and finite volume methods for laminar flows. *Computers & Fluids*, **35**: 888–897, 2006. DOI: 10.1016/j.compfluid.2005.08.009 (see p. 17)

[81] C. PAN, L.-S. LUO, and C. T. MILLER. An evaluation of lattice Boltzmann schemes for porous medium flow simulation. *Computers & Fluids*, **35**: 898–909, 2006. DOI: 10.1016/j.compfluid.2005.03.008 (see pp. 17, 20)

[82] A. KUZMIN. *Multiphase simulations with lattice Boltzmann scheme*. PhD thesis. Canada, University of Calgary, 2009. (see p. 17)

[83] I. GINZBOURG and P. M. ADLER. Boundary flow condition analysis for the three-dimensional lattice Boltzmann model. *Journal de Physique II*, **4**: 191–214, 1994. DOI: 10.1051/jp2:1994123 (see pp. 17, 18)

[84] X. HE, Q. ZOU, L.-S. LUO, and M. DEMBO. Analytic solutions of simple flows and analysis of nonslip boundary conditions for the lattice Boltzmann BGK model. *Journal of Statistical Physics*, **87**: 115–136, 1997. DOI: 10.1007/BF02181482 (see pp. 17, 18)

[85] R. S. MAIER and R. S. BERNARD. Lattice-Boltzmann accuracy in pore-scale flow simulation. *Journal of Computational Physics*, **229**: 233–255, 2010. DOI: 10.1016/j.jcp.2009.09.013 (see pp. 18, 20, 21, 39, 127)

[86] D. KANDHAI, A. KOPONEN, A. G. HOEKSTRA, M. KATAJA, J. TIMONEN, and P. M. A. SLOOT. Implementation aspects of 3D lattice-BGK: boundaries, accuracy, and a new fast relaxation method. *Journal of Computational Physics*, **150**: 482–501, 1999. DOI: 10.1006/jcph.1999.6191 (see p. 18)

[87] P. M. ADLER, M. ZUZOVSKY, and H. BRENNER. Spatially periodic suspensions of convex particles in linear shear flows. II. Rheology. *International Journal of Multiphase Flow*, **11**: 387–417, 1985. DOI: 10.1016/0301-9322(85)90064-3 (see p. 18)

[88] J. M. BUICK and C. A. GREATED. Gravity in a lattice Boltzmann model. *Physical Review E*, **61**: 5307–5320, 2000. DOI: 10.1103/PhysRevE.61.5307 (see p. 18)

[89] J. BEAR. *Dynamics of fluids in porous media*. Dover Publications, 1988. (see pp. 19, 21, 22, 24, 90, 116, 125)

[90] F. A. L. DULLIEN. *Porous media: fluid transport and pore structure*. 2nd ed. Academic Press, 1992. (see pp. 19, 21, 22, 125)

[91] B. CHUN and A. J. C. LADD. Interpolated boundary condition for lattice Boltzmann simulations of flows in narrow gaps. *Physical Review E*, **75**: 066705, 2007. DOI: 10.1103/PhysRevE.75.066705 (see p. 20)

[92] A. A. ZICK and G. M. HOMSY. Stokes flow through periodic arrays of spheres. *Journal of Fluid Mechanics*, **115**: 13–26, 1982. DOI: 10.1017/S0022112082000627 (see p. 20)

[93] A. S. SANGANI and A. ACRIVOS. Slow flow through a periodic array of spheres. *International Journal of Multiphase Flow*, **8**: 343–360, 1982. DOI: 10.1016/0301-9322(82)90047-7 (see p. 20)

[94] E. W. LLEWELLIN. LBflow: An extensible lattice Boltzmann framework for the simulation of geophysical flows. Part II: usage and validation. *Computers & Geosciences*, **36**: 123–132, 2010. DOI: 10.1016/j.cageo.2009.08.003 (see p. 20)

[95] R. S. MAIER, D. M. KROLL, H. T. DAVIS, and R. S. BERNARD. Simulation of flow in bidisperse sphere packings. *Journal of Colloid and Interface Science*, **217**: 341–347, 1999. DOI: 10.1006/jcis.1999.6372 (see p. 21)

[96] C. PAN, M. HILPERT, and C. T. MILLER. Pore-scale modeling of saturated permeabilities in random sphere packings. *Physical Review E*, **64**: 066702, 2001. DOI: 10.1103/PhysRevE.64.066702 (see p. 21)

[97] D. VIDAL, C. RIDGWAY, G. PIANET, J. SCHOELKOPF, R. ROY, and F. BERTRAND. Effect of particle size distribution and packing compression on fluid permeability as predicted by lattice-Boltzmann simulations. *Computers & Chemical Engineering*, **33**: 256–266, 2009. DOI: 10.1016/j.compchemeng.2008.09.003 (see pp. 21, 136)

[98] A. P. PHILIPSE and C. PATHMAMANOHARAN. Liquid permeation (and sedimentation) of dense colloidal hard-sphere packings. *Journal of Colloid and Interface Science*, **159**: 96–107, 1993. DOI: 10.1006/jcis.1993.1301 (see p. 21)

[99] D. COELHO, J.-F. THOVERT, and P. M. ADLER. Geometrical and transport properties of random packings of spheres and aspherical particles. *Physical Review E*, **55**: 1959–1978, 1997. DOI: 10.1103/PhysRevE.55.1959 (see pp. 21, 32, 92, 110, 136)

[100] R. P. DIAS, C. S. FERNANDES, J. A. TEIXEIRA, M. MOTA, and A. YELSHIN. Permeability analysis in bisized porous media: Wall effect between particles of different size. *Journal of Hydrology*, **349**: 470–474, 2008. DOI: 10.1016/j.jhydrol.2007.11.020 (see p. 21)

[101] P. B. WARREN and F. STEPANEK. Wall shear rate distribution for flow in random sphere packings. *Physical Review Letters*, **100**: 084501, 2008. DOI: 10.1103/PhysRevLett.100.084501 (see p. 21)

[102] R. DI FELICE and L. G. GIBILARO. Wall effects for the pressure drop in fixed beds. *Chemical Engineering Science*, **59**: 3037–3040, 2004. DOI: 10.1016/j.ces.2004.03.030 (see p. 22)

[103] S. JUNG, S. EHLERT, J.-A. MORA, K. KRAICZEK, M. DITTMANN, G. P. ROZING, and U. TALLAREK. Packing density, permeability, and separation efficiency of packed microchips at different particle-aspect ratios. *Journal of Chromatography A*, **1216**: 264–273, 2009. DOI: 10.1016/j.chroma.2008.11.073 (see pp. 22, 76, 78, 81, 87, 88)

[104] B. EISFELD and K. SCHNITZLEIN. The influence of confining walls on the pressure drop in packed beds. *Chemical Engineering Science*, **56**: 4321–4329, 2001. DOI: 10.1016/S0009-2509(00)00533-9 (see p. 22)

[105] P. MISHRA, D. SINGH, and I. M. MISHRA. Momentum transfer to Newtonian and non-Newtonian fluids flowing through packed and fluidized beds. *Chemical Engineering Science*, **30**: 397–405, 1975. DOI: 10.1016/0009-2509(75)85004-4 (see p. 22)

[106] Y. COHEN and A. B. METZNER. Wall effects in laminar flow of fluids through packed beds. *AIChE Journal*, **27**: 705–715, 1981. DOI: 10.1002/aic.690270502 (see p. 22)

[107] M. WINTERBERG and E. TSOTSAS. Impact of tube-to-particle–diameter ratio on pressure drop in packed beds. *AIChE Journal*, **46**: 1084–1088, 2000. DOI: 10.1002/aic.690460519 (see p. 22)

[108] A. N. TIKHONOV and A. A. SAMARSKII. *Equations of mathematical physics*. Dover Publications, 1990. (see p. 24)

[109] O. C. ZIENKIEWICZ, P. NITHIARASU, and R. L. TAYLOR. *The finite element method for fluid dynamics*. 6th ed. Elsevier Butterworth–Heinemann, 2005. (see p. 24)

[110] M.-K. LIU and J. H. SEINFELD. On the validity of grid and trajectory models of urban air pollution. *Atmospheric Environment*, **9**: 555–574, 1975. DOI: 10.1016/0004-6981(75)90001-3 (see p. 24)

[111] B. P. LEONARD. The ULTIMATE conservative difference scheme applied to unsteady one-dimensional advection. *Computer Methods in Applied Mechanics and Engineering*, **88**: 17–74, 1991. DOI: 10.1016/0045-7825(91)90232-U (see p. 24)

[112] B. H. DEVKOTA and J. IMBERGER. Lagrangian modeling of advection–diffusion transport in open channel flow. *Water Resources Research*, **45**: W12406, 2009. DOI: 10.1029/2009WR008364 (see p. 24)

[113] W. KINZELBACH. *Numerische Methoden zur Modellierung des Transports von Schadstoffen im Grundwasser*. 2nd ed. Oldenbourg Verlag, 1992. (see p. 24)

[114] B. LIN and R. A. FALCONER. Tidal flow and transport modeling using ULTIMATE QUICKEST scheme. *Journal of Hydraulic Engineering*, **123**: 303–314, 1997. DOI: 10.1061/(ASCE)0733-9429(1997)123:4(303) (see p. 24)

[115] A. CORTIS and B. BERKOWITZ. Anomalous transport in "classical" soil and sand columns. *Soil Science Society of America Journal*, **68**: 1539–1548, 2004. DOI: 10.2136/sssaj2004.1539 (see p. 24)

[116] S. ANWAR, A. CORTIS, and M. C. SUKOP. Lattice Boltzmann simulation of solute transport in heterogeneous porous media with conduits to estimate macroscopic continuous time random walk model parameters. *Progress in Computational Fluid Dynamics*, **8**: 213–221, 2008. DOI: 10.1504/PCFD.2008.018092 (see p. 24)

[117] Y. ZHU and P. J. FOX. Simulation of pore-scale dispersion in periodic porous media using smoothed particle hydrodynamics. *Journal of Computational Physics*, **182**: 622–645, 2002. DOI: 10.1006/jcph.2002.7189 (see p. 24)

[118] S. P. KUTTANIKKAD. *Pore-scale direct numerical simulation of flow and transport in porous media*. PhD thesis. Germany, Ruprecht Karl University of Heidelberg, 2009. (see pp. 24, 27, 33, 35, 39)

[119] P. SALAMON, D. FERNÀNDEZ-GARCIA, and J. J. GÓMEZ-HERNÁNDEZ. Modeling tracer transport at the MADE site: The importance of heterogeneity. *Water Resources Research*, **43**: W08404, 2007. DOI: 10.1029/2006WR005522 (see p. 25)

[120] F. DELAY, P. ACKERER, and C. DANQUIGNY. Simulating solute transport in porous or fractured formations using random walk particle tracking: A review. *Vadose Zone Journal*, **4**: 360–379, 2005. DOI: 10.2136/vzj2004.0125 (see p. 25)

[121] P. SALAMON, D. FERNÀNDEZ-GARCIA, and J. J. GÓMEZ-HERNÁNDEZ. A review and numerical assessment of the random walk particle tracking method. *Journal of Contaminant Hydrology*, **87**: 277–305, 2006. DOI: 10.1016/j.jconhyd.2006.05.005 (see p. 25)

[122] C. W. GARDINER. *Handbook of stochastic methods: for physics, chemistry and the natural sciences*. 2nd ed. Springer-Verlag, 1996. (see p. 25)

[123] R. S. MAIER, D. M. KROLL, R. S. BERNARD, S. E. HOWINGTON, J. F. PETERS, and H. T. DAVIS. Pore-scale simulation of dispersion. *Physics of Fluids*, **12**: 2065–2079, 2000. DOI: 10.1063/1.870452 (see pp. 25, 28, 29, 32–39, 51, 53, 65, 100, 136)

[124] D. SPIVAKOVSKAYA, A. W. HEEMINK, and E. DELEERSNIJDER. Lagrangian modelling of multi-dimensional advection–diffusion with space-varying diffusivities: theory and idealized test cases. *Ocean Dynamics*, **57**: 189–203, 2007. DOI: 10.1007/s10236-007-0102-9 (see pp. 25, 28)

[125] P. E. KLOEDEN and E. PLATEN. *Numerical solution of stochastic differential equations*. Springer-Verlag, 1995. (see pp. 25, 26)

[126] H. V. NGUYEN, J. L. NIEBER, P. ODURO, C. J. RITSEMA, L. W. DEKKER, and T. S. STEENHUIS. Modeling solute transport in a water repellent soil. *Journal of Hydrology*, **215**: 188–201, 1999. DOI: 10.1016/S0022-1694(98)00270-4 (see p. 26)

[127] P. H. ISRAELSSON, Y. D. KIM, and E. E. ADAMS. A comparison of three Lagrangian approaches for extending near field mixing calculations. *Environmental Modelling & Software*, **21**: 1631–1649, 2006. DOI: 10.1016/j.envsoft.2005.07.008 (see p. 26)

[128] A. E. HASSAN and M. M. MOHAMED. On using particle tracking methods to simulate transport in single-continuum and dual continua porous media. *Journal of Hydrology*, **275**: 242–260, 2003. DOI: 10.1016/S0022-1694(03)00046-5 (see p. 26)

[129] H. BRENNER. Dispersion resulting from flow through spatially periodic porous media. *Philosophical Transactions of the Royal Society A: Mathematical, Physical & Engineering Sciences*, **297**: 81–133, 1980. DOI: 10.1098/rsta.1980.0205 (see p. 26)

[130] D. HLUSHKOU and U. TALLAREK. Transition from creeping via viscous-inertial to turbulent flow in fixed beds. *Journal of Chromatography A*, **1126**: 70–85, 2006. DOI: 10.1016/j.chroma.2006.06.011 (see pp. 27, 98)

[131] J. C. GIDDINGS. *Dynamics of chromatography: principles and theory*. Marcel Dekker, 1965. (see pp. 27, 90–95, 99–102, 106, 116–124)

[132] M. R. SCHURE, R. S. MAIER, D. M. KROLL, and H. T. DAVIS. Simulation of packed-bed chromatography utilizing high-resolution flow fields: Comparison with models. *Analytical Chemistry*, **74**: 6006–6016, 2002. DOI: 10.1021/ac0204101 (see pp. 27, 32, 95, 96, 113, 117)

[133] P. SZYMCZAK and A. J. C. LADD. Boundary conditions for stochastic solutions of the convection–diffusion equation. *Physical Review E*, **68**: 036704, 2003. DOI: 10.1103/PhysRevE.68.036704 (see pp. 27, 28, 30)

[134] R. K. NANDIGAM and D. M. KROLL. Three-dimensional modeling of the brain's ECS by minimum configurational energy packing of fluid vesicles. *Biophysical Journal*, **92**: 3368–3378, 2007. DOI: 10.1529/biophysj.106.095547 (see pp. 27, 28)

[135] J. HRABE, S. HRABĚTOVÁ, and K. SEGETH. A model of effective diffusion and tortuosity in the extracellular space of the brain. *Biophysical Journal*, **87**: 1606–1617, 2004. DOI: 10.1529/biophysj.103.039495 (see p. 27)

[136] I. C. KIM and S. TORQUATO. Diffusion of finite-sized Brownian particles in porous media. *Journal of Chemical Physics*, **96**: 1498–1503, 1992. DOI: 10.1063/1.462184 (see p. 27)

[137] P. N. SEN, L. M. SCHWARTZ, P. P. MITRA, and B. I. HALPERIN. Surface relaxation and the long-time diffusion coefficient in porous media: Periodic geometries. *Physical Review B*, **49**: 215–225, 1994. DOI: 10.1103/PhysRevB.49.215 (see pp. 27, 29)

[138] A. S. KIM and H. CHEN. Diffusive tortuosity factor of solid and soft cake layers: A random walk simulation approach. *Journal of Membrane Science*, **279**: 129–139, 2006. DOI: 10.1016/j.memsci.2005.11.042 (see pp. 27, 127)

[139] T. RAGE. *Studies of tracer dispersion and fluid flow in porous media*. PhD thesis. Norway, University of Oslo, 1996. (see p. 28)

[140] S. TRINH, P. ARCE, and B. R. LOCKE. Effective diffusivities of point-like molecules in isotropic porous media by Monte Carlo simulation. *Transport in Porous Media*, **38**: 241–259, 2000. DOI: 10.1023/A:1006616009669 (see p. 28)

[141] J. SALLES, J.-F. THOVERT, R. DELANNAY, L. PREVORS, J.-L. AURIAULT, and P. M. ADLER. Taylor dispersion in porous media. Determination of the dispersion tensor. *Physics of Fluids A: Fluid Dynamics*, **5**: 2348–2376, 1993. DOI: 10.1063/1.858751 (see pp. 28, 29, 32)

[142] F. J. JIMÉNEZ-HORNERO, J. V. GIRÁLDEZ, and A. LAGUNA. Simulation of tracer dispersion in porous media using lattice Boltzmann and random walk models. *Vadose Zone Journal*, **4**: 310–316, 2005. DOI: 10.2136/vzj2004.0090 (see pp. 28, 29)

[143] W. M. CHARLES. *Transport modelling in coastal waters using stochastic differential equations*. PhD thesis. The Netherlands, Delft University of Technology, 2007. (see p. 28)

[144] J. W. STIJNEN. *Numerical methods for stochastic environmental models*. PhD thesis. The Netherlands, Delft University of Technology, 2002. (see p. 28)

[145] D. L. KOCH and J. F. BRADY. Dispersion in fixed beds. *Journal of Fluid Mechanics*, **154**: 399–427, 1985. DOI: 10.1017/S0022112085001598 (see pp. 29, 90, 116)

[146] M. R. SCHURE. In: *Advances in Chromatography*. P. R. BROWN and E. GRUSHKA, eds. Vol. 39, 139–200. Marcel Dekker Publishing, 1998. (see p. 29)

[147] G. TAYLOR. Dispersion of soluble matter in solvent flowing slowly through a tube. *Philosophical Transactions of the Royal Society A: Mathematical, Physical & Engineering Sciences*, **219**: 186–203, 1953. DOI: 10.1098/rspa.1953.0139 (see p. 30)

[148] G. TAYLOR. Conditions under which dispersion of a solute in a stream of solvent can be used to measure molecular diffusion. *Philosophical Transactions of the Royal Society A: Mathematical, Physical & Engineering Sciences*, **225**: 473–477, 1954. DOI: 10.1098/rspa.1954.0216 (see p. 30)

[149] R. ARIS. On the dispersion of a solute by diffusion, convection and exchange between phases. *Philosophical Transactions of the Royal Society A: Mathematical, Physical & Engineering Sciences*, **252**: 538–550, 1959. DOI: 10.1098/rspa.1959.0171 (see p. 30)

[150] D. DUTTA, A. RAMACHANDRAN, and D. T. LEIGHTON. Effect of channel geometry on solute dispersion in pressure-driven microfluidic systems. *Microfluidics and Nanofluidics*, **2**: 275–290, 2006. DOI: 10.1007/s10404-005-0070-7 (see pp. 30, 50, 63, 80)

[151] H. AHN and S. BRANDANI. Analysis of breakthrough dynamics in rectangular channels of arbitrary aspect ratio. *AIChE Journal*, **51**: 1980–1990, 2005. DOI: 10.1002/aic.10432 (see p. 30)

[152] D. LIANG, Q. PENG, K. MITCHELSON, X. GUAN, W. XING, and J. CHENG. A simple and efficient approach for calculating permeability coefficients and HETP for rectangular columns. *Lab on a Chip*, **7**: 1062–1073, 2007. DOI: 10.1039/b706720h (see p. 30)

[153] A. ADROVER, S. CERBELLI, F. GAROFALO, and M. GIONA. Convection-dominated dispersion regime in wide-bore chromatography: A transport-based approach to assess the occurrence of slip flows in microchannels. *Analytical Chemistry*, **81**: 8009–8014, 2009. DOI: 10.1021/ac901504u (see p. 31)

[154] M. GIONA, A. ADROVER, S. CERBELLI, and F. GAROFALO. Laminar dispersion at high Péclet numbers in finite-length channels: Effects of the near-wall velocity profile and connection with the generalized Leveque problem. *Physics of Fluids*, **21**: 123601, 2009. DOI: 10.1063/1.3263704 (see p. 31)

[155] D. J. GUNN and C. PRYCE. Dispersion in packed beds. *Transactions of the Institution of Chemical Engineers*, **47**: T341, 1969. (see p. 32)

[156] H. P. A. SOUTO and C. MOYNE. Dispersion in two-dimensional periodic porous media. Part II. Dispersion tensor. *Physics of Fluids*, **9**: 2253–2263, 1997. DOI: 10.1063/1.869347 (see p. 32)

[157] H. P. A. SOUTO and C. MOYNE. Dispersion in two-dimensional periodic porous media. Part I. Hydrodynamics. *Physics of Fluids*, **9**: 2243–2252, 1997. DOI: 10.1063/1.869365 (see p. 32)

[158] C. P. LOWE and D. FRENKEL. Do hydrodynamic dispersion coefficients exist? *Physical Review Letters*, **77**: 4552–4555, 1996. DOI: 10.1103/PhysRevLett.77.4552 (see pp. 33–36)

[159] A. M. TARTAKOVSKY. Langevin model for reactive transport in porous media. *Physical Review E*, **82**: 026302, 2010. DOI: 10.1103/PhysRevE.82.026302 (see p. 33)

[160] D. BUYUKTAS and W. W. WALLENDER. Dispersion in spatially periodic porous media. *Heat and Mass Transfer*, **40**: 261–270, 2004. DOI: 10.1007/s00231-003-0441-0 (see p. 33)

[161] J. BILLEN, P. GZIL, N. VERVOORT, G. V. BARON, and G. DESMET. Influence of the packing heterogeneity on the performance of liquid chromatography supports. *Journal of Chromatography A*, **1073**: 53–61, 2005. DOI: 10.1016/j.chroma.2004.10.042 (see pp. 33, 124)

[162] B. J. ALDER and T. E. WAINWRIGHT. Decay of the velocity autocorrelation function. *Physical Review A*, **1**: 18–21, 1970. DOI: 10.1103/PhysRevA.1.18 (see p. 33)

[163] D. L. KOCH, R. J. HILL, and A. S. SANGANI. Brinkman screening and the covariance of the fluid velocity in fixed beds. *Physics of Fluids*, **10**: 3035–3037, 1998. DOI: 10.1063/1.869830 (see pp. 33, 34)

[164] D. FRENKEL and M. H. ERNST. Simulation of diffusion in a two-dimensional lattice-gas cellular automaton: A test of mode-coupling theory. *Physical Review Letters*, **63**: 2165–2168, 1989. DOI: 10.1103/PhysRevLett.63.2165 (see p. 35)

[165] R. M. H. MERKS, A. G. HOEKSTRA, and P. M. A. SLOOT. The moment propagation method for advection–diffusion in the lattice Boltzmann method: Validation and Péclet number limits. *Journal of Computational Physics*, **183**: 563–576, 2002. DOI: 10.1006/jcph.2002.7209 (see p. 35)

[166] J. M. P. Q. DELGADO. A critical review of dispersion in packed beds. *Heat and Mass Transfer*, **42**: 279–310, 2006. DOI: 10.1007/s00231-005-0019-0 (see pp. 35, 50, 63, 90, 92, 93, 95, 98, 116, 118, 126)

[167] M. QUINTARD and S. WHITAKER. Transport in ordered and disordered porous media: Volume-averaged equations, closure problems, and comparison with experiment. *Chemical Engineering Science*, **48**: 2537–2564, 1993. DOI: 10.1016/0009-2509(93)80266-S (see p. 35)

[168] M. STÖHR. *Analysis of flow and transport in refractive index matched porous media*. PhD thesis. Germany, Ruprecht Karl University of Heidelberg, 2003. (see p. 35)

[169] A. JAFARI, P. ZAMANKHAN, S. M. MOUSAVI, and K. PIETARINEN. Modeling and CFD simulation of flow behavior and dispersivity through randomly packed bed reactors. *Chemical Engineering Journal*, **144**: 476–482, 2008. DOI: 10.1016/j.cej.2008.07.033 (see p. 35)

[170] B. BIJELJIC and M. J. BLUNT. Pore-scale modeling and continuous time random walk analysis of dispersion in porous media. *Water Resources Research*, **42**: W01202, 2006. DOI: 10.1029/2005WR004578 (see p. 35)

[171] C. SONG, P. WANG, and H. A. MAKSE. A phase diagram for jammed matter. *Nature*, **453**: 629–632, 2008. DOI: 10.1038/nature06981 (see pp. 35, 109, 112, 116, 127)

[172] R. S. MAIER, M. R. SCHURE, J. P. GAGE, and J. D. SEYMOUR. Sensitivity of pore-scale dispersion to the construction of random bead packs. *Water Resources Research*, **44**: W06S03, 2008. DOI: 10.1029/2006WR005577 (see pp. 36–39, 110)

[173] A. A. KHRAPITCHEV and P. T. CALLAGHAN. Reversible and irreversible dispersion in a porous medium. *Physics of Fluids*, **15**: 2649–2660, 2003. DOI: 10.1063/1.1596914 (see p. 36)

[174] D. S. GREBENKOV. NMR survey of reflected Brownian motion. *Reviews of Modern Physics*, **79**: 1077–1137, 2007. DOI: 10.1103/RevModPhys.79.1077 (see p. 36)

[175] D. S. GREBENKOV. Use, misuse, and abuse of apparent diffusion coefficients. *Concepts in Magnetic Resonance Part A*, **36A**: 24–35, 2010. DOI: 10.1002/cmr.a.20152 (see p. 36)

[176] J. D. SEYMOUR and P. T. CALLAGHAN. Generalized approach to NMR analysis of flow and dispersion in porous media. *AIChE Journal*, **43**: 2096–2111, 1997. DOI: 10.1002/aic.690430817 (see pp. 36–38)

[177] F. AUGIER, F. IDOUX, and J. Y. DELENNE. Numerical simulations of transfer and transport properties inside packed beds of spherical particles. *Chemical Engineering Science*, **65**: 1055–1064, 2010. DOI: 10.1016/j.ces.2009.09.059 (see pp. 36–38, 135, 136)

[178] U. M. SCHEVEN, R. HARRIS, and M. L. JOHNS. Intrinsic dispersivity of randomly packed monodisperse spheres. *Physical Review Letters*, **99**: 054502, 2007. DOI: 10.1103/PhysRevLett.99.054502 (see pp. 36–39)

[179] M. SAHIMI. *Flow and transport in porous media and fractured rock: From classical methods to modern approaches*. Wiley-VCH, 1995. (see p. 36)

[180] R. S. MAIER, D. M. KROLL, and H. T. DAVIS. Diameter-dependent dispersion in packed cylinders. *AIChE Journal*, **53**: 527–530, 2007. DOI: 10.1002/aic.11083 (see pp. 37, 39, 50, 61, 92, 98, 118, 135)

[181] P. A. CUNDALL and O. D. L. STRACK. A discrete numerical model for granular assemblies. *Geotechnique*, **29**: 47–65, 1979. DOI: 10.1680/geot.1979.29.1.47 (see pp. 37, 38)

[182] U. M. SCHEVEN. Dispersion in non-ideal packed beds. *AIChE Journal*, **56**: 289–297, 2010. DOI: 10.1002/aic.11993 (see p. 39)

[183] P. G. SAFFMAN. A theory of dispersion in a porous medium. *Journal of Fluid Mechanics*, **6**: 321–349, 1959. DOI: 10.1017/S0022112059000672 (see p. 39)

[184] P. G. SAFFMAN. Dispersion due to molecular diffusion and macroscopic mixing in flow through a network of capillaries. *Journal of Fluid Mechanics*, **7**: 194–208, 1960. DOI: 10.1017/S0022112060001432 (see p. 39)

[185] R. S. MAIER, D. M. KROLL, R. S. BERNARD, S. E. HOWINGTON, J. F. PETERS, and H. T. DAVIS. Enhanced dispersion in cylindrical packed beds. *Philosophical Transactions of the Royal Society A: Mathematical, Physical & Engineering Sciences*, **360**: 497–506, 2002. DOI: 10.1098/rsta.2001.0951 (see pp. 39, 61, 110, 118)

[186] P. MAGNICO. Hydrodynamic and transport properties of packed beds in small tube-to-sphere diameter ratio: pore scale simulation using an Eulerian and a Lagrangian approach. *Chemical Engineering Science*, **58**: 5005–5024, 2003. DOI: 10.1016/S0009-2509(03)00282-3 (see pp. 39, 110)

[187] H. EGHBALI, V. VERDOOLD, L. VANKEERBERGHEN, H. GARDENIERS, and G. DESMET. Experimental investigation of the band broadening arising from short-range interchannel heterogeneities in chromatographic beds under the condition of identical external porosity. *Analytical Chemistry*, **81**: 705–715, 2009. DOI: 10.1021/ac802124p (see pp. 40, 42)

[188] B. HE, N. TAIT, and F. REGNIER. Fabrication of nanocolumns for liquid chromatography. *Analytical Chemistry*, **70**: 3790–3797, 1998. DOI: 10.1021/ac980028h (see p. 40)

[189] P. T. CALLAGHAN and S. L. CODD. Flow coherence in a bead pack observed using frequency domain modulated gradient nuclear magnetic resonance. *Physics of Fluids*, **13**: 421–427, 2001. DOI: 10.1063/1.1336810 (see p. 41)

[190] J. DE SMET, P. GZIL, G. V. BARON, and G. DESMET. On the 3-dimensional effects in etched chips for high performance liquid chromatography-separations. *Journal of Chromatography A*, **1154**: 189–197, 2007. DOI: 10.1016/j.chroma.2007.03.076 (see p. 42)

[191] H. EGHBALI, W. DE MALSCHE, J. DE SMET, J. BILLEN, M. DE PRA, W. TH. KOK, P. J. SCHOENMAKERS, H. GARDENIERS, and G. DESMET. Experimental investigation of the band broadening originating

from the top and bottom walls in micromachined nonporous pillar array columns. *Journal of Separation Science*, **30**: 2605–2613, 2007. DOI: 10.1002/jssc.200700203 (see p. 42)

[192] H. EGHBALI, W. DE MALSCHE, D. CLICQ, H. GARDENIERS, and G. DESMET. Pressure-driven chromatography in perfectly ordered pillar array columns. *LC-GC Europe*, **20**: 208–222, 2007. (see p. 42)

[193] W. DE MALSCHE, H. EGHBALI, D. CLICQ, J. VANGELOOVEN, H. GARDENIERS, and G. DESMET. Pressure-driven reverse-phase liquid chromatography separations in ordered nonporous pillar array columns. *Analytical Chemistry*, **79**: 5915–5926, 2007. DOI: 10.1021/ac070352p (see p. 42)

[194] W. DE MALSCHE, D. CLICQ, V. VERDOOLD, P. GZIL, G. DESMET, and H. GARDENIERS. Integration of porous layers in ordered pillar arrays for liquid chromatography. *Lab on a Chip*, **7**: 1705–1711, 2007. DOI: 10.1039/b710507j (see p. 42)

[195] M. DE PRA, W. TH. KOK, J. G. E. GARDENIERS, G. DESMET, S. EELTINK, J. W. VAN NIEUWKASTEELE, and P. J. SCHOENMAKERS. Experimental study on band dispersion in channels structured with micropillars. *Analytical Chemistry*, **78**: 6519–6525, 2006. DOI: 10.1021/ac060915h (see p. 42)

[196] C. SOSA and B. KNUDSON. *IBM system Blue Gene solution: Blue Gene/P application development*. 4th ed. IBM, International Technical Support Organization, 2009. (see pp. 43, 44)

[197] B. R. DE SUPINSKI et al. BlueGene/L applications: Parallelism on a massive scale. *International Journal of High Performance Computing Applications*, **22**: 33–51, 2008. DOI: 10.1177/1094342007085025 (see p. 43)

[198] S. KHIREVICH, A. DANEYKO, and U. TALLAREK. "Simulation of fluid flow and mass transport at extreme scale" in: *Jülich Blue Gene/P Extreme Scaling Workshop 2010* ed. by B. MOHR and W. FRINGS. Forschungszentrum Jülich, Jülich Supercomputing Centre, 2010. (see pp. 43, 46)

[199] G. WELLEIN, T. ZEISER, G. HAGER, and S. DONATH. On the single processor performance of simple lattice Boltzmann kernels. *Computers & Fluids*, **35**: 910–919, 2006. DOI: 10.1016/j.compfluid.2005.02.008 (see p. 44)

[200] J. HANDY. *The cache memory book*. 2nd ed. Academic Press, 1998. (see p. 44)

[201] B. W. KERNIGHAN and D. M. RITCHIE. *C programming language*. 2nd ed. Prentice Hall, 1988. (see p. 44)

[202] *ISO/IEC 9899:1999: Programming languages — C*. International Organization for Standardization, 1999. (see p. 44)

[203] J. GÖTZ, K. IGLBERGER, M. STÜRMER, and U. RÜDE. "Direct numerical simulation of particulate flows on 294 912 processor cores" in: *ACM/IEEE International Conference for High Performance Computing, Networking, Storage and Analysis*. Los Alamitos, CA, USA, 2010. (see p. 44)

[204] *MPI: A Message-Passing Interface Standard, Version 2.2*. Message Passing Interface Forum, 2009. (see pp. 44, 46)

[205] *Engineering and Scientific Subroutine Library for Linux on POWER, Version 4 Release 2.2*. 4th ed. IBM Corporation, 2005. (see p. 45)

[206] R. HYDE. *Write great code, volume 1: Understanding the machine*. No Starch Press, 2004. (see p. 45)

[207] R. HYDE. *Write great code, volume 2: Thinking low-level, writing high-level*. No Starch Press, 2006. (see p. 45)

[208] S. WEISS and A. GOLDSTEIN. Floating point micropipeline performance. *Journal of Systems Architecture*, **45**: 15–29, 1998. DOI: 10.1016/S1383-7621(97)00070-2 (see p. 45)

[209] *Parallel Environment for AIX and Linux: MPI Subroutine Reference*. IBM Corporation, 2010. (see p. 46)

[210] S. FADDEN. *An Introduction to GPFS Version 3.3*. IBM Corporation, 2010. (see p. 47)

[211] J. BORRILL, L. OLIKER, J. SHALF, H. SHAN, and A. USELTON. HPC global file system performance analysis using a scientific-application derived benchmark. *Parallel Computing*, **35**: 358–373, 2009. DOI: 10.1016/j.parco.2009.02.002 (see p. 47)

[212] W. FRINGS, F. WOLF, and V. PETKOV. "Scalable massively parallel I/O to task-local files" in: *Proceedings of the Conference on High Performance Computing Networking, Storage and Analysis*. New York, NY, USA, 2009. (see p. 47)

[213] S. KHIREVICH, A. HÖLTZEL, D. HLUSHKOU, and U. TALLAREK. Impact of conduit geometry and bed porosity on flow and dispersion in noncylindrical sphere packings. *Analytical Chemistry*, **79**: 9340–9349, 2007. DOI: 10.1021/ac071428k (see pp. 48, 63, 66, 68)

[214] N. LION, T. C. ROHNER, L. DAYON, I. L. ARNAUD, E. DAMOC, N. YOUHNOVSKI, Z.-Y. WU, C. ROUSSEL, J. JOSSERAND, H. JENSEN, J. S. ROSSIER, M. PRZYBYLSKI, and H. H. GIRAULT. Microfluidic systems in proteomics. *Electrophoresis*, **24**: 3533–3562, 2003. DOI: 10.1002/elps.200305629 (see p. 48)

[215] M. J. MADOU. *Fundamentals of microfabrication: the science of miniaturization*. 2nd ed. CRC Press, 2002. (see p. 48)

[216] O. GESCHKE, H. KLANK, and P. TELLEMANN. *Microsystem engineering of lab-on-a-chip devices*. John Wiley & Sons, 2004. (see p. 48)

[217] S. C. JAKEWAY, A. J. DE MELLO, and E. L. RUSSELL. Miniaturized total analysis systems for biological analysis. *Fresenius' Journal of Analytical Chemistry*, **366**: 525–539, 2000. DOI: 10.1007/s002160051548 (see p. 48)

[218] D. R. REYES, D. IOSSIFIDIS, P.-A. AUROUX, and A. MANZ. Micro total analysis systems. 1. Introduction, theory, and technology. *Analytical Chemistry*, **74**: 2623–2636, 2002. DOI: 10.1021/ac0202435 (see p. 48)

[219] P.-A. AUROUX, D. IOSSIFIDIS, D. R. REYES, and A. MANZ. Micro total analysis systems. 2. Analytical standard operations and applications. *Analytical Chemistry*, **74**: 2637–2652, 2002. DOI: 10.1021/ac020239t (see p. 48)

[220] T. VILKNER, D. JANASEK, and A. MANZ. Micro total analysis systems. Recent developments. *Analytical Chemistry*, **76**: 3373–3386, 2004. DOI: 10.1021/ac040063q (see p. 48)

[221] P. S. DITTRICH, K. TACHIKAWA, and A. MANZ. Micro total analysis systems. Latest advancements and trends. *Analytical Chemistry*, **78**: 3887–3908, 2006. DOI: 10.1021/ac0605602 (see pp. 48, 62)

[222] J. XIE, Y. MIAO, J. SHIH, Y.-C. TAI, and T. D. LEE. Microfluidic platform for liquid chromatography–tandem mass spectrometry analyses of complex peptide mixtures. *Analytical Chemistry*, **77**: 6947–6953, 2005. DOI: 10.1021/ac0510888 (see pp. 49, 62)

[223] I. M. LAZAR, P. TRISIRIPISAL, and H. A. SARVAIYA. Microfluidic liquid chromatography system for proteomic applications and biomarker screening. *Analytical Chemistry*, **78**: 5513–5524, 2006. DOI: 10.1021/ac060434y (see pp. 49, 62, 76)

[224] J. CARLIER, S. ARSCOTT, V. THOMY, J.-C. CAMART, C. CREN-OLIVÉ, and S. LE GAC. Integrated microfabricated systems including a purification module and an on-chip nano electrospray ionization interface for biological analysis. *Journal of Chromatography A*, **1071**: 213–222, 2005. DOI: 10.1016/j.chroma.2004.12.037 (see pp. 49, 62)

[225] Y. YANG, C. LI, J. KAMEOKA, K. H. LEE, and H. G. CRAIGHEAD. A polymeric microchip with integrated tips and *in situ* polymerized monolith for electrospray mass spectrometry. *Lab on a Chip*, **5**: 869–876, 2005. DOI: 10.1039/b503025k (see pp. 49, 62, 76)

[226] M.-H. FORTIER, E. BONNEIL, P. GOODLEY, and P. THIBAULT. Integrated microfluidic device for mass spectrometry-based proteomics and its application to biomarker discovery programs. *Analytical Chemistry*, **77**: 1631–1640, 2005. DOI: 10.1021/ac048506d (see p. 49)

[227] A. ISHIDA, T. YOSHIKAWA, M. NATSUME, and T. KAMIDATE. Reversed-phase liquid chromatography on a microchip with sample injector and monolithic silica column. *Journal of Chromatography A*, **1132**: 90–98, 2006. DOI: 10.1016/j.chroma.2006.07.025 (see pp. 49, 62, 76)

[228] D. A. MAIR, E. GEIGER, A. P. PISANO, J. M. J. FRÉCHET, and F. SVEC. Injection molded microfluidic chips featuring integrated interconnects. *Lab on a Chip*, **6**: 1346–1354, 2006. DOI: 10.1039/b605911b (see pp. 49, 62)

[229] J. LIU, K.-W. RO, R. NAYAK, and D. R. KNAPP. Monolithic column plastic microfluidic device for peptide analysis using electrospray from a channel opening on the edge of the device. *International Journal of Mass Spectrometry*, **259**: 65–72, 2007. DOI: 10.1016/j.ijms.2006.08.017 (see pp. 49, 62, 76)

[230] NANOSTREAM. *Brio Cartridges*. (see p. 49)

[231] D. S. PETERSON. Solid supports for micro analytical systems. *Lab on a Chip*, **5**: 132–139, 2005. DOI: 10.1039/b405311g (see pp. 49, 63, 75)

[232] K. W. RO, R. NAYAK, and D. R. KNAPP. Monolithic media in microfluidic devices for proteomics. *Electrophoresis*, **27**: 3547–3558, 2006. DOI: 10.1002/elps.200600058 (see pp. 49, 63)

[233] G. OCVIRK, E. VERPOORTE, A. MANZ, M. GRASSERBAUER, and M. H. WIDMER. High-performance liquid-chromatography partially integrated onto a silicon chip. *Analytical Methods and Instrumentation*, **2**: 74–82, 1995. (see p. 49)

[234] A. J. SEDERMAN, P. ALEXANDER, and L. F. GLADDEN. Structure of packed beds probed by Magnetic Resonance Imaging. *Powder Technology*, **117**: 255–269, 2001. DOI: 10.1016/S0032-5910(00)00374-0 (see pp. 50, 97)

[235] A. DE KLERK. Voidage variation in packed beds at small column to particle diameter ratio. *AIChE Journal*, **49**: 2022–2029, 2003. DOI: 10.1002/aic.690490812 (see pp. 50, 63, 66, 68, 73, 86, 97, 106, 118)

[236] D. TANG, A. JESS, X. REN, B. BLUEMICH, and S. STAPF. Axial dispersion and wall effects in narrow fixed bed reactors: A comparative study based on RTD and NMR measurements. *Chemical Engineering & Technology*, **27**: 866–873, 2004. DOI: 10.1002/ceat.200402076 (see pp. 50, 97)

[237] J. THEUERKAUF, P. WITT, and D. SCHWESIG. Analysis of particle porosity distribution in fixed beds using the discrete element method. *Powder Technology*, **165**: 92–99, 2006. DOI: 10.1016/j.powtec.2006.03.022 (see pp. 50, 97)

[238] R. A. SHALLIKER, B. S. BROYLES, and G. GUIOCHON. Physical evidence of two wall effects in liquid chromatography. *Journal of Chromatography A*, **888**: 1–12, 2000. DOI: 10.1016/S0021-9673(00)00517-3 (see pp. 50, 95, 98, 118)

[239] R. T. KENNEDY and J. W. JORGENSON. Preparation and evaluation of packed capillary liquid chromatography columns with inner diameters from 20 to 50 μm. *Analytical Chemistry*, **61**: 1128–1135, 1989. DOI: 10.1021/ac00185a016 (see pp. 50, 98, 104)

[240] S. HSIEH and J. W. JORGENSON. Preparation and evaluation of slurry-packed liquid chromatography microcolumns with inner diameters from 12 to 33 μm. *Analytical Chemistry*, **68**: 1212–1217, 1996. DOI: 10.1021/ac950682m (see pp. 50, 98, 104)

[241] S. EELTINK, G. P. ROZING, P. J. SCHOENMAKERS, and W. TH. KOK. Study of the influence of the aspect ratio on efficiency, flow resistance and retention factors of packed capillary columns in pressure- and electrically-driven liquid chromatography. *Journal of Chromatography A*, **1044**: 311–316, 2004. DOI: 10.1016/j.chroma.2004.06.007 (see p. 50)

[242] H. POPPE. Mass transfer in rectangular chromatographic channels. *Journal of Chromatography A*, **948**: 3–17, 2002. DOI: 10.1016/S0021-9673(01)01372-3 (see p. 50)

[243] A. AJDARI, N. BONTOUX, and H. A. STONE. Hydrodynamic dispersion in shallow microchannels: The effect of cross-sectional shape. *Analytical Chemistry*, **78**: 387–392, 2006. DOI: 10.1021/ac0508651 (see pp. 50, 63)

[244] N. BONTOUX, A. PÉPIN, Y. CHEN, A. AJDARI, and H. A. STONE. Experimental characterization of hydrodynamic dispersion in shallow microchannels. *Lab on a Chip*, **6**: 930–935, 2006. DOI: 10.1039/b518130e (see p. 50)

[245] H. EGHBALI and G. DESMET. Optimum kinetic performance of open-tubular separations in microfluidic devices. *Journal of Separation Science*, **30**: 1377–1397, 2007. DOI: 10.1002/jssc.200600464 (see p. 50)

[246] R. S. MAIER, D. M. KROLL, Y. E. KUTSOVSKY, H. T. DAVIS, and R. S. BERNARD. Simulation of flow through bead packs using the lattice Boltzmann method. *Physics of Fluids*, **10**: 60–74, 1998. DOI: 10.1063/1.869550 (see p. 58)

[247] D. HLUSHKOU, A. SEIDEL-MORGENSTERN, and U. TALLAREK. Numerical analysis of electroosmotic flow in dense regular and random arrays of impermeable, nonconducting spheres. *Langmuir*, **21**: 6097–6112, 2005. DOI: 10.1021/la050239z (see pp. 58, 87, 97, 110)

[248] U. TALLAREK, K. ALBERT, E. BAYER, and G. GUIOCHON. Measurement of transverse and axial apparent dispersion coefficients in packed beds. *AIChE Journal*, **42**: 3041–3054, 1996. DOI: 10.1002/aic.690421106 (see p. 60)

[249] S. KHIREVICH, A. HÖLTZEL, D. HLUSHKOU, A. SEIDEL-MORGENSTERN, and U. TALLAREK. Structure–transport analysis for particulate packings in trapezoidal microchip separation channels. *Lab on a Chip*, **8**: 1801–1808, 2008. DOI: 10.1039/b810688f (see p. 62)

[250] J. HERNÁNDEZ-BORGES, Z. ATURKI, A. ROCCO, and S. FANALI. Recent applications in nanoliquid chromatography. *Journal of Separation Science*, **30**: 1589–1610, 2007. DOI: 10.1002/jssc.200700061 (see pp. 62, 75)

[251] U. D. NEUE. *HPLC columns: theory, technology, and practice*. Wiley-VCH, 1997. (see p. 62)

[252] P. A. LEVKIN, S. EELTINK, T. R. STRATTON, R. BRENNEN, K. ROBOTTI, H. YIN, K. KILLEEN, F. SVEC, and J. M. J. FRÉCHET. Monolithic porous polymer stationary phases in polyimide chips for the fast high-performance liquid chromatography separation of proteins and peptides. *Journal of Chromatography A*, **1200**: 55–61, 2008. DOI: 10.1016/j.chroma.2008.03.025 (see p. 62)

[253] A. GASPAR, M. E. PIYASENA, and F. A. GOMEZ. Fabrication of fritless chromatographic microchips packed with conventional reversed-phase silica particles. *Analytical Chemistry*, **79**: 7906–7909, 2007. DOI: 10.1021/ac071106g (see p. 62)

[254] S. EHLERT, K. KRAICZEK, J.-A. MORA, M. DITTMANN, G. P. ROZING, and U. TALLAREK. Separation efficiency of particle-packed HPLC microchips. *Analytical Chemistry*, **80**: 5945–5950, 2008. DOI: 10.1021/ac800576v (see pp. 62, 65, 76, 78, 81, 86–89)

[255] J. Billen and G. Desmet. Understanding and design of existing and future chromatographic support formats. *Journal of Chromatography A*, **1168**: 73–99, 2007. doi: 10.1016/j.chroma.2007.07.069 (see p. 63)

[256] M. De Pra, W. Th. Kok, and P. J. Schoenmakers. Topographic structures and chromatographic supports in microfluidic separation devices. *Journal of Chromatography A*, **1184**: 560–572, 2008. doi: 10.1016/j.chroma.2007.09.086 (see pp. 63, 75)

[257] A. R. Abate, D. Lee, T. Do, C. Holtze, and D. A. Weitz. Glass coating for PDMS microfluidic channels by sol–gel methods. *Lab on a Chip*, **8**: 516–518, 2008. doi: 10.1039/b800001h (see p. 63)

[258] K. Horiuchi, P. Dutta, and C. D. Richards. Experiment and simulation of mixed flows in a trapezoidal microchannel. *Microfluidics and Nanofluidics*, **3**: 347–358, 2007. doi: 10.1007/s10404-006-0129-0 (see p. 63)

[259] E. K. Zholkovskij and J. H. Masliyah. Influence of cross-section geometry on band broadening in plug-flow microchannels. *Chemical Engineering Science*, **61**: 4155–4164, 2006. doi: 10.1016/j.ces.2005.10.020 (see p. 63)

[260] M. Bahrami, M. M. Yovanovich, and J. R. Culham. A novel solution for pressure drop in singly connected microchannels of arbitrary cross-section. *International Journal of Heat and Mass Transfer*, **50**: 2492–2502, 2007. doi: 10.1016/j.ijheatmasstransfer.2006.12.019 (see p. 63)

[261] U. Tallarek, E. Bayer, and G. Guiochon. Study of dispersion in packed chromatographic columns by pulsed field gradient nuclear magnetic resonance. *Journal of the American Chemical Society*, **120**: 1494–1505, 1998. doi: 10.1021/ja9726623 (see pp. 63, 92, 95, 106, 117, 123)

[262] D. Kandhai, D. Hlushkou, A. G. Hoekstra, P. M. A. Sloot, H. Van As, and U. Tallarek. Influence of stagnant zones on transient and asymptotic dispersion in macroscopically homogeneous porous media. *Physical Review Letters*, **88**: 234501, 2002. doi: 10.1103/PhysRevLett.88.234501 (see pp. 63, 87, 92)

[263] S. Ehlert, T. Rösler, and U. Tallarek. Packing density of slurry-packed capillaries at low aspect ratios. *Journal of Separation Science*, **31**: 1719–1728, 2008. doi: 10.1002/jssc.200800018 (see pp. 65, 78)

[264] P. S. Dittrich and A. Manz. Lab-on-a-chip: microfluidics in drug discovery. *Nature Reviews Drug Discovery*, **5**: 210–218, 2006. doi: 10.1038/nrd1985 (see p. 75)

[265] K. Ohno, K. Tachikawa, and M. Manz. Microfluidics: Applications for analytical purposes in chemistry and biochemistry. *Electrophoresis*, **29**: 4443–4453, 2008. doi: 10.1002/elps.200800121 (see p. 75)

[266] G. P. Rozing. Trends in HPLC column formats — microbore, nanobore and smaller. *LC-GC Europe*, **16**: 14–19, 2003. (see p. 75)

[267] J. M. Saz and M. L. Marina. Application of micro- and nano-HPLC to the determination and characterization of bioactive and biomarker peptides. *Journal of Separation Science*, **31**: 446–458, 2008. doi: 10.1002/jssc.200700589 (see p. 75)

[268] A. Bhattacharyya and C. M. Klapperich. Thermoplastic microfluidic device for on-chip purification of nucleic acids for disposable diagnostics. *Analytical Chemistry*, **78**: 788–792, 2006. doi: 10.1021/ac051449j (see p. 76)

[269] J. F. Borowsky, B. C. Giordano, Q. Lu, A. Terray, and G. E. Collins. Electroosmotic flow-based pump for liquid chromatography on a planar microchip. *Analytical Chemistry*, **80**: 8287–8292, 2008. doi: 10.1021/ac801497r (see p. 76)

[270] M. T. KOESDJOJO, C. R. KOCH, and V. T. REMCHO. Technique for microfabrication of polymeric-based microchips from an SU-8 master with temperature-assisted vaporized organic solvent bonding. *Analytical Chemistry*, **81**: 1652–1659, 2009. DOI: 10.1021/ac802450u (see p. 76)

[271] J. LI and P. W. CARR. Accuracy of empirical correlations for estimating diffusion coefficients in aqueous organic mixtures. *Analytical Chemistry*, **69**: 2530–2536, 1997. DOI: 10.1021/ac961005a (see p. 78)

[272] D. KANDHAI, U. TALLAREK, D. HLUSHKOU, A. G. HOEKSTRA, P. M. A. SLOOT, and H. VAN AS. Numerical simulation and measurement of liquid hold-up in biporous media containing discrete stagnant zones. *Philosophical Transactions of the Royal Society A: Mathematical, Physical & Engineering Sciences*, **360**: 521–534, 2002. DOI: 10.1098/rsta.2001.0952 (see p. 79)

[273] K. BROECKHOVEN and G. DESMET. Approximate transient and long time limit solutions for the band broadening induced by the thin sidewall-layer in liquid chromatography columns. *Journal of Chromatography A*, **1172**: 25–39, 2007. DOI: 10.1016/j.chroma.2007.09.052 (see p. 86)

[274] J. H. KNOX. Band dispersion in chromatography — a new view of *A*-term dispersion. *Journal of Chromatography A*, **831**: 3–15, 1999. DOI: 10.1016/S0021-9673(98)00497-X (see pp. 87, 94, 95, 98, 118)

[275] J. H. KNOX. Band dispersion in chromatography — a universal expression for the contribution from the mobile zone. *Journal of Chromatography A*, **960**: 7–18, 2002. DOI: 10.1016/S0021-9673(02)00240-6 (see pp. 87, 95, 117)

[276] S. G. WEBER and P. W. CARR. In: *High Performance Liquid Chromatography*. P. R. BROWN and R. A. HARTWICK, eds. Chap. 1. John Wiley & Sons, 1989. (see pp. 90, 103, 116)

[277] F. GRITTI and G. GUIOCHON. General HETP equation for the study of mass-transfer mechanisms in RPLC. *Analytical Chemistry*, **78**: 5329–5347, 2006. DOI: 10.1021/ac060203r (see pp. 92, 94, 116, 117)

[278] U. TALLAREK, F. J. VERGELDT, and H. VAN AS. Stagnant mobile phase mass transfer in chromatographic media: Intraparticle diffusion and exchange kinetics. *Journal of Physical Chemistry B*, **103**: 7654–7664, 1999. DOI: 10.1021/jp990828b (see p. 92)

[279] G. GUIOCHON. The limits of the separation power of unidimensional column liquid chromatography. *Journal of Chromatography A*, **1126**: 6–49, 2006. DOI: 10.1016/j.chroma.2006.07.032 (see pp. 92, 109)

[280] K. BROECKHOVEN and G. DESMET. Numerical and analytical solutions for the column length-dependent band broadening originating from axisymmetrical trans-column velocity gradients. *Journal of Chromatography A*, **1216**: 1325–1337, 2009. DOI: 10.1016/j.chroma.2008.12.065 (see p. 92)

[281] J. H. KNOX, G. R. LAIRD, and P. A. RAVEN. Interaction of radial and axial dispersion in liquid chromatography in relation to the "infinite diameter effect". *Journal of Chromatography*, **122**: 129–145, 1976. DOI: 10.1016/S0021-9673(00)82240-2 (see p. 92)

[282] C. H. EON. Comparison of broadening patterns in regular and radially compressed large-diameter columns. *Journal of Chromatography*, **149**: 29–42, 1978. DOI: 10.1016/S0021-9673(00)80977-2 (see p. 92)

[283] R. A. SHALLIKER, B. S. BROYLES, and G. GUIOCHON. Axial and radial diffusion coefficients in a liquid chromatography column and bed heterogeneity. *Journal of Chromatography A*, **994**: 1–12, 2003. DOI: 10.1016/S0021-9673(03)00311-X (see p. 92)

[284] S. STAPF, K. J. PACKER, R. G. GRAHAM, J.-F. THOVERT, and P. M. ADLER. Spatial correlations and dispersion for fluid transport through packed glass beads studied by pulsed field-gradient NMR. *Physical Review E*, **58**: 6206–6221, 1998. DOI: 10.1103/PhysRevE.58.6206 (see pp. 92, 110)

[285] K. BROECKHOVEN, D. CABOOTER, F. LYNEN, P. SANDRA, and G. DESMET. Errors involved in the existing *B*-term expressions for the longitudinal diffusion in fully porous chromatographic media: Part II: Experimental data in packed columns and surface diffusion measurements. *Journal of Chromatography A*, **1188**: 189–198, 2008. DOI: 10.1016/j.chroma.2008.02.058 (see p. 94)

[286] J. C. GIDDINGS. 'Eddy' diffusion in chromatography. *Nature*, **184**: 357–358, 1959. DOI: 10.1038/184357a0 (see pp. 94, 102, 117, 123, 136)

[287] K. MIYABE and G. GUIOCHON. Measurement of the parameters of the mass transfer kinetics in high performance liquid chromatography. *Journal of Separation Science*, **26**: 155–173, 2003. DOI: 10.1002/jssc.200390024 (see pp. 94, 117)

[288] G. DESMET and K. BROECKHOVEN. Equivalence of the different C_m- and C_s-term expressions used in liquid chromatography and a geometrical model uniting them. *Analytical Chemistry*, **80**: 8076–8088, 2008. DOI: 10.1021/ac8011363 (see p. 94)

[289] J. J. VAN DEEMTER, F. J. ZUIDERWEG, and A. KLINKENBERG. Longitudinal diffusion and resistance to mass transfer as causes of nonideality in chromatography. *Chemical Engineering Science*, **5**: 271–289, 1956. DOI: 10.1016/0009-2509(56)80003-1 (see pp. 94, 123)

[290] P. MAGNICO and M. MARTIN. Dispersion in the interstitial space of packed columns. *Journal of Chromatography*, **517**: 31–49, 1990. DOI: 10.1016/S0021-9673(01)95708-5 (see pp. 95, 117)

[291] O. BEY and G. EIGENBERGER. Fluid flow through catalyst filled tubes. *Chemical Engineering Science*, **52**: 1365–1376, 1997. DOI: 10.1016/S0009-2509(96)00509-X (see p. 96)

[292] G. GUIOCHON, E. DRUMM, and D. CHERRAK. Evidence of a wall friction effect in the consolidation of beds of packing materials in chromatographic columns. *Journal of Chromatography A*, **835**: 41–58, 1999. DOI: 10.1016/S0021-9673(98)01068-1 (see p. 98)

[293] R. A. SHALLIKER, V. WONG, B. S. BROYLES, and G. GUIOCHON. Visualization of bed compression in an axial compression liquid chromatography column. *Journal of Chromatography A*, **977**: 213–223, 2002. DOI: 10.1016/S0021-9673(02)01273-6 (see p. 98)

[294] J. H. KNOX and J. F. PARCHER. Effect of the column to particle diameter ratio on the dispersion of unsorbed solutes in chromatography. *Analytical Chemistry*, **41**: 1599–1606, 1969. DOI: 10.1021/ac60281a009 (see p. 98)

[295] K. D. PATEL, A. D. JERKOVICH, J. C. LINK, and J. W. JORGENSON. In-depth characterization of slurry packed capillary columns with 1.0-μm nonporous particles using reversed-phase isocratic ultrahigh-pressure liquid chromatography. *Analytical Chemistry*, **76**: 5777–5786, 2004. DOI: 10.1021/ac049756x (see pp. 98, 104)

[296] E. VANDRE, R. S. MAIER, D. M. KROLL, A. MCCORMICK, and H. T. DAVIS. Diameter-dependent dispersion in cylindrical bead packs. *AIChE Journal*, **54**: 2024–2028, 2008. DOI: 10.1002/aic.11529 (see p. 98)

[297] J. TOBIS' and D. VORTMEYER. Scale-up effects due to near-wall channelling in isothermal adsorption columns: on the limitations in the use of plug flow models. *Chemical Engineering and Processing: Process Intensification*, **29**: 147–153, 1991. DOI: 10.1016/0255-2701(91)85014-F (see p. 98)

[298] L. L. LATOUR, P. P. MITRA, R. L. KLEINBERG, and C. H. SOTAK. Time-dependent diffusion coefficient of fluids in porous media as a probe of surface-to-volume ratio. *Journal of Magnetic Resonance, Series A*, **101**: 342–346, 1993. DOI: 10.1006/jmra.1993.1056 (see p. 102)

[299] J. M. ZALC, S. C. REYES, and E. IGLESIA. The effects of diffusion mechanism and void structure on transport rates and tortuosity factors in complex porous structures. *Chemical Engineering Science*, **59**: 2947–2960, 2004. DOI: 10.1016/j.ces.2004.04.028 (see p. 102)

[300] K. M. USHER, C. R. SIMMONS, and J. G. DORSEY. Modeling chromatographic dispersion: A comparison of popular equations. *Journal of Chromatography A*, **1200**: 122–128, 2008. DOI: 10.1016/j.chroma.2008.05.073 (see pp. 106, 123)

[301] J. C. GIDDINGS and E. N. FULLER. Particle size nonuniformity in large scale columns. *Journal of Chromatography*, **7**: 255–258, 1962. DOI: 10.1016/S0021-9673(01)86405-0 (see p. 106)

[302] S. KHIREVICH, A. DANEYKO, A. HÖLTZEL, A. SEIDEL-MORGENSTERN, and U. TALLAREK. Statistical analysis of packed beds, the origin of short-range disorder, and its impact on eddy dispersion. *Journal of Chromatography A*, **1217**: 4713–4722, 2010. DOI: 10.1016/j.chroma.2010.05.019 (see p. 108)

[303] S. TORQUATO. *Random heterogeneous materials: microstructure and macroscopic properties*. Springer, 2002. (see p. 108)

[304] J. D. BERNAL. A geometrical approach to the structure of liquids. *Nature*, **183**: 141–147, 1959. DOI: 10.1038/183141a0 (see p. 108)

[305] J. D. BERNAL and J. MASON. Packing of spheres: co-ordination of randomly packed spheres. *Nature*, **188**: 910–911, 1960. DOI: 10.1038/188910a0 (see p. 108)

[306] J. D. BERNAL. The Bakerian Lecture, 1962. The structure of liquids. *Philosophical Transactions of the Royal Society A: Mathematical, Physical & Engineering Sciences*, **280**: 299–322, 1964. DOI: 10.1098/rspa.1964.0147 (see p. 108)

[307] T. ASTE and D. L. WEAIRE. *The pursuit of perfect packing*. Taylor & Francis, 2000. (see p. 108)

[308] A. CONIGLIO, A. FIERRO, H. J. HERRMANN, and M. NICODEMI, eds. *Unifying concepts in granular media and glasses*. Elsevier, 2004. (see p. 108)

[309] S. F. EDWARDS and R. B. S. OAKESHOTT. Theory of powders. *Physica A: Statistical and Theoretical Physics*, **157**: 1080–1090, 1989. DOI: 10.1016/0378-4371(89)90034-4 (see pp. 108, 116)

[310] S. TORQUATO, T. M. TRUSKETT, and P. G. DEBENEDETTI. Is random close packing of spheres well defined? *Physical Review Letters*, **84**: 2064–2067, 2000. DOI: 10.1103/PhysRevLett.84.2064 (see pp. 109, 110, 116)

[311] S. TORQUATO and F. H. STILLINGER. Multiplicity of generation, selection, and classification procedures for jammed hard-particle packings. *Journal of Physical Chemistry B*, **105**: 11849–11853, 2001. DOI: 10.1021/jp011960q (see p. 109)

[312] K. BAGI. On the concept of jammed configurations from a structural mechanics perspective. *Granular Matter*, **9**: 109–134, 2007. DOI: 10.1007/s10035-006-0016-0 (see p. 109)

[313] C. BRISCOE, C. SONG, P. WANG, and H. A. MAKSE. Entropy of jammed matter. *Physical Review Letters*, **101**: 188001, 2008. DOI: 10.1103/PhysRevLett.101.188001 (see p. 109)

[314] N. C. KARAYIANNIS, K. FOTEINOPOULOU, and M. LASO. Contact network in nearly jammed disordered packings of hard-sphere chains. *Physical Review E*, **80**: 011307, 2009. DOI: 10.1103/PhysRevE.80.011307 (see p. 109)

[315] K. K. UNGER, R. SKUDAS, and M. M. SCHULTE. Particle packed columns and monolithic columns in high-performance liquid chromatography — comparison and critical appraisal. *Journal of Chromatography A*, **1184**: 393–415, 2008. DOI: 10.1016/j.chroma.2007.11.118 (see p. 109)

[316] B. G. YEW, J. URETA, R. A. SHALLIKER, E. C. DRUMM, and G. GUIOCHON. Mechanics of column beds: II. Modeling of coupled stress–strain-flow behavior. *AIChE Journal*, **49**: 642–664, 2003. DOI: 10.1002/aic.690490310 (see p. 109)

[317] H. P. ZHU, Z. Y. ZHOU, R. Y. YANG, and A. B. YU. Discrete particle simulation of particulate systems: Theoretical developments. *Chemical Engineering Science*, **62**: 3378–3396, 2007. DOI: 10.1016/j.ces.2006.12.089 (see p. 109)

[318] H. P. ZHU, Z. Y. ZHOU, R. Y. YANG, and A. B. YU. Discrete particle simulation of particulate systems: A review of major applications and findings. *Chemical Engineering Science*, **63**: 5728–5770, 2008. DOI: 10.1016/j.ces.2008.08.006 (see p. 109)

[319] R. D. KAMIEN and A. J. LIU. Why is random close packing reproducible? *Physical Review Letters*, **99**: 155501, 2007. DOI: 10.1103/PhysRevLett.99.155501 (see pp. 109, 113, 116)

[320] A. V. ANIKEENKO, N. N. MEDVEDEV, and T. ASTE. Structural and entropic insights into the nature of the random-close-packing limit. *Physical Review E*, **77**: 031101, 2008. DOI: 10.1103/PhysRevE.77.031101 (see pp. 109, 116, 132)

[321] T. ASTE and T. DI MATTEO. Structural transitions in granular packs: statistical mechanics and statistical geometry investigations. *European Physical Journal B: Condensed Matter and Complex Systems*, **64**: 511–517, 2008. DOI: 10.1140/epjb/e2008-00224-8 (see pp. 109, 116)

[322] K. E. THOMPSON and H. S. FOGLER. Modeling flow in disordered packed beds from pore-scale fluid mechanics. *AIChE Journal*, **43**: 1377–1389, 1997. DOI: 10.1002/aic.690430602 (see pp. 110, 132)

[323] M. D. MANTLE, A. J. SEDERMAN, and L. F. GLADDEN. Single- and two-phase flow in fixed-bed reactors: MRI flow visualisation and lattice-Boltzmann simulations. *Chemical Engineering Science*, **56**: 523–529, 2001. DOI: 10.1016/S0009-2509(00)00256-6 (see p. 110)

[324] R. J. HILL, D. L. KOCH, and A. J. C. LADD. The first effects of fluid inertia on flows in ordered and random arrays of spheres. *Journal of Fluid Mechanics*, **448**: 213–241, 2001. DOI: 10.1017/S0022112001005948 (see p. 110)

[325] M. R. SCHURE and R. S. MAIER. How does column packing microstructure affect column efficiency in liquid chromatography? *Journal of Chromatography A*, **1126**: 58–69, 2006. DOI: 10.1016/j.chroma.2006.05.066 (see pp. 110, 118, 129)

[326] G. VORONOI. Nouvelles applications des paramètres continus à théorie des formes quadratiques. Deuxième mémoire. Recherches sur les parallélo\u00e8dres primitifs. *Journal für die reine und angewandte Mathematik*, **136**: 67–182, 1909. DOI: 10.1515/crll.1909.136.67 (see pp. 113, 114)

[327] J. L. FINNEY. Random packings and the structure of simple liquids. I. The geometry of random close packing. *Philosophical Transactions of the Royal Society A: Mathematical, Physical & Engineering Sciences*, **319**: 479–493, 1970. DOI: 10.1098/rspa.1970.0189 (see p. 113)

[328] R. JULLIEN, P. JUND, D. CAPRION, and D. QUITMANN. Computer investigation of long-range correlations and local order in random packings of spheres. *Physical Review E*, **54**: 6035–6041, 1996. DOI: 10.1103/PhysRevE.54.6035 (see pp. 113, 116)

[329] L. OGER, A. GERVOIS, J.-P. TROADEC, and N. RIVIER. Voronoi tessellation of packings of spheres: Topological correlation and statistics. *Philosophical Magazine*, **74**: 177–197, 1996. DOI: 10.1080/01418639608240335 (see p. 113)

[330] P. L. SPEDDING and R. M. SPENCER. Simulation of packing density and liquid flow fixed beds — II. Voronoi polyhedra studies. *Computers & Chemical Engineering*, **22**: 247–257, 1998. DOI: 10.1016/S0098-1354(97)88452-9 (see p. 113)

[331] P. RICHARD, L. OGER, J. LEMAÎTRE, L. SAMSON, and N. N. MEDVEDEV. Application of the Voronoï tessellation to study transport and segregation of grains inside 2D and 3D packings of spheres. *Granular Matter*, **1**: 203–211, 1999. DOI: 10.1007/s100350050026 (see p. 113)

[332] R. Y. YANG, R. P. ZOU, and A. B. YU. Voronoi tessellation of the packing of fine uniform spheres. *Physical Review E*, **65**: 041302, 2002. DOI: 10.1103/PhysRevE.65.041302 (see pp. 113, 116)

[333] J. Q. XU, R. P. ZOU, and A. B. YU. Analysis of the packing structure of wet spheres by Voronoi–Delaunay tessellation. *Granular Matter*, **9**: 455–463, 2007. DOI: 10.1007/s10035-007-0052-4 (see pp. 113, 132)

[334] A. V. ANIKEENKO and N. N. MEDVEDEV. Polytetrahedral nature of the dense disordered packings of hard spheres. *Physical Review Letters*, **98**: 235504, 2007. DOI: 10.1103/PhysRevLett.98.235504 (see p. 113)

[335] T. ASTE and T. DI MATTEO. Emergence of Gamma distributions in granular materials and packing models. *Physical Review E*, **77**: 021309, 2008. DOI: 10.1103/PhysRevE.77.021309 (see pp. 113, 116, 126)

[336] I. SCHENKER, F. T. FILSER, L. J. GAUCKLER, T. ASTE, and H. J. HERRMANN. Quantification of the heterogeneity of particle packings. *Physical Review E*, **80**: 021302, 2009. DOI: 10.1103/PhysRevE.80.021302 (see pp. 113, 114, 126)

[337] C. B. BARBER, D. P. DOBKIN, and H. HUHDANPAA. The QUICKHULL algorithm for convex hulls. *ACM Transactions on Mathematical Software*, **22**: 469–483, 1996. DOI: 10.1145/235815.235821 (see pp. 114, 128)

[338] A. L. BERDICHEVSKY and U. D. NEUE. Nature of the eddy dispersion in packed beds. *Journal of Chromatography*, **535**: 189–198, 1990. DOI: 10.1016/S0021-9673(01)88944-5 (see p. 116)

[339] J. C. MAXWELL. *A treatise on electricity and magnetism*. 2nd ed. Clarendon Press, 1881. (see pp. 125, 126)

[340] B. P. BOUDREAU. The diffusive tortuosity of fine-grained unlithified sediments. *Geochimica et Cosmochimica Acta*, **60**: 3139–3142, 1996. DOI: 10.1016/0016-7037(96)00158-5 (see pp. 126, 131)

[341] L. SHEN and Z. CHEN. Critical review of the impact of tortuosity on diffusion. *Chemical Engineering Science*, **62**: 3748–3755, 2007. DOI: 10.1016/j.ces.2007.03.041 (see p. 126)

[342] M. MATYKA, A. KHALILI, and Z. KOZA. Tortuosity–porosity relation in porous media flow. *Physical Review E*, **78**: 026306, 2008. DOI: 10.1103/PhysRevE.78.026306 (see pp. 126, 131)

[343] H. L. WEISSBERG. Effective diffusion coefficient in porous media. *Journal of Applied Physics*, **34**: 2636–2639, 1963. DOI: 10.1063/1.1729783 (see pp. 126, 131)

[344] E. MAURET and M. RENAUD. Transport phenomena in multi-particle systems — I. Limits of applicability of capillary model in high voidage beds-application to fixed beds of fibers and fluidized beds of spheres. *Chemical Engineering Science*, **52**: 1807–1817, 1997. DOI: 10.1016/S0009-2509(96)00499-X (see pp. 126, 131)

[345] J. P. DU PLESSIS and J. H. MASLIYAH. Mathematical modelling of flow through consolidated isotropic porous media. *Transport in Porous Media*, **3**: 145–161, 1988. DOI: 10.1007/BF00820342 (see p. 126)

[346] M.-J. YUN, B.-M. YU, B. ZHANG, and M.-T. HUANG. A geometry model for tortuosity of streamtubes in porous media with spherical particles. *Chinese Physics Letters*, **22**: 1464–1467, 2005. DOI: 10.1088/0256-307X/22/6/046 (see p. 126)

[347] P.-Y. LANFREY, Z. V. KUZELJEVIC, and M. P. DUDUKOVIC. Tortuosity model for fixed beds randomly packed with identical particles. *Chemical Engineering Science*, **65**: 1891–1896, 2010. DOI: 10.1016/j.ces.2009.11.011 (see p. 126)

[348] E. DU PLESSIS, S. WOUDBERG, and J. P. DU PLESSIS. Pore-scale modelling of diffusion in unconsolidated porous structures. *Chemical Engineering Science*, **65**: 2541–2551, 2010. DOI: 10.1016/j.ces.2009.12.033 (see p. 126)

[349] M. BARRANDE, R. BOUCHET, and R. DENOYEL. Tortuosity of porous particles. *Analytical Chemistry*, **79**: 9115–9121, 2007. DOI: 10.1021/ac071377r (see p. 131)

[350] S. BRYANT, G. MASON, and D. MELLOR. Quantification of spatial correlation in porous media and its effect on mercury porosimetry. *Journal of Colloid and Interface Science*, **177**: 88–100, 1996. DOI: 10.1006/jcis.1996.0009 (see p. 132)

[351] R. AL-RAOUSH, K. THOMPSON, and C. S. WILLSON. Comparison of network generation techniques for unconsolidated porous media. *Soil Science Society of America Journal*, **67**: 1687–1700, 2003. DOI: 10.2136/sssaj2003.1687 (see p. 132)

[352] R. Y. YANG, R. P. ZOU, A. B. YU, and S. K. CHOI. Pore structure of the packing of fine particles. *Journal of Colloid and Interface Science*, **299**: 719–725, 2006. DOI: 10.1016/j.jcis.2006.02.041 (see p. 132)

[353] S. RÉMOND, J. L. GALLIAS, and A. MIZRAHI. Characterization of voids in spherical particle systems by Delaunay empty spheres. *Granular Matter*, **10**: 329–334, 2008. DOI: 10.1007/s10035-008-0092-4 (see p. 132)

[354] N. REBOUL, ERIC VINCENS, and B. CAMBOU. A statistical analysis of void size distribution in a simulated narrowly graded packing of spheres. *Granular Matter*, **10**: 457–468, 2008. DOI: 10.1007/s10035-008-0111-5 (see p. 132)

[355] S. JUNG, A. HÖLTZEL, S. EHLERT, J.-A. MORA, K. KRAICZEK, M. DITTMANN, G. P. ROZING, and U. TALLAREK. Impact of conduit geometry on the performance of typical particulate microchip packings. *Analytical Chemistry*, **81**: 10193–10200, 2009. DOI: 10.1021/ac902069x (see p. 135)

[356] S. BLANCO and R. FOURNIER. An invariance property of diffusive random walks. *EPL*, **61**: 168–173, 2003. DOI: 10.1209/epl/i2003-00208-x (see p. 136)

[357] O. BÉNICHOU, M. COPPEY, M. MOREAU, P. H. SUET, and R. VOITURIEZ. Averaged residence times of stochastic motions in bounded domains. *EPL*, **70**: 42–48, 2005. DOI: 10.1209/epl/i2005-10001-y (see p. 136)

[358] V. MOURZENKO, J.-F. THOVERT, O. VIZIKA, and P. M. ADLER. Geometrical and transport properties of random packings of polydisperse spheres. *Physical Review E*, **77**: 066306, 2008. DOI: 10.1103/PhysRevE.77.066306 (see p. 136)

[359] A. G. DIXON and M. NIJEMEISLAND. CFD as a design tool for fixed-bed reactors. *Industrial & Engineering Chemistry Research*, **40**: 5246–5254, 2001. DOI: 10.1021/ie001035a (see p. 136)

[360] A. V. ANIKEENKO, N. N. MEDVEDEV, M. K. KOVALEV, and M. S. MELGUNOV. Simulation of gas diffusion in porous layers of varying structure. *Journal of Structural Chemistry*, **50**: 403–410, 2009. DOI: 10.1007/s10947-009-0061-8 (see p. 136)

[361] K. SCHNITZLEIN. Modelling radial dispersion in terms of the local structure of packed beds. *Chemical Engineering Science*, **56**: 579–585, 2001. DOI: 10.1016/S0009-2509(00)00263-3 (see p. 136)

Acknowledgments

I am sincerely grateful to my supervisor Prof. Dr. Ulrich Tallarek for his guidance and help throughout my doctoral studies. It was a great opportunity to work in his group: together with Dr. Alexandra Hoeltzel, Prof. Tallarek created a very productive environment for producing and publishing scientific results.

I thank Dr. Dzmitry Hlushkou for introducing me to the lattice-Boltzmann and random walk particle tracking methods, for many fruitful scientific discussions, and critical appraisal of my ideas.

I am thankful to Prof. Dr. Andreas Seidel-Morgenstern for the opportunity to get the access to the computational centers of Max Planck Society, Gesellschaft für wissenschaftliche Datenverarbeitung mbH Göttingen (GWDG) and Rechenzentrum Garching (RZG). Experience obtained while working with the supercomputers installed at GWDG and RZG allowed me later to access the world's largest systems like JUGENE at Forschungszentrum Jülich (FZJ).

I am deeply indebted to Anton Daneyko for sharing his programming experience, many useful scientific discussions, and friendly conversations. I am grateful to Dr. Steffen Ehlert, Stephanie Jung, and Stefan Bruns for many productive conversations and providing high-quality experimental data.

I am very thankful to Prof. Dr. Irina Ginzburg and Dr. Alexander Kuzmin for the useful discussions on the LBM, and Jan Götz for the conversations on the performance aspects of the LBM program realization.

I thank the staff of GWDG, RZG, and FZJ computational centers for their professional and prompt assistance with problems which occurred before, during, and after the large-scale program runs accompanying a collection of the results for this thesis.

I express my gratitude to Anton Daneyko, Dr. Alina Filatova and Dr. Dmitry Gorbunov, Tibor Müllner, Siarhei Samsonau, and Oleg Lobachev for the thoughtful proofreading of this thesis.

I owe my deepest gratitude to my parents, my wife Snezhana, and my son Igor for their love, support, and understanding.

List of publications

1. D. HLUSHKOU, S. KHIREVICH, V. V. APANASOVICH, and U. TALLAREK. Pore-scale dispersion in electrokinetic flow through a random sphere packing. *Analytical Chemistry*, **79**: 113–121, 2007. DOI: 10.1021/ac061168r
2. S. KHIREVICH, A. HÖLTZEL, D. HLUSHKOU, and U. TALLAREK. Impact of conduit geometry and bed porosity on flow and dispersion in noncylindrical sphere packings. *Analytical Chemistry*, **79**: 9340–9349, 2007. DOI: 10.1021/ac071428k
3. S. KHIREVICH, A. HÖLTZEL, D. HLUSHKOU, A. SEIDEL-MORGENSTERN, and U. TALLAREK. Structure–transport analysis for particulate packings in trapezoidal microchip separation channels. *Lab on a Chip*, **8**: 1801–1808, 2008. DOI: 10.1039/b810688f
4. S. KHIREVICH, A. HÖLTZEL, S. EHLERT, A. SEIDEL-MORGENSTERN, and U. TALLAREK. Large-scale simulation of flow and transport in reconstructed HPLC-microchip packings. *Analytical Chemistry*, **81**: 4937–4945, 2009. DOI: 10.1021/ac900631d
5. S. KHIREVICH, A. HÖLTZEL, A. SEIDEL-MORGENSTERN, and U. TALLAREK. Time and length scales of eddy dispersion in chromatographic beds. *Analytical Chemistry*, **81**: 7057–7066, 2009. DOI: 10.1021/ac901187d
6. S. KHIREVICH, A. DANEYKO, A. HÖLTZEL, A. SEIDEL-MORGENSTERN, and U. TALLAREK. Statistical analysis of packed beds, the origin of short-range disorder, and its impact on eddy dispersion. *Journal of Chromatography A*, **1217**: 4713–4722, 2010. DOI: 10.1016/j.chroma.2010.05.019
7. S. KHIREVICH, A. HÖLTZEL, and U. TALLAREK. Transient and asymptotic dispersion in confined sphere packings with cylindrical and noncylindrical conduit geometries. *Philosophical Transactions of the Royal Society A: Mathematical, Physical & Engineering Sciences*, accepted.

This thesis, containing 51 figures and 5 tables, was typeset with LaTeX using Bitstream Charter, Computer Modern, and TeX Gyre Heros type faces. The artwork was prepared using CorelDRAW® (vector graphics; publishing of final figures to PDF), Corel PHOTO-PAINT® (bitmap graphics), and POV-Ray™ (3D graphics). A copy of this thesis can be downloaded from the author's web site: www.khirevich.com